Acta Pharmacologica Sinica (2012) 33: 1217–1245
 1671-4083/12 $32.00
www.nature.com/aps

Review

Natural products possessing protein tyrosine phosphatase 1B (PTP1B) inhibitory activity found in the last decades

Cheng-shi JIANG#, Lin-fu LIANG#, Yue-wei GUO*

State Key Laboratory of Drug Research, Shanghai Institute of Materia Medica, Chinese Academy of Sciences, Shanghai 201203, China

This article provides an overview of approximately 300 secondary metabolites with inhibitory activity against protein tyrosine phosphatase 1B (PTP1B), which were isolated from various natural sources or derived from synthetic process in the last decades. The structure-activity relationship and the selectivity of some compounds against other protein phosphatases were also discussed. Potential pharmaceutical applications of several PTP1B inhibitors were presented.

Keywords: natural products; phytochemistry; protein tyrosine phosphatase 1B (PTP1B); inhibitor; structure-activity relationship (SAR); type 2 diabetes; obesity

Acta Pharmacologica Sinica (2012) 33: 1217–1245; doi: 10.1038/aps.2012.90; published online 3 Sep 2012

Introduction

Type 2 diabetes is a chronic disorder characterized by hyperglycemia associated with a gradual decline in insulin sensitivity and/or insulin secretion. Long-term complications from hyperglycemia can lead to an increased risk of heart attack, stroke, amputation, and kidney failure. According to statistics, more than 220 million people worldwide have diabetes. In 2004, an estimated 3.4 million people died from consequences of hyperglycemia, and this rate continues to increase each year. The WHO projected that diabetes death rates would double between 2005 and 2030. There are four main types of diabetes, including type 1, type 2, gestational diabetes, and drug-induced or chronic pancreatitis-induced diabetes. Type 2 diabetes accounts for 90% the cases of diabetes around the world[1], with obesity contributing to approximately 55% of the cases of type 2 diabetes[2]. It has been suggested that replacing saturated fats and trans fatty acids with unsaturated fats has beneficial effects on insulin sensitivity and may reduce the risk of type 2 diabetes[3]. Thus, it is not surprising that considerable efforts have been made to find drug targets or candidates to treat or cure type 2 diabetes and obesity. Natural products have proved to be an important source of new drugs[4]. An article written by Jung *et al* reviewed medicinal plants that have shown experimental or clinical anti-diabetic activity and that have been used in traditional systems of medicine[5].

Reversible protein tyrosine phosphorylation catalyzed by the coordinated actions of protein tyrosine kinases (PTKs) and phosphatases (PTPs) is important for the regulation of signaling events. Consequently, cellular pathways regulated by tyrosine phosphorylation offer many drug targets for developing novel therapeutics[6]. PTPs are enzymes that catalyze protein tyrosine dephosphorylation. In humans, more than one hundred PTPs exist and function as either negative or positive modulators in various signal transduction pathways[7]. Among the various members of the PTP superfamily, PTP1B is considered to be a negative regulator of insulin receptor (IR) signaling. PTP1B is a promising drug target for the treatment of type 2 diabetes and obesity and is also involved in cancer[8, 9].

A systematic literature search revealed that various natural compounds were reported to exhibit PTP1B inhibitory activity. There are several reviews regarding the development of PTP1B inhibitors but most of them focused on synthetic PTP1B inhibitors[6, 9–15]. Only one review, written by Thareja *et al*, briefly reviewed approximately 50 natural PTP1B inhibitors[15]. According to our literature search, sulfircin **236**, a sesterterpene sulfate isolated as its *N,N*-dimethylguanidinium salt from a deep-water sponge *Ircinia* (unknown species) collected from Andros, Bahamas, appears to be the first reported

# These two authors contributed equally to this article.
* To whom correspondence should be addressed.
E-mail ywguo@mail.shcnc.ac.cn
Received 2012-02-16 Accepted 2012-06-08

natural product with PTP1B inhibitory activity[16]. In 2002, five natural flavonoids were reported as PTP1B inhibitors[17]. Since then, approximately 300 new or known natural products, which possess PTP1B inhibitory activity, have been isolated and identified from various natural resources. Many of the products identified are characterized by remarkable structural diversity with rare carbon and heterocyclic skeletons. Because of the rapid development of natural PTP1B inhibitors and the lack of a comprehensive review regarding natural PTP1B inhibitors until now, it appears a comprehensive review is urgently needed on this topic. This review first gives a brief introduction on the definition and function of PTP1B, and then focuses on the isolation, bioactivities, and synthetic progress of the natural PTP1B inhibitors reported. The structure-activity-relationship (SAR) and the selectivity of some compounds against other protein phosphatases (PPs) are mentioned as well. (In the interest of space, if the activity or inhibitory activity below is not specified, it means PTP1B inhibitory activity.)

Structural biology, mechanism of PTP1B, and its validation as a drug target for diabetes and obesity

The structural biology, mechanism of PTP1B, and its validation as a drug target for diabetes and obesity have been discussed in detail in several reviews[6, 12, 15, 18, 19]. Nevertheless, a brief introduction on PTP1B is presented below.

PTP1B was the first PTP to be isolated in its pure form. The structure of PTP1B was elucidated by X-ray crystallography in 1994, and it has served as a model to illustrate several of the properties of PTPs[20]. The structure consists of 435 amino acids with the catalytic domain comprised of residues 30 to 278 and the 35 COOH-terminal residues target the enzyme to the cytoplasmic face of the endoplamic reticulum. The active site of PTP1B is approximately 8 to 9 Å deep and is defined by residues 214 to 221 (P-loop, phosphate binding loop, His-Cys-Ser-Ala-Gly-Ile-Gly-Arg). The phosphate group of the substrate forms a series of hydrogen bonds with the backbone amide protons of the P-loop and Arg-221. Upon binding of the substrate, the WPD loop (residues 79–187) shifts 10 Å to cover the phenyl phosphate group. This results in Asp-181 being in position to act as a general acid and protonate the ester oxygen. Cys-215 attacks the phosphorous atom resulting in cleavage of the P-O bond and formation of a phosphocysteine intermediate that is then hydrolyzed to give the final products. A number of other residues contribute significantly to peptide substrate recognition, such as Phe182, Tyr46, Lys120, Gln262, Val49, Arg47, and Asp181, by a mixture of hydrophobic, electrostatic and hydrogen-bonding interactions. Studies with phosphotyrosine (pTyr or pY)-bearing peptides indicate that PTP1B has a preference for acidic residues at several positions N-terminal to the pTyr residue[21].

Substantial evidence indicates that PTP1B, as a negative regulator in both insulin and leptin signaling, is a promising drug target for type 2 diabetes and obesity. In the insulin signaling pathway, PTP1B can associate with and dephosphorylate activated IRs or insulin receptor substrates (IRSs). In the leptin pathway, it binds and dephosphorylates JAK2, which is downstream of the receptor. Overexpression of PTP1B in cell cultures decreases insulin-stimulated phosphorylaton of IR and/or IRS-1, whereas a reduction in the level of PTP1B augments insulin-initiated signaling[6]. The genetic analysis of the PTPN1 gene, coding for PTP1B in humans, revealed a significant association with metabolic traits consistent with the proposed *in vivo* role of PTP1B[22]. In murine models, disruption of the PTPN1 gene resulted in resistance to diet-induced obesity and increased insulin sensitivity. The *PTP1B*$^{-}$/$^{-}$ mice had significantly lower triglyceride levels even at feeding on a high-fat diet, and showed an enhanced response toward leptin-mediated weight loss and suppression of feeding[23–25]. In addition, small molecule PTP1B inhibitors can act as both insulin mimetics and insulin sensitizers[26]. Consequently, it has been suggested that the PTP1B inhibitors might have a role in the treatment of type 2 diabetes and obesity.

Natural PTP1B inhibitors

Phenolics

Phenolics are characterized by having at least one aromatic ring with one or more hydroxyl groups attached[27]. According to their structural characteristics, the phenolics discussed below are classified into seven groups, including flavonoids, bromophenol, phenolic acid, phenolics containing furan or pyran rings, coumarins, lignans and miscellaneous phenolics.

Flavonoids

Flavonoids are polyphenolic compounds comprised of 15 carbons, with two aromatic rings connected by a three-carbon bridge. They are the most numerous natural products and exist extensively in nature. Flavonoids include flavonols, flavones, flavanones, isoflavones, catechins, anthocyanidins and chalcones. Their potential beneficial effects, such as antiviral, antitumor, antiplatelet, anti-inflammatory and antioxidant activities, greatly interest chemists and pharmacologists. For example, just between January 2007 and December 2009, 796 new naturally occurring flavonoids were isolated from various natural resources[28].

In 2002, five natural flavonoids, including 8-(1,1-dimethylallyl)-5′-(3-methylbut-2-enyl)-3′,4′,5,7-tetrahydroxyflanvonol **1**, 3′-(3-methylbut-2-enyl)-3′,4′,7-trihydroxyflavane **2**, quercetin **3**, uralenol **4**, and broussochalcone A **5** were isolated from the roots of the plant *Broussonetia papyrifera* collected from Zhibo, Anhui province, China[17]. Flavonoids **1–5** showed inhibitory activity against PTP1B with IC_{50} values ranging from 4.3 to 36.8 μmol/L. The preliminary SAR study indicated that less polar substituents at the 3′,4′,5,7-tetrahydroxyflanvonol skeleton produced stronger inhibitory activities.

Licochalcones A **6**, C **7**, and E **8** were isolated from the CH_2Cl_2 extract of plant *Glycyrrhiza inflate*[29]. Evaluation of the inhibitory activity of licochalcones **6–8**, together with their 4- and/or 4′-hydroxyl group methylated and/or acetylated derivatives indicated that the presence of the allyl group in ring B might increase inhibitory activity. However, the degree of activation varied depending on the configuration and substitution position of the allyl group in ring B and the inhibitory

activity was strongest when 4′-hydroxyl group in **6** was methylated. Licochalcone A **6** was concisely synthesized through water-accelerated [3,3]-sigmatropic rearrangement of an aryl isoprenyl ether as a key step[30]. Licochalcones C **7** was synthesized by a simple, inexpensive high yield method starting from 3-(3-methyl-2-butenyl)-2,4-dihydroxybenzaldehyde[31]. Licochalcone E **8** was first synthesized by employing Claisen rearrangement for synthesis of the key intermediate[32].

Three PTP1B inhibitors, glycyrrhisoflavone **9**, glisoflavone **10**, and licoflavone A **11**, were isolated from the roots of plant *G uralensis*[33]. Of these isolates, glisoflavone **10** showed the strongest inhibitory activity with an IC_{50} of 27.9 μmol/L, and kinetic analysis indicated that it inhibited PTP1B in a mixed-type manner. The presence of an isoprenyl group and an *ortho*-hydroxyl group was considered to be important for exhibiting the activity.

Bioassay-guided fractionation of the $CHCl_3$-soluble fraction of plant *Morus bombycis* led to the isolation of three chalcone-derived Diels-Alder products: kuwanons J **12**, R **13**, and V **14**[34]. All of these kuwanons showed remarkable inhibitory activity with IC_{50} values ranging from 4.3 to 13.8 μmol/L. The order of inhibitory activity of kuwanons was **12>13>14**, suggesting that increasing the number of hydroxyl groups improved the inhibitory effect. Additionally, a kinetics analysis suggested that these kuwanons inhibited PTP1B in a mixed-type manner, indicating that they might displace at both the active site and an additional binding site of the PTP1B.

The plant *Cyclocarya paliurus* has been used as a traditional tonic, and its leaves have been processed as tea products. Quercetin-3-*O*-β-*D*-glucuronide **15** and myricetin-3-*O*-β-*D*-glucuronide **16** were isolated from the leaves of *C paliurus*[35]. Compound **16** (IC_{50}=9.47±3.31 μg/mL) was slightly less active than **15** (IC_{50}=7.39±1.15 μg/mL), indicating that the decrease in activity is attributed to the addition of one hydroxyl group to C-5′ in ring B. As an epimer of **15**, quercetin-3-*O*-α-*D*-glucuronide was inactive, implying that sugar configuration played a key role in *in vitro* inhibitory activity. The synthesis of **15** was achieved in 1970 by coupling 7,4′-dibenzylquercetin with methyl(tri-*O*-acetyl-α-*D*-glucopyranosyl bromide)-uronate followed by total acetylation of the product and subsequent removal of the protecting groups[36].

The herb *Scutellaria indica*, known as 'Han-Xin-Cao' distributed widely in Asia, is traditionally used for hemoptysis, hematemesis, antitumor activity, and the treatment of other diseases in China. From the extract of *S indica*, wogonin **17** and (2*S*)-5,7-dihydroxy-8,2′-dimethoxyflavanone **18** were isolated with weak inhibitory activity[37]. In 2003, Huang *et al* synthesized **17** in 3 steps by a concise and efficient method[38].

Flavonoids **19–23** were isolated from an EtOAc-soluble partition of the MeOH extract of the plant *Tetracera scandens*, a traditional Vietnamese medicinal plant showing some therapeutic activities in inflammation, hepatitis and gout[39]. Flavonoids **19**, **21–23** exhibited stronger inhibitory activity (IC_{50} values ranging from 20.63±0.17 to 37.52±0.31 μmol/L) than **20** (IC_{50}>80 μmol/L). Moreover, compounds **19** and **21–23** exhibited significant glucose-uptake activity in basal and insulin-stimulated L6 myotubes, stimulated AMPK, phosphorylation, and inhibited GLUT4 and GLUT1 mRNA expressions. Furthermore, compounds **19**, **22**, and **23** showed no muscle cell toxicity at levels up to 60 μmol/L, indicating that they could be possible lead candidates for the treatment of type 2 diabetes. Compound **23** had been synthesized by Rao *et al* in 1987[40] (Figure 1).

From fruits of the plant *Pongamia pinnata*, the flowers of which were found to have anti-hyperglycemic and antilipidperoxidative activities[41], pongamol **24** and karanjin **25** were obtained. Both flavonoids exhibited inhibitory activity with IC_{50} values of 75.0 μmol/L and 84.5 μmol/L, and with K_i values of 58 μmol/L and 76 μmol/L, respectively[42]. In Streptozotocin (STZ)-induced diabetic rats, single-dose treatment with **24** and **25** lowered the blood glucose level by 12.8% (P<0.05) and 11.7% (P<0.05) at a 50 mg/kg dose and 22.0% (P<0.01) and 20.7% (P<0.01) at a 100 mg/kg dose, respectively, 6 h post-oral administration. Additionally, they significantly lowered the blood glucose level in db/db mice, which is well characterized as a mode of type 2 diabetes, with percent activities of 35.7% (P<0.01) and 30.6% (P<0.01), respectively, at a 100 mg/kg dose after consecutive treatment for 10 d. Therefore, the anti-hyperglycemic activity of *P pinnata* for STZ-induced diabetic rats and type 2 diabetic db/db mice is likely due to the PTP1B inhibitory effect of **24** and **25**. Pongamol **24** was synthesized by Goel *et al* in 2004 and Yadav *et al* in 2005[43, 44]. Karanjin **25** was synthesized by Hossain *et al* in 2003[45].

The plants in genus *Erythrina* of the Leguminosae family are distributed in tropical and subtropical zones of the world and have been used to treat many ailments. During a study to search for PTP1B inhibitors, Oh *et al* isolated and characterized a series of flavonoids (**26–114**) described below from the extract of the species *Erythrina*. Most of the flavonoids isolated showed significant inhibitory activity against PTP1B[46–54].

Six prenylated isoflavonoids **26–31** were isolated from the EtOAc extract of the stem bark of *E addisoniae*[46]. The bioassay results indicated that **30** (IC_{50}=2.6±0.5 μmol/L) and **31** (IC_{50}=4.1±0.2 μmol/L), both bearing an isoprenyl group and a dimethylpyran moiety in the ring A, exhibited stronger inhibitory activity than **26** (IC_{50}=10.1±0.3 μmol/L), suggesting that cyclization between a hydroxy group at C-7 and one of the isoprenyl groups at C-6 or C-8 in ring A may be important for activity. Moreover, the 2′,4′-dihydroxy group in ring B of isoflavanoids appears to correlate with the inhibitory activity, and a double bond between C-2 and C-3 of the ring might be responsible for a loss of activity.

Bioassay-guided fractionation of an EtOAc-soluble extract of the root bark of *E mildbraedii* yielded flavonoids **19** and **32–39**, which show significant inhibitory activity (IC_{50} ranging from 14.8±1.1 to 39.7±2.5 μmol/L)[47]. Flavonoid **35** (IC_{50}=39.7±2.5 μmol/L), with one more hydroxyl group at C-5, was less active than **36**. A similar observation was made for flavonoids **32** and **33**, indicating that addition of a hydroxyl group to C-5 in ring A may be responsible for the loss of *in vitro* activity. Flavonoid **34** (IC_{50}>60 μmol/L), in which an additional

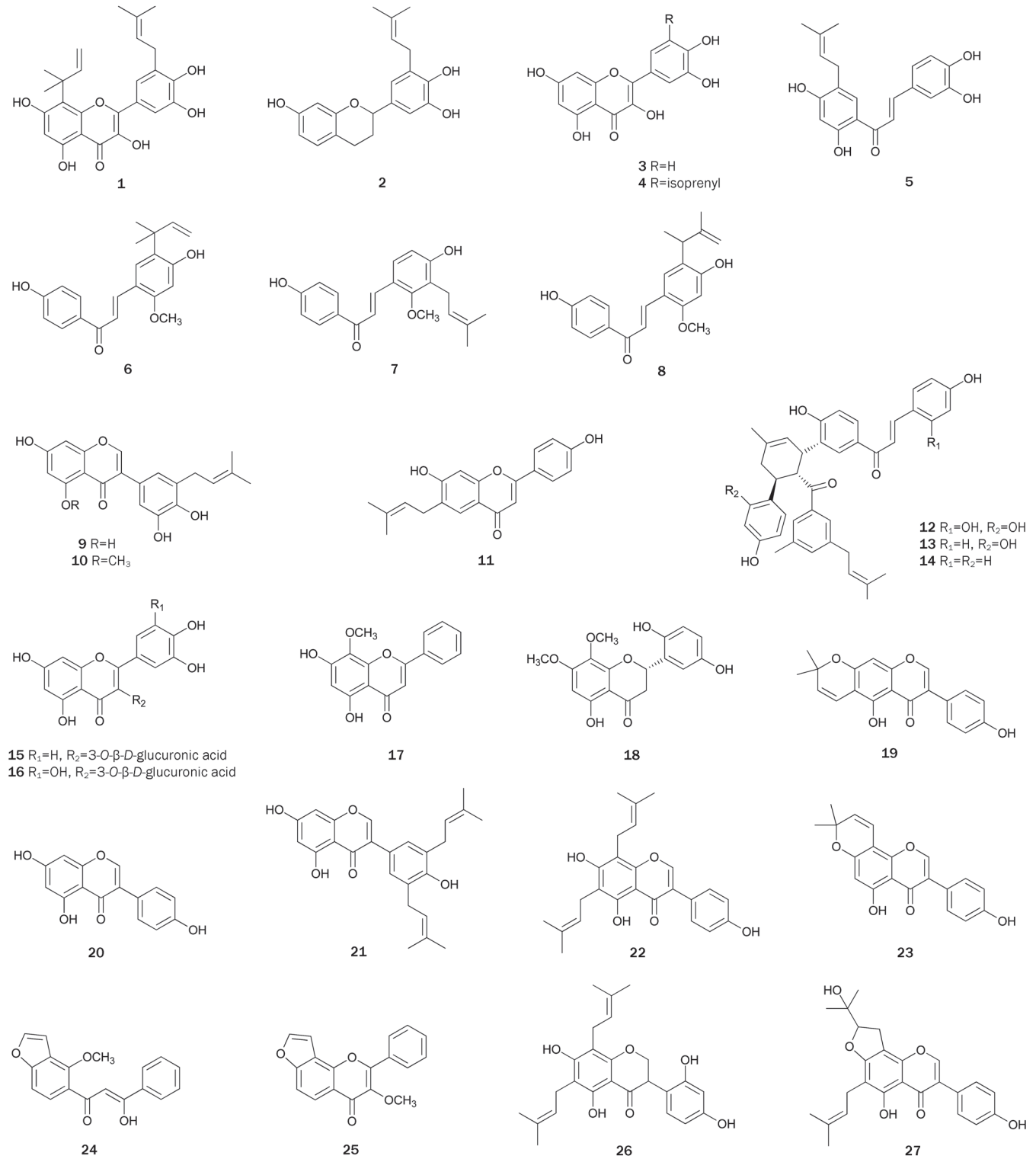

Figure 1. Structures of flavonoids **1–27**.

hydroxyl group is present at C-3″ of the isoprenyl group, exhibited a significantly lower inhibitory activity than **33**. The inhibitory activity of **38** was similar to that of **35**, suggesting that cyclization between a hydroxyl group and one of the isoprenyl groups in ring B may not affect the resultant activity. A group of related flavonoids, commercially available or isolated from other plants[55], was assayed to evaluate the role of the isoprenyl group in ring B in the bioactivity. The

results indicated that substitution of isoprenyl groups in the ring B might be important for inhibitory activity *in vitro*, and introduction of one more hydroxyl group to C-5 of ring A or one of the isoprenyl groups in ring B may be responsible for the loss of activity. Likewise, the presence of isoprenyl groups in ring A seems to be essential for the activity of chalcones[47]. Further studies on the EtOAc-soluble extract of the root bark of *E mildbraedii* led to the isolation of flavonoids **40–45**[48]. With the exception of **43**, which has an isoprenyl group in ring A, the other flavonoids inhibited PTP1B *in vitro* with IC_{50} values ranging from 5.5±0.3 to 42.6±2.4 μmol/L, thus demonstrating that the isoprenyl group in the ring B played an important role in suppressing PTP1B. Recently, flavonoid **33** was synthesized as an inhibitor of prostate cancer and MMP-2 expression[56]. The first synthesis of other flavonoids, such as **35**, **39**, **40**, and **45**, has also been reported[40, 57–59] (Figure 2).

Abyssinoflavanones V–VII **46–48**, together with sigmoidins A-C **49–51**, F **52**, abyssinins I **53**, II **44**, 5-deoxyabyssinin II **54**, 3′-prenylnarringenin **55**, abyssinone-VI **56**, licoagrochalcone A **57**[49], flavonoids **58–73**[50], flavanones **74-79** with a dihydrofuran moiety, erylatissin C **80**, abyssinin III **81**[51], and flavanones **82–93**[52] were isolated from the stem bark of *E abyssinica*. Among the isolates **46–57**, compounds **47–50** and **52–57** strongly inhibited PTP1B in *in vitro* assays with IC_{50} values ranging from 14.2±1.7 to 26.7±1.2 μmol/L. Flavonoids **58**, **60**, **62**, **63**, **65**, and **66** exhibited inhibitory effects on PTP1B in *in vitro* assays with IC_{50} values ranging from 13.9±2.1 to 19.0±1.8 μmol/L. Additionally, compounds **59**, **61**, **64**, and **67–71** with 2,2-dimethylpyrano ring(s), in which isoprenyl and/or methoxyl groups are absent, showed very weak inhibitory effects. Flavonoids **74**, **75**, **77**, and **79–81** inhibited PTP1B in a dose-dependent manner, with IC_{50} values ranging from 15.2±1.2 to 19.6±2.3 μmol/L. Flavonoids **74** and **77** with the isoprenyl group at C-3′, and **75** with methoxyl group at C-3′ exhibited stronger inhibitory activity (IC_{50} 15.2±1.2, 17.9±2.6 μmol/L, respectively) than **76** and **78** (IC_{50}>60 μmol/L, respectively) without an isoprenyl or a methoxyl group. Among flavonoids **82–93**, most flavanones exhibited potent inhibitory effects on PTP1B (IC_{50} ranging from 14.9 to 35.8 μmol/L) except for **83**, **86**, **90**, and **92** (IC_{50}>72 μmol/L). All of these results indicated that the significant inhibitory activity of these flavonoids could be attributed to the isoprenyl or methoxyl groups in the ring B, while the presence of a polar functionality (*eg*, hydroxyl group) caused the activity to decrease. However, the 2,2-dimethylpyrano or dihydrofurano residue was considered to have almost no effect on the inhibitory activity when the isoprenyl or methoxy groups exist in the ring B. Treatment of CHO/*h*IR cells with **75** resulted in a time-dependent increase of the insulin-induced tyrosine phosphorylation of IR and IRS, and cytotoxicity was not observed in cells treated with over 20 μmol/L of **75** for 48 h. These results indicated that **75** might also act in the cells as an insulin-sensitizing agent. Given that those

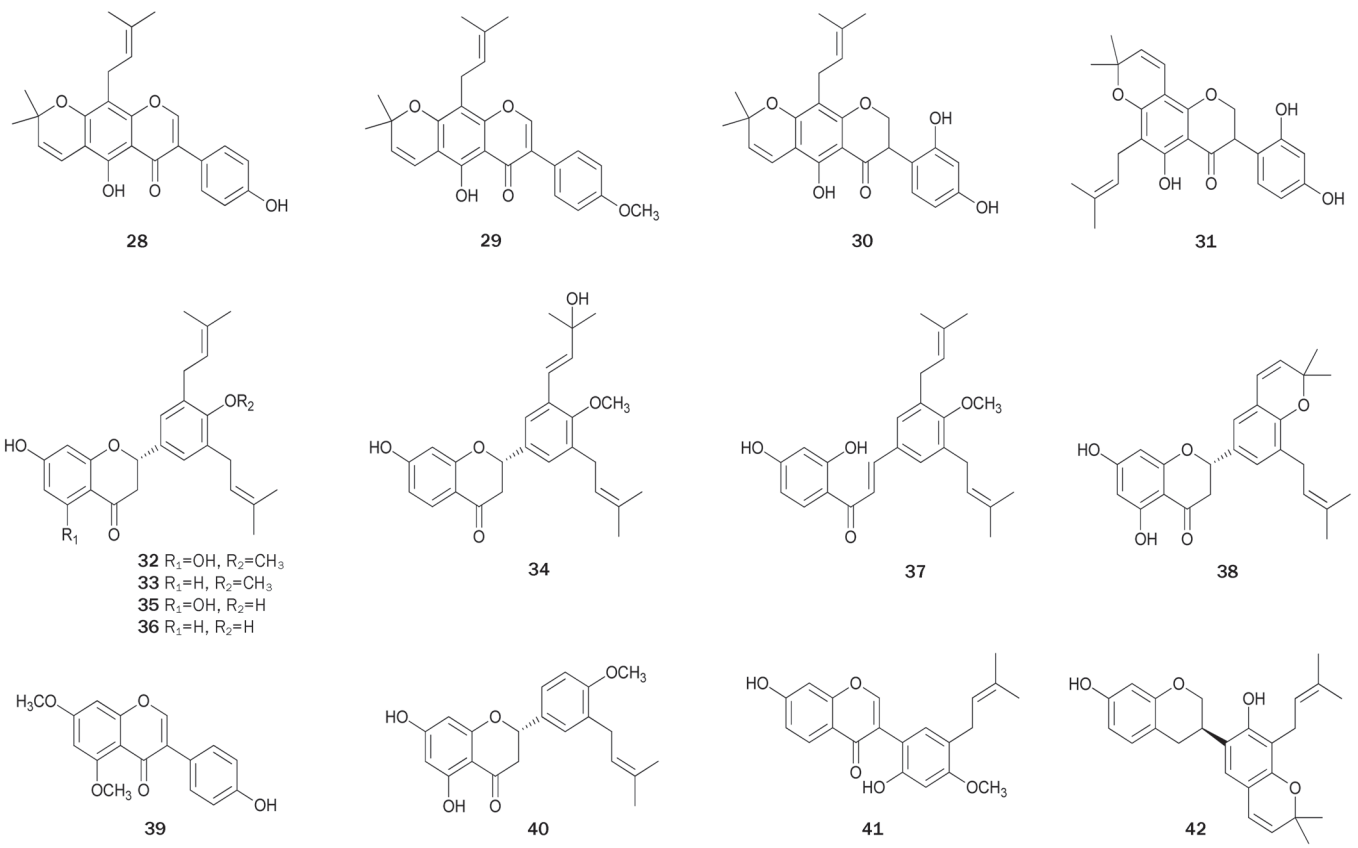

Figure 2. Structures of flavonoids **28–42**.

flavonoids showed promising bioactivity, some have been synthesized. The complete synthesis of **46** was first achieved through C-prenylation, selective protection of the phenolic hydroxyl group, aldol condensation, cyclization and deprotection starting from the inexpensive materials 4-hydroxybenzaldehyde and 2,4,6-trihydroxyacetophenone with a total yield of 24%[60]. Rao *et al* prepared **83** by condensing 2,2-dimethyl chrom-3-6-carboxaldehyde with protected resacetophenone under phase transfer conditions followed by deprotection and cyclization[61]. In 2006, abyssinone II **84** was synthesized via condensation of the aldehyde with an *o*-hydroxyacetophenone under Claisen-Schmidt conditions followed by cyclization and deprotection[62]. Using a synthetic procedure similar to the one described above, Maiti *et al* synthesized **87**, an analog of **84**[63] (Figure 3).

Bioassay-guided fractionation of the EtOAc extract of the stem bark of *E abyssinica* resulted in the isolation of nine pterocarpan derivatives **94–102**, which showed inhibitory activity[53]. Compounds **94**, **96**, **98**, **99**, and **101** exhibited inhibitory activity with IC_{50} values ranging from 4.2±0.2 to 19.3±0.3 μmol/L, and showed strong cytotoxic activities against MCF7, MCF7/TAMR, MCF7/ADR and MDA-MB-231 breast cancer cell lines with IC_{50} values from 5.6±0.7 to 28.0±0.2 μmol/L. Additionally, the other pterocarpan derivatives were weakly active or not active against PTP1B and cancer cell lines. Thus, the antitumor activity of **94**, **96**, **98**, **99**, and **101** was possibly attributed to their PTP1B inhibitory effects. From the MeOH extract of the stem bark of *E lysistemon*, other pterocarpan derivatives **103–114** were isolated[54]. All of the isolates, with the exception of **105**, **108**, and **113**, inhibited PTP1B activity with IC_{50} values ranging from 1.01±0.3 to 18.1±0.9 μg/mL. The diisoprenylated **114** (IC_{50}=1.01±0.3 μg/mL) had the strongest activity. Compounds **104**, **111**, **112**, and **114** were highly active compared to the weak **103**, **106**, and **107** compounds, which only have a pyran ring. These results suggested that isoprenylation of ring A and/or ring D played an important role in PTP1B inhibitory properties. Phaseollin **107** was synthesized by Mohamed *et al* in 1987[64] (Figure 4).

From the MeOH extract of plant *Selaginella tamariscina*, used to treat infectious disease and malignant tumors, amentoflavone **115** was obtained and characterized as a noncompetitive PTP1B inhibitor (IC_{50} value of 7.3±0.5 μmol/L and K_i value of 5.2 μmol/L)[65]. Treatment with **115** of 32D cells overexpressing the IR resulted in a dose-dependent increase in tyrosine phosphorylation of IR, possibly through inhibition of PTP1B to enhance insulin-induced intracellular signaling.

The leaf of *Morus* sp has been used in traditional Chinese medicinal to treat diabetes mellitus, and 'Sang-Bai-Pi', the root bark of the same plant, is also well known as a Chinese crude drug. From the extract of 'Sang-Bai-Pi', sanggenons C **116**, G **117**, and kuwanon L **118** were isolated[66]. Compounds **116–118** inhibited PTP1B (IC_{50} values ranging from 1.6±0.3 to 16.9±1.1 μmol/L) with good selectivity over other PPs, expecially **116** and **118**, which showed no inhibitory effects toward VHR and PP1 at levels up to 50 μmol/L. In addition, sanggenons **116** and **117** inhibited PTP1B in the mixed-type manner (Figure 5).

Bromophenols

The marine environment is a rich source of bromophenols, which exhibit interesting and useful biological activities, including feeding deterrent, antimicrobial, and radical-scavenging activities[67]. Several species of marine algae are found to contain bromophenols with PTP1B inhibitory activity.

Bromophenol **119**, isolated from the red alga *Polysiphonia urceolata* collected at the coast of Weihai, China, showed potent inhibition against PTP1B with an IC_{50} value of 4.9 μg/mL[68].

Isolation of the ethanol extract from the red alga *Rhodomela confervoides* collected at the coast of Qingdao, China, which displayed anti-hyperglycemic effects of on STZ-induced diabetes in male Wistar rats fed with high fat diet, produced four bromophenols **120–123**. All four bromophenols **120–123** showed significant inhibitory activity with IC_{50} values ranging from 0.84 to 2.4 μmol/L, which might be responsible for the *in vivo* anti-hyperglycemic activity of the extract[69]. Bromophenols **124–126**, isolated from algae *R confervoides* collected at the coast of Qingdao, China, and *Leathesia nan* collected at the coast of Weihai, China, showed significant inhibitory activity with IC_{50} values ranging from 2.8 to 4.5 μmol/L[70]. Additional studies on chemical constituents of *R confervoides* and *P urceolata* produced two more PTP1B inhibitors with bromophenol structures **127** and **128**[67]. Bromophenol **120** was synthesized in four steps with an overall yield of 14.7%[71]. Bromophenol **122** and its related analogs were synthesized to test for their antifungal activity[72]. Bromophenols **123**, **127** and **128** were synthesized in eight steps with overall yields of 14.4%, 14.4%, and 18.2%, respectively, via a practical approach using bromination, Wolff-Kishner-Huang reduction and a Friedel-Crafts reaction as key steps[67]. Bromophenol **123** exhibited better inhibitory activity than **127** and **128**, suggesting that the long side chain at the R_1 position and the bromine atom at the R_2 position enhanced the biological inhibitory activity.

Bromophenols **129** and **130**, isolated from the Hainan red alga *Laurencia similis*, showed strong inhibitory activity with IC_{50} of 2.97 and 2.66 μmol/L, respectively[73]. Bromophenols **131–135**, together with **124**, were isolated from the red alga *Symphyocladia latiuscula,* collected from the Weihai coastline of Shandong Province. Bromophenols **132–134** showed potent activity with IC_{50} values of 3.9, 4.3, and 3.5 μmol/L, respectively[74]. The first synthesis of **133** was reported by Balaydin *et al*[75] (Figure 6).

Phenolic acids

Caffeic acid **136** is a widespread phenolic acid that occurs naturally in many agriculture products such as fruits, vegetables, wine, olive oil, and coffee[76]. Isolated from the aerial parts of *Artemisia minor*, phenolic acid **136** was found to be a PTP1B inhibitor with an IC_{50} value of 3.06 μmol/L[77]. Together with **136**, another three phenolic acids **137**[35], **138** and **139**[78] were isolated from the leaves of the plant *Cyclocarya paliurus* and the fruiting body of the fungus *Phellinus linteus*, respectively. Compounds **137-139** had inhibitory activity with IC_{50} values of 16.64±0.04[35], 52.9±3.6 and 26.2±1.9 μmol/L[78], respectively. 2-Acetylaminogentisic acid **140**, isolated from fungus *Strepto-*

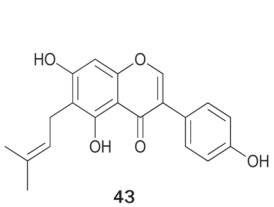

43

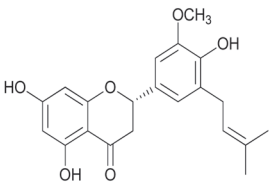

44

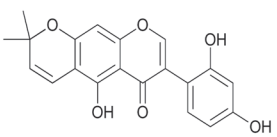

45

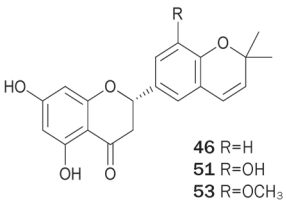

46 R=H
51 R=OH
53 R=OCH_3

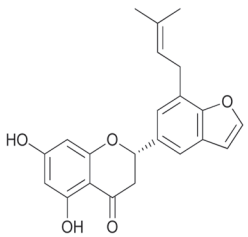

47

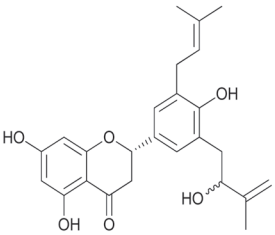

48

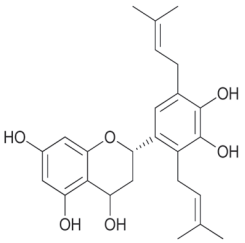

49

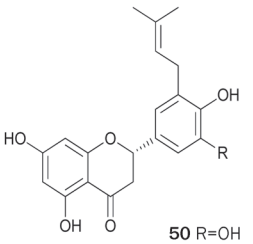

50 R=OH
55 R=H

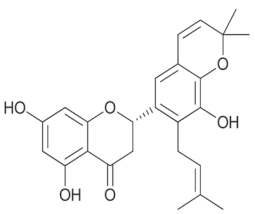

52

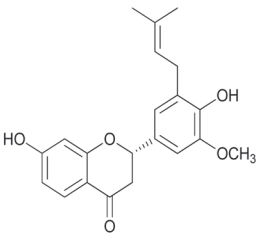

54

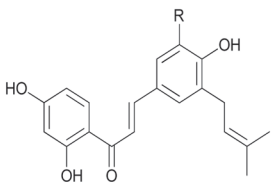

56 R=isoprenyl
57 R=H

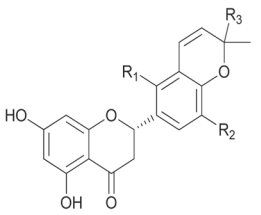

58 R_1=isoprenyl, R_2=OH, R_3=CH_3
59 R_1=H, R_2=OH, R_3=CH_2OH
60 R_1=H, R_2=OCH_3, R_3=CH_2OH

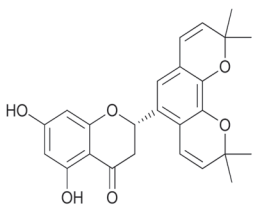

61

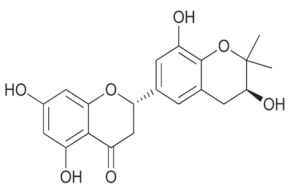

70

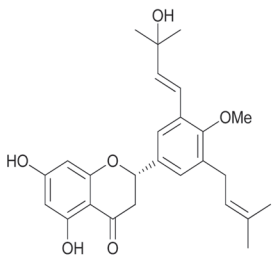

72

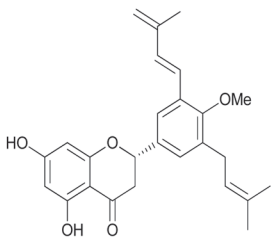

73

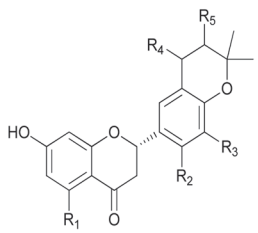

62 R_1=R_5=OH, R_2=R_4=H, R_3=isoprenyl
63 R_1=R_5=OH, R_2=R_4=H, R_3=OCH_3
64 R_1=R_4=R_5=OH, R_2=R_3=H
65 R_1=R_4=R_5=OH, R_2=H, R_3=isoprenyl
66 R_1=R_4=R_5=OH, R_2=isoprenyl, R_3=H
67 R_1=R_3=OH, R_2=R_5=H, R_4=(=O)
68 R_1=R_2=R_4=H, R_3=R_5=OH
69 R_1=R_2=H, R_3=R_4=R_5=OH
71 R_1=R_3=R_4=R_5=OH, R_2=H

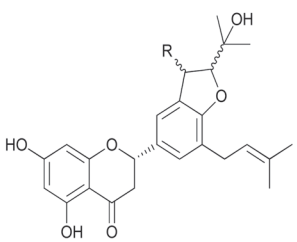

74 R_1=H
77 R_1=OH

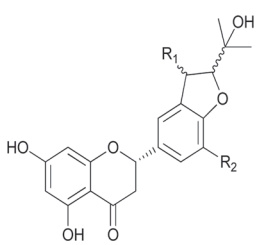

75 R_1=H, R_2=OCH_3
76 R_1=H, R_2=OH
78 R_1=OH, R_2=OH

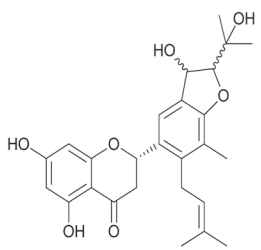

79

Figure 3. Structures of flavonoids **43**–**79**.

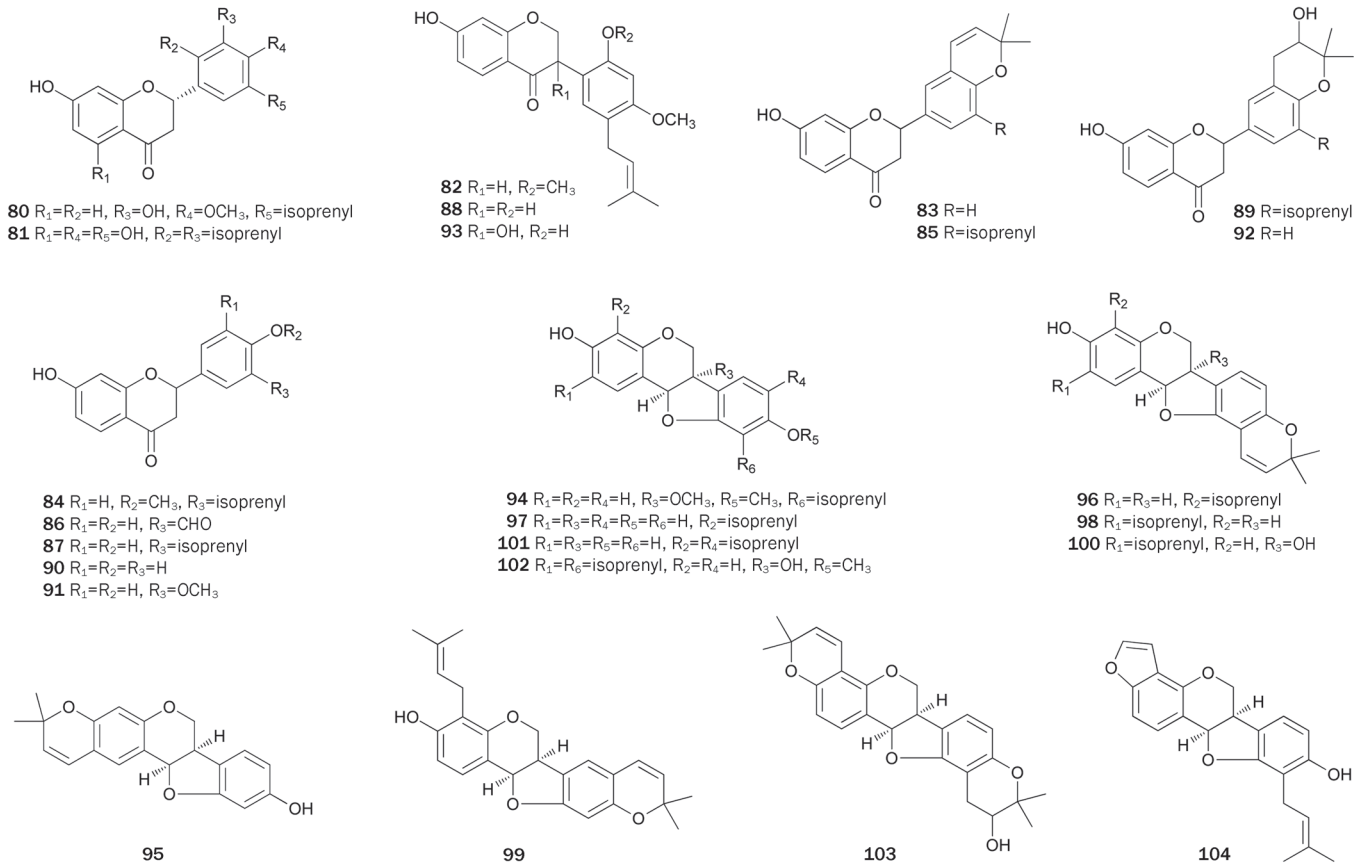

Figure 4. Structures of flavonoids **80–104**.

myces (unknown species), exhibited inhibitory activity with an IC value of 20.4±1.9 μmol/L[79].

PTP1B inhibitors **141** and **142**[80], **143–145**[81], and **146–148**[82], respectively, were isolated from the MeOH extracts of the Antarctic lichens *Lecidella carpathica, Umbilicaria antarctica*, and *Stereocaulon alpinum* by Seo *et al*. Although phenolic acids **143-145** share a similar structural pattern with the monomeric hydroxylbenzoic acid, compound **143** showed the strongest inhibitory effect (IC_{50}=3.6±0.04 μmol/L)[81], suggesting that the molecular size could be an important factor for the activity among these compounds. The fact that the activity of methyl ester derivative of **143** was four-fold weaker than that of **143**, suggests that the acid functionality in **143** was crucial to exhibiting the inhibitory activity. Phenol acids **146–148** exhibited potent inhibitory activity with IC_{50} values of 0.87, 6.86, and 2.48 μmol/L, respectively[82]. The preliminary SAR from **146–148** indicated that the presence of acidic protons was, at least in part, required in the inhibition mechanism, presumably to provide hydrogen-bonding sites that were relevant to the interaction with PTP1B. Kinetic analysis suggested that **142** inhibited PTP1B activity in a competitive manner[80], while **143**, **146**, and **147** inhibited PTP1B activity in non-competitive manner[81, 82].

KS-506a **149** and KS-506m **150**, both containing sulfur atoms, were PTP1B inhibitors both isolated from the culture of the fungus *Mortierella vinacea*[83]. KS-506a **149** showed potent inhibitory activity with an IC_{50} value of 4.9 μmol/L, while KS-506m **150** showed moderate inhibitory activity (IC_{50}=69.9 μmol/L). Kinetic analysis suggested that 149 was a competitive inhibitor with a K_i value of 2.7 μmol/L. Additionally, both compounds showed no inhibitory effects toward other PPs, such as VHR and PP1, at levels up to 200 μmol/L.

Caloporoside **151**, originally found as a phospholipase C inhibitor isolated from the fungus *Caloporus dichrous*, was totally synthesized in 1998[84]. Later, compound **151** was found to inhibit PTP1B with an IC_{50} value of 1.6±0.8 μmol/L, approximately three-fold in inhibitory activity against Cdc25A[85]. During a bioassay-guided study on the EtOAc extract of a culture broth of the marine-derived fungus *Cosmospora* (unknown species), aquastatin A **152** was isolated as a PTP1B inhibitor with an IC_{50} value of 0.19 μmol/L[86]. Kinetic analyses suggested that **152** competitively inhibited PTP1B and showed modest but selective inhibitory activity against PTP1B over other PTPs, such as TCPTP, SHP-2, LAR, and CD45.

1,2,3,4,6-penta-*O*-galloyl-*D*-glucopyranose **153**, a PTP1B inhibitor (IC_{50}=4.8 μmol/L) isolated from the roots of plant *Paeonia lactiflora*, was shown to act as an insulin sensitizer in human hepatoma cells (HCC-1.2) at 10 μmol/L[87, 88]. Additionally, **153** inhibited TCPTP with an IC_{50} value of 0.07 μmol/L, but did not inhibit LAR and SHP-2 at concentrations below 50

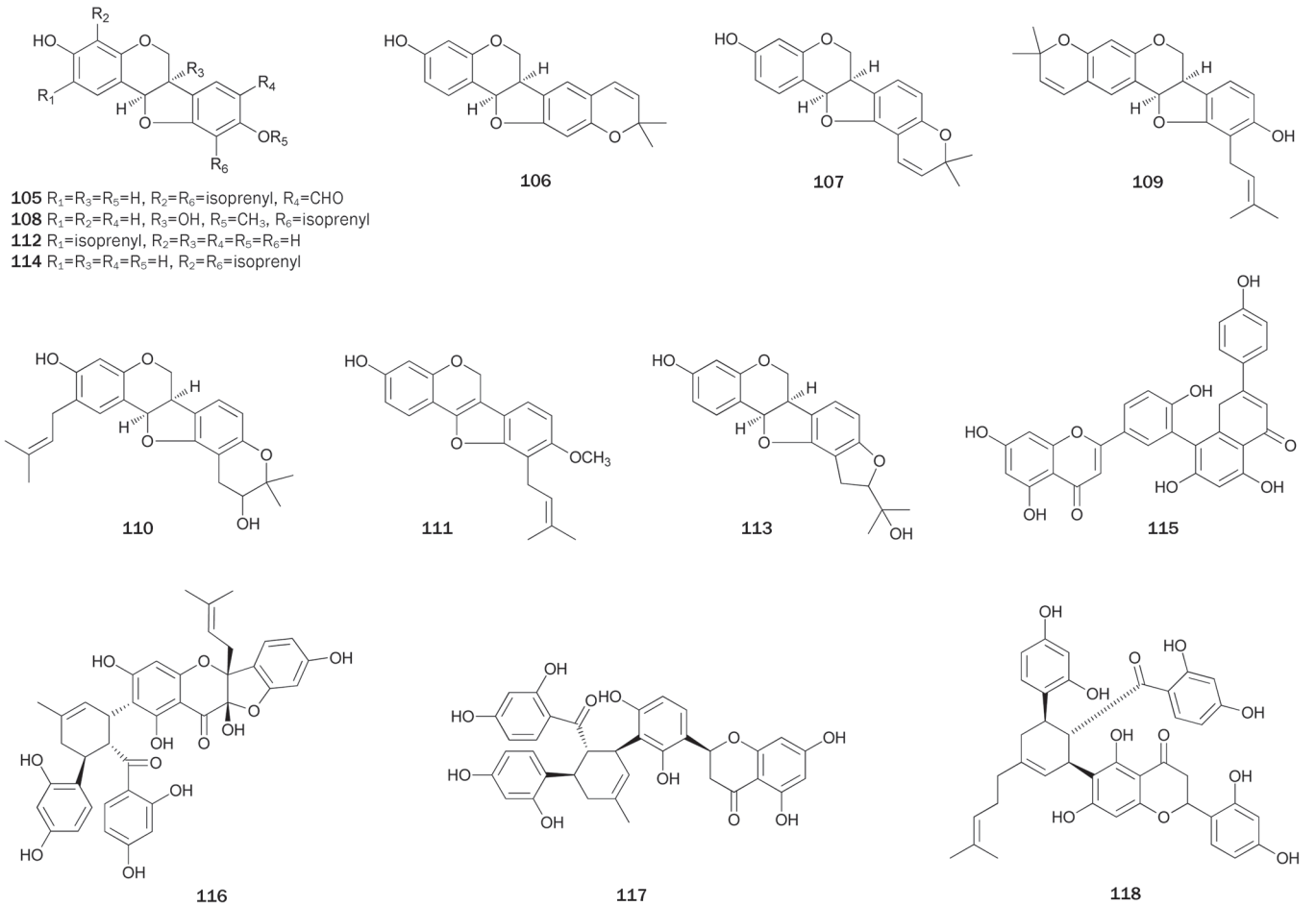

Figure 5. Structures of flavonoids **105–118**.

μmol/L (Figure 7).

Phenolics containing furan or pyran rings

Two 2-arylbenzofuran PTP1B inhibitors, glycybenzofuran **154** and licocoumarone **155**, were isolated from the roots of the plant *Glycyrrhiza uralensis*[33]. Compound **154** showed stronger inhibitory activity *in vitro* with an IC_{50} value of 25.5 μmol/L by a competitive manner.

The bioassay-guided fractionation of 'Sang-Bai-Pi' mentioned above also resulted in isolation of mulberrofuran C **156**, which inhibited PTP1B with an IC_{50} of 4.9±0.2 μmol/L in a mixed-type manner[66]. The bioassay for the inhibitory effects on other PPs showed that **156** had no inhibitory effects toward VHR and PP1 at levels up to 50 μmol/L. Albafuran A **157**, mulberrofurans W **158** and D **159** were isolated from the chloroform-soluble fraction of the plant *Morus bombycis*[34]. An analysis of the inhibition kinetics suggested **157–159** inhibited PTP1B in a mixed-type manner (IC_{50} values ranging from 2.7 to 9.2 μmol/L). The respective lipophilic and hydroxyl groups of **157–159** are considered to play an important role in inhibition of PTP1B.

2-Arylbenzofurans **160–165** were isolated from the plant *Erythrina addisoniae* by Na *et al*[89]. Compounds **160-162** inhibited PTP1B (IC_{50} values ranging from 13.6±1.1 to 17.5±1.2 μmol/L *in vitro* assay) much more strongly than **163–165** (IC_{50} values ranging from 62.7±2.0 to 74.1±1.9 μmol/L), indicating that cyclization between an isoprenyl group and one of the phenolic hydroxyl group in ring B or loss of the isoprenyl group might be responsible for the loss of *in vitro* activity.

Dibenzofuran derivatives 166 and its sulfate adduct **167** were isolated from the green alga *Cladophora socialis*, which was supplied by the Queensland Museum[90]. Both dibenzofurans showed potent inhibitory activity against PTP1B, with IC_{50} values of 3.7 and 1.7 μmol/L. It was speculated that the dibenzofuran and phenyl ring systems at each end of **166** acted as two binding sites with PTP1B, and the phenyl ring in the middle of **166** acted as the linker. The carboxyl group at C-3 and the phenolic hydroxyl group at C-4″ may contribute to the binding, while the presence of more highly acidic sulfate functionality at C-4″ in **167** may enhance its activity (Figure 8).

Usimines A-C **168–170** and usnic acid **171**, were isolated from a MeOH extract of the Antarctic lichen *Stereocaulon alpinum*[91]. The absolute configurations of the chiral centers in **168–170** were determined by comparison of optical rotations and Marfey's derivatization of the mixture from acid hydrolysis. Compounds **168–171** showed inhibitory activity with

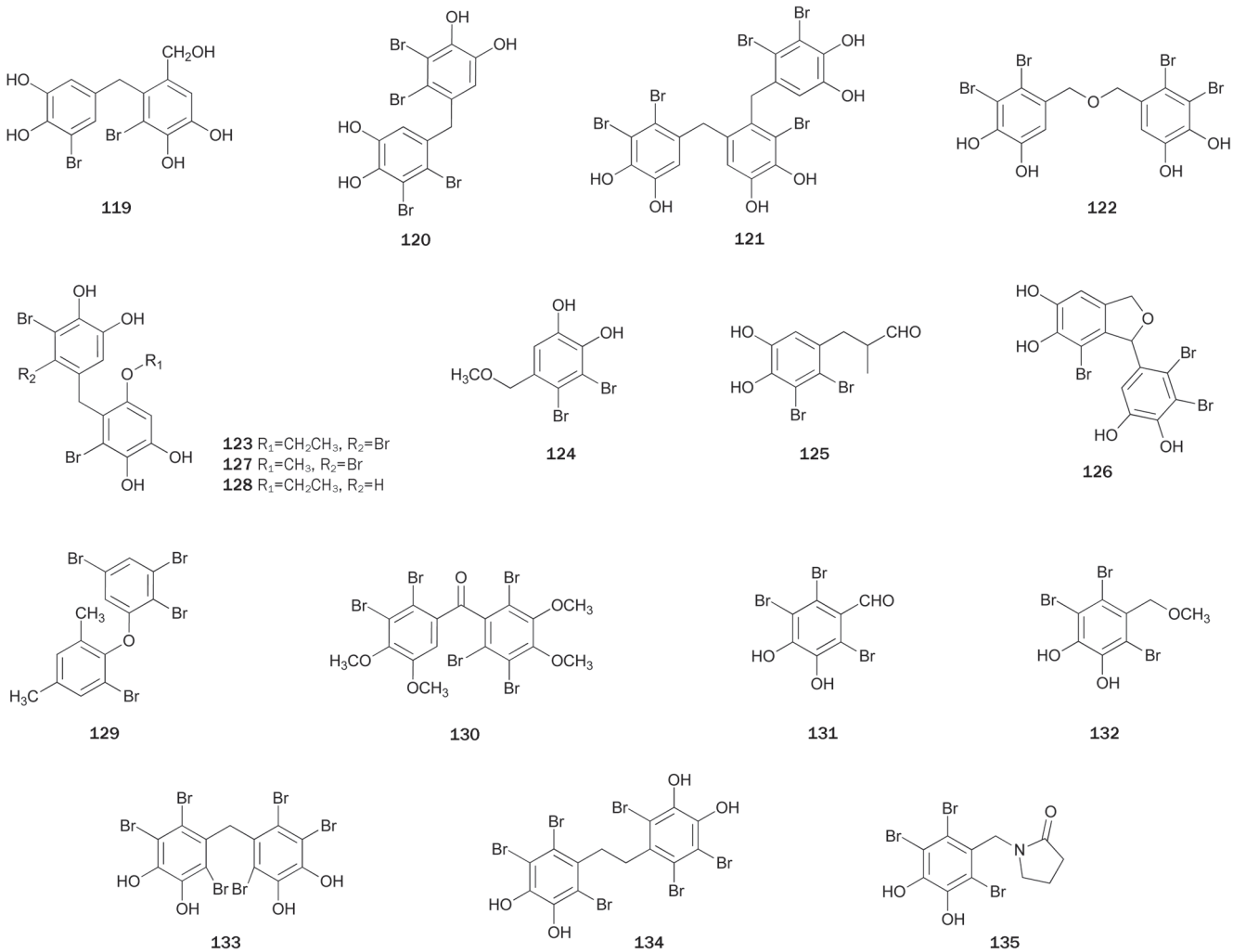

Figure 6. Structures of bromophenols **119–135**.

IC_{50} values ranging from 15.0±0.1 to 27.7±2.1 μmol/L. Synthesis of **171** from commercially available starting material was achieved in two steps, the methylation of phloracetophenone followed by oxidation with horseradish peroxidase[92].

A tricyclic polyketide ortho-quinone, nocardione A **172**, was produced by the fungus *Nocardiam* (unknown species)[93]. Compound **172** showed inhibition of intracellular PTP1B with a similar potency to Cdc25b (IC_{50}=17 μmol/L) and showed weaker inhibition of FAP-1 (IC_{50}=89 μmol/L). Additionally, it showed moderated *in vitro* antifungal and cytotoxic activities. In 2001, two routes for total synthesis of **172** were achieved by starting from a propylene oxide and a 5-benzyloxy-1-tetralone, chloropropene and 5-methoxyl-1-naphthol, respectively[94, 95]. Clive *et al* reported another route based on a method for achieving formal cyclization of a radical onto a benzene ring to synthesized (+)-**172**[96, 97]

Ohioensins A **173**, C **174**, F **175**, and G **176** were isolated from the MeOH extract of the Antarctic moss *Polytrichastrum alpinum*[98]. All these compounds showed inhibitory activity with IC_{50} values ranging from 3.5±0.2 to 7.6±0.7 μmol/L. Kinetic analysis of PTP1B inhibition by **175** suggested that these benzopyrans inhibited PTP1B activity in a non-competitive manner.

Chemical investigation of the species of fungus *Phelliuns* resulted in the isolation of several α-pyrone PTP1B inhibitors, such as pyrano[4,3-c]isochromen-4-one derivatives, phelligridins H **177** and I **178** from *P igniarius*[99], and hispidin derivatives, phelligridimer A **179**, davallialactone **180**, hypholomine B **181**, interfungins A **182** and inoscavin A **183** from *P linteus*[78]. Phelligridins **180** and **181** inhibited PTP1B with IC_{50} values of 3.1 and 3.0 μmol/L, respectively, and also exhibited antioxidant activity against rat liver microsomal lipid peroxidation. Compounds **180** and **181** with a hispidin moiety exhibited higher inhibitory activity than **179**, **182**, and **183** (Figure 9).

Coumarins and lignans

Coumarin is a fragrant chemical compound of benzopyrone found in many plants. It has a distinctive odor which has led to its use as a food additive and ingredient in perfume. Natural coumarin displays extensively interesting bioactivities,

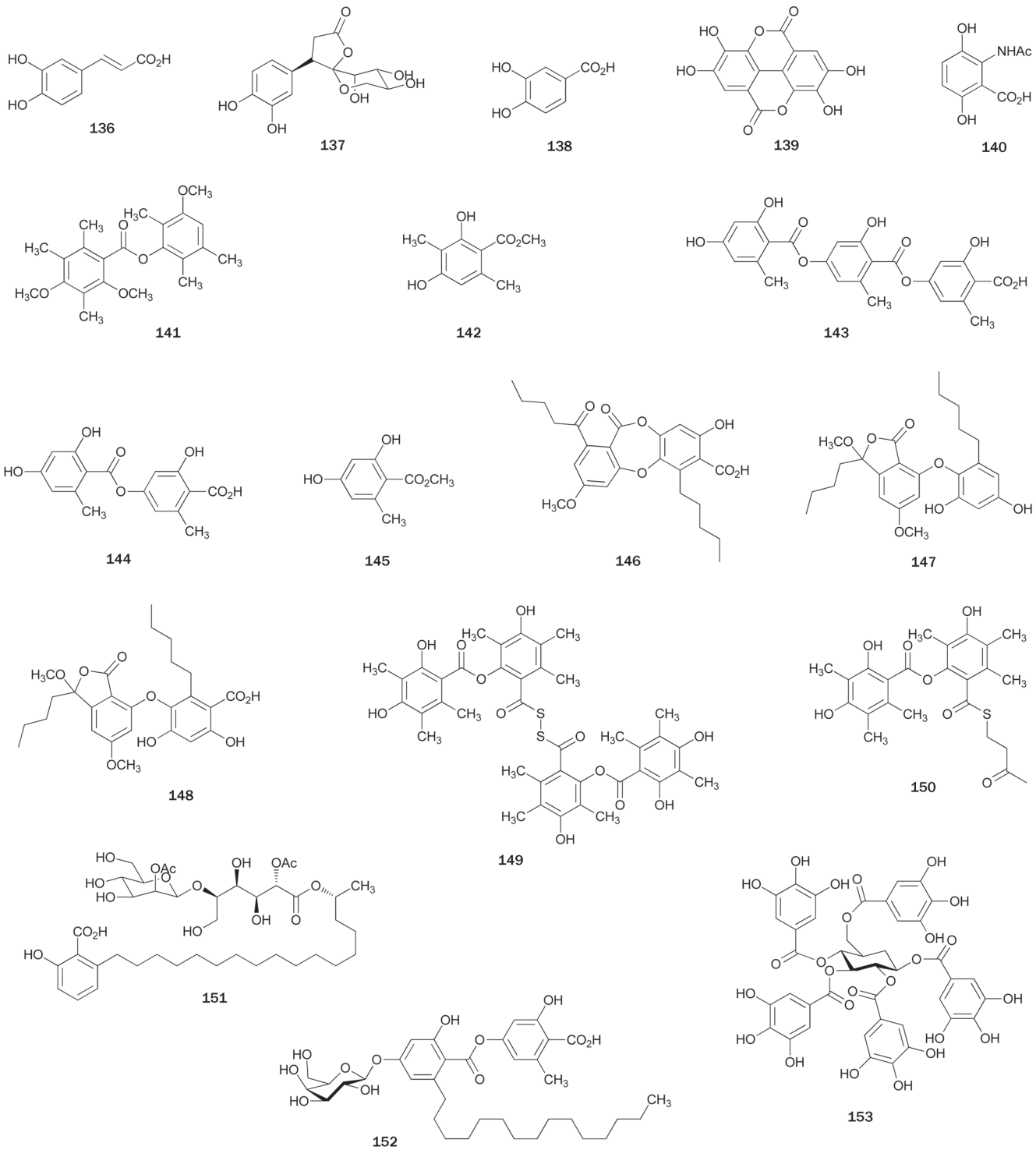

Figure 7. Structures of phenolic acids **136–153**.

intriguing chemists and medicinal chemists for decades to explore their applicability as drugs[100–102]. Lignans are phenylpropanoid demers, where the phenylpropane units are linked by the central carbon (C8) of their side chains. Lignans also have a number of medically important biological activities, *eg*, antitumor, antimitotic and antiviral properties[103]. However, there are only a few reports about natural coumarins or lignans with PTP1B inhibitory activity.

The seed of the plant *Psoralea corylifolia* is a commonly used traditional Chinese medicine against gynecological bleeding, vitiligo and psoriasis. Bioassay-guided fractionation of the EtOAc-soluble extract of *P corylifolia* produced psoralidin **184**,

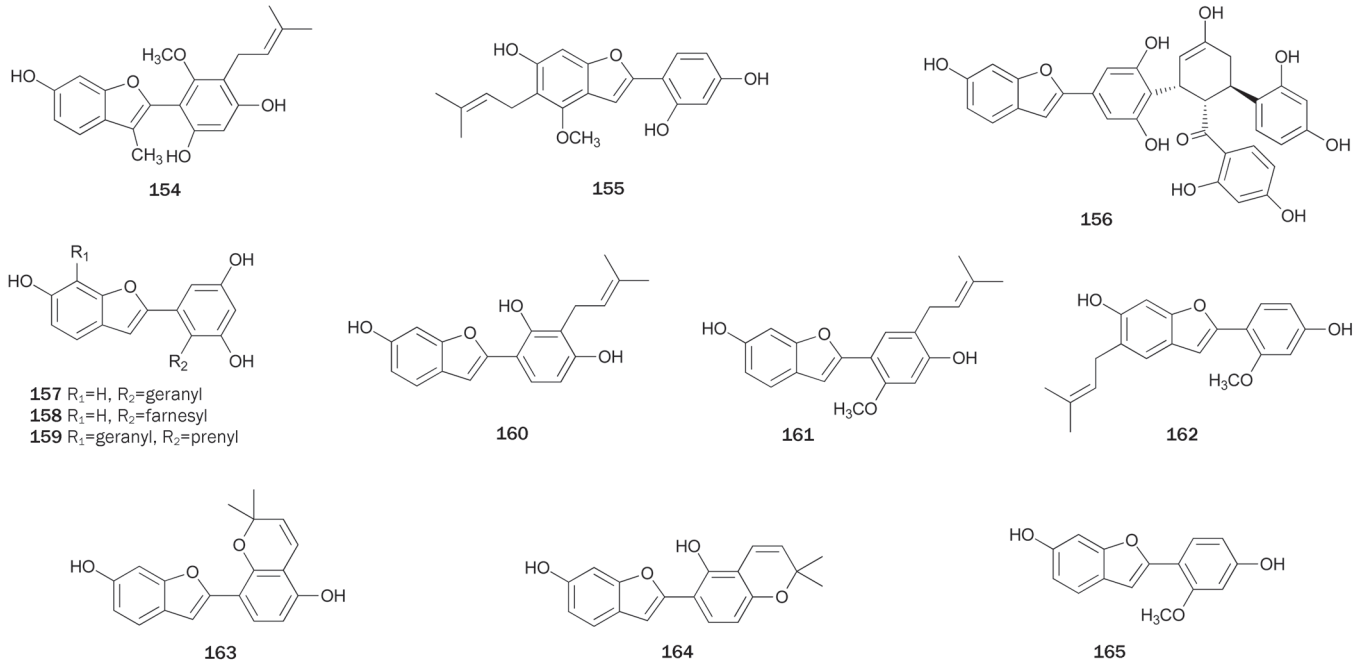

Figure 8. Structures of phenolics containing furan or pyran ring **154–165**.

which is a non-competitive PTP1B inhibitor with an IC_{50} value of 9.4±0.5 μmol/L that showed no inhibitory effects toward VHR and PP1 at levels up to 100 μmol/L[104]. Chemical studies on the roots of plant *Fraxinus rhynchophylla* (Qinpi), a traditional Chinese herbal drug used as anti-inflammatory agent, led to the isolation of a coumarin-secoiridoid hybrid glycoside, fraxisecoside **185**. Compound **185** exhibited moderate inhibitory activity (IC_{50}=21 μmol/L) and inhibited the proliferation of the lymphocyte T and B cells[105]. Glycycoumarin **186**, isolated from the roots of the plant *G uralensis*, showed weak inhibitory activity with an IC_{50} value of 183.9±4.5 μmol/L[33]. A based-catalyzed condensation of phenyl acetate with acid chloride, followed by intramolecular cyclization and microwave-assisted cross-metathesis reaction, led to the first total synthesis of **184**[106].

Bioassay-guided fractionation of the MeOH extract of plant *Myristica fragrans* Houtt (Myristicaceae) afforded *meso*-dihydroguaiaretic acid **187** and otobaphenol **188**[107]. Both compounds inhibited PTP1B with IC_{50} values of 19.6±0.3 and 48.9±0.5 μmol/L, respectively, in a non-competitive manner. Compound **187** was reported to increase the tyrosine phosphorylation of 32D cells overexpressing the IR in a dose-dependent manner, possibly through the inhibition of PTP1B activity. 1,4-Benzodioxane lignan **189**, isolated from the MeOH extract of the plant *Artemisia minor* collected from Tibet, inhibited PTP1B with an IC_{50} of 1.62 μg/mL[108] (Figure 10).

Miscellaneous

Bakuchiol **190**, isolated from the extract of the seeds of the plant *Psoralea corylifolia*, was found to inhibit PTP1B in a dose-dependent manner with an IC_{50} value of 20.8±1.9 μmol/L and with good selectivity against other PPs, such as VHR and PP1 (IC_{50}>100 μmol/L)[104]. The first enantiocontrolled synthesis of **190** was completed by starting from (S)-*O*-benzylglycidol[109]. Later, several simple and convenient methods were reported for the total synthesis of **190**[110-114].

A study on the constituents of the mangrove plant *Lumnitzera racemosa* produced two alkylphenols **191** and **192**[115]. Both alkylphenols showed inhibitory activity with IC_{50} values of 13.38±1.98 and 10.40±0.88 μmol/L, respectively. Alkylphenol **192** had been synthesized in 1989 to test for cytotoxicity against the KB cell lines (ED_{50}=2.4 μmol/mL)[116].

Curcumin **193**, the principal constituent of the rhizomes of the plant *Curucma longa*[117], was found to inhibit PTP1B and subsequently improve insulin and leptin sensitivity in the liver of rats, which protects against fructose-induced hypertriglyceridemia and hepatic steatosis[118]. Compound **193** was prepared by condensing dimethyl malonate with vanillin in the presence of B_2O_3 and $(BuO)_3B$ to prevent Knoevenagel condensation[119, 120].

4-Di-*O*-β-*D*-glucopyranoside **194**, isolated from the leaves of the plant *Cyclocarya paliurus*, showed inhibitory activity against PTP1B with an IC_{50} value of 10.50±2.67 μmol/L[35].

Physcion **195**, isolated from the ethanol extract of the plant *Ardisia japonica*, showed weak inhibitory activity[121]. The total synthesis of **195** was completed in two steps by the regioselective two-fold Diels-Alder reaction[122].

From the EtOH extract of the roots of the plant *Saussurea lappa*, Li *et al* also obtained three PTP1B inhibitors, including chrysophanol **196** and its glucopyranoside derivatives **197** and **198**[123]. The first total synthesis of **196** was achieved by the

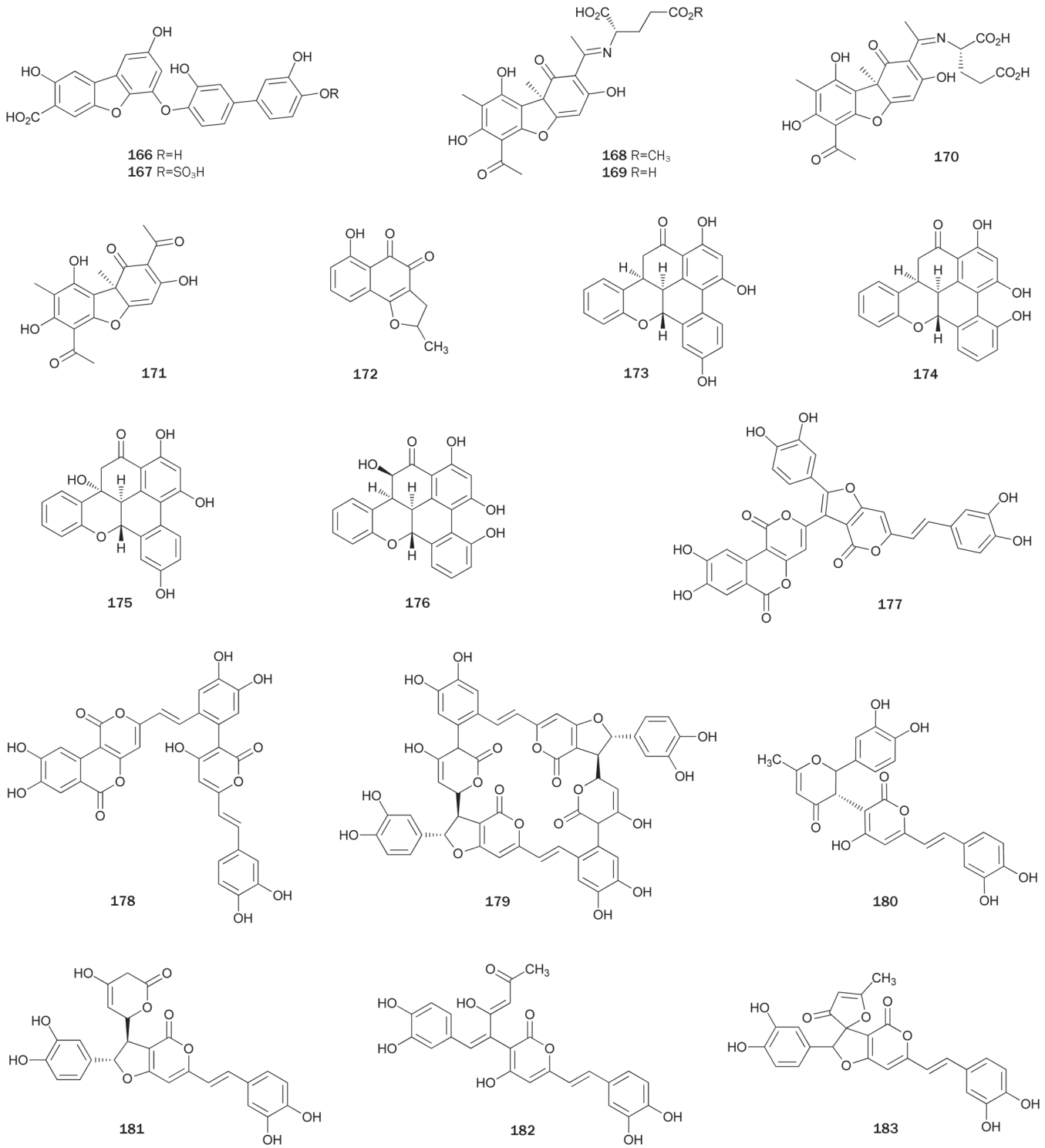

Figure 9. Structures of phenolics containing furan or pyran ring **166–183**.

cycloaddition reaction of 6-methoxy-3-methyl-2-pyrone with naphthoquinone as the key step[124]. In 1990, another synthetic route for **196** using dihydro-oxazoles and Grignard reagents from Mg(Anthracene)$(THF)_3$ was reported[125].

A phenanthraquinone-type metabolite **199**, with inhibitory activity with an IC_{50} value of 38.0±1.5 μmol/L, was isolated from the EtOAc-soluble extract of the plant *Dendrobium moniliforme*[126]. Compound **199** showed no inhibition against PP1 at levels up to 200 μmol/L, but lacked selectivity against PTP1B over VHR (IC_{50}=3.0±1.5 μmol/L).

Grecocycline B **200**, an angucycline with a thiol substitution at C-6a, was isolated from fungus *Streptomyces* (unknown spe-

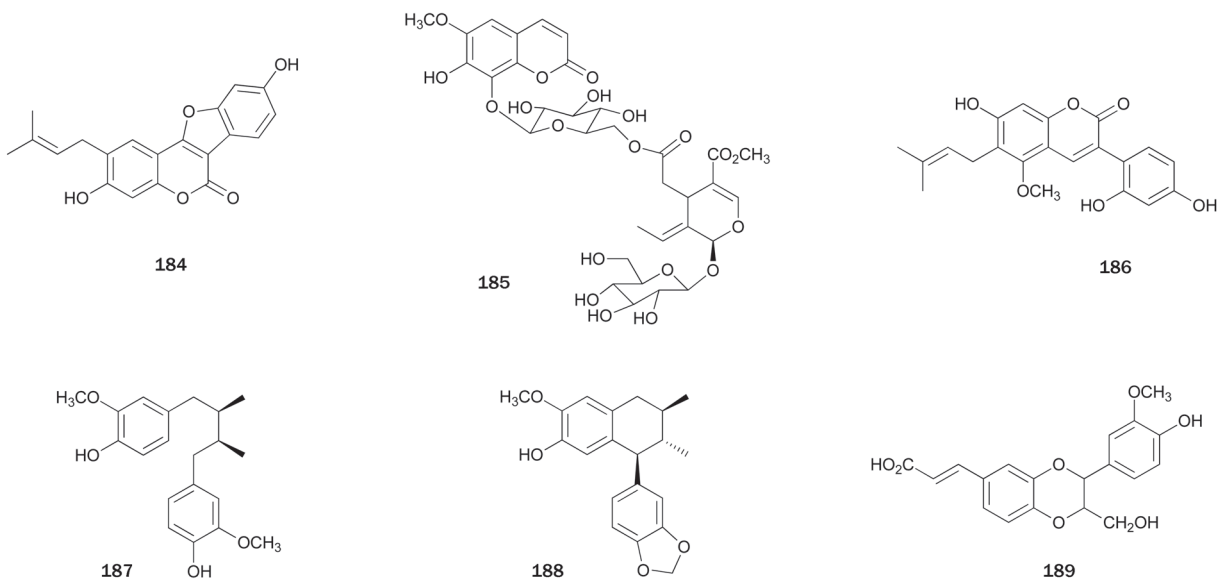

Figure 10. Structures of coumarins and lignans **184–189**.

cies)[127]. Compound **200** was reported to exhibit strong inhibitory activity with an IC_{50} value of 0.52±0.17 μmol/L. The free SH group in the C-6a position is proposed to be responsible for the irreversible inhibition of PTP1B (Figure 11).

Terpenes

Terpenes are a large and varied class of organic compounds produced by a wide variety of plants, animals, and marine organisms. Terpenes, which are derived biosynthetically from units of isoprene (C_5H_8), are classified sequentially by size as hemiterpenes, monoterpenes, sesquiterpenes, diterpenes, sesterterpenes, triterpenes, tetraterpenes, and polyterpenes. Naturally occurring terpenes usually display remarkable pharmacological activities, including antitumor, antimicrobial, antifungal, antiviral, anti-hyperglycemic, anti-inflammatory, and antiparasitic activities as well as a skin permeability effect[128, 129]. There are also many terpenes, primarily sesquiterpenes, diterpenes, sesterterpenes, triterpenes, that are found

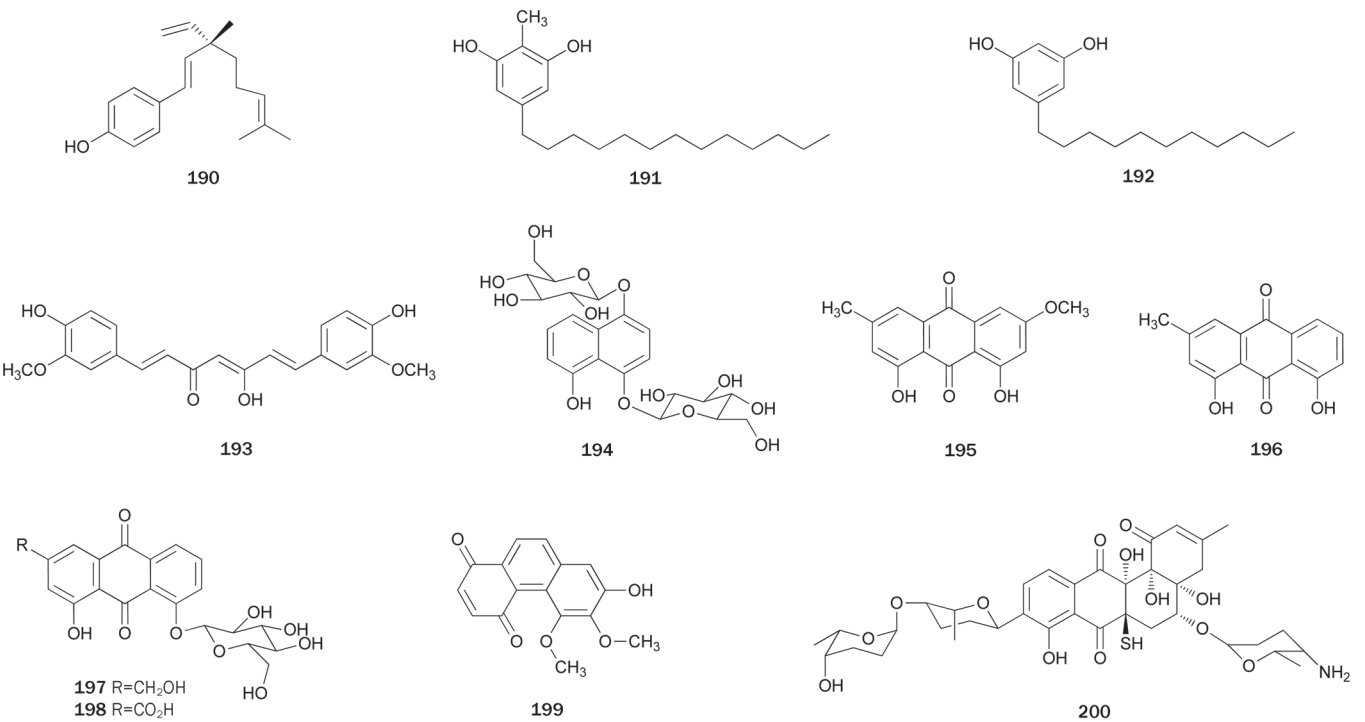

Figure 11. Structures of coumarins and lignans **190–200**.

to act as PTP1B inhibiters.

Sesquiterpenes

The plant *Ligularia fischeri* is common in southwestern China and has been used as a traditional Chinese medicine since ancient time. From the roots of *L fischeri*, an eremophilane sesquiterpene **201** was isolated[130]. Its structure was elucidated by spectroscopic methods including 1D and 2D NMR spectra and was further confirmed by a single-crystal X-ray diffraction analysis. Sesquiterpene **201** exhibited *in vivo* inhibitory activity with an IC_{50} value of 1.34 μmol/L.

O-Methyl nakafuran-8 lactone **202** was isolated from a Hainan sponge *Dysidea* (unknown species) and its structure proposed by spectral data was confirmed by X-ray diffraction analysis[131]. Lactone **202** showed strong inhibitory activity with an IC_{50} value of 1.58 μmol/L. Further studies on several species of *Dysidea* from Hainan produced other sesquiterpene PTP1B inhibitors, such as **203–206** from *D septosa*[132], and **207** and **208** from *D villosa*[133]. Sesquiterpene **203** had the strongest inhibitory effect among **203–206**[132]. Compound **207**, a member of the family of sesquiterpene quinine derivatives with a further rearranged drimane skeketon characterized by the abnormal position of the quinine moiety, showed moderate inhibitory activity and moderate cytotoxicity against HeLa cell lines. Moreover, **208** showed much stronger inhibitory activity with an IC_{50} value of 6.70 μmol/L. More-in-depth pharmacology studies revealed that **208** is a novel slow-binding PTP1B inhibitor with moderate inhibitory selectivity over other PTPs. Further cell based evaluation indicated that **208** could strongly activate the insulin signaling pathway and promote membrane translocation of the glucose transporter 4 (GLUT4) in CHO-K1 and 3T3-L1 cells. Additionally, **208** could significantly increase glucose uptake in 3T3-L1 cells by 2.3 fold[133]. The total synthesis of **204** was accomplished starting from 1-methoxy-4,5,8-endo-trimethylbicyclo[2.2.2]oct-5-en-2-one by a rearrangement strategy[134, 135]. The absolute configuration of **207** was confirmed by total synthesis with the key reaction being a Chiron-mediated asymmetric Aza-Claisen rearrangement[136].

Lactucin **209**, isolated from the root of the plant *Cichorium glandulosum*, was reported to inhibit PTP1B with an IC_{50} value of ≈1 μmol/L[137]. Activity-guided fractionation of a MeOH extract of the roots of the plant *Saussurea lappa* led to the isolation of guaiane sesquiterpenoids, mokko lactone **210** and dehydrocostuslactone **211** with inhibitory activity (IC_{50}=1.41±0.02 and 6.51±0.64 μg/mL, respectively)[138]. The lactones **210** and **211** were first synthesized in 1984[139]. Later, they were synthesized with their related guaianolides, starting from 1-α-santonin, in an effort to examine their SAR as inhibitors as the killing function of cytotoxic T lymphocytes (CTL) and the induction of intercellular adhesion molecule-1 (ICAM-1)[140].

Psidials B **212** and C **213** are sesquiterpenoid-based meroterpenoids representing the new skeleton of the 3,5-diformylbenzyl phloroglucinol-coupled sesquiterpenoid. Compounds **212** and **213** were isolated from the leaves of the plant *Psidium guajava*, which is used in folk medicine as anti-inflammatory and hemostatic agents and for treating pulmonary disease, cough, vomiting, and diarrhea[141]. Their complete structures were elucidated by spectral and chemical methods. Both psidials showed inhibitory activity at the concentration of 10 μmol/L (Figure 12).

Diterpenes

Kaurane-type diterpenes **214–216** were isolated from a MeOH extract of the aerial part of the plant *Siegesbeckia glabrescens*[142]. Diterpene **214**, possesssing an isobutyryloxyl moiety at C-17 of the kaurane skeleton, exhibited the strongest inhibitory activity (IC_{50}=8.7±0.9 μmol/L) among these isolates. Compound **215**, with an acetoxy and an isobutyryloxy group at C-17 and C-18, respectively, inhibited PTP1B with an IC_{50} value of 30.6±2.1 μmol/L, which was less effective than **214**. However, compound **216** (IC_{50}>200 μmol/L), substituted with a hydroxyl group at C-17, exhibited significantly lower activity than **214**, suggesting that an ester moiety at C-17 of the kaurane diterpene is essential for activity. Additionally, **214** and **215** had no inhibitory effects on VHR and PP1 at levels up to 200 μmol/L and kinetic analyses suggested that both compounds are non-competitive inhibitors with K_i values of 9.1 and 31.8 μmol/L, respectively.

The roots and stem barks of the plant *Acanthopanax koreanum* have been traditionally used as a tonic and to treat rheumatism, hepatitis, and diabetes in Korea. Diterpenes **217–224** were isolated from a CH_2Cl_2-soluble extract of the roots of *A koreanum*[143]. Of the isolates tested, diterpene **223**, possessing an isovaleryloxy group at C-17 of kaurane-type, exhibited the most potent inhibitory activity (IC_{50}=7.1±0.9 μmol/L) by a non-competitive manner. Diterpene **224** (IC_{50}>30 μmol/L), with a hydroxyl group substituted at C-16 of **223**, exhibited significantly lower activity than **223**. A similar case was observed between **221** and **222**. These results indicate that substitution of a hydroxyl group at C-16 of kaurane-type diterpenes decreases the inhibitory activity. The pimarane-type diterpene **218** inhibited PTP1B in a dose-dependent manner (IC_{50}=23.5±1.8 μmol/L). However, **217**, with conversion of a carboxyl group at C-19 to a primary alcohol, did not exhibit PTP1B inhibitory activity up to 30 μmol/L, suggesting that a carboxyl group at C-19 of pimarane-type is essential for the activity. Other pimarane-type diterpenes **219** and **220**, with hydroxyl groups at C-7 and C-9, respectively, had no activity at levels up to 30 μmol/L. Another three kaurane-type PTP1B inhibitors **225–227** (IC_{50}=12.6, 200, 21.3 μmol/L, respectively) were isolated from the plant *S orientalis*[144]. Diterpene **218** was synthesized from stevioside via two skeletal rearrangements in nine steps, with a total yield of 9%[145]. An enantioselective synthesis of **221** is described by Ling *et al*[146].

Bioassay-guided fractionation and purification of the MeOH extract of the dried root of the plant *Salvia miltiorrhiza* called 'Dan-Shen' in China, produced three related abietane-type diterpene metabolites, namely isotanshinone IIA **228**, dihydroisotanshinone I **229**, and isocryptotanshinone **230**[147]. Diterpenes **228–230** non-competitively inhibited PTP1B with IC_{50} values of 11.4±0.6, 22.4±0.6, and 56.1±6.3 μmol/L,

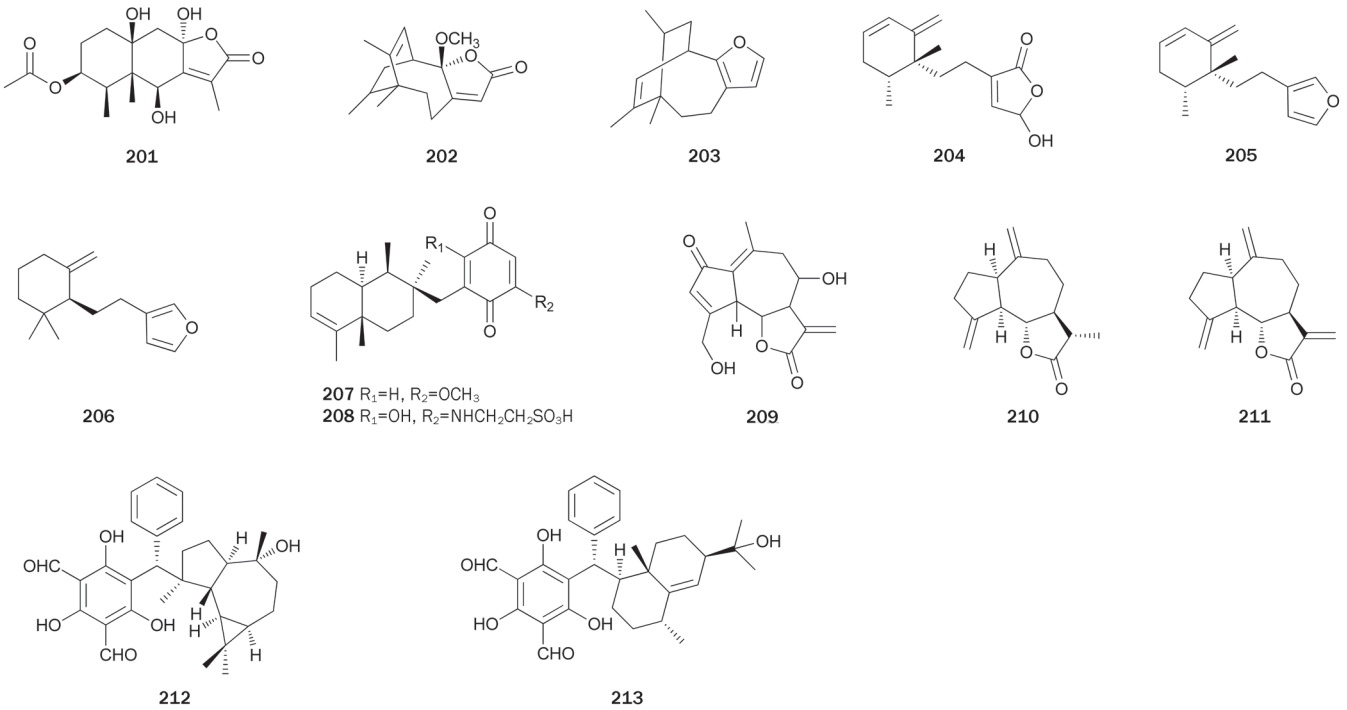

Figure 12. Structures of sesquiterpenes **201–213**.

respectively. Isotanshinone IIA **228** had been prepared as an intermediate to synthesize tanshinones[148], which were also obtained by partial synthesis from 16-hydroxycarnosol[149].

Lipidyl pseudopteranes A **231** and D **232** were isolated from the soft coral *Pseudopterogorgia acerosa* collected from the Bahamas[150]. Their structures represent the first report of a pseudopterane diterpene with a fatty acid moiety. Compounds **231** and **232** exhibited modest inhibitory activity, but were inactive against other PTPs, including LAR, SHP-1, and MKPX. Their lipidyl moiety appears to aid in their ability to diffuse into mammalian cells and inhibit PTP1B (Figure 13).

Sesterterpenes

Hyrtiosal **233**, a sesterterpenoid possessing a novel, rearranged tricarbocyclic skeleton, was isolated from the Okinawan sponge *Hyrtios erectus*[151]. A possible biosynthesis pathway of **233** was proposed in which the olefinic bond of the tricarbocyclic precursor containing a cheilanthane skeleton is oxidized to give an epoxy intermediate. The subsequent rearrangement produces a ring-contracted hyrtiosane skeleton. Sun *et al* found that **233** inhibited PTP1B activity in a dose-dependent, non-competitive manner with an IC_{50} value of 42 μmol/L[152]. Further research showed that **233** displayed potent activity for abolishing the retardation of AKT membrane translocation caused by PTP1B overexpression in CHO cells, dramatically enhanced the membrane translocation of the key glucose transporter Glut4 in PTP1B-overexpressed CHO cells, and effectively facilitated insulin inhibition of Smad2 activation. Moreover, hyrtiosal **233** was found to inhibit HIV-1 integrase from binding to viral DNA by a new inhibitor binding site[153].

The absolute configuration of natural (-)-**233** was confirmed by total synthesis, together with its C-16 epimer, starting from sclareol in moderate yield[154, 155]. Lunardi *et al* also completed the total synthesis of (-)-**233** along with its enantiomer (+)-**233** and their C-16 epimers starting from 30% ee copalic acid[156].

Bioassay-directed separation of the extract from the sponge *Thorectandra* (unknown species) collected in Papua New Guinea led to the isolation of luffariellolide-type sesterterpenoids, luffariellolide **234** and dehydroluffariellolide diacid 235[157]. Both compounds had no inhibitory activity against VHR at concentrations as high as 40 μg/mL and they lacked inhibitory selectivity against PTP1B over Cdc25B. The first synthesis of **234** was achieved by a convergent pathway involving sp^3–sp^3 cross-coupling and silyloxyfuran oxyfunctionalisation as key steps[158].

Sulfircin **236**, a sesterterpene sulfate mentioned at the beginning of this paper, was found to act as a nonspecific PPs inhibitor with moderate PTP1B inhibitory activity (IC_{50}=29.8 μmol/L) as well as activity against other PTPs (VHR, Cdc25A) with slightly better potencies[16, 159] (Figure 14).

Triterpenes

Five oleanane-type PTP1B inhibitors, including 3α,24-dihydroxyolean-12-en-27-oic acid **237**, 3-oxoolean-12-en-27-oic acid **238**, 3β-hydroxyolean-12-en-27-oic acid **239** (β-peltoboykinolic acid), 3β-hydroxyurs-12-en-27-oic acid **240**, and 3β,6β-dihydroxyolean-12-en-27-oic acid **241** (astilbic acid) were isolated from a MeOH extract of the rhizomes of the plant *Astilbe koreana*[160]. Of the isolates, **238** and **239** exhibited the strongest inhibitory activity with IC_{50} values of 4.9±0.4

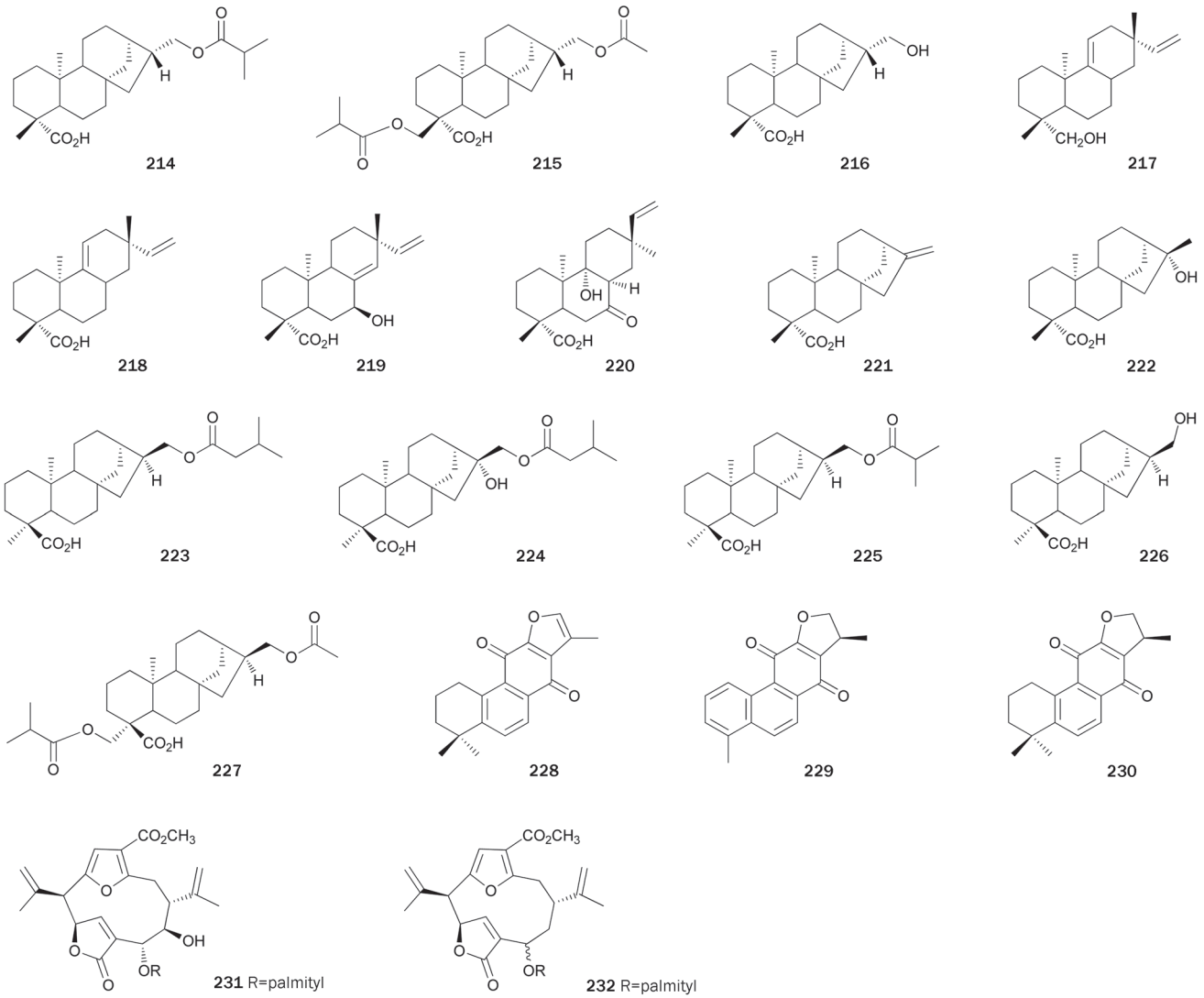

Figure 13. Structures of diterpenes **214–232**.

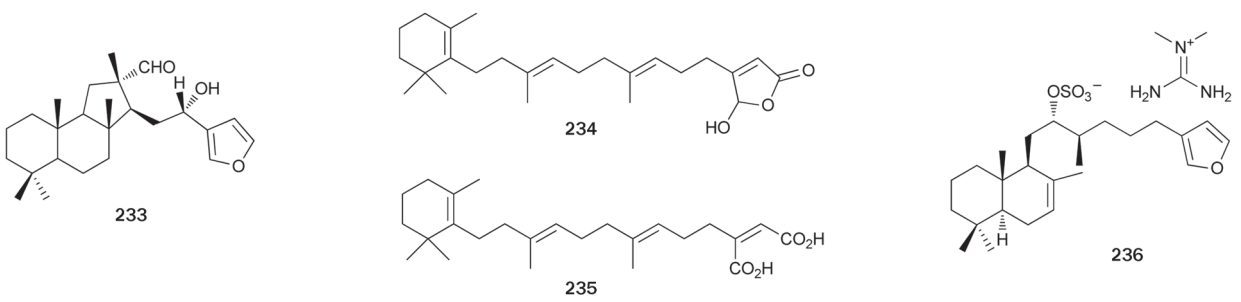

Figure 14. Structures of sesterterpenes **233–236**.

and 5.2±0.5 μmol/L, respectively. This result indicated that a positional change only of methyl groups at C-29 and C-30 might not affect the inhibitory activity. The preliminary SAR of **238** and **239** with their related synthetic analog indicated that a 3-hydroxyl group and a carboxyl group in this type of triterpenes might be required for activity. Moreover, addition of one more hydroxyl group at C-6 or C-24 may be responsible for a loss of activity.

Three ursane-type triterpenes, ursolic acid **242**, corosolic acid **243** and 2α,3α,19α,23-tetrahydroxyurs-12-en-28-oic acid

244, were isolated from a MeOH extract of the leaves and stems of the plant *Symplocos paniculata* using an *in vitro* PTP1B inhibitory assay[161]. Comparison of the activity of triterpenes **242–244** (IC_{50} values of 3.8±0.5, 7.2±0.8, and 42.1±1.5 μmol/L, respectively) indicated that the substitution of hydroxyl groups on the ursane-type triterpenes was responsible for the loss of activity. Kinetic studies suggest that **242** is a competitive inhibitor with a K_i value of 2.0 μmol/L, whereas **243** is a mixed-type PTP1B inhibitor. Furthermore, ursolic acid **242** was found to stimulate glucose uptake in L6 myotubes and facilitate glucose transporter isoform 4 translocation in CHO/hIR cells via enhancing IR phosphorylation. Additionally, **242** could inhibit other PTPs, including TCPTP, SHP1, and SHP2 (IC_{50} values ranging from 10.50±0.29 to 24.56±0.56 μmol/L)[162].

Triterpene metabolites with inhibitory activity, identified as oleanolic acid **245**, 3β,28-dihydroxy-12-en-olean **246**, maslinic acid **247** and 3β-O-acetyl aleuritolic acid 248, were obtained from the plant *Macaranga adenantha*[163]. Triterpenes **245–248** showed inhibitory activity with IC_{50} values ranging from 6.2±0.9 to 12.4±5.5 μg/mL. Qian *et al* designed and synthesized a variety of oleanolic acid **245** derivatives with modified C-17 moieties and rings A and C. These compounds were PTP1B inhibitors and the bioassay results suggested that the integrity of ring A and the 12-ene moieties was important in the retention of PTP1B enzyme inhibitory activities. Additionally, hydrophilic and acidic groups as well as the distance between the oleanene and acid moieties were associated with inhibitory activities[164]. Preparing a series of derivatives of **247** by introducing various fused heterocyclic rings at the C-2 and C-3 positions, Qiu *et al* found some derivatives with improved inhibitory activity and selectivity against PTP1B over related PTPs, such as TCPTP, LAR, SHP-1, and SHP-2[165]. The first enantioselective total synthesis of **245** and **246** from 7-methoxy-1-tetraline was reported by Corey *et al*[166].

Two more PTP1B inhibitors, moronic acid **249** and **250**, together with **242** and **245**, were purified and characterized from the acetone extract of the leaves and stems of the plant *Phoradendron reichenbachianum*[167]. All isolates were docked with a crystal structure of PTP1B and completely inhibited PTP1B at 50 μmol/L. Docking results suggested the potential binding of the triterpenic acids in a binding pocket next to the catalytic site. An extensive hydrogen bond network with the carboxyl group along with Van der Waals interactions stabilized the protein-ligand complexes. The efficient syntheses of **249** and **250** were accomplished starting from betulin **251**[168, 169]. Compound **251** from an ethanolic extract of the roots of the plant *Euphorbia micractina* showed inhibitory activity with an IC_{50} value of 15.3 μmol/L, and a selective cytotoxicity against A2780 ovarian cells[170].

Triterpenes **252–256** were isolated from the stem-bark of the plant *Styrax japonica*, whose pericarps are used as soap, cough medicine and a piscicidal agent[171]. Of the isolates, **253** and **254** exhibited the strongest inhibitory activities with IC_{50} values of 7.8 and 9.3 μmol/L, respectively. Triterpenoid **252**, which converted a carbonyl group at C-28 to a hydroxymethyl group, showed weak inhibitory activity (IC_{50}=44.4 μmol/L) compared with **253**. Moreover, replacement of a carbonyl group at C-28 to a hydroxyl group (**255**, IC_{50}>50 μmol/L) and/or a methyl group (**256**, IC_{50}>50 μmol/L) resulted in the loss of *in vitro* inhibitory activity. These results also indicated that the C-28 carbonyl group in oleanane-type triterpenoids might be required for PTP1B inhibitory activity.

24-Norursane triterpenes, ilekudinols A **257** and B **258**, were isolated as active metabolites from the MeOH extract of the leaves and stems of the plant *Weigela subsessilis*[172]. Both ilekudinols inhibited PTP1B in a non-competitive manner with IC_{50} values of 29.1±2.8 and 5.3±0.5 μmol/L, respectively. Comparison of the activities of **257** and **258** indicated that the free carboxyl group at C-28 in this type of triterpenes might play a critical role in the inhibition of PTP1B.

Activity-guided fractionation of a MeOH extract of the roots of the plant *S lappa* led to the isolation of two active constituents, betulinic acid **259** and betulinic acid methyl ester **260**[138]. The bioassay revealed that **259** and **260** inhibited PTP1B activity with IC_{50} values of 0.70±0.03 and 0.93±0.07 μg/mL, respectively. Bioassay-guided fractionation of the MeOH extract of the stem barks of the plant *Sorbus commixta* resulted in the isolation of two lupine-type triterpenes, lupenone **261** and lupeol **262**[173]. Both **261** and **262** inhibited PTP1B in a non-competitive manner with IC_{50} values of 13.7±2.1 and 5.6±0.9 μmol/L, respectively. A bioassay for the inhibitory effects on other PPs revealed that **261** and **262** had no inhibitory effects toward VHR and PP1 at levels up to 100 μmol/L. Csuk *et al* developed a practical synthetic route for the synthesis of **259** in one step with a 92% yield. The synthesis used TEMPO, $NaCl_2O$ and NaClO to selectively oxidize the primary alcohol function of **251** without affecting the secondary hydroxyl group[174]. A successful multistep enantioselective synthesis of **262** was reported by Surendra *et al*[175].

Hopane-6α,22-diol **263**, a hopane-based triterpene isolated from an MeOH extract of the Antarctic lichen *L carpathica*, inhibited PTP1B in a competitive manner with an IC_{50} value of 3.7 μmol/L[80]. Additionally, compound **263** displayed selectivity toward PTP1B over other PTPs, such as TCPTP (IC_{50}=8.4 μmol/L), SHP-2 (IC_{50}>68 μmol/L), LAR (IC_{50}>68 μmol/L), and CD45 (IC_{50}>68 μmol/L) (Figure 15).

The plant *Gynostemma pentaphyllum* is traditionally used as in Vietnamese folk medicine for the treatment of diabetes. Isolation of the $CHCl_3$-soluble extract of *G pentaphyllum* produced dammarne derivatives **264–270**, which display inhibitory activity[176]. Compound **270** is a 20R epimer of **269**, compounds **264–266** possess an epoxy group, while **267** and **268** possess a side chain of 20S, 23-ene, respectively. Compared with those compounds above, dammarne derivative **269** showed the most potent inhibitory activity (IC_{50}=5.3±0.4 μmol/L). Additionally, all these isolates showed a very weak inhibitory effect toward VHR with IC_{50} values of more than 100 μmol/L, and kinetic analysis indicated that **269** inhibited PTP1B by a competitive manner (K_i=2.8 μmol/L).

Steroids

Thousands of distinct steroids are found in natural resources.

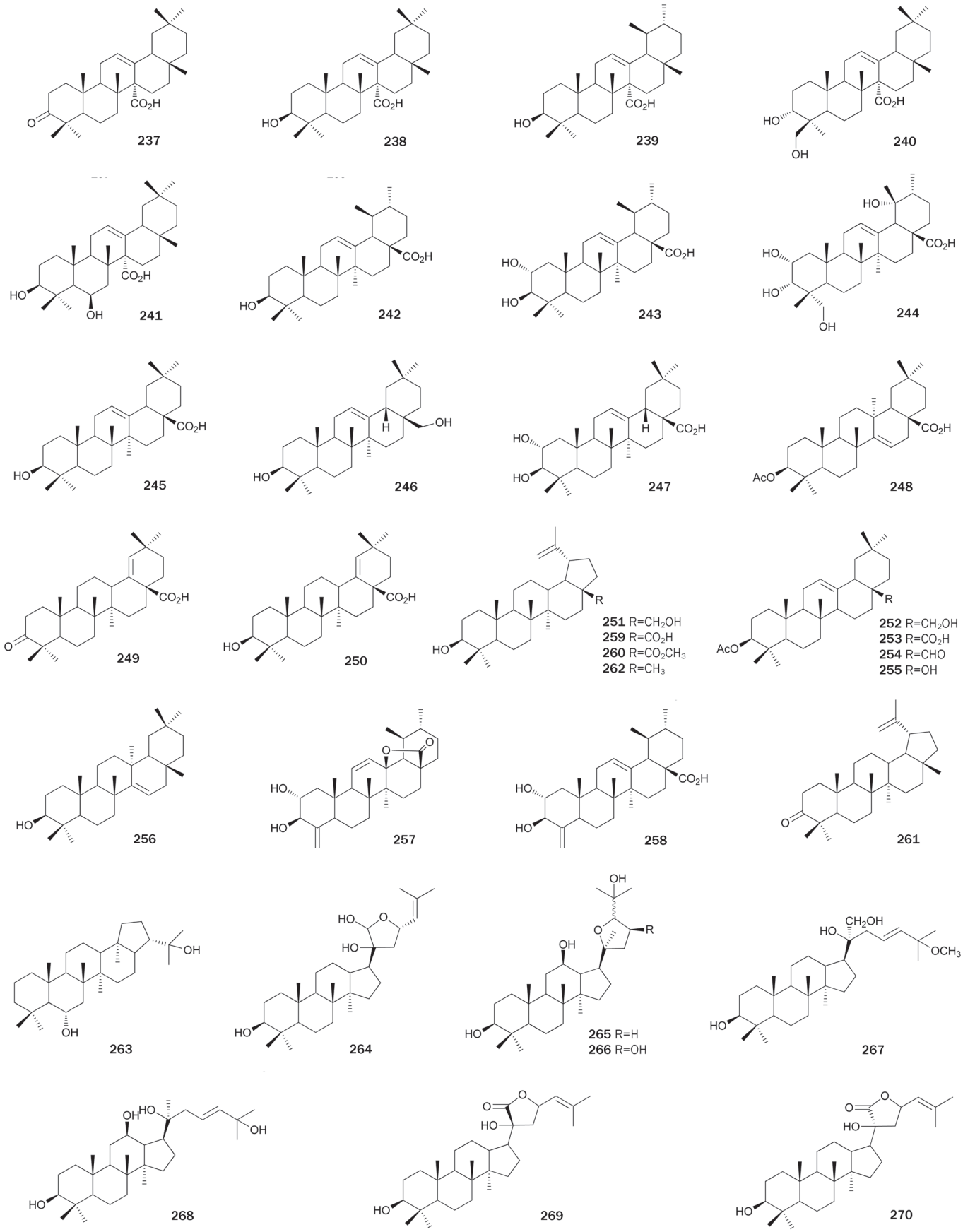

Figure 15. Structures of triterpenes **237**–**270**.

A variety of steroids play important roles in the life of animals and plants and are extensively used in medicinal chemistry[177]. There are also several steroids that act as PTP1B inhibitors.

The MeOH extract of the sclerotia of the fungus *Polyporus umbellatus* showed PTP1B inhibitory activity at a level of 30 μg/mL and produced three steroids **271–273**[178]. These steroids showed inhibitory activity with IC_{50} values of 8.9±0.3, 6.5±0.6, and 7.5±0.2 μg/mL, respectively.

Arenicolsterol A **274**, a novel cytotoxic enolic sulphated sterol, was isolated from the marine annelid *Arenicola cristata*[179]. The study of its selectivity on other PTPs indicated that **274** exhibited inhibition on intracellular PTP1B, with a similar potency to Cdc25a, Cdc25b, JSP1, and SHP1, weaker inhibition on mPTPσ, TCPTP, and PTP-PEST, and almost no inhibition on receptor-like PTP-LAR and PTPα. The reduction in apoptosis of HeLa cells caused by **274** was found to be correlative with the inhibition of the PTPs.

Phytochemical investigation on the stem bark of the plant *Toona ciliata* var *pubescens* produced (*Z*)-aglawone **275**[180]. (*Z*)-aglawone **275** inhibited PTP1B in a competitive manner with an IC_{50} value of 1.12 μg/mL. It is interesting to note that the (*E*)-isomer of **275** showed no inhibition of PTP1B.

Calicoferol E **276**, a secosterol isolated from the gorgonian *Muricella sinensis* collected from the South China Sea, exhibited inhibitory activity with an IC_{50} value of 27.28 μmol/L[181]. Compound **276** has been synthesized via a concise linear synthesis[182]. Key steps of the synthetic process included the preparation of 9α-hydroxycholest-1,4-diene-3-one from commercially available 5α-cholestan-3β-ol followed by acid-catalyzed rearrangement (Figure 16).

N- or S-containing compounds

Acylic manoalide derivatives, hippolides A **277** and B **278**, were isolated from the sponge *Hippospongia lachne* of the South China Sea. Their absolute configurations were established by the modified Mosher's method and CD data[183]. Both hippolides exhibited inhibitory activity with IC_{50} values of 23.81 and 39.67 μmol/L, respectively, and showed moderate cytotoxicity against HCT-116 cell lines. Additionally, hippolides A **277** showed weak anti-inflammatory activity.

Caulerpin **279**, an indole derivative isolated from the Chinese green alga *Caulerpa taxifolia*, showed inhibitory activity with an IC_{50} value of 3.77 μmol/L[184]. Three 3-bromoamino-7-bromomethylnaphthalene analogs **280–282**, isolated from the red alga *L similis*, showed weak inhibitory activity with IC_{50} values ranging from 65.3 to 102 μmol/L[73].

Berberine **283** is an isoquinoline alkaloid of wide distribution in nature[185] that is widely used in traditional eastern homeotherapy, particularly in treating gastrointestinal infections and as an anti-hyperglycemic agent by many Chinese physicians[186]. In docking experiments, compound **283** was found to fit readily within the binding pocket of PTP1B in a low energy orientation and to potently and competitively inhibit recombinant PTP1B *in vitro* (K_i=91.3 nmol/L). This finding suggests at least one of the reasons for the reported anti-hyperglycemic activities of berberine[186]. Additionally, compound **283** demonstrated insulin-mimicry effects on both adipocytes and myocytes, which may occur through the inhibition of PTP1B activity (inhibitory activity up to 40% and 60% at 50 and 100 μmol/L, respectively)[187].

Papaverine **284**, found in the opium poppy, is an opium alkaloid used primarily in the treatment of visceral spasm, vasospasm (especially those involving the heart and the brain), and occasionally in the treatment of erectile dysfunction[188]. Inspired by the structural similarity with **283**, papaverine **284** was inferred to exhibit inhibitory activity. It was shown that **284** readily docked within the binding pocket of PTP1B in a low-energy orientation via an optimal set of attractive interactions[189]. Compound **284** exhibited a potent *in vitro* inhibitory effect (IC_{50}=1.20 μmol/L), and significantly decreased fasting blood glucose levels of Balb/c mice *in vivo*.

Ceramide **285**, determined to be a C_{23}-phytosphingosineing unit containing three hydroxyl groups and C_{19}-fatty acid, was isolated from a MeOH extract of the sclerotia of the fungus *P umbellatus*[178]. This compound showed inhibitory activity with an IC_{50} value of 25.1±0.1 μmol/L. Albidopyrone **286**, a α-pyrone-containing secondary metabolite isolated from the fungus *Streptomyces albidoflavus*, exhibited weak inhibitory activity[190]. A macrolactam polyketide antibiotic, piceamycin **287** was isolated from the extract of the fungus *Streptomyces* (unknown species) found in the mycorrhizosphere of the Norway spruce. Compound **287** showed inhibitory activity with an IC_{50} value of 10.1 μmol/L as well as antitumor and antifungal activities[191]. Stereocalpin A **288**, a unique cyclic peptide incorporating a 5-hydroxy-2,4-dimethyl-3-oxo-octanoic acid in the structure, was isolated from the MeOH extract of the Antarctic lichen *S alpinum*[192]. Compound **288** inhibited PTP1B with an IC_{50} value of 40 μmol/L and showed moderate cytotoxicity against three human solid tumor cell lines, including HT-29, B16/F10 and HepG2. However, the spectral data

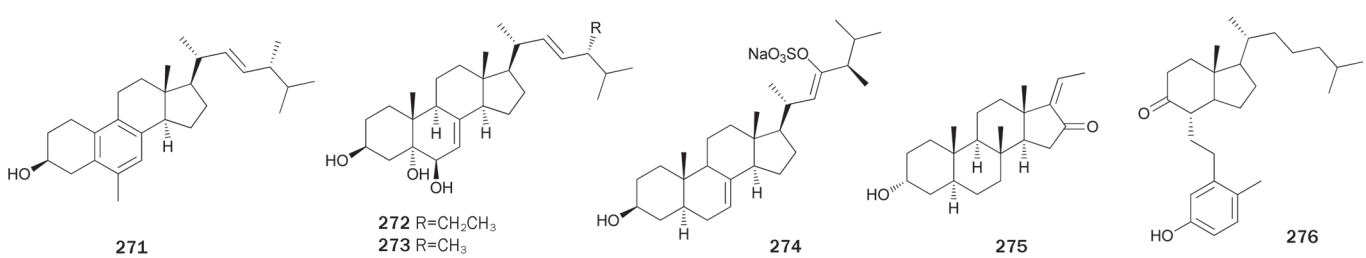

Figure 16. Structures of steroids **271–276**.

of synthetic **288** did not match with the data reported for the naturally derived **288**, suggesting that the structure of natural **288** had been assigned incorrectly[193].

Two 17-membered carbocyclic tetraenes, chejuenolides A **289** and B **290**, were isolated from the EtOAc extract of the marine bacteria *Hahella chejuensis* and their absolute configurations were assigned by application of modified Mosher method[194]. Both chejuenolides showed weak inhibitory activity (65% and 75% at a concentration of 150 μg/mL, respectively) (Figure 17).

Gymnorrhizol **291**, a novel, unusual 15-membered macyrocylic polydisulfide with an unprecedented carbon skeleton composed of three repeated 1,3-dimercaptopropan-2-ol units, was isolated from the Chinese mangrove *Brugiera gymnorrhiza*[195]. Its structure was determined by extensive spectroscopic studies and further confirmed by X-ray crystallographic analysis[196]. Compound **291** exhibited inhibitory activity with an IC_{50} value of 14.9 μmol/L. Its total synthesis was achieved in only three steps with a 25% overall yield[197].

Further research on the chemical constituents of *B gymnorrhiza* collected from Guangdong Province, China, led to the isolation of bruguiesulfurol **292**, an analog of **291**. Compound **292** inhibited PTP1B with an IC_{50} value of 17.5 μmol/L[198].

Miscellaneous

RK-682 **293** (3-hexadecanoyl-5-hydroxymethyl tetronic acid), isolated from the fungus *Streptomyces* (unknown species), was originally found to be a potent inhibitor of tyrosine phosphatease[199] and was therefore used as a positive control in PTP1B inhibitory activity assays (IC_{50}=4.5±0.5 μmol/L)[66]. Early stereoselective syntheses by Sodeoka *et al*[200] and others[201,202] served to ascertain the absolute configuration of **293**. Recently, **293** was prepared in solution and on a solid support from (2R)-glycerates in five steps with a yield of approximately 40%[203]. A chemical constituent study of *S griseoruber* produced an α-pyrone-containing secondary metabolite, BE 51068 **294**, with weak inhibitory activity[204]. Dihydrocarolic acid **295** and penitricin D **296**, isolated from a fermentation

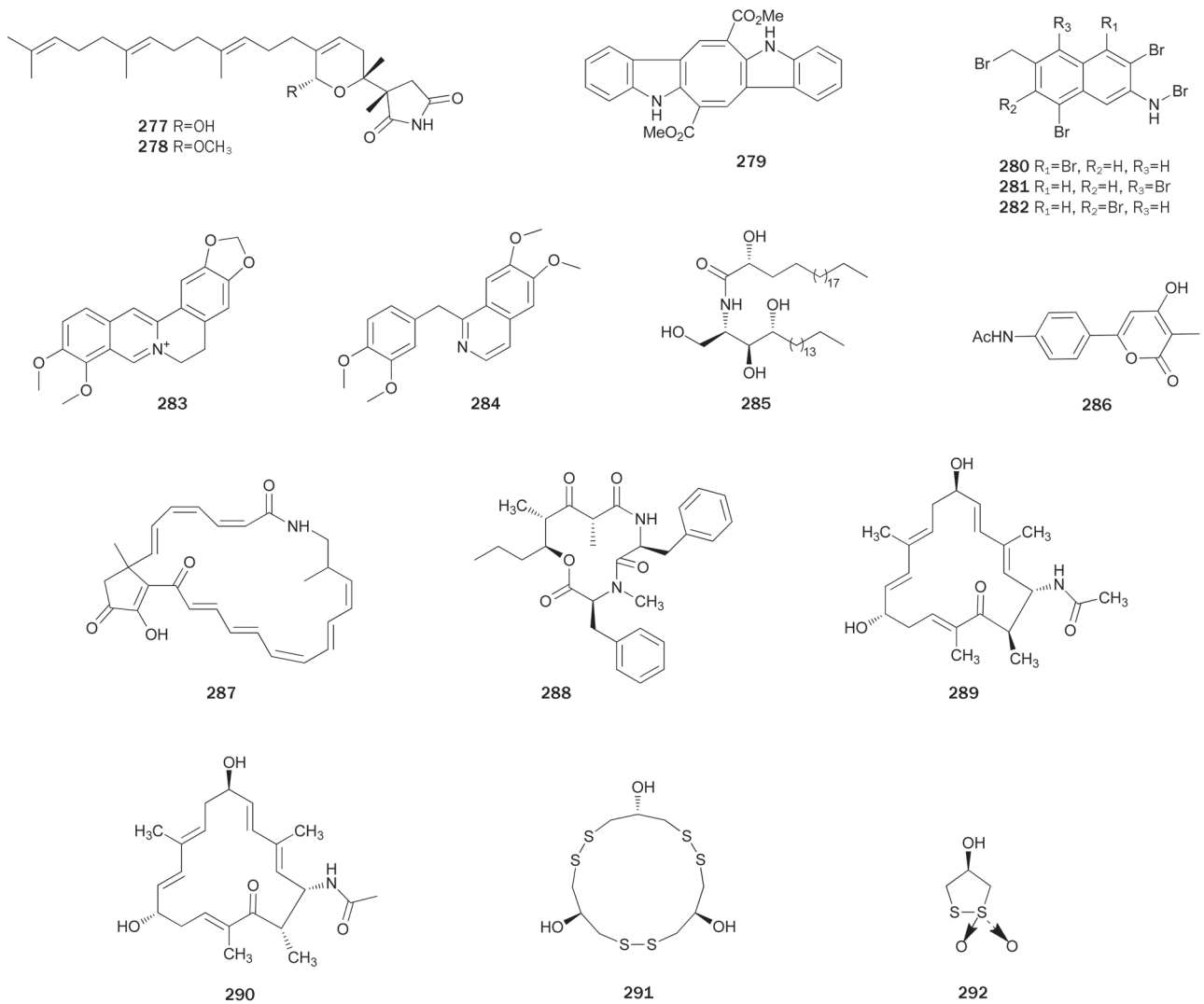

Figure 17. Structures of N- or S-containing compounds **277–292**.

broth of the fungus *Aspergillus niger*, inhibited PTP1B with IC_{50} values of 38.0 and 15.8 μmol/L, respectively[205]. Both compounds **295** and **296** also exhibited a dose-dependent inhibition of CD45. Ascochitine **297**, a polyketide isolated from the marine-derived fungus *Ascochyta salicorniae*, was found to inhibit PTP1B with an IC_{50} value of 38.5±6.5 μmol/L[206]. Compound **297** was also active against other PPs, such as Cdc25a and MPtpB, but inactive against VHR, MPtpA, and VE-PTP. The first total synthesis of **297** was reported by Galbraith *et al* in 1966[207].

Research on the chemical constituents of the Chinese mangrove *Aegiceras corniculatum* led to the isolation of falcarindiol **298**, which showed inhibitory activity with an IC_{50} value of 9.15±2.48 μmol/L[208]. Zheng *et al* reported the first stereoselective synthesis of **298** from *L*-tartaric acid and *D*-xylose via the Cadiot-Chodkiczwicz reaction as a key step[209]. Further synthetic studies have reported several strategies for the stereoselective synthesis of **298**[210–212].

Further research on the chemical constituents of the EtOH extract of the plant *Ardisia japonica* by Li *et al* led to the isolation of [1,4]benzoquinones **299–302**[213]. Benzoquinones **299–302** showed significant *in vitro* inhibitory activities with IC_{50} values ranging from 3.01±0.9 to 19.15±1.0 μmol/L. Because **299–302** have the same substituted [1,4]benzoquinone skeleton and length of the aliphatic side chain at C-3, it seems that nonpolar 5-*O*-substituents increase inhibitory activity. In 1992, Yadav *et al* reported a practical route for preparing **299** from 3-bromo-4-hydroxy-5-methoxybenzaldehyde[214]. Later, two synthetic routes for the preparation of **299** were reported by Poigny *et al* and Pfeifer *et al*, respectively[215, 216].

A naphthoquinone derivative, cyclonoside A **303**, was isolated from the leaves of the plant *C paliurus*. The absolute configuration of **303** was determined by X-ray analysis. This compound showed inhibition of PTP1B with an IC_{50} value of 2.11±0.66 μmol/L[35]. Research on an extract of the Okinawan sponge *Plakortis* (unknown species) led to the isolation of manzamenones B **304** and E **305**, which are fatty acid derivatives possessing a bicycle[4,3,0]nonane skeketon[217]. Both manzamenones exhibited inhibitory activity with IC_{50} values of 10.8 and 13.5 μmol/L, respectively[218] (Figure 18).

Conclusions

Much research has established PTP1B inhibitors as potential therapeutic options for the treatment of type 2 diabetes and obesity. Research has led to the development of approximately 300 PTP1B inhibitors isolated from a variety of natural resources, which have been reviewed here in detail. Many of these inhibitors have promising *in vivo* activities and selectivity profiles. These inhibitors should be considered for development as promising clinical drug candidates or drugs.

For example, in the group of phenolics, compounds **24** and **25** showed potent anti-hyperglycemic activity in the STZ-induced diabetic rats and db/db mouse models. Compound **75** exhibited inhibition on PTP1B without cytotoxicity against CHO cells at concentrations greater than 20 μmol/L for 48 h. Compounds **94**, **96**, **99**, and **101** showed PTP1B inhibitory activity and strong *in vitro* anticancer activity against an array of cancer cells. Compounds **116–118** showed good selectivity over other PPs. The preliminary SAR of some flavonoids suggests that less polar substituents (*eg*, isoprenyl group, methylation or aceylation of hydroxyl group) on their skeletons are usually beneficial to activity, while addition of one

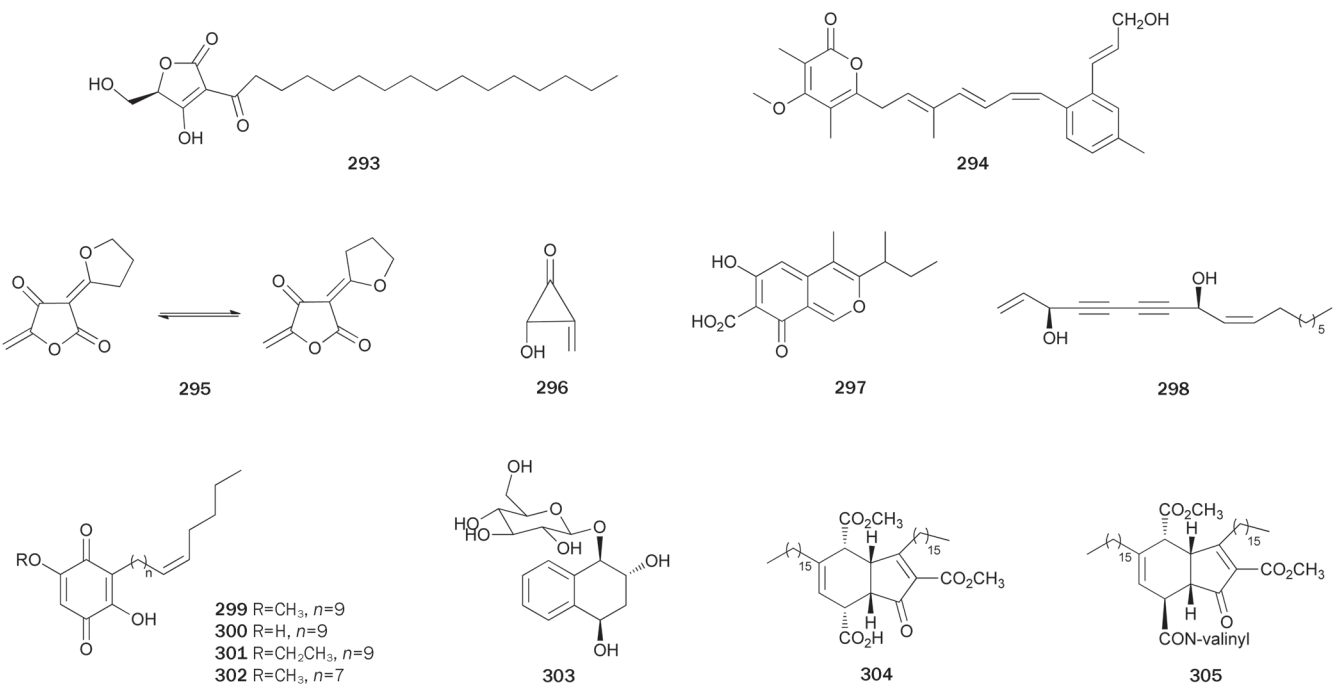

Figure 18. Structures of miscellaneous **293–305**.

hydroxyl group may lead to decreased activity. According to these results, various series of flavonoid PTP1B inhibitors with different substituents on the aromatic rings should be synthesized and evaluated to find PTP1B inhibitors with better activities and selectivity profiles. Moreover, the flavonoid skeleton is easily synthesized, providing many opportunities for medicinal chemists to carry out detailed SAR studies. Additionally, flavonoids are abundant in many foods (*eg*, fruits or vegetable) and usually have antiviral, antitumor, antiplatelet, anti-inflammatory or antioxidant activities, which makes them a preferred scaffold with favorable properties for drug design. Other phenolics also exhibited good activity profiles. For example, bromophenols **120–123** might be responsible for the *in vivo* anti-hyperglycemic activity of the extract from red alga. Phenolic acids **149**, **150**, **152**, **184** also showed good selectivity over other PPs.

In the terpene group, diterpene **214** and its isobutyryloxy derivate **215** exhibited inhibition on PTP1B without inhibitory effects toward VHR and PP1. Compounds **231** and **232** are inactive against PTPs, such as LAR, SHP-1, and MKPX. The preliminary SAR for kaurane-type diterpene PTP1B inhibitors suggests that an ester moiety at C-17 position, such as isobutyryloxy group, is essential for activity. Additionally, the hydroxyl group substituent at the C-17 or C-16 position usually decreases activity. Some important triterpene PTP1B inhibitors, such as **245**, **247**, and **269**, are widely distributed in food and medicinal plants. Additionally, compound **245** is relatively non-toxic, hepatoprotective, and exhibits antitumor and antiviral properties. Currently, many studies on the structural modification of this class of PTP1B inhibitors have been performed by several research groups. The SAR information obtained is very helpful for the design of triterpene-type antidiabetic drug candidates.

Most of the pharmaceuticals currently on the market are N-containing compounds, so the finding that alkaloid drugs (*eg*, berberine **283** and papaverine **284**) have inhibitory activity on PTP1B is very important and positive to design new N-containing PTP1B inhibitors. Moreover, the rare natural polydisulfides **291** and **292** represent a group of PTP1B inhibitors with an unusual carbon skeleton. These compounds provide a new chemical molecular template for designing novel anti-diabetic drug candidates. More synthetic and pharmacologic studies on this type of compounds are needed to obtain detailed SAR information.

As presented above, although many natural PTP1B inhibitors exhibit promising clinical potential, to the best of our knowledge there are no clinically used PTP1B inhibitors approved by the FDA for use in the USA, which is most likely due to relatively low activities (micromole level for IC_{50}) or lack of selectivity. Designing more drug-like PTP1B inhibitors as oral agents is a challenging task for two reasons. The first reason is the highly charged nature of the catalytic domain of PTP1B. The other reason is the structural homogeneity of the active and secondary binding sites in PTPs, which leads to a lack of targeting selectivity. However, it is very important to note that many of the natural PTP1B inhibitors, summarized herein, possess fascinating molecular architectures, potent activity, and better PTP1B selectivity. These compounds could be developed as anti-diabetic drugs or at least promising drug candidates in the near future. Additionally, the information provided herein is helpful for designing and synthesizing new PTP1B inhibitors. With the ongoing efforts and interest from chemists and pharmacologists, it is highly probable that more potent and selective PTP1B inhibitors will emerge, either directly from natural resources or derived from the structural optimization of natural products.

Acknowledgements

This work was supported financially by National Marine "863" Project (No 2011AA09070102), Natural Science Foundation of China (No 31070310, 40976048, 21021063, 21072204, and 81072572), the SKLDR/SIMM Projects (No SIMM1203ZZ-03 and SIMM1105KF-04), and was partially funded by National S&T Major Projects (No 2011ZX09307-002-03), and the EU 7th Framework Programme-IRSES Project (2010-2014).

Supplementary information

Supplementary data (names, PTP1B inhibitory activity data, source species, and references of compounds **1–305**) associated with this article are available at website of Acta Pharmacologica Sinica on NPG.

References

1 WHO. Diabetes. Available from: http://www.who.int/mediacentre/factsheets/fs312/en/index.html.
2 Eberhardt MS, Ogden C, Engelgau M, Cadwell B, Hedley AA, Saydah SH. Prevalence of overweight and obesity among adults with diagnosed diabetes — United States, 1988–1994 and 1999–2002. MMWR 2004; 53: 1066–8.
3 Risérus U, Willett WC, Hu FB. Dietary fats and prevention of type 2 diabetes. Prog Lipid Res 2009; 48: 44–51.
4 Newman DJ, Cragg GM. Natural products as sources of new drugs over the last 25 years. J Nat Prod 2007; 70: 461–77.
5 Jung M, Park M, Lee HC, Kang YH, Kang ES, Kim SK. Antidiabetic agents from medicinal plants. Curr Med Chem 2006; 13: 1203–18.
6 Zhang S, Zhang ZY. PTP1B as a drug target: recent developments in PTP1B inhibitor discovery. Drug Discov Today 2007; 12: 373–81.
7 Alonso A, Sasin J, Bottini N, Friedberg I, Friedberg I, Osterman A, *et al*. Protein tyrosine phosphatases in the human genome. Cell 2004; 117: 699–711.
8 Lessard L, Stuible M, Tremblay ML. The two faces of PTP1B in cancer. Biochim Biophys Acta 2010; 1804: 613–9.
9 Combs AP. Recent advances in the discovery of competitive protein tyrosine phosphatase 1B inhibitors for the treatment of diabetes, obesity, and cancer. J Med Chem 2010; 53: 2333–44.
10 Nichols AJ, Mashal RD, Balkan B. Toward the discovery of small molecule PTP1B inhibitors for the treatment of metabolic diseases. Drug Dev Res 2006; 67: 559–66.
11 Taylor SD, Hill B. Recent advances in protein tyrosine phosphatase 1B inhibitors. Expert Opin Invest Drugs 2004; 13: 199–214.
12 Taylor SD. Inhibitors of protein tyrosine phosphatase 1B (PTP1B). Curr Top Med Chem 2003; 3: 759–82.
13 Lee S, Wang Q. Recent development of small molecular specific inhibitor of protein tyrosine phosphatase 1B. Med Res Rev 2007; 27:

553–73.
14 Mohler ML, He Y, Wu Z, Hwang DJ, Miller DD. Recent and emerging anti-diabetes targets. Med Res Rev 2009; 29: 125–95.
15 Thareja S, Aggarwal S, Bhardwaj TR, Kumar M. Protein tyrosine phosphatase 1B inhibitors: A molecular level legitimate approach for the management of diabetes mellitus. Med Res Rev 2012; 32: 459–517.
16 Cebula RE, Blanchard JL, Boisclair MD, Pal K, Bockovich NJ. Synthesis and phosphatase inhibitory activity of analogs of sulfircin. Bioorg Med Chem Lett 1997; 7: 2015–20.
17 Chen RM, Hu LH, An TY, Li J, Shen Q. Natural PTP1B inhibitors from Broussonetia papyrifera. Bioorg Med Chem Lett 2002; 12: 3387–90.
18 Zhang ZY. Protein-tyrosine phosphatases: Biological function, structural characteristics, and mechanism of catalysis. Crit Rev Biochem Mol Biol 1998; 33: 1–52.
19 Wang WQ, Sun JP, Zhang ZY. An overview of the protein tyrosine phosphatase superfamily. Curr Top Med Chem 2003; 3: 739–48.
20 Barford D, Flint AJ, Tonks NK. Crystal structure of human protein tyrosine phosphatase 1B. Science 1994; 263: 1397–404.
21 Zhang ZY, Maclean D, McNamara DJ, Sawyer TK, Dixon JE. Protein tyrosine phosphatase substrate specificity: size and phosphotyrosine positioning requirements in peptide substrates. Biochemistry 1994; 33: 2285–90.
22 Palmer ND, Bento JL, Mychaleckyj JC, Langefeld CD, Campbell JK, Norris JM, *et al*. Association of protein tyrosine phosphatase 1B gene polymorphisms with measures of glucose homeostasis in Hispanic Americans: the insulin resistance atherosclerosis study (IRAS) family study. Diabetes 2004; 53: 3013–9.
23 Elchebly M, Payette P, Michaliszyn E, Cromlish W, Collins S, Loy AL, *et al*. Increased insulin sensitivity and obesity resistance in mice lacking the protein tyrosine phosphatase-1B gene. Science 1999; 283: 1544–8.
24 Klaman LD, Boss O, Peroni OD, Kim JK, Martino JL, Zabolotny JM, *et al*. Increased energy expenditure, decreased adiposity, and tissue-specific insulin sensitivity in protein-tyrosine phosphatase 1B-deficient mice. Mol Cell Biol 2000; 20: 5479–89.
25 Cheng A, Uetani N, Simoncic PD, Chaubey VP, Lee-Loy A, McGlade CJ, *et al*. Attenuation of leptin action and regulation of obesity by protein tyrosine phosphatase 1B. Dev Cell 2002; 2: 497–503.
26 Xie L, Lee SY, Andersen JN, Waters S, Shen K, Guo XL, *et al*. Cellular effects of small molecule PTP1B inhibitors on insulin signaling. Biochemistry 2003; 42: 12792–804.
27 Crozier A, Jaganath IB, Clifford MN. Dietary phenolics: chemistry, bioavailability and effects on health. Nat Prod Rep 2009; 26: 1001–43.
28 Veitch NC, Grayer RJ. Flavonoids and their glycosides, including anthocyanins. Nat Prod Rep 2011; 28: 1626–95.
29 Yoon G, Lee W, Kim SN, Cheon SH. Inhibitory effect of chalcones and their derivatives from *Glycyrrhiza inflata* on protein tyrosine phosphatase 1B. Bioorg Med Chem Lett 2009; 19: 5155–7.
30 Jeon JH, Kim MR, Jun JG. Concise synthesis of licochalcone A through water-accelerated [3,3]-sigmatropic rearrangement of an aryl prenyl ether. Synthesis 2011; 2011: 370–6.
31 Nielsen SF, Chen M, Theander TG, Kharazmi A, Christensen SB. Synthesis of antiparasitic licorice chalcones. Bioorg Med Chem Lett 1995; 5: 449–52.
32 Na Y, Cha JH, Yoon HG, Kwon Y. A concise synthesis of licochalcone E and its regio-isomer, licochalcone F. Chem Pharm Bull 2009; 57: 607–9.
33 Li S, Li W, Wang Y, Asada Y, Koike K. Prenylflavonoids from *Glycyrrhiza uralensis* and their protein tyrosine phosphatase-1B inhibitory activities. Bioorg Med Chem Lett 2010; 20: 5398–401.
34 Hoang DM, Ngoc TM, Dat NT, Ha DT, Kim YH, Luong HV, *et al*. Protein tyrosine phosphatase 1B inhibitors isolated from *Morus bombycis*. Bioorg Med Chem Lett 2009; 19: 6759–61.
35 Zhang J, Shen Q, Lu JC, Li JY, Liu WY, Yang JJ, *et al*. Phenolic compounds from the leaves of *Cyclocarya paliurus* (Batal.) Ijinskaja and their inhibitory activity against PTP1B. Food Chem 2010; 119: 1491–6.
36 Wagner H, Danninger H, Seligmann O, Farkas L. Synthese von glucuroniden der flavonoid-reihe, I. Erste synthese eines natürlich vorkommenden flavonoid-glucuronids (quercetin-3-β-*D*-glucuronid). Chem Ber 1970; 103: 3674–7.
37 Min BS. Revision of structures of flavanoids from *Scutellaria indica* and their protein tyrosine phosphatase 1B inhibitory activity. Nat Prod Sci 2006; 12: 205–9.
38 Huang WH, Chien PY, Yang CH, Lee AR. Novel synthesis of flavonoids of *Scutellaria baicalensis* Georgi. Chem Pharm Bull 2003; 51: 339–40.
39 Lee MS, Kim CH, Hoang DM, Kim BY, Sohn CB, Kim MR, *et al*. Genistein-derivatives from *Tetracera scandens* stimulate glucose-uptake in L6 myotubes. Biol Pharm Bull 2009; 32: 504–8.
40 Rao KSRM, Iyer CSR, Iyer PR. Synthesis of alpinum isoflavone, derrone and related pyranoisoflavones. Tetrahedron 1987; 43: 3015–9.
41 Punitha R, Manoharan S. Antihyperglycemic and antilipidperoxidative effects of *Pongamia pinnata* (Linn.) *Pierre* flowers in alloxan induced diabetic rats. J Ethnopharmacol 2006; 105: 39–46.
42 Tamrakar AK, Yadav PP, Tiwari P, Maurya R, Srivastava AK. Identification of pongamol and karanjin as lead compounds with antihyperglycemic activity from *Pongamia pinnata* fruits. J Ethnopharmacol 2008; 118: 435–9.
43 Goel A, Dixit M. Amberlyst 15-catalyzed efficient synthesis of 5-acetyl-4-hydroxy-coumarone and 5-acetyl-6-hydroxy-coumarone: Crucial precursors for several naturally occurring furanoflavones. Synlett 2004; 2004: 1990–4.
44 Yadav PP, Ahmad G, Maurya R. An efficient route for commercially viable syntheses of furan- and thiophene-anellated β-hydroxychalcones. Tetrahedron Lett 2005; 46: 5621–4.
45 Hossain MA, Das AK, Salehuddin SM. Synthesis of karanjin, naturally occurring furanoflavone. Pak J Sci Ind Res 2003; 46: 31–2.
46 Bae EY, Na M, Njamen D, Mbafor JT, Fomum ZT, Cui L, *et al*. Inhibition of protein tyrosine phosphatase 1B by prenylated isoflavonoids isolated from the stem bark of *Erythrina addisoniae*. Planta Med 2006; 72: 945–8.
47 Na M, Jang J, Njamen D, Mbafor JT, Fomum ZT, Kim BY, *et al*. Protein tyrosine phosphatase-1B inhibitory activity of isoprenylated flavonoids isolated from *Erythrina mildbraedii*. J Nat Prod 2006; 69: 1572–6.
48 Jang J, Na M, Thuong PT, Njamen D, Mbafor JT, Fomum ZT, *et al*. Prenylated flavonoids with PTP1B inhibitory activity from the root bark of *Erythrina mildbraedii*. Chem Pharm Bull 2008; 56: 85–8.
49 Cui L, Ndinteh DT, Na M, Thuong PT, Silike-Muruumu J, Njamen D, *et al*. Isoprenylated flavonoids from the stem bark of *Erythrina abyssinica*. J Nat Prod 2007; 70: 1039–42.
50 Cui L, Thuong PT, Lee HS, Ndinteh DT, Mbafor JT, Fomum ZT, *et al*. Flavanones from the stem bark of *Erythrina abyssinica*. Bioorg Med Chem 2008; 16: 10356–62.
51 Cui L, Lee HS, Ndinteh DT, Mbafor JT, Kim YH, Le TVT, *et al*. New prenylated flavanones from *Erythrina abyssinica* with protein tyrosine phosphatase 1B (PTP1B) inhibitory activity. Planta Med 2010; 76:

713–8.
52 Nguyen PH, Dao TT, Kim J, Phong DT, Ndinteh DT, Mbafor JT, *et al*. New 5-deoxyflavonoids and their inhibitory effects on protein tyrosine phosphatase 1B (PTP1B) activity. Bioorg Med Chem 2011; 19: 3378–83.
53 Nguyen PH, Le TV, Thuong PT, Dao TT, Ndinteh DT, Mbafor JT, *et al*. Cytotoxic and PTP1B inhibitory activities from *Erythrina abyssinica*. Bioorg Med Chem Lett 2009; 19: 6745–9.
54 Dao TT, Nguyen PH, Thuong PT, Kang KW, Na M, Ndinteh DT, *et al*. Pterocarpans with inhibitory effects on protein tyrosine phosphatase 1B from *Erythrina lysistemon* Hutch. Phytochemistry 2009; 70: 2053–7.
55 Na M. Inhibitory effect of constituents from *Cercis chinensis* on cellular aging [dissertation]. Daejeon, Korea: Chungnam National University; 2004. 114 p.
56 Farmer RL, Biddle MM, Nibbs AE, Huang X, Bergan RC, Scheidt KA. Concise syntheses of the abyssinones and discovery of new inhibitors of prostate cancer and MMP-2 expression. ACS Med Chem Lett 2010; 1: 400–5.
57 Hu LH, Qin ZL, Li C, Huang Q, Wang FH. Synthesis and fungicidal activity of flavanone derivatives containing isopentene group. Chin J Appl Chem 2003; 20: 1161–5.
58 Pelter A, Ward RS, Ashdown DHJ. The synthesis of mono-, di-, and trihydroxyisoflavones. Synthesis 1978; 1978: 843.
59 Tsukayama M, Kawamura Y, Tamaki H, Horie T. Synthesis of parvisoflavones A and B. Chem Pharm Bull 1991; 39: 1704–6.
60 Yang JH, Zhao YM, Ji CB. First total synthesis of (±)-abyssinoflavanone V. Chin Chem Lett 2008; 19: 658–60.
61 Rao GV, Swamy BN, Chandregowda V, Reddy GC. Synthesis of (±)Abyssinone I and related compounds: Their anti-oxidant and cytotoxic activities. Eur J Med Chem 2009; 44: 2239–45.
62 Moriarty RM, Grubjesic S, Surve BC, Chandersekera SN, Prakash O, Naithani R. Synthesis of Abyssinone II and related compounds as potential chemopreventive agents. Eur J Med Chem 2006; 41: 263–7.
63 Maiti A, Cuendet M, Croy VL, Endringer DC, Pezzuto JM, Cushman M. Synthesis and biological evaluation of (±)-abyssinone II and its analogues as aromatase inhibitors for chemoprevention of breast cancer. J Med Chem 2007; 50: 2799–806.
64 Mohamed SEN, Thomas P, Whiting DA. Synthesis of the phytoalexin (±)-phaseollin: 3-phenylthiochromans as masked 2*H*-chromenes and *o*-prenyl phenols. J Chem Soc, Perkin Trans 1 1987; 431–7.
65 Na M, Kim KA, Oh H, Kim BY, Oh WK, Ahn JS. Protein tyrosine phosphatase 1B inhibitory activity of amentoflavone and its cellular effect on tyrosine phosphorylation of insulin receptors. Biol Pharm Bull 2007; 30: 379–81.
66 Cui L, Na M, Oh H, Bae EY, Jeong DG, Ryu SE, *et al*. Protein tyrosine phosphatase 1B inhibitors from *Morus* root bark. Bioorg Med Chem Lett 2006; 16: 1426–9.
67 Guo S, Li J, Li T, Shi D, Han L. Synthesis of three bromophenols from red algae as PTP1B inhibitors. Chin J Oceanol Limnol 2011; 29: 68–74.
68 Liu Q, Xu H, Zhang T, Fan X, Han L. A new compound as PTP1B inhibitor from the red alga *Polysiphonia urceolata*. Hua Xue Tong Bao 2006; 69: 708–10.
69 Shi D, Xu F, He J, Li J, Fan X, Han L. Inhibition of bromophenols against PTP1B and anti-hyperglycemic effect of *Rhodomela confervoides* extract in diabetic rats. Chin Sci Bull 2008; 53: 2476–9.
70 Shi DY, Xu F, Li J, Guo SJ, Su H, Han LJ. PTP1B inhibitory activities of bromophenol derivatives from algae. Zhongguo Zhong Yao Za Zhi 2008; 33: 2238–40.
71 Oh KB, Lee JH, Lee JW, Yoon KM, Chung SC, Jeon HB, *et al*. Synthesis and antimicrobial activities of halogenated bis(hydroxyphenyl) methanes. Bioorg Med Chem Lett 2009; 19: 945–8.
72 Oh KB, Jeon HB, Han YR, Lee YJ, Park J, Lee SH, *et al*. Bromophenols as *Candida albicans* isocitrate lyase inhibitors. Bioorg Med Chem Lett 2010; 20: 6644–8.
73 Qin J, Su H, Zhang Y, Gao J, Zhu L, Wu X, *et al*. Highly brominated metabolites from marine red alga *Laurencia similis* inhibit protein tyrosine phosphatase 1B. Bioorg Med Chem Lett 2010; 20: 7152–4.
74 Liu X, Li X, Gao L, Cui C, Li C, Li J, *et al*. Extraction and PTP1B inhibitory activity of bromophenols from the marine red alga *Symphyocladia latiuscula*. Chin J Oceanol Limnol 2011; 29: 686–90.
75 Balaydin HT, Akbaba Y, Menzek A, Şahin E, Göksu S. First and short syntheses of biologically active, naturally occurring brominated mono- and dibenzyl phenols. ARKIVOC 2009; 2009: 75–87.
76 Chung TW, Moon SK, Chang YC, Ko JH, Lee YC, Cho G, *et al*. Novel and therapeutic effect of caffeic acid and caffeic acid phenyl ester on hepatocarcinoma cells: complete regression of hepatoma growth and metastasis by dual mechanism. FASEB J 2004; 18: 1670–81.
77 He ZZ, Yan JF, Song ZJ, Ye F, Liao X, Peng SL, *et al*. Chemical constituents from the aerial parts of *Artemisia minor*. J Nat Prod 2009; 72: 1198–201.
78 Lee YS, Kang IJ, Won MH, Lee JY, Kim JK, Lim SS. Inhibition of protein tyrosine phosphatase 1β by hispidin derivatives isolated from the fruiting body of *Phellinus linteus*. Nat Prod Commun 2010; 5: 1927–30.
79 Yao XS, Li J, Hong K, Tang JS, Gao H, Gao LX, *et al*. Application of 2-acetylamino gentisic acid to preparing insulin sensitizer. China patent CN 101919835 A. 2010 December 22.
80 Seo C, Yim JH, Lee HK, Oh H. PTP1B inhibitory secondary metabolites from the Antarctic lichen *Lecidella carpathica*. Mycology 2011; 2: 18–23.
81 Seo C, Choi YH, Ahn JS, Yim JH, Lee HK, Oh H. PTP1B inhibitory effects of tridepside and related metabolites isolated from the Antarctic lichen *Umbilicaria antarctica*. J Enzyme Inhib Med Chem 2009; 24: 1133–7.
82 Seo C, Sohn JH, Ahn JS, Yim JH, Lee HK, Oh H. Protein tyrosine phosphatase 1B inhibitory effects of depsidone and pseudodepsidone metabolites from the Antarctic lichen *Stereocaulon alpinum*. Bioorg Med Chem Lett 2009; 19: 2801–3.
83 Oh H, Kim BS, Bae EY, Kim MS, Kim BY, Lee HB, *et al*. Inhibition of PTP1B by metabolites from *Micromucor ramannianus* var *angulisporus* CRM000232. J Antibiot 2004; 57: 528–31.
84 Fürstner A, Konetzki I. Total synthesis of caloporoside. J Org Chem 1998; 63: 3072–80.
85 Fürstner A. Total syntheses and biological assessment of macrocyclic glycolipids. Eur J Org Chem 2004; 2004: 943–58.
86 Seo C, Sohn JH, Oh H, Kim BY, Ahn JS. Isolation of the protein tyrosine phosphatase 1B inhibitory metabolite from the marine-derived fungus *Cosmospora* sp SF-5060. Bioorg Med Chem Lett 2009; 19: 6095–7.
87 Baumgartner RR, Steinmann D, Heiss EH, Atanasov AG, Ganzera M, Stuppner H, *et al*. Bioactivity-guided isolation of 1,2,3,4,6-penta-*O*-galloyl-*D*-glucopyranose from *Paeonia lactiflora* roots as a PTP1B inhibitor. J Nat Prod 2010; 73: 1578–81.
88 Baumgartner RR, Steinmann D, Heiss EH, Atanasov AG, Ganzera M, Stuppner H, *et al*. Bioactivity-guided isolation of 1,2,3,4,6-penta-*O*-galloyl-*D*-glucopyranose from *Paeonia lactiflora* roots as a PTP1B inhibitor. J Nat Prod 2010; 73: 1742.
89 Na M, Hoang DM, Njamen D, Mbafor JT, Fomum ZT, Thuong PT, *et al*. Inhibitory effect of 2-arylbenzofurans from *Erythrina addisoniae* on

protein tyrosine phosphatase-1B*. Bioorg Med Chem Lett 2007; 17: 3868–71.
90 Feng Y, Carroll AR, Addepalli R, Fechner GA, Avery VM, Quinn RJ. Vanillic acid derivatives from the green algae *Cladophora socialis* as potent protein tyrosine phosphatase 1B inhibitors. J Nat Prod 2007; 70: 1790–2.
91 Seo C, Sohn JH, Park SM, Yim JH, Lee HK, Oh H. Usimines A–C, bioactive usnic acid derivatives from the Antarctic lichen *Stereocaulon alpinum*. J Nat Prod 2008; 71: 710–2.
92 Hawranik DJ, Anderson KS, Simmonds R, Sorensen JL. The chemoenzymatic synthesis of usnic acid. Bioorg Med Chem Lett 2009; 19: 2383–5.
93 Otani T, Sugimoto Y, Aoyagi Y, Igarashi Y, Furumai T, Saito N, *et al*. New Cdc25B tyrosine phosphatase inhibitors, nocardiones A and B, produced by *Nocardia* sp TP-A0248: taxonomy, fermentation, isolation, structural elucidation and biological properties. J Antibiot 2000; 53: 337–44.
94 Tanada Y, Mori K. Synthesis and absolute configuration of nocardione A and B, furano-o-naphthoquinone-type metabolites of *Nocardia* sp with antifungal, cytotoxic, and enzyme inhibitory activities. Eur J Org Chem 2001; 2001: 4313–9.
95 Yang H, Lu W, Bao JX, Aisa HA, Cai JC. Total synthesis of (±)-nocardione A and (±)-nocardione B, two Cdc25B tyrosine phosphatase inhibitors. Chin Chem Lett 2001; 12: 883–6.
96 Clive DL, Fletcher SP. Synthesis of (+)-nocardione A — use of formal radical cyclization onto a benzene ring. Chem Commun 2003; (19): 2464–5.
97 Clive DL, Fletcher SP, Liu D. Formal radical cyclization onto benzene rings: A general method and its use in the synthesis of *ent*-nocardione A. J Org Chem 2004; 69: 3282–93.
98 Seo C, Choi YH, Sohn JH, Ahn JS, Yim JH, Lee HK, *et al*. Ohioensins F and G: Protein tyrosine phosphatase 1B inhibitory benzonaphthoxanthenones from the Antarctic moss *Polytrichastrum alpinum*. Bioorg Med Chem Lett 2008; 18: 772–5.
99 Wang Y, Shang XY, Wang SJ, Mo SY, Li S, Yang YC, *et al*. Structures, biogenesis, and biological activities of pyrano[4,3-c]isochromen-4-one derivatives from the fungus *Phellinus igniarius*. J Nat Prod 2007; 70: 296–9.
100 Murray RD. Coumarins. Nat Prod Rep 1989; 6: 591–624.
101 Murray RDH. Coumarins. Nat Prod Rep 1995; 12: 477–505.
102 Estévez-Braun A, González AG. Coumarins. Nat Prod Rep 1997; 14: 465–75.
103 Umezawa T. Diversity in lignan biosynthesis. Phytochem Rev 2003; 2: 371–90.
104 Kim YC, Oh H, Kim BS, Kang TH, Ko EK, Han YM, *et al*. *In vitro* protein tyrosine phosphatase 1B inhibitory phenols from the seeds of *Psoralea corylifolia*. Planta Med 2005; 71: 87–9.
105 Xiao K, Song QH, Zhang SW, Xuan LJ. Water-soluble constituents of the root barks of *Fraxinus rhynchophylla* (Chinese drug Qinpi). J Asian Nat Prod Res 2008; 10: 205–10.
106 Pahari P, Rohr J. Total synthesis of psoralidin, an anticancer natural product. J Org Chem 2009; 74: 2750–4.
107 Yang S, Min Kyun N, Jang JP, Kim KA, Kim BY, Sung NJ, *et al*. Inhibition of protein tyrosine phosphatase 1B by lignans from *Myristica fragrans*. Phytother Res 2006; 20: 680–2.
108 He ZZ, Yan JF, Liao X, Zhang WY, Ji JX, Ding LS. Novel lignan compound and application thereof. China patent CN 101805325 A. 2010 August 18.
109 Takano S, Shimazaki Y, Ogasawara K. Enantiocontrolled synthesis of natural (+)-bakuchiol. Tetrahedron Lett 1990; 31: 3325–6.
110 Araki S, Bustugan Y. Short synthesis of (±)-bakuchiol via a geranylindium reagent. J Chem Soc, Perkin Trans 1 1991; 2395–7.
111 Du XL, Chen HL, Feng HJ, Li YC. Stereoselective total synthesis of natural (S)-bakuchiol and its enantiomer. Helv Chim Acta 2008; 91: 371–8.
112 Chen H, Li Y. Simple and convenient synthesis of (±)-bakuchiol. Lett Org Chem 2008; 5: 467–9.
113 Esumi T, Shimizu H, Kashiyama A, Sasaki C, Toyota M, Fukuyama Y. Efficient construction of a chiral all-carbon quaternary center by asymmetric 1,4-addition and its application to total synthesis of (+)-bakuchiol. Tetrahedron Lett 2008; 49: 6846–9.
114 Bequette JP, Jungong CS, Novikov AV. Enantioselective synthesis of Bakuchiol using diazosulfonate C–H insertion to install the quaternary center. Tetrahedron Lett 2009; 50: 6963–4.
115 Wang JD, Dong ML, Zhang W, Shen X, Guo YW. Chemical constituents of mangrove plant *Lumnitzera racemosa*. Chin J Nat Med 2006; 4: 185–7.
116 Arisawa M, Ohmura K, Kobayashi A, Morita N. A cytotoxic constituent of *Lysimachia japonica* THUNB. (Primulaceae) and the structure-activity relationships of related compounds. Chem Pharm Bull 1989; 37: 2431–4.
117 Kolev TM, Velcheva EA, Stamboliyska BA, Spiteller M. DFT and experimental studies of the structure and vibrational spectra of curcumin. Int J Quantum Chem 2005; 102: 1069–79.
118 Li JM, Li YC, Kong LD, Hu QH. Curcumin inhibits hepatic protein-tyrosine phosphatase 1B and prevents hypertriglyceridemia and hepatic steatosis in fructose-fed rats. Hepatology 2010; 51: 1555–66.
119 Pedersen U, Rasmussen PB, Lawesson SO. Synthesis of naturally occurring curcuminoids and related compounds. Liebigs Ann Chem 1985; 1985: 1557–69.
120 Qiu X, Du Y, Lou B, Zuo Y, Shao W, Huo Y, *et al*. Synthesis and identification of new 4-arylidene curcumin analogues as potential anticancer agents targeting nuclear factor-κB signaling pathway. J Med Chem 2010; 53: 8260–73.
121 Li YF, Hu LH, Lou FC, Li J, Shen Q. PTP1B inhibitors from *Ardisia japonica*. J Asian Nat Prod Res 2005; 7: 13–8.
122 Motoyoshiya J, Masue Y, Nishi Y, Aoyama H. Synthesis of hypericin via emodin anthrone derived from a two-fold Diels-Alder reaction of 1,4-benzoquinone. Nat Prod Commun 2007; 2: 67–70.
123 Li S, An TY, Li J, Shen Q, Lou FC, Hu LH. PTP1B inhibitors from *Saussrurea lappa*. J Asian Nat Prod Res 2006; 8: 281–6.
124 Ahmed SA, Bardshiri E, Simpson TJ. A convenient synthesis of isotopically labelled anthraquinones, chrysophanol, islandicin, and emodin. Incorporation of [methyl-$^2H_3$]chrysophanol into tajixanthone in *Aspergillus variecolor*. J Chem Soc, Chem Commun 1987; 12: 883–4.
125 Nicoletti TM, Raston CL, Sargent MV. A new synthesis of anthraquinones using dihydro-oxazoles and Grignard reagents derived from Mg(anthracene)$(THF)_3$. J Chem Soc, Perkin Trans 1 1990; 133–8.
126 Bae EY, Oh H, Oh WK, Kim MS, Kim BS, Kim BY, *et al*. A new VHR dual-specificity protein tyrosine phosphatase inhibitor from *Dendrobium moniliforme*. Planta Med 2004; 70: 869–70.
127 Paululat T, Kulik A, Hausmann H, Karagouni AD, Zinecker H, Imhoff JF, *et al*. Grecocyclines: New angucyclines from *Streptomyces* sp Acta 1362. Eur J Org Chem 2010; 2010: 2344–50.
128 Paduch R, Kandefer-Szerszeń M, Trytek M, Fiedurek J. Terpenes: substances useful in human healthcare. Arch Immunol Ther Exp 2007; 55: 315–27.
129 Wagner KH, Elmadfa I. Biological relevance of terpenoids. Ann Nutr Metab 2003; 47: 95–106.
130 Deng M, Dong W, Jiao W, Lu R. New eremophilane sesquiterpenes

from the roots of *Ligularia fischeri*. Helv Chim Acta 2009; 92: 495–501.
131 Shao ZY, Li J, Sim CJ, Li JY, Li ZY, Nan FJ, *et al*. O-methyl nakafuran-8 lactone, a new sesquiterpenoid from a Hainan marine sponge *Dysidea* sp. J Asian Nat Prod Res 2006; 8: 223–7.
132 Huang XC, Li J, Li ZY, Shi L, Guo YW. Sesquiterpenes from the Hainan sponge *Dysidea septosa*. J Nat Prod 2008; 71: 1399–403.
133 Li Y, Zhang Y, Shen X, Guo YW. A novel sesquiterpene quinone from Hainan sponge *Dysidea villosa*. Bioorg Med Chem Lett 2009; 19: 390–2.
134 Uyehara T, Sugimoto M, Suzuki I, Yamamoto Y. Total synthesis of (±)-nakafuran-8, a marine metabolite with antifeedant properties, based on formal bridgehead substitution of a bicyclo[2.2.2]oct-5-en-2-one system. J Chem Soc, Chem Commun 1989; 1841–2.
135 Uyehara T, Sugimoto M, Suzuki I, Yamamoto Y. Rearrangement approaches to cyclic skeletons. Part 8. Total synthesis of (±)-nakafuran-8, a marine metabolite with antifeedant properties, on the basis of bridgehead substitution of a bicyclo[2.2.2]oct-5-en-2-one system. J Chem Soc, Perkin Trans 1 1992; 1785–8.
136 Kurth MJ, Soares CJ. Asymmetric aza-Claisen rearrangement: Synthesis of (+)-dihydropallescensin-2 [(+)-penlanpallescensin]. Tetrahedron Lett 1987; 28: 1031–4.
137 Aisa A, Xin XL, Li YM; Lactucin and its preparation method and application. China patent CN 101099566 B. 2008 November 10.
138 Choi JY, Na M, Hwang IH, Lee SH, Bae EY, Kim BY, *et al*. Isolation of betulinic acid, its methyl ester and guaiane sesquiterpenoids with Protein Tyrosine Phosphatase 1B inhibitory activity from the roots of *Saussurea lappa* CB Clarke. Molecules 2009; 14: 266–72.
139 Rigby JH, Wilson JZ. Total synthesis of guaianolides: (±)-dehydrocostus lactone and (±)-estafiatin. J Am Chem Soc 1984; 106: 8217–24.
140 Yuuya S, Hagiwara H, Suzuki T, Ando M, Yamada A, Suda K, *et al*. Guaianolides as immunomodulators. Synthesis and biological activities of dehydrocostus lactone, mokko lactone, eremanthin, and their derivatives. J Nat Prod 1998; 62: 22–30.
141 Fu HZ, Luo YM, Li CJ, Yang JZ, Zhang DM. Psidials A–C, three unusual meroterpenoids from the leaves of *Psidium guajava* L. Org Lett 2010; 12: 656–9.
142 Kim S, Na M, Oh H, Jang J, Sohn CB, Kim BY, *et al*. PTP1B inhibitory activity of kaurane diterpenes isolated from *Siegesbeckia glabrescens*. J Enzyme Inhib Med Chem 2006; 21: 379–83.
143 Na M, Oh WK, Kim YH, Cai XF, Kim S, Kim BY, *et al*. Inhibition of protein tyrosine phosphatase 1B by diterpenoids isolated from *Acanthopanax koreanum*. Bioorg Med Chem Lett 2006; 16: 3061–4.
144 Cui L, Wu X, An ZS, Li DH; Kaurane-type diterpenoid compound as well as preparation method and medical application thereof. China patent CN 101786953 A. 2010 July 28.
145 Cheng YX, Zhou WS. Study on the tetracyclic diterpenoids 5. Synthesis of *ent*-kaur-16-en-19-oic acid. Acta Chim Sinica 1993; 51: 819–24.
146 Ling T, Chowdhury C, Kramer BA, Vong BG, Palladino MA, Theodorakis EA. Enantioselective synthesis of the antiinflammatory agent (−)-acanthoic acid. J Org Chem 2001; 66: 8843–53.
147 Han YM, Oh H, Na M, Kim BS, Oh WK, Kim BY, *et al*. PTP1B inhibitory effect of abietane diterpenes isolated from *Salvia miltiorrhiza*. Biol Pharm Bull 2005; 28: 1795–7.
148 Kakisawa H, Inouye Y. Total syntheses of tanshinone-I, tanshinone-II, and cryptotanshinone. Chem Commun (London) 1968; 1327–8.
149 Marrero JG, Andrés LS, Luis JG. Quinone derivatives by chemical transformations of 16-hydroxycarnosol from *Salvia species*. Chem Pharm Bull 2005; 53: 1524–9.
150 Kate AS, Aubry I, Tremblay ML, Kerr RG. Lipidyl pseudopteranes A-F: isolation, biomimetic synthesis, and PTP1B inhibitory activity of a new class of pseudopteranoids from the Gorgonian *Pseudopterogorgia acerosa*. J Nat Prod 2008; 71: 1977–82.
151 Iguchi K, Shimada Y, Yamada Y. Hyrtiosal, a new sesterterpenoid with a novel carbon skeleton from the Okinawan marine sponge *Hyrtios erectus*. J Org Chem 1992; 57: 522–4.
152 Sun T, Wang Q, Yu Z, Zhang Y, Guo Y, Chen K, *et al*. Hyrtiosal, a PTP1B inhibitor from the marine sponge *Hyrtios erectus*, shows extensive cellular effects on PI3K/AKT activation, glucose transport, and TGFβ/Smad2 signaling. ChemBioChem 2007; 8: 187–93.
153 Du L, Shen L, Yu Z, Chen J, Guo Y, Tang Y, *et al*. Hyrtiosal, from the marine sponge Hyrtios erectus, inhibits HIV-1 integrase binding to viral DNA by a new inhibitor binding site. ChemMedChem 2008; 3: 173–80.
154 Basabe P, Diego A, Díez D, Marcos IS, Urones JG. Synthesis and absolute configuration of (−)-hyrtiosal. Synlett 2000; 2000: 1807–9.
155 Basabe P, Diego A, Díez D, Marcos IS, Mollinedo F, Urones JG. Hyrtiosanes from labdanes: (−)-hyrtiosal from sclareol. Synthesis 2002; 2002: 1523–9.
156 Lunardi I, Santiago GMP, Imamura PM. Synthesis of (−)- and (+)-hyrtiosal and their C-16 epimers. Tetrahedron Lett 2002; 43: 3609–11.
157 Cao S, Foster C, Lazo JS, Kingston DG. Sesterterpenoids and an alkaloid from a *Thorectandra* sp as inhibitors of the phosphatase Cdc25B. Bioorg Med Chem 2005; 13: 5094–8.
158 Boukouvalas J, Robichaud J, Maltais F. A unified strategy for the regiospecific assembly of homoallyl-substituted butenolides and γ-hydroxybutenolides: First synthesis of luffariellolide. Synlett 2006; 2006: 2480–2.
159 Wright AE, McCarthy PJ, Schulte GK. Sulfircin: a new sesterterpene sulfate from a deep-water sponge of the genus Ircinia. J Org Chem 1989; 54: 3472–4.
160 Na M, Cui L, Min BS, Bae K, Yoo JK, Kim BY, *et al*. Protein tyrosine phosphatase 1B inhibitory activity of triterpenes isolated from *Astilbe koreana*. Bioorg Med Chem Lett 2006; 16: 3273–6.
161 Na M, Yang S, He L, Oh H, Kim BS, Oh WK, *et al*. Inhibition of protein tyrosine phosphatase 1B by ursane-type triterpenes isolated from *Symplocos paniculata*. Planta Med 2006; 72: 261–3.
162 Shi L, Zhang W, Zhou YY, Zhang YN, Li JY, Hu LH, *et al*. Corosolic acid stimulates glucose uptake via enhancing insulin receptor phosphorylation. Eur J Pharmacol 2008; 584: 21–9.
163 Ma M, Wang SJ, Li S, Yang YC, Shi JG, Ye F, *et al*. Triterpenes with protein tyrosine phosphotase 1B inhibitory activity from *Macaranga adenantha*. Zhongcaoyao 2006; 37: 1128–31.
164 Qian S, Li H, Chen Y, Zhang W, Yang S, Wu Y. Synthesis and biological evaluation of oleanolic acid derivatives as inhibitors of protein tyrosine phosphatase 1B. J Nat Prod 2010; 73: 1743–50.
165 Qiu WW, Shen Q, Yang F, Wang B, Zou H, Li JY, *et al*. Synthesis and biological evaluation of heterocyclic ring-substituted maslinic acid derivatives as novel inhibitors of protein tyrosine phosphatase 1B. Bioorg Med Chem Lett 2009; 19: 6618–22.
166 Corey EJ, Lee J. Enantioselective total synthesis of oleanolic acid, erythrodiol, β-amyrin, and other pentacyclic triterpenes from a common intermediate. J Am Chem Soc 1993; 115: 8873–4.
167 Ramírez-Espinosa JJ, Rios MY, López-Martínez S, López-Vallejo F, Medina-Franco JL, Paoli P, *et al*. Antidiabetic activity of some pentacyclic acid triterpenoids, role of PTP-1B: *In vitro*, *in silico*, and *in vivo* approaches. Eur J Med Chem 2011; 46: 2243–51.
168 Zhang P, Hao J, Liu J, Zhang L, Sun H. Efficient synthesis of morolic

acid and related triterpenes starting from betulin. Tetrahedron 2009; 65: 4304–9.
169 Flekhter O, Medvedeva N, Tolstikov GA, Galin F, Yunusov M, Mai H, *et al*. Synthesis of olean-18(19)-ene derivatives from betulin. Russ J Bioorg Chem 2009; 35: 233–9.
170 Xu W, Zhu C, Cheng W, Fan X, Chen X, Yang S, *et al*. Chemical constituents of the roots of *Euphorbia micractina*. J Nat Prod 2009; 72: 1620–6.
171 Kwon JH, Chang MJ, Seo HW, Lee JH, Min BS, Na M, *et al*. Triterpenoids and a sterol from the stem-bark of *Styrax japonicaand* their protein tyrosine phosphatase 1B inhibitory activities. Phytother Res 2008; 22: 1303–6.
172 Na M, Thuong PT, Hwang IH, Bae K, Kim BY, Osada H, *et al*. Protein tyrosine phosphatase 1B inhibitory activity of 24-norursane triterpenes isolated from *Weigela subsessilis*. Phytother Res 2010; 24: 1716–9.
173 Na M, Kim BY, Osada H, Ahn JS. Inhibition of protein tyrosine phosphatase 1B by lupeol and lupenone isolated from *Sorbus commixta*. J Enzyme Inhib Med Chem 2009; 24: 1056–9.
174 Csuk R, Schmuck K, Schäfer R. A practical synthesis of betulinic acid. Tetrahedron Lett 2006; 47: 8769–70.
175 Surendra K, Corey EJ. A short enantioselective total synthesis of the fundamental pentacyclic triterpene lupeol. J Am Chem Soc 2009; 131: 13928–9.
176 Hung TM, Hoang DM, Kim JC, Jang HS, Ahn JS, Min BS. Protein tyrosine phosphatase 1B inhibitory by dammaranes from Vietnamese Giao-Co-Lam tea. J Ethnopharmacol 2009; 124: 240–5.
177 Hanson JR. Steroids: partial synthesis in medicinal chemistry. Nat Prod Rep 2010; 27: 887–99.
178 Lee HS, Hwang IH, Kim JA, Choi JY, Jang TS, Osada H, *et al*. Isolation of protein tyrosine phosphatase 1B inhibitory constituents from the sclerotia of *Polyporus umbellatus* Fries. Bull Korean Chem Soc 2011; 32: 697–700.
179 Wang L, Chen B, Shen XR, Zhou YY, Jiang DW, Li J, *et al*. Growth inhibition and induction of early apoptosis by arenicolsterol A, a novel cytotoxic enolic sulphated sterol from the marine annelid, *Arenicola cristata*. J Asian Nat Prod Res 2007; 9: 753–61.
180 Wang JR, Shen Q, Fang L, Peng SY, Yang YM, Li J, *et al*. Structural and stereochemical studies of five new pregnane steroids from the stem bark of *Toona ciliata* var *pubescens*. Steroids 2011; 76: 571–6.
181 Yan XH, Guo YW, Zhu XZ. Chemical constituents of the gorgonian *Muricella sinensis* (Verrill). Nat Prod Res Dev 2005; 17: 412–4.
182 Singh TV, Kaur R, Agnihotri KR, Bali M. Synthesis of calicoferol E. ARKIVOC 2002; 2002: 82–90.
183 Piao SJ, Zhang HJ, Lu HY, Yang F, Jiao WH, Yi YH, *et al*. Hippolides A–H, acyclic manoalide derivatives from the marine sponge *Hippospongia lachne*. J Nat Prod 2011; 74: 1248–54.
184 Mao SC, Guo YW, Shen X. Two novel aromatic valerenane-type sesquiterpenes from the Chinese green alga *Caulerpa taxifolia*. Bioorg Med Chem Lett 2006; 16: 2947–50.
185 Wikipedia. Berberine. Available from: http://en.wikipedia.org/wiki/Berberine.
186 Bustanji Y, Taha MO, Yousef AM, Al-Bakri AG. Berberine potently inhibits protein tyrosine phosphatase 1B: Investigation by docking simulation and experimental validation. J Enzyme Inhib Med Chem 2006; 21: 163–71.
187 Chen C, Zhang Y, Huang C. Berberine inhibits PTP1B activity and mimics insulin action. Biochem Biophys Res Commun 2010; 397: 543–7.
188 Wikipedia. Papaverine. Available from: http://en.wikipedia.org/wiki/Papaverine.
189 Bustanji Y, Taha MO, Al-masri IM, Mohammad MK. Docking simulations and *in vitro* assay unveil potent inhibitory action of papaverine against protein tyrosine phosphatase 1B. Biol Pharm Bull 2009; 32: 640–5.
190 Hohmann C, Schneider K, Bruntner C, Brown R, Jones AL, Goodfellow M, *et al*. Albidopyrone, a new α-pyrone-containing metabolite from marine-derived *Streptomyces* sp NTK 227. J Antibiot 2009; 62: 75–9.
191 Schulz D, Nachtigall J, Riedlinger J, Schneider K, Poralla K, Imhoff JF, *et al*. Piceamycin and its N-acetylcysteine adduct is produced by *Streptomyces* sp GB 4-2*. J Antibiot 2009; 62: 513–8.
192 Seo C, Yim JH, Lee HK, Park SM, Sohn JH, Oh H. Stereocalpin A, a bioactive cyclic depsipeptide from the Antarctic lichen *Stereocaulon alpinum*. Tetrahedron Lett 2008; 49: 29–31.
193 Ghosh AK, Xu CX. A convergent synthesis of the proposed structure of antitumor depsipeptide stereocalpin A. Org Lett 2009; 11: 1963–6.
194 Choi YH, Sohn JH, Lee D, Kim JK, Kong IS, Ahn SC, *et al*. Chejuenolides A and B, new macrocyclic tetraenes from the marine bacterium *Hahella chejuensis*. Tetrahedron Lett 2008; 49: 7128–31.
195 Sun YQ, Guo YW. Gymnorrhizol, an unusual macrocyclic polydisulfide from the Chinese mangrove *Bruguiera gymnorrhiza*. Tetrahedron Lett 2004; 45: 5533–5.
196 Sun YQ, Sun J, Guo YW. Crystal structure of 1,2,6,7,11,12-hexathiacyclopentadecane, C9H18S6. Z Kristallogr - NCS 2004; 219: 119–20.
197 Gong JX, Shen X, Yao LG, Jiang H, Krohn K, Guo YW. Total synthesis of gymnorrhizol, an unprecedented 15-membered macrocyclic polydisulfide from the Chinese mangrove *Bruguiera gymnorrhiza*. Org Lett 2007; 9: 1715–6.
198 Huang XY, Wang Q, Liu HL, Zhang Y, Xin GR, Shen X, *et al*. Diastereoisomeric macrocyclic polydisulfides from the mangrove *Bruguiera gymnorrhiza*. Phytochemistry 2009; 70: 2096–100.
199 Hamaguchi T, Sudo T, Osada H. RK-682, a potent inhibitor of tyrosine phosphatase, arrested the mammalian cell cycle progression at G_1 phase. FEBS Lett 1995; 372: 54–8.
200 Sodeoka M, Sampe R, Kagamizono T, Osada H. Asymmetric synthesis of RK-682 and its analogs, and evaluation of their protein phosphatase inhibitory activities. Tetrahedron Lett 1996; 37: 8775–8.
201 Shinagewa S, Muroi M, Ito T, Hida T; Tetronic acid derivative, its production and use. Japan patent JP 05-43568 A. 1993 February 23.
202 Mittra A, Yamashita M, Kawasaki I, Murai H, Yoshioka T, Ohta S. A useful oxidation procedure for the preparation of 3-alkanoyltetronic acids. Synlett 1997; 1997: 909–10.
203 Schobert R, Jagusch C. Solution-phase and solid-phase syntheses of enzyme inhibitor RK-682 and antibiotic agglomerins. J Org Chem 2005; 70: 6129–32.
204 Helaly S, Schneider K, Nachtigall J, Vikineswary S, Tan GY, Zinecker H, *et al*. Gombapyrones, new α-pyrone metabolites produced by *Streptomyces griseoruber* Acta 3662*. J Antibiot 2009; 62: 445–52.
205 Alvi KA, Nair BG, Rabenstein J, Davis G, Baker DD. CD45 tyrosine phosphatase inhibitory components from *Aspergillus niger*. J Antibiot 2000; 53: 110–3.
206 Seibert SF, Eguereva E, Krick A, Kehraus S, Voloshina E, Raabe G, *et al*. Polyketides from the marine-derived fungus *Ascochyta salicorniae* and their potential to inhibit protein phosphatases. Org Biomol Chem 2006; 4: 2233–40.

207 Galbraith MN, Whalley WB. The synthesis of (±)-ascochitine. Chem Commun (London) 1966; 620a–a.
208 Wang JD, Dong ML, Zhang W, Shen X, Guo YW. Chemical constituents of mangrove plant *Aegiceras corniculatum*. Chin J Nat Med 2006; 4: 275–7.
209 Zheng G, Lu W, Cai J. Stereoselective total synthesis of (3*R*,8S)-falcarindiol, a common polyacetylenic compound from umbellifers. J Nat Prod 1999; 62: 626–8.
210 Sabitha G, Bhaskar V, Reddy CS, Yadav JS. Stereoselective approaches for the total synthesis of polyacetylenic (3*R*,8S)-falcarindiol. Synthesis 2008; 2008: 115–21.
211 Schmiech L, Alayrac C, Witulski B, Hofmann T. Structure determination of bisacetylenic oxylipins in carrots (*Daucus carota* L) and enantioselective synthesis of falcarindiol. J Agric Food Chem 2009; 57: 11030–40.
212 Tamura S, Ohno T, Hattori Y, Murakami N. Establishment of absolute stereostructure of falcarindiol, algicidal principle against *Heterocapsa circularisquama* from Notopterygii Rhizoma. Tetrahedron Lett 2010; 51: 1523–5.
213 Li YF, Li J, Shen Q, Hu LH. Benzoquinones from *Ardisia japonica* with inhibitory activity towards human protein tyrosine phosphatase 1B (PTP1B). Chem Biodivers 2007; 4: 961–5.
214 Yadav JS, Upender V, Rao AVR. A practical preparation of functionalized alkylbenzoquinones: synthesis of maesanin and irisquinone. J Org Chem 1992; 57: 3242–5.
215 Poigny S, Guyot M, Samadi M. Total synthesis of maesanin and analogues. Tetrahedron 1998; 54: 14791–802.
216 Pfeifer J, Gerlach H. Synthese von naturstoffen mit alkyl-methoxy-1,4-benzochinon-struktur. Liebigs Ann 1995; 1995: 131–7.
217 Tsukamoto S, Takeuchi S, Ishibashi M, Kobayashi J. Manzamenones A–F from the Okinawan marine sponges *Plakortis* sp: novel dimeric fatty acid derivatives possessing a bicyclo[4.3.0]nonane skeleton. J Org Chem 1992; 57: 5255–60.
218 Wakuda Y, Kubota T, Shima H, Okada T, Mitsuhashi S, Aoki N, *et al*. Manzamenones Inhibit T-Cell Protein Tyrosine Phosphatase. Mar Drugs 2006; 4: 9–14.

Acta Pharmacologica Sinica (2012) 33: 1246–1253
 1671-4083/12 $32.00
www.nature.com/aps

Original Article

Toll-like receptor 3 agonist Poly I:C protects against simulated cerebral ischemia *in vitro* and *in vivo*

Lin-na PAN[1, 2], Wei ZHU[3], Cai LI[1, 2], Xu-lin XU[1, 2], Lian-jun GUO[1, 2], Qing LU[1, 2, *]

[1]*Department of Pharmacology, Tongji Medical College, Huazhong University of Science and Technology, Wuhan 430030, China;* [2]*Key Laboratory of Drug Target Research and Pharmacodynamic Evaluation, Hubei Province, Wuhan 430030, China;* [3]*Department of Emergency Internal Medicine, Tongji Hospital, Tongji Medical College, Huazhong University of Science and Technology, Wuhan 430030, China*

Aim: To examine the neuroprotective effects of the Toll-like receptor 3 (TLR3) agonist Poly I:C in acute ischemic models *in vitro* and *in vivo*.
Methods: Primary astrocyte cultures subjected to oxygen-glucose deprivation (OGD) were used as an *in vitro* simulated ischemic model. Poly I:C was administrated 2 h before OGD. Cell toxicity was measured using MTT assay and LDH leakage assay. The levels of TNFα, IL-6 and interferon-β (IFNβ) in the media were measured using ELISA. Toll/interleukin receptor domain-containing adaptor-inducing IFNβ (TRIF) protein levels were detected using Western blot analysis. A mouse middle cerebral artery occlusion (MCAO) model was u sed for *in vivo* study. The animals were administered Poly I:C (0.3 mg/kg, im) 2 h before MCAO, and examined with neurological deficit scoring and TTC staining. The levels of TNFα and IL-6 in ischemic brain were measured using ELISA.
Results: Pretreatment with Poly I:C (10 and 20 μg/mL) markedly attenuated OGD-induced astrocyte injury, and significantly raised the cell viability and reduced the LDH leakage. Poly I:C significantly upregulated TRIF expression accompanied by increased downstream IFNβ production. Moreover, Poly I:C significantly suppressed the pro-inflammatory cytokines TNFα and IL-6 production. In mice subjected to MCAO, administration of Poly I:C significantly attenuated the neurological deficits, reduced infarction volume, and suppressed the increased levels of TNFα and IL-6 in the ischemic striatum and cortex.
Conclusion: Poly I:C pretreatment exerts neuroprotective and anti-inflammatory effects in the simulated cerebral ischemia models, and the neuroprotection is at least in part due to the activation of the TLR3-TRIF pathway.

Keywords: Toll-like receptor; Poly I:C; stroke; astrocyte; oxygen-glucose deprivation; middle cerebral artery occlusion; inflammation; TNFα; IL-6; interferon-β; Toll/interleukin receptor domain-containing adaptor-inducing interferon β (TRIF)

Acta Pharmacologica Sinica (2012) 33: 1246–1253; doi: 10.1038/aps.2012.122; published online 17 Sep 2012

Introduction

Cerebral ischemic preconditioning (IPC) refers to a transient, sublethal ischemia which results in tolerance to a subsequent lethal cerebral ischemia. IPC is believed to trigger the most effective form of intrinsic neuroprotective mechanism[1, 2]. A better understanding of this endogenous neuroprotective mechanism could help in the development of prophylactic strategies in high-risk populations for pathological cerebrovascular events and neurosurgical procedures. Many attempts have been made to explore the mechanisms underlying this intrinsic neuroprotection of ischemic preconditioning. Post-ischemic inflammation is a significant factor that increases damage associated with ischemic brain injury[3, 4]. Many studies have shown that the prevention of the inflammatory response might be a contributing mechanism by which IPC induces protection against brain ischemia[5, 6]. Bowen *et al* showed that prior IPC, a 10 min middle cerebral artery occlusion (MCAO), decreases the infarct volume and neurological deficits caused by focal ischemia (60 min MCAO 72 h after PC). IPC has also been shown to reduce the post-ischemia increase in the expression of many pro-inflammatory genes and prevent neutrophil and macrophage infiltration in the ipsilateral cortex of rats subjected to focal ischemia[5, 6].

Recent evidence indicates that Toll-like receptors (TLRs) are involved in the preconditioning-induced inflammatory prevention and ischemic tolerance[7, 8]. TLRs are innate immunity receptors that are expressed in a wide range of cell types, including in the central nervous system (CNS). Ten currently

* To whom correspondence should be addressed.
E-mail qinglu@mail.hust.edu.cn
Received 2012-05-08 Accepted 2012-07-20

known TLR family members signal through two main pathways: a myeloid differentiation factor 88- (MyD88-) dependent pathway and a Toll/interleukin receptor domain-containing adaptor-inducing interferon β (TRIF)-dependent pathway. The MyD88-dependent pathway acts via nuclear factor κB (NF-κB) to induce pro-inflammatory cytokines such as tumor necrosis factor-α (TNFα). The TRIF-dependent pathway acts via type I interferon to increase expression of anti-inflammatory molecules such as interferon β (IFNβ).

Of the TLRs, only TLR4 utilizes both of these pathways, and TLR3 signals exclusively through the MyD88-independent pathway. In contrast to the detrimental role of TLRs in response to ischemia, stimulation of TLR4 with low dose systemic administration of lipopolysaccharide (LPS) prior to ischemia provides robust neuroprotection accompanied by attenuated inflammatory response in the animal brain[9, 10]. Mice lacking TLR4 show less IPC-induced neuroprotection than wild-type mice[11]. Studies have suggested pretreatment with LPS or IPC cause cells to switch their transcriptional response by enhancing the TRIF-induced anti-inflammatory cytokine and suppressing the NF-κB induced pro-inflammatory cytokine[7, 8, 12]. Interestingly, LPS stimulation of macrophages has been shown to upregulate TLR3 expression[13], suggesting that LPS preconditioning may upregulate TLR3 to further enhance the TRIF pathway signaling. Because TLR3 signals exclusively through TRIF pathway, TLR3 stimulation may contribute to the finely controlled shift in the balance of pro-inflammatory and anti-inflammatory cytokines and represent an endogenous neuroprotective mechanism. However, whether TLR3 regulates the inflammatory response in the brain during cerebral ischemia and exerts cytoprotective effects against ischemia remains unexplored.

We have previously shown that TLR3 ligand polyinosinic-polycytidylic acid (Poly I:C) preconditioning can protect rat mixed cortical neuronal-glial cell cultures against oxygen-glucose deprivation (OGD)-induced injury and inhibited OGD-induced inflammatory cytokine IL-6 release into the medium[14]. In the present study, an *in vivo* model of focal cerebral ischemia and an *in vitro* model of cultured astrocytes subjected to OGD injury were used to further verify the neuroprotection of Poly I:C. The protective effects of Poly I:C were also investigated to determine whether this neuroprotection is related to Poly I:C's regulation of the inflammatory response during the ischemic period.

Materials and methods

Drugs and reagents

Poly I:C was obtained from Guangdong BangMin Pharmaceutical Co, Ltd (Jiangmen, China) and dissolved in saline. For *in vitro* experiments, Poly I:C was diluted with culture medium before being added to cell cultures. Poly-*D*-lysine and 3-(4,5-dimethylthiazol-2-yl)-2,5-diphenyl-tetrazolium bromide (MTT) were purchased from Sigma Chemical Co (St Louis, MO, USA). A lactate dehydrogenase (LDH) assay kit was purchased from Roche Molecular Biochemicals (Mannheim, Germany). Rat IFN-β, IL-6, and TNF-α ELISA kits were purchased from R&D Systems (Minneapolis, MN, USA). Polyvinylidene difluoride (PVDF) membrane was purchased from Bio-Rad Laboratories Inc (Hercules, CA, USA). Antibody against TRIF was supplied by ABCAM (Cambridge, UK) and antibody against β-actin was from Santa Cruz Biotechnology (Santa Cruz, CA, USA). Other analytical grade chemicals were from commercial sources.

For primary astrocyte cultures, 1-d-old Sprague-Dawley rats were supplied by the Animal Center of Tongji Medical College of Huazhong University of Science and Technology (Wuhan, China). Kun-Ming strain mice at an age of 8 to 10 weeks and weighing 20 to 22 g were also supplied by the Animal Center. All animal experiments were carried out in compliance with the National Institutes of Health Guide for Care and Use of Laboratory Animals.

Astrocyte cell culture

Astrocytes were isolated from 1-d-old Sprague-Dawley rats. Briefly, brain hemispheres of newborn rats were removed from the skulls aseptically, and the meninges were carefully removed from the hemispheres in cold D-Hanks solution. The tissues were minced and incubated in 0.125% trypsin at 37°C for 8 min. Dulbecco's modified Eagle's medium/Nutrient Mixture F-12 Ham's (DMEM/F-12) medium containing 20% fetal bovine serum (FBS) was added to terminate digestion. The suspension was filtered through stainless steel (200 mesh, hole width 95 μm). The filtrate was twice centrifuged at 300×*g* for 10 min. The precipitation was resuspended in DMEM/F-12 medium containing 20% FBS, penicillin (100 U/mL) and streptomycin (100 mg/mL). The concentration of cells in suspension was adjusted to 1×10^6 cells/mL and plated in 25-cm^2 flasks. Cultures were incubated in DMEM/F-12 containing 20% FBS at 37°C in 95% air and 5% CO_2 with 95% relative humidity (CO_2-Incubator, SHELLAB, USA). The total volume of culture medium was changed twice a week. The cells were cultured for two weeks until they reached confluence. On the 14th day *in vitro* (DIV), contaminated microglia and oligodendrocytes were removed by shaking at 200 rounds per minute with an orbital shaker for 5 h. After 5 d, shaking was repeated at 200 rounds per minute with an orbital shaker for 5 h. Under these conditions, microglial cells were almost completely detached from the layer of astrocytes. Astrocytes remaining in the flask were harvested with 0.125% trypsin. The suspension was centrifuged at 300×*g* for 10 min. The concentration of cells in precipitation was adjusted to $1–2\times10^5$ cells/mL with culture medium containing 20% FBS. Cells were plated to achieve a confluent monolayer on plastic 96-well culture plates and 35-mm (diameter) plastic dishes (Costar, Vitaris, Baar, France) that were previously coated with poly-*D*-lysine (100 μg/mL). To identify astrocytes, cultures were analyzed by immunochemical staining for glial fibrillary acidic protein (GFAP) (Sigma, USA) and counterstained using DAPI. Analyses of the cultures showed that 95%–98% of the cells were GFAP-positive, and 2%–5% cells were indeterminate types. All experiments were performed on 22-day old cultures.

Treatment of astrocyte cultures

At 22 DIV, a portion of the astrocytes were exposed to Poly I:C (10 and 20 μg/mL) for 24 h in serum-free DMEM, and a separate portion was cultured in serum-free DMEM for 24 h without Poly I:C treatment. Then, the culture medium was removed and replaced with pre-warmed glucose-free Earle's balanced salt solution, which was pre-incubated with 95% N_2 and 5% CO_2 for 30 min to remove the oxygen in the medium. The cultures were further incubated for 12 h in an airtight box that was continuously filled with 95% N_2 and 5% CO_2 to induce an oxygen-glucose deprivation (OGD) condition as described by Liu *et al*[15]. Cultures treated with Earle's balanced salt solution containing 10 mmol/L glucose in CO_2-incubator throughout were assigned to the control group.

Cell viability assay

The cell viability of the astrocytes was evaluated using the MTT conversion method[16]. The cells' ability to convert MTT to an insoluble purple formazan indicates mitochondrial integrity and activity, which in turn indicates cell viability. Briefly, after exposure to 12 h OGD, MTT was added to the cultures at a final concentration of 0.5 mg/mL and incubated for 4 h at 37 °C. The blue reaction product formazan was dissolved by 100 μL DMSO. The absorbance value at 570 nm was read using a microplate reader. Each experimental condition was performed in triplicate.

LDH release assay

Cell injury was quantitatively assessed using a cytotoxicity detection kit that measures cytosolic LDH release into the medium during OGD exposure. Absorbance at 492 nm was read on a microplate reader, and LDH values were normalized to the mean maximal LDH value in sister cultures continuously exposed to 0.1% Triton X-100, which causes near-complete glial cell death (100%). The results are expressed as a percentage of the maximal LDH level. Each experimental condition was performed in triplicate.

IFNβ, IL-6, and TNFα levels analysis

Secreted IFNβ, IL-6, and TNFα levels in the culture supernatants and in the ischemic brain were determined with commercially available ELISA kits according to the manufacturer's instructions. Absorbance at 450 nm was read on a microplate reader.

Protein extraction and Western blot analysis for TRIF

Astrocyte cultures were washed with ice-cold phosphate-buffered saline (PBS) and the proteins were extracted with 80 μL of lysis buffer: 50 mmol/L Tris-HCl, pH 7.4, 150 mmol/L NaCl, 0.5% Igepal, 0.1% SDS, 10 μg/mL phenylmethylsulfonyl fluoride, 10 μg/mL leupeptin, 10 μg/mL pepstatin and 10 μg/mL of heat-activated sodium orthovanadate. After 30 min on ice, the cell lysates were centrifuged at 12000×*g* for 15 min at 4 °C and the supernatants were harvested. The protein concentrations in the samples were determined according to the Bradford method with serum albumin as a standard. Equal amounts of the protein samples were loaded per lane and electrophoresed in 12% dodecylsulfate-polyacrylamide gel and transferred onto a polyvinylidene difluoride (PVDF) membrane. The membranes were blocked with 5% nonfat dry milk in Tris-buffered saline containing 0.1% Tween 20, and the membranes were incubated overnight at 4 °C with rabbit anti-TRIF polyclonal antibody (1:600 dilution) and goat polyclonal β-actin antibody (1:500 dilution). The membranes were then incubated with horseradish peroxidase–conjugated secondary antibodies diluted at 1:5000 for 1 h at room temperature. The positive bands were revealed using enhanced chemiluminescence detection reagents and autoradiography film. The optical densities of the bands were scanned and quantified with ImageJ software (National Institutes of Health, Bethesda, Maryland, USA). β-Actin served as an internal control.

Induction of focal cerebral ischemia and reperfusion in mice

Transient focal ischemia was produced by intraluminal MCAO with a nylon filament, as we have previously described[17]. All animal experiments were carried out in compliance with the National Institutes of Health Guide for Care and Use of Laboratory Animals. After performing a midline neck incision, the left common carotid artery, external carotid artery and internal carotid artery were carefully separated. The proximal left common carotid artery and the external carotid artery were ligated. A 6–0 nylon monofilament (Ethicon) with a heat-blunted tip was introduced through a small arteriotomy of the common carotid artery into the distal internal carotid artery and was advanced 8–9 mm distal to the origin of the middle cerebral artery (MCA) until the MCA was occluded. The suture was withdrawn from the carotid artery under anesthesia 2 h after insertion to enable reperfusion. Then, the wound was closed. Mice were maintained in an air-conditioned room at 25 °C during the reperfusion period of 22 h. Mice that failed to extend the contralateral forelimb were verified as adequate occlusion and selected for further measurements. Poly I:C (0.3 mg/kg in saline, im) was administered 24 h before MCAO. In sham-operated mice, the arteries were separated without occlusion. In each group, 8 animals were used to determine infarct volume. An additional 8 animals were used to determine IL-6 and TNFα levels in the brain by ELISA.

Evaluation of neurological deficit score and determination of infarct size

Neurological deficits of each mouse were evaluated at 23 h after MCAO by the Zea-Longa method: 0=normal spontaneous movement; 1=failure to extend the contralateral forelimb; 2=circling to affected side; 3=partial paralysis on affected side; 4=no spontaneous motor activity. Mice were then killed with an overdose of pentobarbital at 24 h after MCAO. The brains were immediately removed and frozen at -20 °C for 20 min and sectioned into five coronal slices. The brain slices were incubated in 2% 2,3,5-triphenyltetrazolium chloride monohydrate (TTC) at 37 °C for 15 min, followed by 4% paraformaldehyde overnight. The brain slices were photographed and the area of ischemic damage was measured by an image analysis

system. The total infarct volume was calculated by integration of the infarct areas in sequential 1-mm-thick brain sections.

Statistical analysis

All results were expressed as the mean±SD. The significance of the differences among different groups was determined using SPSS (Statistical Package for the Social Sciences) for Windows (version 18.0) with one-way ANOVA. Ranked data of neurological deficit were analyzed by the nonparametric Kruskal-Wallis test. Differences were considered significant when $P<0.05$.

Results

Protective effects of Poly I:C on cultured astrocytes against OGD-induced injury

In cultured rat astrocytes, 95%–98% of the astrocytes were identified (Figure 1A). OGD induced significant cell injury as indicated by morphological observation. Cultured rat astrocytes exposed to OGD for 12 h demonstrated a marked decrease in the cell number and branches of the cell bodies, and the remaining cells were round and small. However, the cells appeared to be much healthier in the groups pretreated with 10 μg/mL and 20 μg/mL Poly I:C (Figure 1B). This observation indicates some degree of protection by Poly I:C against OGD-induced injury in cultured astrocytes. The cytoprotection by Poly I:C was further evaluated by MTT assay and LDH leakage.

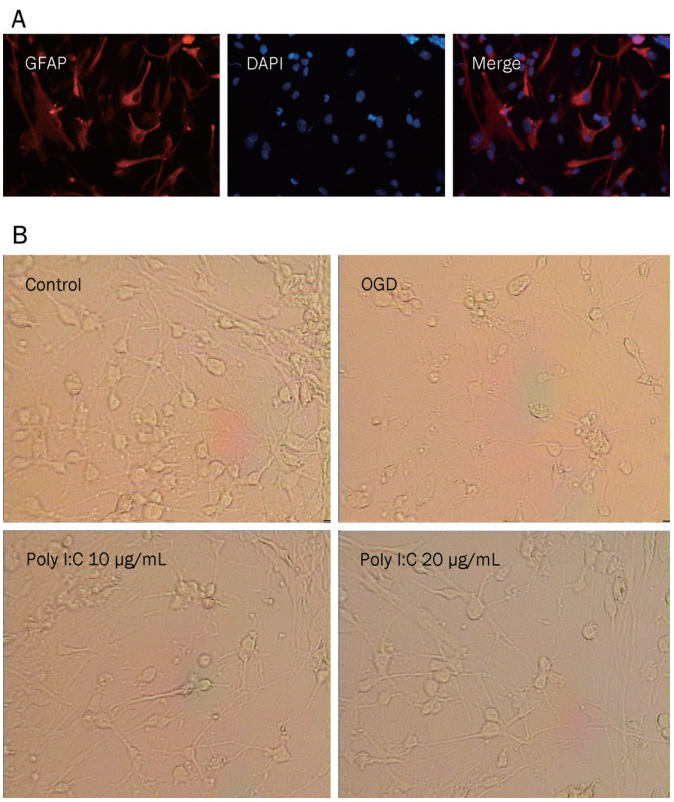

Figure 1. Microphotographs of cultured astrocytes. (A) 95%–98% GFAP-positive cells are shown in the cultures. Anti-GFAP antibody was used to identify cultured rat astrocytes (red), in which nuclei were counterstained using DAPI (blue). The microphotographs were taken at the 22nd DIV under a fluorescent microscope (Magnification, 400×). (B) Effects of Poly I:C against OGD-induced injury in cultured astrocytes. Astrocyte cultures treated with 10 μg/mL and 20 μg/mL Poly I:C (added 24 h before OGD) or untreated (OGD alone). The microphotographs were taken with a conventional optical microscope (Magnification, 200×) 12 h after exposure to OGD.

The 12 h OGD exposure of astrocytes markedly decreased OD value *vs* the normal group as determined by the MTT assay (0.46±0.04, 0.93±0.17 in OD value, respectively, $P<0.05$) (Figure 2A). However, pretreatment with Poly I:C significantly attenuated OGD-induced cell toxicity. Pretreatment with 10 μg/mL and 20 μg/mL Poly I:C prior to exposure to 12 h OGD markedly raised astrocyte viability to 0.59±0.04 and 0.64±0.07 in OD value, respectively $P<0.05$).

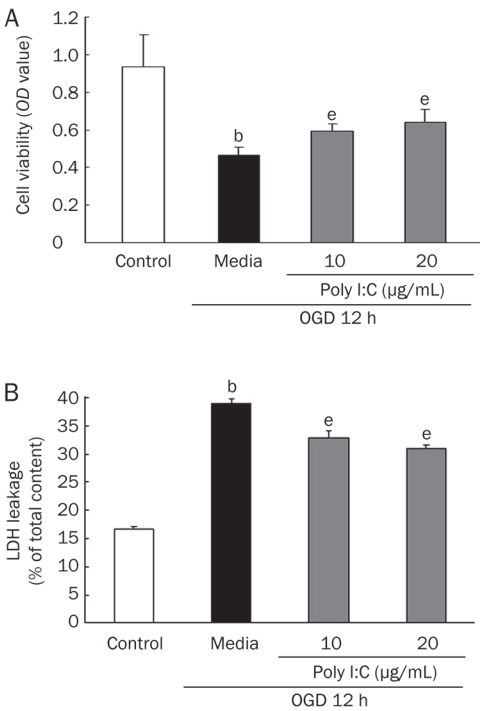

Figure 2. MTT assay (A) and LDH release (B) in astrocyte cells under simulated ischemia. Astrocyte cultures treated with 10 μg/mL and 20 μg/mL Poly I:C (added 24 h before OGD) or untreated (OGD alone). Each independent experiment was carried out in triplicate. Values are expressed as the mean±SD. $^{b}P<0.05$ compared with control group, $^{e}P<0.05$ compared with cells exposed to OGD alone.

LDH leakage, another indicator of cell toxicity, was evaluated to further investigate the protective effect of Poly I:C. As shown in Figure 2B, LDH leakage increased to 39.0%±0.9% compared with the control group after the cells were exposed to 12 h OGD, double the level of the control group ($P<0.05$). Pretreatment with 10 μg/mL and 20 μg/mL Poly I:C markedly attenuated OGD-induced cell death, reducing LDH leakage to 32.9%±1.2% and 31.0%±0.9%, respectively ($P<0.05$).

Effects of Poly I:C on IFNβ, TNFα, and IL-6 release in astrocyte cell cultures exposed to simulated ischemia *in vitro*

Exposure of astrocytes to simulated ischemia for 12 h resulted in notably increased IFNβ release. 10 μg/mL Poly I:C did not increase IFNβ levels in comparison with ischemic cultures. However, 20 μg/mL Poly I:C pretreatment significantly increased IFNβ levels after 12 h exposure to ischemia (P<0.05) (Figure 3A). *In vitro* exposure of astrocytes to 12 h of OGD also markedly increased TNFα and IL-6 levels, indicating that ischemic conditions stimulated astrocytes *in vitro* to produce pro-inflammatory cytokines. A lower Poly I:C concentration (10 μg/mL) did not decrease TNFα level in comparison with ischemic cultures (P>0.05). However, 20 μg/mL Poly I:C pretreatment notably decreased TNFα levels after 12 h exposure to ischemia (P<0.05) (Figure 3C). Pretreatment with 10 μg/mL and 20 μg/mL Poly I:C both attenuated IL-6 release induced by ischemia *in vitro* (P<0.05) (Figure 3B).

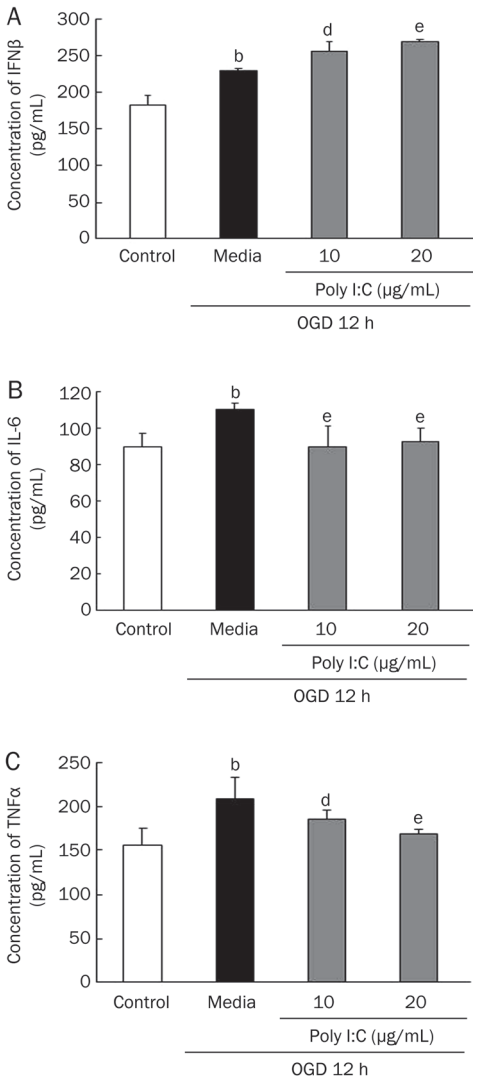

Figure 3. Anti-inflammatory effects of Poly I:C in astrocyte cells subjected to 12 h OGD. (A) The effects of Poly I:C on IFNβ levels in culture medium are shown. (B) The effects of Poly I:C on IL-6 levels in culture medium are shown. (C) The effects of Poly I:C on TNFα levels in culture medium are shown. Each independent experiment was carried out in triplicate. Values are expressed as the mean±SD. ^{b}P<0.05 *vs* control group, ^{d}P>0.05, ^{e}P<0.05 *vs* cells exposed to OGD alone.

Poly I:C preconditioning upregulates TRIF protein expression in astrocyte cell cultures exposed to simulated ischemia *in vitro*

TLR3 is unique among the TLRs because its signaling occurs solely via recruitment of the protein TRIF. TRIF signaling occurs via the interferon-regulated factor-3 (IRF3) complex and induces the anti-viral IFNβ via the TRIF-IRF3 axis. We examined the expression of TRIF protein in astrocyte cultures by Western blot analysis. We found that TRIF levels were reduced in astrocyte cultures exposed to simulated ischemia compared with the control group. However, TRIF levels were upregulated in Poly I:C-pretreated cultures at both concentrations (P<0.05) (Figure 4).

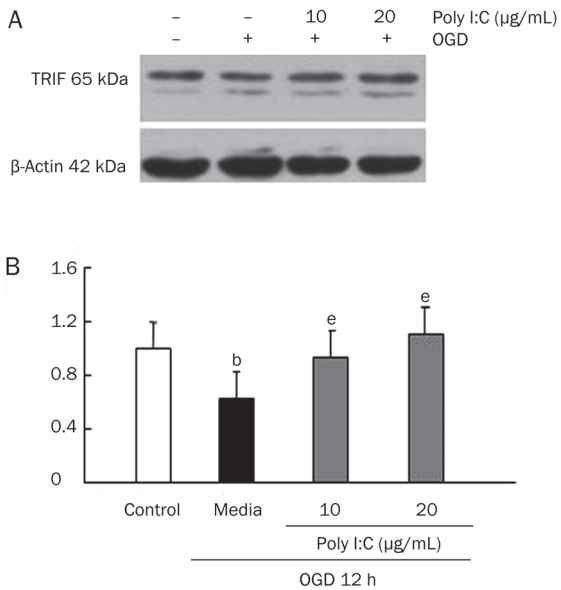

Figure 4. Western blot analysis of the modulatory effects of Poly I:C on TRIF protein expression in astrocytes subjected to 12 h OGD. Astrocyte cultures were pretreated with 10 μg/mL and 20 μg/mL Poly I:C and then exposed to OGD for 12 h. At the end of the treatment, cells were harvested for Western blot analysis with β-actin as a protein loading control. (A) representative Western blot; (B) statistical results. Each independent experiment was carried out in triplicate. Values are expressed as the mean±SD. ^{b}P<0.05 *vs* control group; ^{e}P<0.05 *vs* OGD alone.

Neuroprotective and anti-inflammatory effects of Poly I:C on mice subjected to transient MCAO

Because the present experiments in cultured astrocytes suggested anti-inflammatory activities of Poly I:C under ischemic conditioning, further *in vivo* evaluation of this compound in the MCAO model was performed. A 2 h transient MCAO in mice resulted in an infarct that included almost 50% of the

ipsilateral brain and caused obvious neurological dysfunction. However, the total infarct volume was greatly reduced by the administration of Poly I:C compared with that in the untreated mice (P<0.05) (Figure 5). Similarly, neurological deficit after MCAO was ameliorated in Poly I:C-treated animals (P<0.05) (Figure 5). In addition, inflammatory responses were investigated in ipsilateral and contralateral brains. The 2 h transient MCAO in mice caused increased TNFα and IL-6 levels in the ischemic brain compared with those in the sham group, whereas 0.3 mg/kg Poly I:C pretreatment markedly reduced TNFα and IL-6 levels in the ischemic brain (P<0.05) (Figure 6). The expression of these pro-inflammatory cytokines remained the same in the contralateral brain (data not shown).

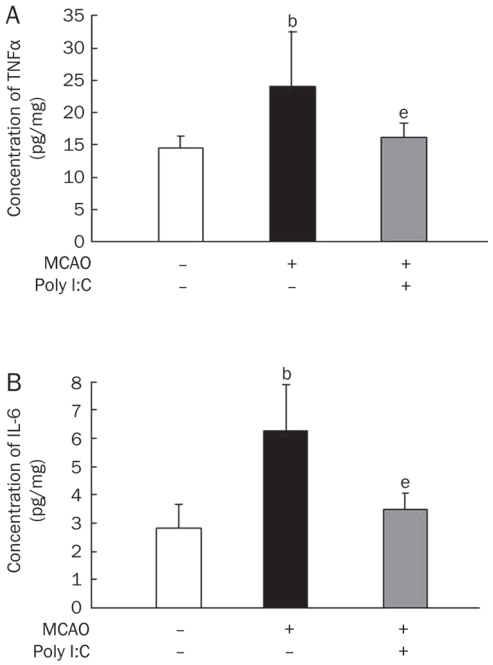

Figure 6. Anti-inflammatory effects of Poly I:C (0.3 mg/kg) in mice subjected to MCAO. (A) Poly I:C reduced TNFα levels in the ischemic striatum and cortex. (B) Poly I:C reduced IL-6 levels in the ischemic striatum and cortex. TNFα and IL-6 levels in the contralateral brain between groups showed no notable difference (data not shown). Values are expressed as the mean±SD, n=8. ^{b}P<0.05 *vs* control group, ^{e}P<0.05 *vs* MCAO group.

Discussion

Astrocytes are the most abundant cells in the CNS and perform many functions, including maintenance of the blood–brain barrier, supply of nutrients to neurons, modulation of synaptic transmission, and regulation of the inflammatory response to brain injury. Neurons may undergo damage that is more severe when astrocytes are injured by ischemia[18, 19]. TLR3 is expressed throughout the CNS and is most prominent in astrocytes[8]. Unique among the TLRs, TLR3 signals exclusively through the TRIF-dependent pathway and is purported to participate in a comprehensive neuroprotective action. It has been reported that the activation of TRIF reduces neuronal death in *in vitro* stroke models. Mice lacking TRIF/IRF3 were not protected by LPS preconditioning in an *in vivo* model[7].

Our previous studies showed that TLR3 ligand Poly I:C preconditioning protects mixed cortical cultures against OGD-induced injury and inhibits OGD-induced IL-6 release[14]. In the present study, we further examined the neuroprotective potential of Poly I:C in cultured rat astrocytes in a simulated ischemia model, which may contribute to clarifying our understanding of drug mechanisms that protect the brain against ischemic injury[20–22]. Our study showed that the TLR3 agonist Poly I:C can reduce ischemic damage to astrocytes in a simulated ischemic condition, as indicated by cellular morphology, mitochondrial function and LDH leakage. Bsibsi *et al*[23] reported that Poly I:C-conditioned medium improves neuronal survival in organotypic human brain slice cultures, and freshly added Poly I:C to control medium promoted neuronal survival equally well. This finding suggests that in the context of such slices, local astrocytes can be activated by Poly I:C to produce neuroprotective mediators in culture. Poly I:C has also shown neuroprotective effects under ischemic condi-

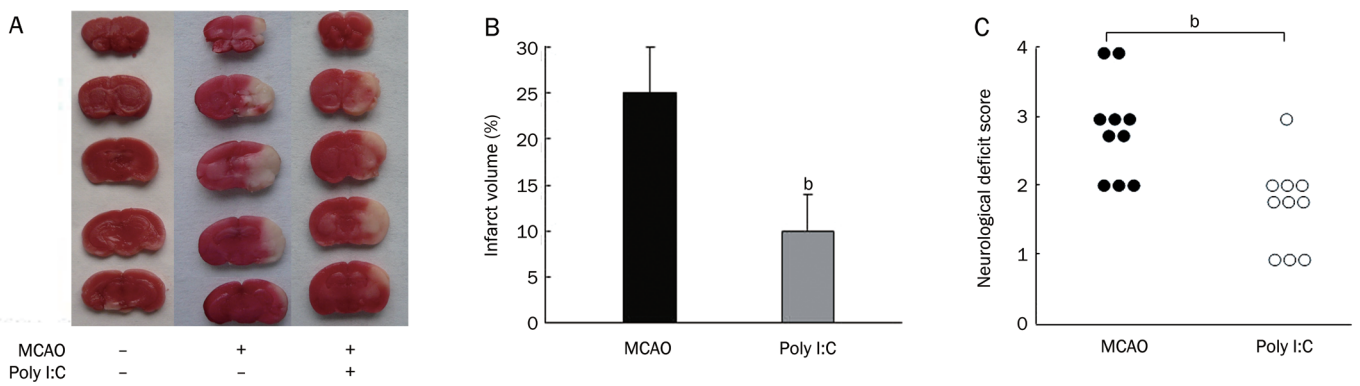

Figure 5. Poly I:C (0.3 mg/kg) reduced cerebral infarct size and improved neurological deficit in mice subjected to MCAO. Poly I:C was administered intramuscularly 24 h before MCAO. (A) Five consecutive TTC-stained coronal brain slices are arranged in cranial to caudal order. (B) Statistical results of infarct volumes in groups are shown. Values are expressed as the mean±SD, n=8. ^{b}P<0.05 *vs* MCAO group. (C) Results of neurological deficit score in groups are shown, and the data were analyzed by the nonparametric Kruskal-Wallis test. n=10. ^{b}P<0.05 *vs* MCAO group.

tions. Marsh *et al*[7] found that acute Poly I:C *in vitro* treatment in mouse mixed cortical cultures exposed to OGD markedly reduced OGD-mediated cell death. Our findings in the present study are consistent with those of Marsh *et al*.

In several models of brain ischemia, systemic administration of the TLR4 ligand LPS induces tolerance to injury[24–26] that is most likely through induction of IFNβ and interferon-stimulated genes through the TLR4 adapter molecule TRIF[7]. Poly I:C-induced tolerance to ischemic damage is similar to the phenomenon of LPS-induced tolerance to ischemic injury. IFNβ is an important downstream chemical product of TLR3 and TLR4 via TRIF. It has been shown that direct administration of IFNβ reduced ischemic brain damage in both rat and rabbit models of ischemic stroke[27–29]. The protective effects of IFNβ are associated with both preventing neutrophil infiltration and attenuating blood-brain barrier damage[28]. IFNβ has already been approved for human use as a treatment for the chronic inflammatory disorder multiple sclerosis. In contrast to IFNβ, TNFα, and IL-6 are important downstream products of the TLR-MyD88 pathway. TNFα and IL-6 are critically important in mediating leukocyte infiltration in tissues via the initial induction of leukocyte adhesion molecules such as vascular cell adhesion molecule-1, intercellular cell adhesion molecule-1 and E-selection on endothelial cells[30, 31]. Because TLR3 activation exclusively signals through the TRIF pathway, signaling via the TRIF-dependent pathway might serve as a neuroprotective mechanism associated with Poly I:C preconditioning in ischemia. To explore the neuroprotective mechanism related to Poly I:C, we examined IFNβ, TNFα, and IL-6 levels in the cultured medium of ischemic astrocytes. It was demonstrated that preconditioning with the TLR3 ligand Poly I:C enhanced IFNβ levels in the culture medium from ischemic astrocytes and inhibited TNFα and IL-6 production from the ischemic astrocytes. Similar inhibitory effects of Poly I:C on TNFα and IL-6 levels in ischemic mouse brains were observed *in vivo*. The results of Western blot analysis further showed that Poly I:C preconditioning markedly enhanced TRIF protein expression in the ischemic astrocyte cultures. These findings suggest that Poly I:C preconditioning may activate TLR3 in astrocytes and signal through TRIF to induce its downstream component IFNβ production. Reduced TNFα and IL-6 production is purported to be a result of disrupted signaling through the TLR-MyD88 pathway. Poly I:C preconditioning, similar to LPS, may inhibit the pro-inflammatory MyD88 pathway by upregulating inflammatory pathway inhibitors in the brain; alternatively, the activation of the TLR3-TRIF pathway before a stroke can directly inhibit the activation of TLR-MyD88 pathway in the setting of ischemia.

In conclusion, the protective potential of TLR3 ligand Poly I:C has been investigated in brain ischemia models *in vivo* and *in vitro*. The underlying protective mechanisms for Poly I:C preconditioning may be partly related to its activation of the TRIF–IFNβ pathway, which results in reduced pro-inflammatory cytokine production and enhanced anti-inflammatory cytokine IFNβ production from the ischemic astrocytes. This is the first demonstration of the neuroprotective mechanism of Poly I:C and its modulation of the TRIF-dependent signaling pathway. Activation of TLR3-TRIF by drug preconditioning might be a useful and novel anti-inflammatory strategy to protect the brain from ischemic damage.

Acknowledgements

This research was funded by the National Natural Science Foundation of China (No 81001432) and the 40th batch of Scientific Research Foundation for Returned Scholars, Ministry of Education of China.

Author contribution

Dr Qing LU and Dr Wei ZHU designed the study and wrote the manuscript; Dr Xu-lin XU helped write the manuscript, Lin-na PAN conducted the research and analyzed the data; Cai LI helped with portions of the research; Prof Lian-jun GUO helped design the study and revised the paper.

References

1 Shpargel KB, Jalabi W, Jin Y, Dadabayev A, Penn MS, Trapp BD. Preconditioning paradigms and pathways in the brain. Cleve Clin J Med 2008; 75: S77–82.
2 Liu XQ, Sheng R, Qin ZH. The neuroprotective mechanism of brain ischemic preconditioning. Acta Pharmacol Sin 2009; 30: 1071–80.
3 Harari OA, Liao JK. NF-kappaB and innate immunity in ischemic stroke. Ann N Y Acad Sci 2010; 1207: 32–40.
4 Lakhan SE, Kirchgessner A, Hofer M. Inflammatory mechanisms in ischemic stroke: therapeutic approaches. J Transl Med 2009; 7: 97.
5 Bowen KK, Naylor M, Vemuganti R. Prevention of inflammation is a mechanism of preconditioning-induced neuroprotection against focal cerebral ischemia. Neurochem Int 2006; 49: 127–35.
6 Wang YC, Lin S, Yang QW. Toll-like receptors in cerebral ischemic inflammatory injury. J Neuroinflammation 2011; 8: 134.
7 Marsh B, Stevens SL, Packard AE, Gopalan B, Hunter B, Leung PY, *et al*. Systemic lipopolysaccharide protects the brain from ischemic injury by reprogramming the response of the brain to stroke: a critical role for IRF3. J Neurosci 2009; 29: 9839–49.
8 Marsh BJ, Stenzel-Poore MP. Toll-like receptors: novel pharmacological targets for the treatment of neurological diseases. Curr Opin Pharmacol 2008; 8: 8–13.
9 Rosenzweig HL, Lessov NS, Henshall DC, Minami M, Simon RP, Stenzel-Poore MP. Endotoxin preconditioning prevents cellular inflammatory response during ischemic neuroprotection in mice. Stroke 2004; 35: 2576–81.
10 Tasaki K, Ruetzler CA, Ohtsuki T, Martin D, Nawashiro H, Hallenbeck JM. Lipopolysaccharide pre-treatment induces resistance against subsequent focal cerebral ischemic damage in spontaneously hypertensive rats. Brain Res 1997; 748: 267–70.
11 Pradillo JM, Fernandez-Lopez D, Garcia-Yebenes I, Sobrado M, Hurtado O, Moro MA, *et al*. Toll-like receptor 4 is involved in neuroprotection afforded by ischemic preconditioning. J Neurochem 2009; 109: 287–94.
12 Broad A, Kirby JA, Jones DE. Toll-like receptor interactions: tolerance of MyD88-dependent cytokines but enhancement of MyD88-independent interferon-beta production. Immunology 2007; 120: 103–11.
13 Nhu QM, Cuesta N, Vogel SN. Transcriptional regulation of lipopolysaccharide (LPS)-induced Toll-like receptor (TLR) expression in murine macrophages: role of interferon regulatory factors 1 (IRF-1) and 2

(IRF-2). J Endotoxin Res 2006; 12: 285–95.
14 Pan L, Lu Q, Guo L. Protective effects of poly I:C on mixed cortical cultures against oxygen glucose deprivation induced injury. Chin J Pharmacol Toxicol 2011; 25: 17.
15 Liu C, Wu J, Xu K, Cai F, Gu J, Ma L, *et al*. Neuroprotection by baicalein in ischemic brain injury involves PTEN/AKT pathway. J Neurochem 2010; 112: 1500–12.
16 Mosmann T. Rapid colorimetric assay for cellular growth and survival: application to proliferation and cytotoxicity assays. J Immunol Methods 1983; 65: 55–63.
17 Lu Q, Xia N, Xu H, Guo L, Wenzel P, Daiber A, *et al*. Betulinic acid protects against cerebral ischemia-reperfusion injury in mice by reducing oxidative and nitrosative stress. Nitric Oxide 2011; 24: 132–8.
18 Kim BT, Rao VL, Sailor KA, Bowen KK, Dempsey RJ. Protective effects of glial cell line-derived neurotrophic factor on hippocampal neurons after traumatic brain injury in rats. J Neurosurg 2001; 95: 674–9.
19 Barreto G, White RE, Ouyang Y, Xu L, Giffard RG. Astrocytes: targets for neuroprotection in stroke. Cent Nerv Syst Agents Med Chem 2011; 11: 164–73.
20 Gabryel B, Trzeciak HI. Role of astrocytes in pathogenesis of ischemic brain injury. Neurotox Res 2001; 3: 205–21.
21 Gabryel B, Adamek M, Pudelko A, Malecki A, Trzeciak HI. Piracetam and vinpocetine exert cytoprotective activity and prevent apoptosis of astrocytes *in vitro* in hypoxia and reoxygenation. Neurotoxicology 2002; 23: 19–31.
22 Gabryel B, Labuzek K, Malecki A, Herman ZS. Immunophilin ligands decrease release of pro-inflammatory cytokines (IL-1beta, TNF-alpha and IL-2 in rat astrocyte cultures exposed to simulated ischemia *in vitro*. Pol J Pharmacol 2004; 56: 129–36.
23 Bsibsi M, Persoon-Deen C, Verwer RW, Meeuwsen S, Ravid R, Van Noort JM. Toll-like receptor 3 on adult human astrocytes triggers production of neuroprotective mediators. Glia 2006; 53: 688–95.
24 Tasaki K, Ruetzler CA, Ohtsuki T, Martin D, Nawashiro H, Hallenbeck JM. Lipopolysaccharide pre-treatment induces resistance against subsequent focal cerebral ischemic damage in spontaneously hypertensive rats. Brain Res 1997; 748: 267–70.
25 Rosenzweig HL, Lessov NS, Henshall DC, Minami M, Simon RP, Stenzel-Poore MP. Endotoxin preconditioning prevents cellular inflammatory response during ischemic neuroprotection in mice. Stroke 2004; 35: 2576–81.
26 Delehanty JB, Johnson BJ, Hickey TE, Pons T, Ligler FS. Binding and neutralization of lipopolysaccharides by plant proanthocyanidins. J Nat Prod 2007; 70: 1718–24.
27 Liu H, Xin L, Chan BP, Teoh R, Tang BL, Tan YH. Interferon-beta administration confers a beneficial outcome in a rabbit model of thromboembolic cerebral ischemia. Neurosci Lett 2002; 327: 146–8.
28 Veldhuis WB, Floris S, van der Meide PH, Vos IM, de Vries HE, Dijkstra CD, *et al*. Interferon-beta prevents cytokine-induced neutrophil infiltration and attenuates blood-brain barrier disruption. J Cereb Blood Flow Metab 2003; 23: 1060–9.
29 Veldhuis WB, Derksen JW, Floris S, Van Der Meide PH, De Vries HE, Schepers J, *et al*. Interferon-beta blocks infiltration of inflammatory cells and reduces infarct volume after ischemic stroke in the rat. J Cereb Blood Flow Metab 2003; 23: 1029–39.
30 Bevilacqua MP. Endothelial-leukocyte adhesion molecules. Annu Rev Immunol 1993; 11: 767–804.
31 Ramilo O, Saez-Llorens X, Mertsola J, Jafari H, Olsen KD, Hansen EJ, *et al*. Tumor necrosis factor alpha/cachectin and interleukin 1 beta initiate meningeal inflammation. J Exp Med 1990; 172: 497–507.

Acta Pharmacologica Sinica (2012) 33: 1254–1259
 1671-4083/12 $32.00
www.nature.com/aps

Original Article

Tanshinone IIA protects rabbits against LPS-induced disseminated intravascular coagulation (DIC)

Liang-cai WU[1, #, *], Xi LIN[2, #], Hao SUN[2]

[1]*Department of Dermatology, Huangpu Hospital of the First Affiliated Hospital, Sun Yat-sen University, Guangzhou 510080, China;*
[2]*Department of Pharmacology, Medical College, Ji-nan University, Guangzhou 510632, China*

Aim: To evaluate the effects of tanshinone IIA (Tan IIA), a lipophilic diterpene from the Chinese herb *Salvia miltiorrhiza*, on lipopolysaccharide (LPS)-induced disseminated intravascular coagulation (DIC) in rabbits.
Methods: LPS-induced DIC model was made in adult male New Zealand rabbits by continuous intravenous infusion of LPS (0.5 mg/kg) via marginal ear vein for 6 h. The animals were simultaneously administered with Tan IIA (1, 3 and 10 mg/kg) or heparin (500 000 IU/kg) through continuous infusion via the contralateral marginal ear vein for 6 h. Before and 2 and 6 h after the start of LPS infusion, blood samples were taken for biochemical analyses.
Results: Continuous infusion of LPS into the rabbits gradually impaired the hemostatic parameters, damaged renal and liver functions, increased the plasma TNF-α level, and led to a high mortality rate (80%). Treatment of the rabbits with Tan IIA dose-dependently attenuated the increase in activated partial thromboplastin time (APTT), prothrombin time (PT) and fibrin-fibrinogen degradation products (FDP); ameliorated the decrease in plasma levels of fibrinogen and platelets; and reversed the decline in activity of protein C and antithrombin III. Meanwhile, the treatment significantly suppressed the increase in the plasma levels of aminotransferase, creatinine and TNF-α, and led to much lower mortality (46.7% and 26.7% for the medium- and high-dose groups). Treatment of the rabbits with the high dose of heparin also effectively improved the hemostatic parameters, ameliorated liver and renal injuries, and reduced the plasma level of TNF-α, and significantly reduced the mortality (33.3%).
Conclusion: Tan IIA exerts a protective effect against DIC in rabbits.

Keywords: disseminated intravascular coagulation (DIC); lipopolysaccharides; tanshinone IIA; heparin; tumor necrosis factor-α

Acta Pharmacologica Sinica (2012) 33: 1254–1259; doi: 10.1038/aps.2012.84; published online 17 Sep 2012

Introduction

Disseminated intravascular coagulation (DIC) is an acquired syndrome characterized by the activation of intravascular coagulation and subsequent intravascular fibrin formation. It occurs secondary to an underlying disorder such as cancer, trauma, or infection. DIC frequently results in organ failure because numerous microthrombi form in the organ, creating a disturbance in the microcirculation[1, 2]. This process is a serious health hazard and is a cause for the poor prognosis in cases of DIC. The basic pathological mechanism of DIC includes the spread of microvascular thromboses and the excessive release of pro-inflammatory cytokines such as tumor necrosis factor alpha (TNF-α)[3]. Current clinical trials aim at an interruption of the "latent coagulation" in DIC by administering coagulation inhibitors such as heparin, which depend on activating the antithrombin (AT) in plasma; however, in DIC, AT is also consumed, so the anticoagulant effect of heparin could be limited[4].

Chinese herbs have been widely used to treat inflammatory and thrombotic diseases throughout history. The dried root, or rhizome, of *Salvia miltiorrhiza* is officially listed in the Chinese Pharmacopoeia (Pharmacopoeia Commission of the People's Republic of China, 2000) for the treatment of inflammation and cardiovascular diseases, including thrombolytic diseases[5, 6]. Tanshinone IIA (Tan IIA) is a lipophilic diterpene compound found as a marker component in *Salvia miltiorrhiza*. Previous pharmacological studies indicated that Tan IIA could inhibit platelet aggregation[7], suppress LPS-induced TNF-α release[8], and inhibit thrombus formation[9]. Furthermore, our previous study also found that an injection of a compound Salvia miltiorrhiza injection could have a protective effect on LPS-induced DIC in rabbits[10]. These research advances suggested that Tan IIA may be an attractive agent for the treatment of

# These two authors contributed equally to this article.
* To whom correspondence should be addressed.
E-mail wulc_sysu@hotmail.com
Received 2011-12-27 Accepted 2012-05-28

DIC.

Although many of the properties of Tan IIA are known, there are few studies investigating its effects on DIC. In this study, we found that Tan IIA protected against LPS-induced DIC through its anticoagulation activity and its inhibition of TNF-α.

Materials and methods

Reagents

Sodium tanshinone IIA sulfonate (Tan IIA, $C_{19}H_{17}NaO_6S$, purity 99.0%) was purchased from Topharman Shanghai Co Ltd (Shanghai, China). The solution of Tan IIA was freshly prepared before use. Lipopolysaccharide (LPS) and heparin were purchased from Sigma (St Louis, USA). A TNF-α ELISA kit was purchased from RapidBio Lab (Calabasas, USA). The reagent packs for the activity assays of antithrombin III (ATIII) and protein C were obtained from Sun Biotechnology Company (Shanghai, China). All other reagents were of analytical grade and obtained from commercial sources.

Animals

Adult male New Zealand white rabbits (weighing 2–3 kg, Grade II) were supplied by the Experimental Animal Center of Zhongshan Medical College, Sun Yat-sen University, China.

Experimental models and drug treatments

All animal experiments were conducted in accordance with the National Research Council Guide for the Care and Use of Laboratory Animals and were approved by the Sun Yat-sen University Animal Care and Use Committee (Guangzhou, China).

Animals were anesthetized by an intramuscular injection of 30 mg/kg of ketamine hydrochloride, followed by intramuscular supplements of 10 mg/kg of ketamine hydrochloride given 2 h, 4 h, and 6 h after the start of the ketamine infusion. DIC experimental models were performed according to the previous report [11] and were induced by infusing an LPS solution (0.5 mg/kg of LPS into 60 mL of saline) at a rate of 10 mL/h through the marginal ear vein of the rabbits over a period of 6 h. The LPS control group was infused with 60 mL of saline solution. Treatments were started through the contralateral marginal ear vein simultaneously with the LPS infusion.

Twelve different treatment groups were established, 6 containing 10 animals each (for the measurement of biochemical indexes and TNF-α) and 6 containing 15 animals each (for the measurement of survival rate). Within each set of 6, treatment groups were given either 1, 3, or 10 mg/kg of Tan IIA (low-, medium-, or high-dose, respectively) in 60 mL of saline solution over a period of 6 h (a solution infusion rate of 10 mL/h). The heparin control group was infused with 500 000 IU/kg of heparin in 60 mL of saline solution over a period of 6 h. The additional rabbits, which were given neither LPS nor Tan IIA, were infused with 60 mL of saline solution (10 mL/h) through both marginal ear veins.

Biochemical analyses

Blood samples of 1 mL were taken immediately before LPS infusion and at 2 h and 6 h after the start of the infusion. The activities of ATIII and protein C were measured according to the reagent pack instructions based on chromogenic substrates. An automatic analyzer (Sysmex SE-9500, Sysmex CA 1500, Japan) was used to determine the activated partial thromboplastin time (APTT) and, prothrombin time (PT), as well as the plasma levels of platelets, fibrinogen and fibrin-fibrinogen degradation products (FDP). A 7170A automatic analyzer (HITACHI, Japan) was used to detect the plasma levels of alanine aminotransferase (ALT, the marker of liver injury) and creatinine (Cr, the marker of renal injury).

Measurement of TNF-α concentration

One milliliter of each rabbit's plasma was collected in a tube and stored at -20 °C until assayed. The concentrations of TNF-α in the animal plasma samples were determined using an ELISA kit.

Measurement of survival rate

After the experiment, animals were allowed to recover from anesthesia with access to food and water *ad libitum*. The 24-h survival rate in the different groups was recorded.

Data analyses

Differences between group data were evaluated for significance using either a non-parametric test (the Kruskal-Wallis H test) or two-way repeated measures. The repeated measures analysis of variance was used for the multivariate analyses. All experiments were repeated at least three times, and the data were presented as the mean±SD unless otherwise noted. Data of the activities of ATIII and protein C and the concentration of ALT and Cr at 2 h and 6 h were converted to percentages, with a value of 100% assumed for basal data. Survival curves of LPS-induced DIC were analyzed by the Kaplan-Meyer log-rank test. Differences with P values of less than 0.05 were considered to be statistically significant.

Results

Protective effects of Tan IIA on LPS-induced DIC

We investigated the protective effects of Tan IIA on LPS-induced DIC using a rabbit model, a clinically relevant animal model for human DIC[12]. Twenty percent (3/15) of the rabbits infused with LPS survived 24 h following the start of the experiment. Tan IIA treatment was started simultaneously with LPS induction of DIC. Our results showed that the Tan IIA treatment significantly increased the survival rate (P<0.05, compared with the LPS control group, Figure 1). Eight of fifteen rabbits (53.3%) survived in the medium-dose of Tan IIA-treated group, and eleven of fifteen rabbits (73.3%) survived in the high-dose Tan IIA-treated group. Heparin, the agent clinically used in DIC therapy, increased the survival rate from 20% to 66.7%. All of the animals in the sham group

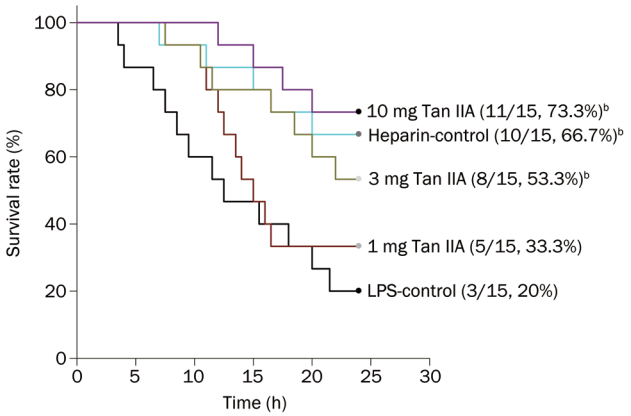

Figure 1. The protective effect of Tan IIA on LPS-induced DIC rabbits. DIC was induced by LPS. 1, 3, and 10 mg/kg Tan IIA and 500 000 IU/kg heparin was administered simultaneously with LPS by intravenous injection. Survival was monitored on over 24 h. $^{b}P<0.05$ *vs* the LPS control group; (n=15).

without LPS survived (data not shown).

Effects of Tan IIA on biochemical and pathological damages in LPS-induced DIC

To further elucidate the outcome of Tan IIA on DIC induced by LPS, we systematically investigated the biochemical and pathological effects using a rabbit model. Table 1 summarizes the plasma APTT, PT, platelet counts, fibrinogen levels, and FDP levels as well as the activities of protein C and ATIII for all the groups — normal rabbits, LPS-induced DIC rabbits, Tan IIA-treated rabbits and heparin-treated rabbits. The values of APTT, PT, and FDP for the LPS-induced DIC rabbits were all significantly higher than those for the normal rabbits ($P<0.05$, Table 1); however, the values of both fibrinogen and platelet counts and the activities of protein C and ATIII were significantly lower than those for the normal rabbits ($P<0.05$, Table 1). The infusions of both Tan IIA and heparin significantly attenuated the increased APTT, PT, and levels of FDP as well as the decreased levels of fibrinogen and platelets; treatment also improved the decreased activities of protein C and ATIII ($P<0.05$, compared with the LPS control group, Table 1). Furthermore, the infusion of heparin significantly moderated the increased APTT and PT at 6 h along with the decreased platelet counts at 2 h and 6 h when compared with the low-dose Tan IIA-treated group ($P<0.05$, Table 1).

Effects of Tan IIA on liver and renal injury in LPS-induced DIC

We investigated the effects of Tan IIA on liver and renal injuries in LPS-induced DIC rabbits. The plasma levels of ALT, an indicator of liver injury, were increased by LPS infusion. However, the levels of ALT were significantly lower in Tan IIA- and heparin-treated rabbits ($P<0.05$, compared with the LPS control group, Figure 2). A similar finding was observed in the plasma levels of Cr, which is an indicator of renal injury. An increase in Cr levels was observed in the LPS group, which was significantly suppressed by both Tan IIA and heparin ($P<0.05$, compared with the LPS control group, Figure 3). Furthermore, the infusion of heparin significantly suppressed the increased plasma levels of ALT and Cr at 6 h compared with the low-dose Tan IIA-treated group ($P<0.05$, Figure 2, 3).

Effect of Tan IIA on TNF-α *in vivo*

TNF-α is an important inflammatory marker and generally increases significantly during the early period of DIC. Therefore, we tested whether Tan IIA had any effect on the plasma levels of TNF-α. Rabbits were injected with 0.5 mg/kg of LPS, and the levels of TNF-α were dramatically increased at 1, 4, 8, and 12 h ($P<0.05$, compared with normal rabbits, Figure 4). However, the infusions of 1, 3, and 10 mg/kg of Tan IIA sig-

Table 1. Hemostatic and inflationary parameters 2 and 6 h after LPS infusion into rabbits in different treatment groups. Data are presented as the mean±SD. n=10. $^{b}P<0.05$ *vs* the LPS control group. $^{e}P<0.05$ *vs* the normal control group.

Group	Time (h)	APTT (s)	PT (s)	Platelets (*10^9/L)	Fibrinogen (g/L)	FDP (μg/L)	Protein C (%)	ATIII (%)
Normal	2 h	14.32±2.01^{b}	5.27±0.76^{b}	447.72±30.58^{b}	4.35±1.27	<0.05^{b}	103.34±4.77^{b}	101.53±4.72
	6 h	15.75±1.46^{b}	5.83±0.56^{b}	442.67±36.18^{b}	4.83±1.56^{b}	<0.05^{b}	98.91±5.03^{b}	98.75±4.56^{b}
LPS-control	2 h	33.72±5.83^{e}	10.54±2.18^{e}	253.62±38.39^{e}	3.08±0.76	73.5±17.8^{e}	55.57±14.32^{e}	84.72±16.78
	6 h	82.41±10.57^{e}	19.30±4.86^{e}	163.72±20.57^{e}	1.44±0.38^{e}	98.3±20.2^{e}	41.63±13.08^{e}	52.40±15.51^{e}
Tan IIA								
Low-dose	2 h	24.38±6.19^{be}	10.37±2.07^{e}	308.71±42.46^{be}	4.08±1.06	45.3±11.3^{be}	79.16±18.67^{be}	86.38±12.19
(1 mg/kg)	6 h	53.51±5.43^{be}	13.68±4.51^{be}	230.49±40.76^{be}	2.35±0.50^{be}	69.7±20.6^{be}	70.36±11.54^{be}	72.62±16.92^{be}
Medium-dose	2 h	19.24±1.86^{be}	6.34±1.37^{b}	380.27±38.15^{be}	4.06±1.31	30.6±10.1^{be}	83.25±16.42^{be}	89.42±12.81
(3 mg/kg)	6 h	30.13±4.92^{be}	8.65±1.92^{be}	374.84±32.10^{be}	3.17±0.72^{be}	60.2±12.4^{be}	85.61±16.46^{b}	90.62±14.17^{b}
High-dose	2 h	15.96±1.78^{be}	5.67±1.08^{b}	415.24±41.78^{b}	4.12±1.58	27.3±8.1^{be}	87.46±17.37^{b}	90.18±10.05
(10 mg/kg)	6 h	28.67±4.26^{be}	6.02±0.94^{b}	383.76±30.19^{be}	3.45±1.17^{be}	51.7±7.9^{be}	84.01±15.42^{b}	98.73±7.69^{b}
Heparin-control	2 h	18.58±2.11^{be}	7.67±1.46^{be}	401.17±28.63^{b}	3.97±1.46	34.3±10.8^{be}	78.62±18.23^{be}	89.54±11.36
	6 h	34.64±3.07^{be}	7.82±1.85^{be}	386.37±20.43^{be}	3.31±0.85^{be}	52.2±11.4^{be}	79.66±14.35^{be}	88.68±10.94^{b}

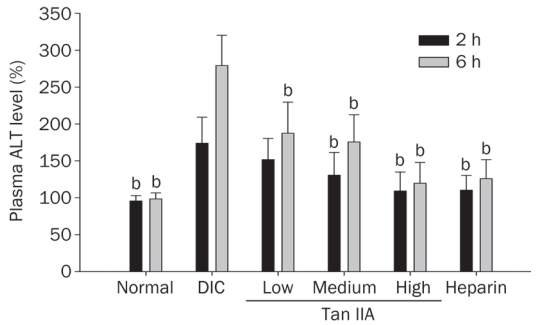

Figure 2. Effect of Tan IIA 1, 3, and 10 mg/kg on the plasma levels of ALT in LPS-induced DIC rabbits. Blood samples were taken immediately before LPS infusion and 2 h, 6 h after the start of the infusion. An automatic analyzer detected the plasma levels of ALT. Results of ALT at 2 h and 6 h were converted to percentages assuming a value of 100% for basal data. Values are expressed as the mean±SD percent of the initial value before LPS infusion. $^{b}P<0.05$ *vs* the LPS control group; $n=10$.

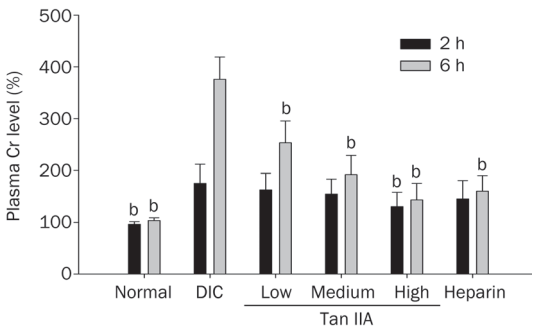

Figure 3. Effect of Tan IIA 1, 3, and 10 mg/kg on the plasma levels of Cr in LPS-induced DIC rabbits. Blood samples were taken immediately before LPS infusion and 2 h, 6 h after the start of the infusion. An automatic analyzer detected the plasma levels of Cr. Results of Cr at 2 h and 6 h were converted to percentages assuming a value of 100% for basal data. Values are expressed as the mean±SD. percent of the initial value before LPS infusion. $^{b}P<0.05$ *vs* DIC group. $n=10$.

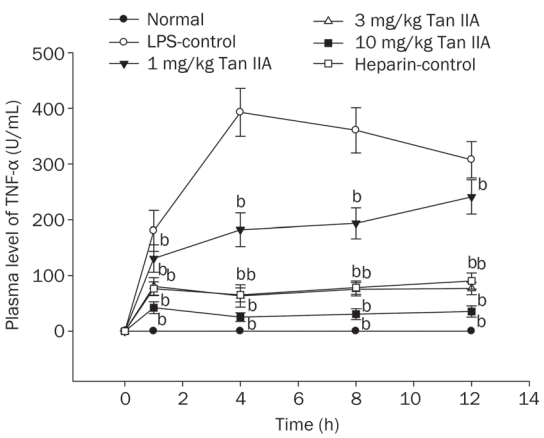

Figure 4. Effect of Tan IIA on the plasma levels of TNF-α in LPS-induced DIC rabbits. $n=10$. $^{b}P<0.05$ *vs* the LPS control group.

nificantly reduced the increased plasma levels of TNF-α at each of those time points ($P<0.05$, compared with normal rabbits, Figure 4). An infusion of 500 000 IU/kg of heparin also significantly reduced the increased plasma levels of TNF-α at 1, 4, 8, and 12 h ($P<0.05$, compared with the LPS control group; $P<0.05$, compared with the low-dose Tan IIA-treated group, Figure 4).

Discussion

LPS, a constituent of the outer membrane of gram-negative bacteria, is a major pathogenic factor contributing to the initiation of life-threatening DIC, which occurs often in intensive care unit patients. Induction of DIC leads to the generation of pro-inflammatory cytokines by monocytes and endothelial cells, which in turn activate coagulation and fibrinolytic pathways[13]. In this study, an infusion of LPS resulted in the typical changes of DIC: a significant increase in APTT, PT, FDP levels, and TNF-α levels; a severe decrease in the activities of ATIII and protein C; a decrease in the levels of fibrinogen and platelets; and a high mortality rate, which was consistent with our previous results[10].

In this study, we reported that Tan IIA had a significant protective effect against the lethal effects of LPS-induced DIC in rabbits. Using this rabbit model of DIC, we found that all 3 doses of Tan IIA administered could not only improve the biochemical signs of DIC but could also ameliorate organ injury and decrease the mortality of LPS-treated animals ($P<0.05$). This dramatic benefit was further verified by a significant reduction in the levels of TNF-α observed in Tan IIA-treated rabbits.

The hallmark of the coagulation disorder in DIC is the imbalance between intravascular fibrin formation and its removal. The serious reduction in anticoagulant capacity and the inhibition of fibrinolysis result in a massive activation of coagulation, finally leading to overwhelming fibrin formation and the consumption of clotting factors and inhibitors. Abundant intravascular fibrin formation leads to microvascular thrombosis, which contributes to the development of multiple organ failure[14].

To investigate whether the coagulation process was altered in Tan IIA-treated animals, we first measured the APTT and PT to evaluate the intrinsic and extrinsic pathways of coagulation, respectively. It was observed that the infusion of Tan IIA induced a decrease in PT and APTT when compared to the LPS control group. Platelet aggregation is one of the important triggers of blood coagulation in the pathologic thrombosis associated with DIC[15]. DIC produces massive thrombin, stimulates platelet aggregation and triggers the blood coagulation cascades. Those cascades result in a lowering of the blood's platelet counts and its fibrinogen level, enhancing the FDP concentration and prolonging both PT and APTT. The procoagulant environment predisposes the animals to develop excessive microthrombi and increases the consumption of platelets and fibrinogen. Thus, we also measured platelet counts, fibrinogen concentrations, and FDP, which were the useful parameters in diagnosing DIC. It was observed that

an infusion of Tan IIA could improve all of these parameters when compared with the LPS control group. In our previous study, we found that an injection of a compound from *Salvia miltiorrhiza* could have a protective effect on LPS-induced DIC in rabbits. These current results suggested that the increase in the activation times of the extrinsic and intrinsic coagulation pathways was related to a delay in the coagulation process, which in turn was due to a slowing of fibrin clot formation and an inhibition of platelet aggregation (as shown by the improvement in platelet numbers).

The initial decrease in protein C and/or ATIII levels may have particular prognostic significance for the clinical management of DIC, which has an almost absolute lethality[16, 17]. In this study, the improvements in protein C and ATIII activity by the infusion of Tan IIA were remarkable among the observed coagulation-related parameters. The chief cause of protein C and ATIII deficiency in LPS-induced DIC is not a decrease in production but an increase in consumption due to the enhanced generation of thrombin. The antithrombotic and/or anticoagulant effect of Tan IIA would reduce the consumption of coagulation factors during the development of DIC. Lastly, we also observed that Tan IIA significantly attenuated both the increased APTT and PT and the decreased plasma levels of platelets and fibrinogen as well as treatment with heparin.

Abundant evidence has shown that inflammation and thrombosis are closely related during DIC. Severe inflammation can both induce coagulation and lead to disturbances of coagulation. Severe coagulation dysfunction can promote further inflammation, causing increased morbidity and mortality[18, 19]. Among proinflammatory cytokines, TNF-α is the trigger of an inflammatory cascade and is thus crucial in local and distant organ injury; its levels also correlate well with the severity of DIC[20, 21]. In the present study, Tan IIA reduced the TNF-α levels in LPS-induced DIC rabbits. These results could suggest one of the main mechanisms of action of Tan IIA against DIC.

As the onset of multiorgan dysfunction syndrome has been shown to forecast mortality in patients with DIC, the protection of organs, particularly the liver and kidney, is important in DIC treatment[22]. In the present study, we demonstrated that Tan IIA had a protective effect on LPS-induced DIC in rabbits by ameliorating organ dysfunction. Two possible mechanisms are implicated in these favorable results. First, the effect of Tan IIA on biochemical plasma levels may be a consequence of its effect of improving blood flow to organs; we observed that plasma levels of ALT and Cr, which were increased by LPS infusion, were significantly decreased in Tan IIA-treated animals. Second, Tan IIA has been shown to have an anti-inflammatory result through its proteolytic effect on TNF-α, which is the critical mediator of LPS-induced organ failure. Taken together, these two actions of Tan IIA have a favorable therapeutic effect on LPS-induced DIC rabbits.

We also analyzed the effects of heparin on LPS-induced DIC in rabbits. The traditional anticoagulant heparin, especially at high therapeutic dosages, is effective in interrupting intravascular clotting in cases of acute DIC, which confirms the results of clinical studies in humans as well as experimental studies on rats and rabbits[23, 24]. In the present study, a high dose of heparin (500 000 IU/kg) was used for modulation of the DIC process and aided in prevention as well as treatment. When rabbits were treated with heparin alone, hemostatic parameters were improved, liver and renal injuries were ameliorated, mortality was significantly reduced, and the concentration of TNF-α was reduced.

In conclusion, Tan IIA may have protective effects on DIC by reducing coagulation, aiding the breakdown of TNF-α, and ameliorating organ dysfunction. Our study indicated that Tan IIA could be a good candidate for the development of new agents to fight against DIC. However, we emphasize that the true utility of Tan IIA in combating DIC will require further direct testing through clinical trials.

Acknowledgements

This project was supported by the National Natural Science Foundation of China (No 81000209), the Key Project of the Chinese Ministry of Education (No 210255), and the Fundamental Research Funds for the Central Universities (No 21609304). The authors declare that they have no competing financial interest in Tan IIA.

Abbreviations

APTT, activated partial thromboplastin time; PT, prothrombin time; Tan IIA, sodium tanshinone IIA; LPS, lipopolysaccharide; FDP, fibrin-fibrinogen degradation products; ALT, alanine aminotransferase; Cr, creatinine; TNF-α, tumor necrosis factor alpha.

Author contribution

Liang-cai WU designed the study; Hao SUN performed the research; Xi LIN contributed new analytical tools and reagents; Liang-cai WU and Xi LIN analyzed the data and wrote the paper.

References

1 Markwardt F, Nowak G, Meerbach W, Rudiger KD. Studies in experimental animals on disseminated intravascular coagulation (DIC). Thromb Diath Haemorrh 1975; 34: 513–21.
2 Wilde JT, Roberts KM, Greaves M, Preston FE. Association between necropsy evidence of disseminated intravascular coagulation and coagulation variables before death in patients in intensive care units. J Clin Pathol 1988; 41: 138–42.
3 Levi M, ten Cate H. Disseminated intravascular coagulation. N Engl J Med 1999; 341: 586–92.
4 Klein HG, Bell WR. Disseminated intravascular coagulation during heparin therapy. Ann Intern Med 1974; 80: 477–81.
5 Lei XL, Chiou GC. Studies on cardiovascular actions of *Salvia miltiorrhiza*. Am J Chin Med 1986; 14: 26–32.
6 Wang N, Luo HW, Niwa M, Ji J. A new platelet aggregation inhibitor from *Salvia miltiorrhiza*. Planta Med 1989; 55: 390–1.
7 Liu JQ, Lee TF, Miedzyblocki M, Chan GC, Bigam DL, Cheung PY. Effects of tanshinone IIA, a major component of *Salvia miltiorrhiza*, on platelet aggregation in healthy newborn piglets. J Ethnopharmacol

2011; 137: 44–9.
8 Wan JM, Sit WH, Lee CL, Fu KH, Chan DK. Protection of lethal toxicity of endotoxin by *Salvia miltiorrhiza* BUNGE is via reduction in tumor necrosis factor alpha release and liver injury. Int Immunopharmacol 2006; 6: 750–8.
9 Ji HS, Yu F, Yang J. Comparative research on pharmacodynamics of Danshen co-microemulsion on hemorheology in rats with hyperlipidemia. Zhong Yao Cai 2008; 31: 566–9.
10 Lin X, Qi JZ, Qiu PX, Chen JS. Effect of compound *Salvia miltiorrhiza* injection on LPS-induced disseminated intravascular coagulation in rabbits. Chin J Pathophysiol 2011; 27: 464–8.
11 Lin X, Liang XX, Chen JS, Chen Q, Qiu PX, Yan GM. The effect of fibrinolytic enzyme FIIa from *Agkistrodon acutus* venom ondisse minated intravascular coagulation in rabbits. Transl Res 2007; 150: 295–302.
12 Levi M, ten Cate H, van der Poll T, van Deventer SJ. Pathogenesis of disseminated intravascular coagulation in sepsis. JAMA 1993; 270: 975–9.
13 Warr TA, Rao LV, Rapaport SI. Disseminated intravascular coagulation in rabbits induced by administration of endotoxin or tissue factor: effect of anti-tissue factor antibodies and measurement of plasma extrinsic pathway inhibitor activity. Blood 1990; 75: 1481–9.
14 Zeerleder S, Hack CE, Wuillemin WA. Disseminated intravascular coagulation in sepsis. Chest 2005; 128: 2864–75.
15 Hathcock JJ. Flow effects on coagulation and thrombosis. Arterioscler Thromb Vasc Biol 2006; 26: 1729–37.
16 Sakata Y. Treatment of DIC associated with myelogenous leukemia. Nihon Rinsho 2009; 67: 1978–83.
17 Oh D, Jang MJ, Lee SJ, Chong SY, Kang MS, Wada H. Evaluation of modified non-overt DIC criteria on the prediction of poor outcome in patients with sepsis. Thromb Res 2010; 126: 18–23.
18 Taveira da Silva AM, Kaulbach HC, Chuidian FS, Lambert DR, Suffredini AF, Danner RL. Brief report: shock and multiple-organ dysfunction after self-administration of *Salmonella* endotoxin. N Engl J Med 1993; 328: 1457–60.
19 Fong Y, Tracey KJ, Moldawer LL, Hesse DG, Manogue KB, Kenney JS, *et al*. Antibodies to cachectin/tumor necrosis factor reduce interleukin 1 beta and interleukin 6 appearance during lethal bacteremia. J Exp Med 1989; 170: 1627.
20 Schabbauer G, Tencati M, Pedersen B, Pawlinski R, Mackman N. PI3K-Akt pathway suppresses coagulation and inflammation in endotoxemic mice. Arterioscler Thromb Vasc Biol 2004; 24: 1963–9.
21 Cataldegirmen G, Zeng S, Feirt N, Lppagunta N, Dun H, Qu W, *et al*. RAGE limits regeneration after massive liver injury by coordinated suppression of TNF-α and NF-κB. J Exp Med 2005; 201: 473–84.
22 Levi M. Disseminated intravascular coagulation: what's new? Crit Care Clin 2005; 21: 449–67.
23 Fujishima Y, Yokota K, Sukamoto T. The effect of danaparoid sodium (danaparoid) on endotoxin-induced experimental disseminated intravascular coagulation (DIC) in rats. Thromb Res 1998; 91: 221–7.
24 Hamano S, Kinukawa M, Komatsu H, Miyata H, Sakuragawa N. Effects of low molecular weight heparin (FR-860) on the experimental disseminated intravascular coagulation models. Nihon Yakurigaku Zasshi 1991; 98: 53–62.

Acta Pharmacologica Sinica (2012) 33: 1260–1270
 1671-4083/12 $32.00
www.nature.com/aps

Original Article

Differential hepatoprotective mechanisms of rutin and quercetin in CCl_4-intoxicated BALB/cN mice

Robert DOMITROVIĆ[1, *], Hrvoje JAKOVAC[2], Vanja VASILJEV MARCHESI[3], Sanda VLADIMIR-KNEŽEVIĆ[4], Olga CVIJANOVIĆ[5], Žarko TADIĆ[6], Željko ROMIĆ[7], Dario RAHELIĆ[8]

[1]Department of Chemistry and Biochemistry, Medical Faculty, University of Rijeka, Rijeka, Croatia; [2]Department of Physiology and Immunology, Medical Faculty, University of Rijeka, Rijeka, Croatia; [3]Department of Social Medicine and Epidemiology, Medical Faculty, University of Rijeka, Rijeka, Croatia; [4]Department of Pharmacognosy, Faculty of Pharmacy and Biochemistry, University of Zagreb, Zagreb, Croatia; [5]Department of Anatomy, Medical Faculty, University of Rijeka, Rijeka, Croatia; [6]Medical Faculty, University of Rijeka, Rijeka, Croatia; [7]Department of Laboratory Diagnostics, Clinical Hospital Dubrava, Zagreb, Croatia; [8]Department of Internal Diseases, Clinical Hospital Dubrava, Zagreb, Croatia

Aim: To investigate the mechanisms underlying the protective effects of quercetin-rutinoside (rutin) and its aglycone quercetin against CCl_4-induced liver damage in mice.
Methods: BALB/cN mice were intraperitoneally administered rutin (10, 50, and 150 mg/kg) or quercetin (50 mg/kg) once daily for 5 consecutive days, followed by the intraperitoneal injection of CCl_4 in olive oil (2 mL/kg, 10% *v/v*). The animals were sacrificed 24 h later. Blood was collected for measuring the activities of ALT and AST, and the liver was excised for assessing Cu/Zn superoxide dismutase (SOD) activity, GSH and protein concentrations and also for immunoblotting. Portions of the livers were used for histology and immunohistochemistry.
Results: Pretreatment with rutin and, to a lesser extent, with quercetin significantly reduced the activity of plasma transaminases and improved the histological signs of acute liver damage in CCl_4-intoxicated mice. Quercetin prevented the decrease in Cu/Zn SOD activity in CCl_4-intoxicated mice more potently than rutin. However, it was less effective in the suppression of nitrotyrosine formation. Quercetin and, to a lesser extent, rutin attenuated the inflammation in the liver by down-regulating the CCl_4-induced activation of nuclear factor-kappa B (NF-κB), tumor necrosis factor-α (TNF-α) and cyclooxygenase (COX-2). The expression of inducible nitric oxide synthase (iNOS) was more potently suppressed by rutin than by quercetin. Treatment with both flavonoids significantly increased NF-E2-related factor 2 (Nrf2) and heme oxygenase (HO-1) expression in injured livers, although quercetin was less effective than rutin at an equivalent dose. Quercetin more potently suppressed the expression of transforming growth factor-β1 (TGF-β1) than rutin.
Conclusion: Rutin exerts stronger protection against nitrosative stress and hepatocellular damage but has weaker antioxidant and anti-inflammatory activities and antifibrotic potential than quercetin, which may be attributed to the presence of a rutinoside moiety in position 3 of the C ring.

Keywords: hepatotoxicity; carbon tetrachloride (CCl_4) poisoning; rutin; quercetin; nuclear factor-kappa B; tumor necrosis factor-α; cyclooxygenase-2; nitric oxide synthase; NF-E2-related factor 2; heme oxygenase-1; transforming growth factor-β1

Acta Pharmacologica Sinica (2012) 33: 1260–1270; doi: 10.1038/aps.2012.62; published online 20 Aug 2012

Introduction

Toxic liver injury may lead to acute liver failure, resulting in organ dysfunction. Numerous drugs and toxic substances could cause hepatic damage, with the severity of the changes proportional to the duration of the toxic exposure[1]. Carbon tetrachloride (CCl_4) poisoning is one of the most commonly used models of acute liver damage. The hepatotoxic effects of CCl_4 were attributed to the excessive production of free radicals[2]. Previous studies have shown that natural compounds with antioxidant activity could ameliorate CCl_4-induced liver damage, thus preventing acute liver failure[3, 4].

Rutin is a naturally occurring flavonol consisting of aglycone quercetin and a rutinoside moiety in position 3 of the C ring (Figure 1). These widespread flavonoids, commonly found in various foods[5], exert numerous biochemical and pharmacological activities, such as antioxidant[6], anti-inflammatory[7] and antitumor activities[8]. However, the pharmacological effects of rutin and its aglycone may differ, suggesting

* To whom correspondence should be addressed.
E-mail robertd@medri.hr
Received 2012-01-17 Accepted 2012-05-07

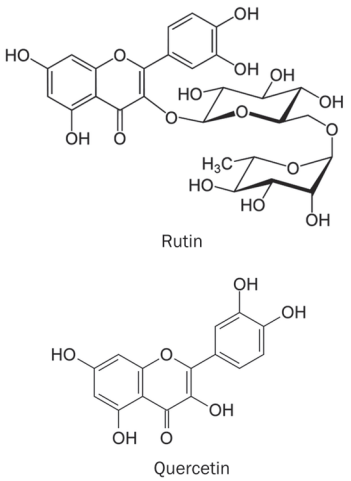

Figure 1. The chemical structures of rutin and quercetin.

that the presence of the rutinoside moiety is crucial for some of the protective effects of rutin. In several studies, rutin exerted anti-inflammatory activity, whereas quercetin was either not effective against or actually aggravated the inflammatory response both *in vivo* and *in vitro*[9, 10]. However, other authors demonstrated that quercetin acted as a strong inhibitor of inflammation in an experimental model of rat colitis[11]. Interestingly, rutin was an effective anti-inflammatory agent in chronic inflammatory conditions, such as adjuvant arthritis, whereas quercetin, but not rutin, potently suppressed acute inflammation and reduced carrageenan-induced paw edema[7]. Similarly, the cytochromes CYP1A1 and CYP1B1 were strongly inhibited by quercetin, while rutin exerted no inhibition or only weak inhibitory potential[12]. Thus, the pharmacological activities of rutin and quercetin may differ substantially, which could be attributed to the presence of a sugar moiety in position 3 of the C ring.

Previous investigations showed that rutin and quercetin could ameliorate chemically induced liver damage in rodents[13, 14]. The objective of this study was to elucidate the molecular mechanisms of the hepatoprotective activity of rutin against acute toxic liver damage in mice and compare this activity to its aglycone quercetin.

Materials and methods

Chemicals and antibodies

Rutin, quercetin, olive oil, bovine superoxide dismutase (SOD), xanthine, xanthine oxidase, cytochrome *c*, ethylenediaminetetraacetic acid (EDTA), bovine serum albumin (BSA), bovine Cu/Zn superoxide dismutase (Cu/Zn SOD), glutathione (GSH), glutathione reductase (GR), reduced nicotinamide adenine dinucleotide phosphate (NADPH), metaphosphoric acid, 5,5′-dithiobis-(2-nitrobenzoic acid) (DTNB), dimethyl sulfoxide (DMSO), ammonium molybdate, 2,2-diphenyl-1-picryl-hydrazyl (DPPH$^{\cdot}$), hydrogen peroxide, potassium ferricyanide, Trolox, sodium acetate, Tris(hydroxymethyl) aminomethane (Tris), Tween 20 and Entelan were purchased from Sigma-Aldrich (Taufkirchen, Germany). Trichloroacetic acid was purchased from Acros Organics (Geel, Belgium). Iron (III) chloride was obtained from Riedel-de Haën (Seelze, Germany). The radioimmunoprecipitation assay (RIPA) buffer (sc-24948) was purchased from Santa Cruz Biotechnology (Santa Cruz, CA, USA). CCl_4, ethanol, sodium phosphate and sulfuric acid were purchased from Kemika (Zagreb, Croatia). The diagnostic kits for the determination of alanine aminotransferase (ALT) and aspartate aminotransferase (AST) were from Dijagnostika (Sisak, Croatia). Mouse monoclonal antibodies to tumor necrosis factor-alpha (TNF-α) (ab1793) and 3-nitrotyrosine (3-NT) (ab78163) and rabbit polyclonal antibodies to nuclear factor-kappa B (NF-κB) p65 (ab7970), cyclooxygenase (COX)-2 (ab15191), inducible nitric oxide synthase (iNOS) (ab3523), heme oxygenase (HO)-1 (ab13243), NF-E2-related factor 2 (Nrf2) (ab31163) and TGF-β1 (ab92486) were purchased from Abcam (Cambridge, UK). The DAKO EnVision+ System was from DAKO Corporation (Carpinteria, CA, USA).

Reducing power assay

The reducing power of the samples was determined by the method of Oyaizu[15], as described previously[16]. Briefly, an aliquot of the sample (1.0 mL) at various concentrations (1.25–100 μg/mL) was mixed with phosphate buffer (0.2 mol/L, pH 6.6, 2.5 mL) and 1% potassium ferricyanide (2.5 mL). The mixture was incubated at 50 °C for 20 min. After the addition of 10% trichloroacetic acid (2.5 mL), the mixture was centrifuged at 1000×*g* for 10 min. The supernatant (2.5 mL) was mixed with distilled water (2.5 mL) and 0.1% iron (III) chloride (0.5 mL), and the absorbance was measured at 700 nm using an appropriate blank. All experiments were performed in triplicate. Trolox was used as a reference.

DPPH radical scavenging assay

The free radical scavenging activity of the samples was measured using the stable DPPH$^{\cdot}$ radical according to the method of Blois[17], as described previously[18]. Briefly, a 0.1 mmol/L solution of DPPH$^{\cdot}$ in ethanol was prepared, and this solution (0.5 mL) was added to sample solution in ethanol (1.5 mL) at different concentrations (0.39–50 μg/mL). After the reaction was performed in the dark at room temperature for 30 min, the absorbance was measured at 517 nm. The capability to scavenge the DPPH$^{\cdot}$ radical was calculated using the following equation: (%)=$[(A_0-A_1)/A_0]\times100$, where A_0 is the absorbance of the control reaction and A_1 is the absorbance in the presence of the sample, corrected for the absorbance of the sample itself. All experiments were performed in triplicate. Trolox was used as a reference.

Total antioxidant capacity assay

The total antioxidant capacity of rutin and quercetin was evaluated by the phosphomolybdenum method according to the procedure of Prieto *et al*[19], as described previously[16]. Briefly, the sample was dissolved in ethanol, and an aliquot of the solution (0.3 mL) was combined in a vial with the reagent

solution (0.6 mol/L sulfuric acid, 28 mmol/L sodium phosphate and 4 mmol/L ammonium molybdate, 2.7 mL). The vials were capped and incubated in a water bath at 95 °C for 90 min. After the mixture was cooled to room temperature, the absorbance was measured at 695 nm against a blank. All experiments were performed in triplicate. The antioxidant capacity of the sample was expressed as Trolox equivalents, utilizing a calibration curve of Trolox in the concentration range from 0.78 to 100 μg/mL.

Nitric oxide radical scavenging assay

The nitric oxide ($NO^{\cdot}$) scavenging activity of the samples was determined according to the method described by Rai *et al*[20] with a slight modification. The $NO^{\cdot}$ generated from sodium nitroprusside in an aqueous solution at physiological pH interacts with oxygen to produce nitrite ions, which were measured by the Griess reaction. Equal volumes of 10 mmol/L sodium nitroprusside in phosphate buffered-saline (pH 7.4) were mixed with different concentrations of the sample (0.39–50 μg/mL) and incubated at 25 °C for 150 min. After the incubation, 1.0 mL of the reaction mixture was mixed with 1% sulfanilamide (0.5 mL). After 5 min, 0.1% naphthylethylenediamine dihydrochloride (0.5 mL) was added, the solution was mixed, and the absorbance of a pink-colored chromophore was measured at 540 nm against the corresponding blank solution. Trolox was used as a standard. All experiments were performed in triplicate. The $NO^{\cdot}$ scavenging activity was expressed as the percentage of inhibition according to the following equation: $(\%)=[(A_0-A_1)/A_0]\times100$, where A_0 is the absorbance of the control without a sample and A_1 is the absorbance in the presence of the sample.

Animals

Male BALB/cN mice, 10–12 weeks old and weighing 23–25 g, were obtained from our breeding colony. The animals were housed under standard environmental conditions and had free access to tap water and a standard rodent diet (pellet, type 4RF21 GLP, Mucedola, Italy). All experimental procedures were approved by the Ethical Committee of the Medical Faculty, University of Rijeka.

Experimental design

The mice were divided into six groups, each containing five animals. The normal control (group I) received saline, and group II received CCl_4 dissolved in olive oil (2 mL/kg, 10% *v/v*) intraperitoneally (ip). Rutin or quercetin, dissolved in 5% (*v/v*) DMSO, was administered ip at 10, 50, and 150 mg/kg (groups III, IV, and V, respectively) and 50 mg/kg (group VI), respectively, once daily for five consecutive days. Immediately after the last dose, the mice were given CCl_4. The doses of rutin were selected on the basis of our preliminary studies (data not shown), whereas the middle dose of quercetin (50 mg/kg) was used for the comparison with rutin. The mice were sacrificed 24 h after the injection of CCl_4. Blood was collected by cardiac puncture, and heparinized plasma was separated for the determination of the ALT and AST activities. The gall bladder was removed, and the liver was carefully excised, washed with saline, blotted dry and divided into samples. The tissue specimens were snap frozen in liquid nitrogen and stored at -80 °C if not used on the same day. The liver samples were used to assess the Cu/Zn SOD activity, GSH and protein concentration and also for immunoblotting. Portions of the livers were immersed in 4% paraformaldehyde for histology and immunohistochemistry.

Determination of hepatotoxicity

The activity of transaminases (ALT and AST) in plasma was measured using a Bio-Tek EL808 Ultra Microplate Reader (BioTek Instruments, Winooski, VT, USA) according to the manufacturer's instructions.

Measurement of oxidative stress

Mouse livers were homogenized in 50 mmol/L phosphate buffer saline (PBS), pH 7.4, using a Polytron homogenizer (Kinematica, Lucerne, Switzerland). The supernatants were separated by centrifugation at 15000×*g* for 20 min at 4 °C (Beckman L7-65 Ultracentrifuge, Beckman, Fullerton, CA, USA) and used to measure the Cu/Zn SOD activity and GSH content. The Cu/Zn SOD activity was determined as described previously[3]. The GSH content was evaluated according to Anderson[21], with modifications. Briefly, the supernatants were deproteinized with 1.25 mol/L metaphosphoric acid and centrifuged at 5000×*g* for 10 min at room temperature (Rotina 420R, Andreas Hettich GmbH, Tuttlingen, Germany). Then, 25 μL of the deproteinized sample was mixed in a cuvette with 700 μL of 0.3 mmol/L NADPH in PBS, 100 μL of 6 mmol/L DTNB and water to give a final volume of 1.0 mL. The reaction was started by the addition of 10 μL of GR (50 units/mL), and the absorbance was monitored at 405 nm for 25 min. The GSH concentration in the samples was determined using the standard curve generated with different GSH solutions under the same condition. The protein content in the liver homogenates was estimated by the Bradford method[22].

Histopathology

Paraformaldehyde-fixed tissues were processed routinely, embedded in paraffin, sectioned, deparaffinized and rehydrated using standard techniques[23]. Hepatocellular necrosis was evaluated by measuring the size of the necrotic area in hematoxylin and eosin (H&E) stained liver sections. The necrotic areas were manually selected, and their size was determined using Cell F v3.1 software (Olympus Soft Imaging Solutions, Münster, Germany).

Immunohistochemistry

For immunohistochemistry, 4-μm thick liver tissue sections were used, as described elsewhere[3]. Briefly, the slides were deparaffinized using xylene and washed with ethanol. The liver slices were incubated overnight with antibodies against TNF-α (diluted 1:50), NF-κB (diluted 1:1000) and iNOS, 3-NT, Nrf2, and TGF-β1 (diluted 1:100). The detection of antibodies was performed using DAKO EnVision+ System, Peroxidase/

DAB kit (DAKO Corporation, Carpinteria, CA, USA). Later, the slides were counterstained with hematoxylin, dehydrated using graded ethanol and xylene and mounted with Entelan. The expression profile and cellular localization of NF-κB, iNOS, Nrf2, and 3-NT were analyzed by light microscopy (Olympus BX51, Tokyo, Japan). The relative staining intensity was analyzed with ImageJ software (National Institutes of Health, Bethesda, MD, USA)[23].

Immunoblotting

The liver samples were lysed in radioimmunoprecipitation assay (RIPA) buffer containing 50 mmol/L Tris-HCl, pH 7.4, 150 mmol/L NaCl, 1% NP-40, 0.5% sodium deoxycholate, 0.1% SDS, 2 mmol/L PMSF, 1 mmol/L sodium orthovanadate and 2 μg/mL each of aprotinin, leupeptin and pepstatin. Volumes equivalent to 50 μg of proteins were loaded onto a 12% polyacrylamide gel. After electrophoresis, the gels were blotted onto a polyvinylidene fluoride membrane (Roche Diagnostics GmbH, Mannheim, Germany). After the protein transfer, the membranes were blocked overnight with a milk blocking reagent (Santa Cruz Biotechnology, Santa Cruz, CA, USA) at 4 °C. TNF-α, COX-2, and HO-1 were visualized by the addition of their respective antibodies, followed by peroxidase-labeled goat anti-mouse or anti-rat antibodies (Amersham Pharmacia Biotech, Uppsala, Sweden). β-Actin was used as a control for protein loading. The membranes were washed with Tris-buffered saline containing 0.1% Tween 20 (TBST), pH 7.6, incubated with Amersham ECL Prime (GE Healthcare, Uppsala, Sweden) for 5 min and exposed to X-ray film (Ortho CP-G Plus film, Agfa-Gevaert NV, Belgium) for 1 min.

Statistical analysis

The data were analyzed using StatSoft STATISTICA version 7.1 and Microsoft Excel 2000 software. Differences between the groups were assessed by a one-way ANOVA and Dunnett's *post hoc* test. The values in the text are mean±standard deviation (SD). For the *in vitro* studies, the concentration of samples that provide 50% inhibition (IC_{50}) was obtained by interpolation from a linear regression analysis. Differences from $P<0.05$ were considered statistically significant.

Results

In vitro antioxidant activity

The ability of the tested samples to reduce iron (III) and scavenge $DPPH^{\cdot}$ and $NO^{\cdot}$ was assessed on the basis of their IC_{50} values. Figure 2A shows the plot of the reducing power of rutin and quercetin compared with Trolox as a reference antioxidant. Quercetin exhibited the most powerful effect (IC_{50}=2.42 μg/mL) compared with rutin (IC_{50}=7.18 μg/mL) and Trolox (IC_{50}=6.66 μg/mL) ($P<0.05$). Quercetin also showed the most effective $DPPH^{\cdot}$ and $NO^{\cdot}$ radical scavenging activity (IC_{50}=0.56 μg/mL and 4.04±1.03 μg/mL, respectively), which was significantly stronger ($P<0.05$) than that of both rutin (IC_{50}=2.07 μg/mL and 9.32±1.24 μg/mL, respectively) and Trolox (IC_{50}=1.11 μg/mL and 8.51±1.03 μg/mL, respectively) (Figure 2B and 2C). Similarly, the total antioxidant capacity of quercetin (Figure 2D) was higher than that of rutin ($P<0.05$).

Liver weight and plasma activity of transaminases

The relative liver weight in CCl_4-intoxicated mice decreased compared with that in the controls. Rutin dose-dependently prevented liver weight loss significantly more than quercetin at the equivalent dose. The plasma AST and ALT activities significantly increased 24 h after CCl_4-intoxication ($P<0.05$). Treatment with rutin decreased the activity of these transaminases in a dose-dependent manner (Table 1). However, quercetin showed a less protective effect against hepatocellular damage than rutin at the equivalent dose.

Effect of rutin and quercetin on hepatic oxidative stress

Our results showed that CCl_4 administration induced oxidative stress in mouse livers. The Cu/Zn SOD activity and GSH concentration were significantly lower compared with the control group (Table 1) ($P<0.05$). Treatment with rutin elevated the Cu/Zn SOD activity and GSH concentration in a dose-dependent manner. Quercetin at 50 mg/kg significantly attenuated the decrease in the oxidative stress markers in CCl_4-intoxicated mice, restoring Cu/Zn SOD activity more potently than rutin at 50 mg/kg ($P<0.05$).

Table 1. Effect of CCl_4, rutin and quercetin on relative liver weight, plasma transaminase activity and oxidative stress markers in mice liver.

Group		Relative liver weight (g/100 g)	AST (U/L)	ALT (U/L)	Cu/Zn SOD (U/g protein)	GSH (μmol/g liver)
I	Control	5.7±0.4	41.4±8.6	16.1±1.2	14.4±0.7	7.5±0.5
II	CCl_4	4.7±0.6[b]	3261±365[b]	5208±466[b]	8.1±0.5[b]	3.7±0.3[b]
III	CCl_4+rutin 10 mg/kg	4.9±0.5	3241±319	5066±205	8.5±0.5	4.2±0.6
IV	CCl_4+rutin 50 mg/kg	5.3±0.6	990±143[e]	2190±56[e]	10.8±1.1[e]	5.5±0.8[e]
V	CCl_4+rutin 150 mg/kg	5.8±0.7[e]	226±74[e]	662±98[e]	13.6±0.9[e]	5.8±0.6[e]
VI	CCl_4+quercetin 50 mg/kg	5.1±0.4	1621±74[eh]	3892±294[eh]	14.3±0.7[eh]	6.3±0.7[e]

Mice were treated with rutin or quercetin intraperitoneally (ip) once daily for five consecutive days. Immediately after the last dose, mice received CCl_4 dissolved in olive oil (10% *v/v*, 2 mg/kg), ip, except the control group that received saline. Relative liver weights were expressed as liver weight/100 g of body weight. Each value represents the mean±SD for five mice. [b]$P<0.05$, CCl_4-intoxication *vs* control. [e]$P<0.05$, rutin and quercetin treatment *vs* CCl_4-intoxication. [h]$P<0.05$, rutin 50 mg/kg *vs* quercetin 50 mg/kg.

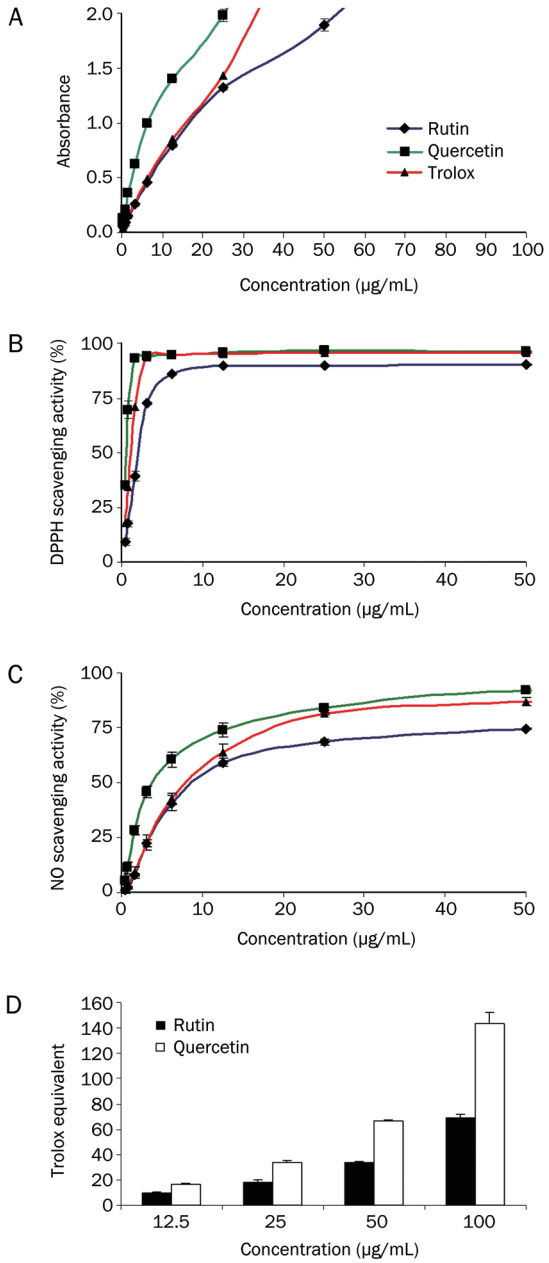

Figure 2. Evaluation of the *in vitro* antioxidant properties of rutin and quercetin. (A) Reducing power, (B) DPPH˙ radical scavenging effect, (C) NO˙ radical scavenging effect and (D) total antioxidant activity of rutin and quercetin. Each value represents the mean±SD from three independent measurements.

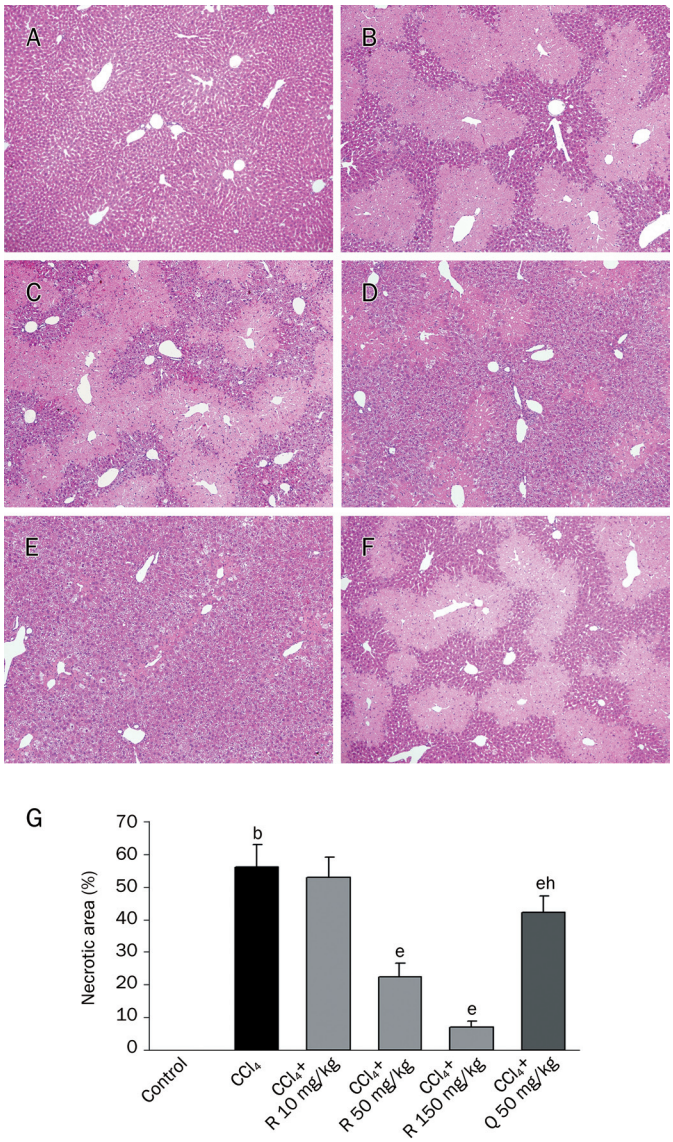

Figure 3. Representative hematoxylin and eosin stained sections of livers from experimental mice. (A) Control group. (B) CCl_4-intoxicated mice. (C–F) Mice treated with CCl_4 and protected with rutin (R) at 10 mg/kg, 50 mg/kg and 150 mg/kg and with quercetin (Q) at 50 mg/kg. Original magnification ×100, insets ×400. (G) Measurement of the size of the necrotic areas (n=5). ^{b}P<0.05, CCl_4-intoxication *vs* control. ^{e}P<0.05, rutin and quercetin treatment *vs* CCl_4-intoxication. ^{h}P<0.05, 50 mg/kg rutin *vs* 50 mg/kg quercetin.

Amelioration of histopathological changes by rutin and quercetin in the liver

Representative images of histological sections from the experimental groups are shown in Figure 3. The livers of the control mice showed a normal morphology and architecture (Figure 3A). In the CCl_4-intoxicated mice, severe hepatic damage with a massive centrilobular necrosis was detected (Figure 3B). In the livers of mice treated with rutin at 10 mg/kg, no histological improvement was found (Figure 3C). Rutin at 50 mg/kg markedly reduced the size of the hepatic necrotic areas (Figure 3D), whereas the high-dose rutin (150 mg/kg) almost completely prevented hepatocellular damage (Figure 3E). In mice treated with quercetin at 50 mg/kg, larger necrotic areas were present than in the livers of mice treated with rutin at the equivalent dose (Figure 3F and 3G).

Amelioration of hepatic inflammation by rutin and quercetin

To determine whether rutin or quercetin could reverse the acute liver inflammation induced by CCl_4, we analyzed pro-

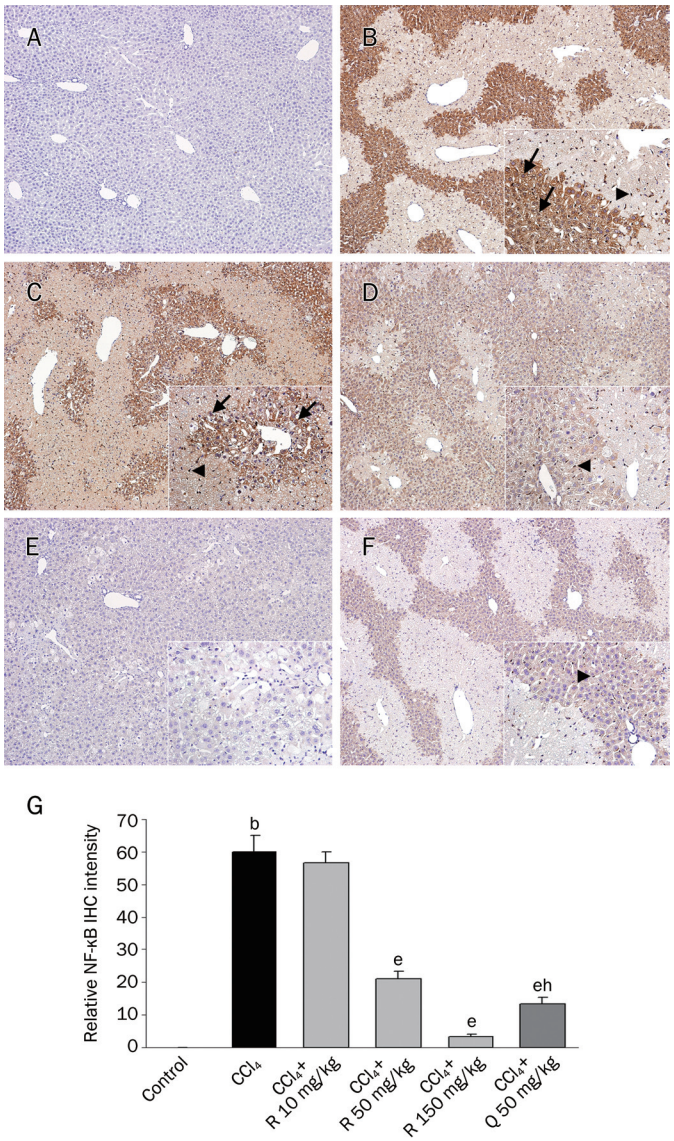

Figure 4. NF-κB immunostaining in liver sections. (A) Control group. (B) CCl_4-intoxicated mice. (C–F) Mice treated with CCl_4 and protected with rutin (R) at 10, 50, and 150 mg/kg and with quercetin (Q) at 50 mg/kg. The arrows show NF-κB p65-positive hepatocyte nuclei, and the arrowheads show NF-κB p65-positive Kupffer cells. Original magnification ×100, insets ×400. Representative results from five mice. (G) Measurement of NF-κB immunostaining intensity (n=5). ^{b}P<0.05, CCl_4-intoxication *vs* control; ^{e}P<0.05, rutin and quercetin treatment *vs* CCl_4-intoxication; ^{h}P<0.05, 50 mg/kg rutin *vs* 50 mg/kg quercetin.

teins involved in the proinflammatory response, such as NF-κB, TNF-α, and COX-2. The livers of control mice were NF-κB immunonegative (Figure 4A). In contrast, strong NF-κB immunoreactivity was detected in the CCl_4-treated mice (Figure 4B). Immunohistochemical analysis revealed NF-κB p65 localization in both the cytoplasm and the nucleus of hepatocytes and in Kupffer cells. The low-dose rutin treatment (10 mg/kg) did not substantially affect NF-κB immunopositivity (Figure 4C). However, the higher doses of rutin, 50 and 150 mg/kg, gradually decreased NF-κB expression and prevented the accumulation of NF-κB p65 in the nuclei (Figure 4D and 4E). Quercetin had a more pronounced effect on NF-κB suppression than rutin at the equivalent dose (Figure 4F and 4G). CCl_4 administration also increased the hepatic levels of TNF-α and COX-2 (Figure 5). Rutin dose-dependently reduced both TNF-α and COX-2 expression compared with the CCl_4-treated mice. Similarly to NF-κB, quercetin more effectively suppressed TNF-α and COX-2 expression than rutin at the equivalent dose.

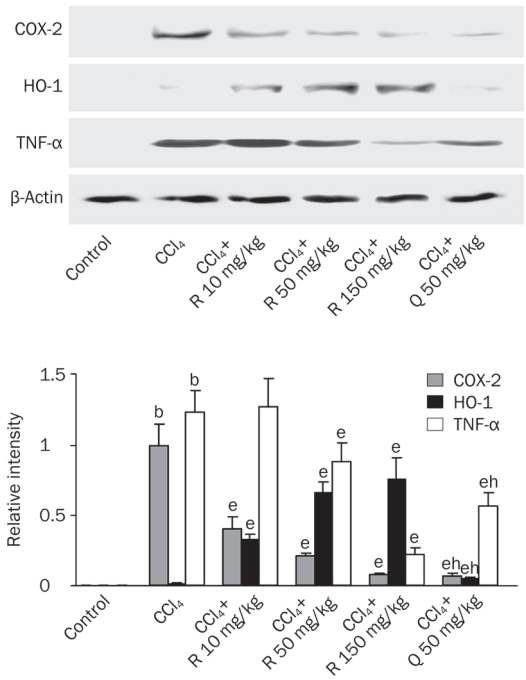

Figure 5. Western blot analysis of TNF-α, COX-2, and HO-1 in mouse livers. Representative results from five mice. Quantification of band intensity relative to β-actin intensity is shown below the Western blot. ^{b}P<0.05, CCl_4-intoxication *vs* control. ^{e}P<0.05, rutin and quercetin treatment *vs* CCl_4-intoxication. ^{h}P<0.05, 50 mg/kg rutin *vs* 50 mg/kg quercetin. R, rutin; Q, quercetin.

Effect of rutin and quercetin on hepatic nitrosative stress

The analysis of the hepatic expression of iNOS and the formation of the $NO^{\cdot}$-dependent product, 3-NT, revealed no immunopositivity in the control mice (Figure 6A and 7A). CCl_4 administration induced a strong expression of iNOS and 3-NT (Figure 6B and 7B). Rutin dose-dependently reduced the iNOS (Figure 6C, 6D, and 6E) and 3-NT (Figure 7C, 7D, and 7E) immunopositivity compared with the CCl_4-treated mice. However, quercetin was less effective than rutin in the reduction of both iNOS (Figure 6F and 6G) and 3-NT (Figure 7F and 7G) immunoreactivity.

Induction of the Nrf2/HO-1 pathway in the liver by rutin and quercetin

The hepatic expression of HO-1 (Figure 5), the cytoprotective

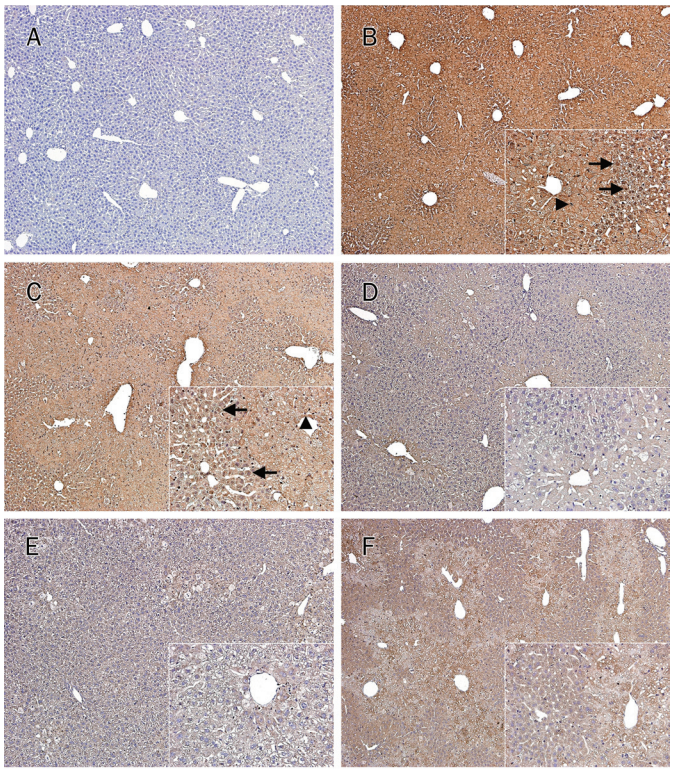

Figure 6. Immunohistochemical analysis of iNOS expression in mouse livers. (A) Control group. (B) CCl_4-intoxicated mice. (C–F) Mice treated with CCl_4 and protected with rutin (R) at 10, 50, and 150 mg/kg and with quercetin (Q) at 50 mg/kg. The arrows show iNOS-positive hepatocyte nuclei, and the arrowheads show iNOS-positive Kupffer cells. Original magnification ×100, insets ×400. Representative results from five mice. (G) Measurement of iNOS immunostaining intensity (n=5). ^{b}P<0.05, CCl_4-intoxication *vs* control. ^{e}P<0.05, rutin and quercetin treatment *vs* CCl_4-intoxication. ^{h}P<0.05, 50 mg/kg rutin *vs* 50 mg/kg quercetin.

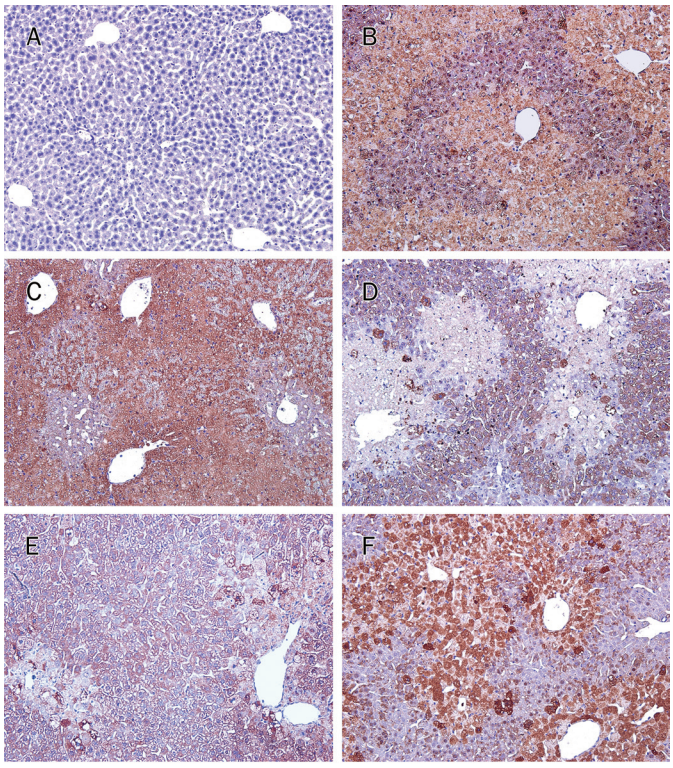

Figure 7. Immunohistochemical detection of 3-NT production in mouse livers. (A) Control group. (B) CCl_4-intoxicated mice. (C–F) Mice treated with CCl_4 and protected with rutin (R) at 10, 50, and 150 mg/kg and with quercetin (Q) at 50 mg/kg. Original magnification ×200. Representative results from 5 mice. (G) Measurement of 3-NT immunostaining intensity (n=5). ^{b}P<0.05, CCl_4-intoxication vs control. ^{e}P<0.05, rutin and quercetin treatment *vs* CCl_4-intoxication. ^{h}P<0.05, 50 mg/kg rutin *vs* 50 mg/kg quercetin.

enzyme that plays a critical role in the response to stressful conditions, and Nrf2, its upstream inducer[24], is shown in Figure 8. The livers of control mice were Nrf2 immunonegative (Figure 8A). The livers of CCl_4-intoxicated mice were weakly Nrf2 immunopositive (Figure 8B). However, the treatment with rutin resulted in a marked dose-dependent induction of Nrf2 (Figure 8C, 8D, and 8E) in the cytoplasm and nucleus of hepatocytes and Kupffer cells. Nrf2 immunoreactivity in hepatocytes of mice treated with quercetin (Figure 8F) markedly increased compared with the CCl_4 group but was less expressed compared with mice receiving rutin at the equivalent dose (Figure 8G). Similarly, rutin dose-dependently increased the hepatic HO-1 levels compared with CCl_4-treated mice, whereas quercetin was a less potent up-regulator of HO-1 than rutin at the equivalent dose (Figure 5).

Antifibrotic potential of rutin and quercetin in the liver

The livers of control mice did not show substantial TGF-β1 immunopositivity (Figure 9A). In contrast, TGF-β1 was over-

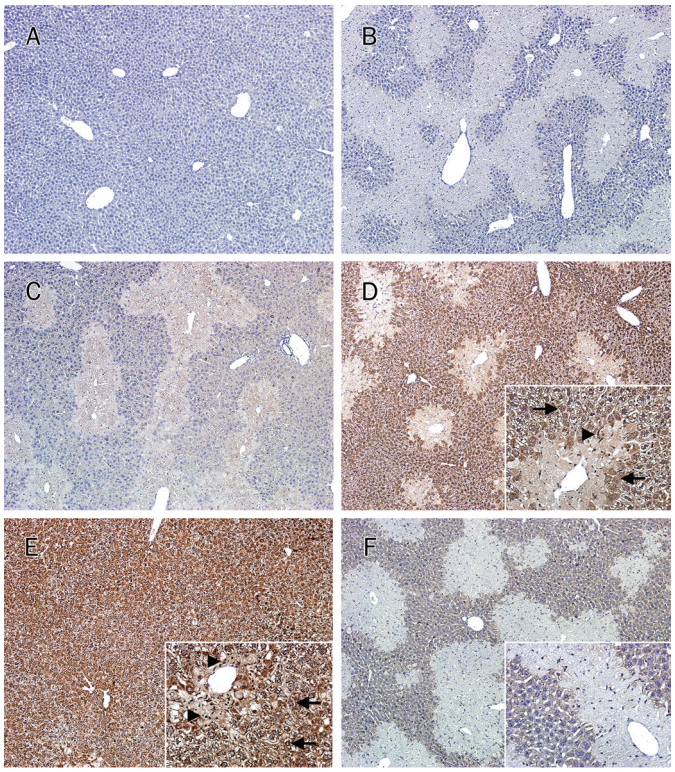

Figure 8. Immunohistochemical detection of Nrf2 expression in mouse livers. (A) Control group. (B) CCl_4-intoxicated mice. (C–F) Mice treated with CCl_4 and protected with rutin (R) at 10, 50, and 150 mg/kg and with quercetin (Q) at 50 mg/kg. The arrows show Nrf2-positive hepatocyte nuclei, and the arrowheads show Nrf2-positive Kupffer cells. Original magnification ×100, insets ×400. Representative results from five mice. (G) Measurement of Nrf2 immunostaining intensity (n=5). ^{b}P<0.05, CCl_4-intoxication *vs* control. ^{e}P<0.05, rutin and quercetin treatment *vs* CCl_4-intoxication. ^{h}P<0.05, 50 mg/kg rutin *vs* 50 mg/kg quercetin.

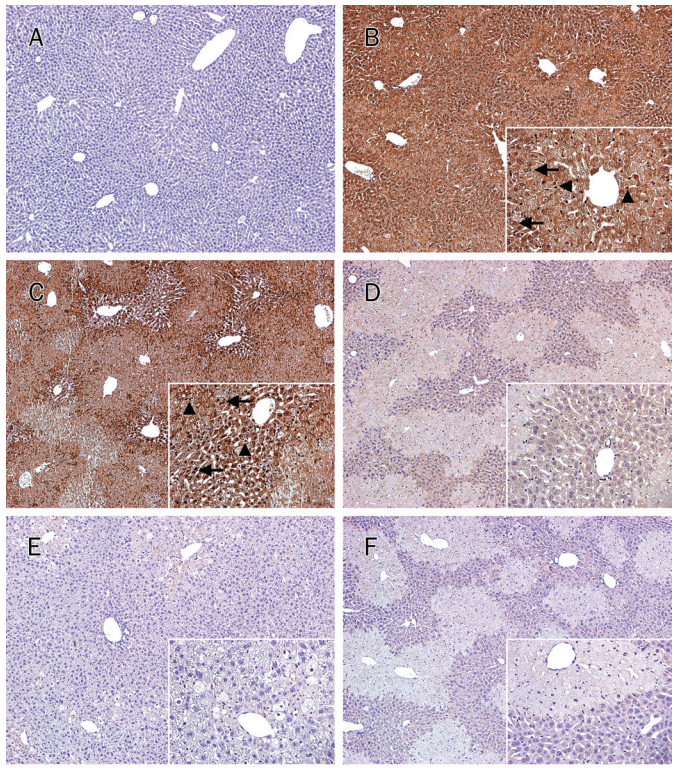

Figure 9. Immunohistochemistry of TGF-β1 expression in mouse livers. (A) Control group. (B) CCl_4-intoxicated mice. (C–F) Mice treated with CCl_4 and protected with rutin (R) at 10, 50, and 150 mg/kg and with quercetin (Q) at 50 mg/kg. The arrows show TGF-β1-positive hepatocyte nuclei, and the arrowheads show TGF-β1-positive Kupffer cells. Original magnification ×100, insets ×400. Representative results from five mice. (G) Measurement of TGF-β1 immunostaining intensity (n=5). ^{b}P<0.05, CCl_4-intoxication *vs* control. ^{e}P<0.05, rutin and quercetin treatment *vs* CCl_4-intoxication. ^{h}P<0.05, 50 mg/kg rutin *vs* 50 mg/kg quercetin.

expressed in the livers of CCl_4-intoxicated mice (Figure 9B). The administration of rutin dose-dependently ameliorated TGF-β1 expression (Figure 9C, 9D, and 9E). However, the hepatic TGF-β1 immunoreactivity in mice treated with quercetin (Figure 9F) was significantly lower than that in mice receiving rutin at the equivalent dose (Figure 9G) (P<0.05).

Discussion

The results of the present study suggest the importance of the sugar moiety in position 3 of the C ring for the specific pharmacological activities of rutin and quercetin. The glycosylation of flavonoids reduces their antioxidant activity compared with their corresponding aglycones[25]. Our results showed that quercetin possessed higher reducing power and DPPH$^{\cdot}$ and NO$^{\cdot}$ free radical scavenging abilities *in vitro* compared with rutin. Quercetin more potently prevented the decrease in Cu/Zn SOD activity in mouse livers. However, it was less effective in the amelioration of protein nitrosylation, suggesting

that the *in vitro* free radical scavenging ability of compounds does not necessary correlate with their *in vivo* efficacy, which indicates that absorption and/or metabolism are key modulators of *in vivo* activity[26]. Additionally, the hepatic lesions and necrosis induced by CCl_4 were markedly reduced in mice treated with rutin, whereas quercetin was less effective. The results of the current study showed that the amelioration of hepatic necrosis was closely related to the reduction of nitrosative but not oxidative stress.

Reactive oxygen species (ROS) generated during CCl_4 intoxication may induce NF-κB activation and consequently stimulate the production of cytotoxic and proinflammatory cytokines, such as TNF-α[27]. Our results showed that rutin, and more potently quercetin, suppressed both NF-κB and TNF-α expression in injured livers. NF-κB is also involved in the regulation of COX-2 and iNOS gene expression by binding to their promoter regions[28]. COX-2 and iNOS exert a prominent role under inflammatory conditions by producing prostaglandins and $NO^{\cdot}$, respectively[29, 30]. Thus, the anti-inflammatory effect of quercetin and rutin in CCl_4-injured liver could be attributed to the inhibition of the NF-κB pathway, which is in agreement with previous findings[31]. Additionally, the increased $NO^{\cdot}$ synthesis and superoxide generation could result in the formation of peroxynitrite[32] and nitration of protein tyrosine residues[33], which actively contribute to the development of hepatic necrosis[34]. In this study, the activation and nuclear accumulation of NF-κB p65 in CCl_4-intoxicated mice coincided with COX-2 and iNOS overexpression, which was prevented by both flavonoids. The nuclear presence of COX-2 and iNOS suggests their involvement in the regulation of some nuclear functions. However, rutin exhibited lower potency in reducing COX-2 expression compared with quercetin, which is in agreement with previous findings[35]. Interestingly, rutin more effectively suppressed the expression of both iNOS and 3-NT compared with quercetin. The latter coincided with the amelioration of hepatic necrosis. These findings agree with Raghav *et al*[36], who showed a stronger inhibition of iNOS than COX-2 gene expression by rutin in murine macrophages.

TGF-β, a pleiotrophic growth factor, has been shown to stimulate fibroblast proliferation and increase the synthesis of ECM proteins[37]. Previously, we showed that the fibrogenic potential of the CCl_4-injured liver is closely related to TGF-β1 expression[38]. In the current study, TGF-β1 expression markedly increased in both hepatocytes and non-parenchymal cells of the CCl_4-intoxicated liver. Although Kupffer cells and HSCs are considered the main sources of TGF-β[39], hepatocytes may also produce TGF-β. In cultured hepatocytes, latent TGF-β was rapidly detectable during culture due to demasking of the mature TGF-β by calpains[40]. The nuclear presence of TGF-β1 could be attributed to increased nuclear membrane permeability during the activation of apoptosis[41]. Our results showed that treatment with both flavonoids markedly ameliorated the overexpression of TGF-β1, suggesting the reduction of the fibrogenic potential in the liver.

HO-1, the inducible isoform of heme oxygenase, plays a critical role in cell protection against acute and chronic liver injury[42]. The transcription factor Nrf2 is considered a key regulator of HO-1 expression[24]. In the current study, hepatic injury was associated with low expression of HO-1 and its upstream inducer Nrf2 but with high expression of NF-κB. The treatments with rutin and, to a lesser extent, quercetin were associated with increased Nrf2 and HO-1 expression in the liver, which coincided with the suppression of NF-κB activation. Most recently, Liu *et al*[43] showed that quercetin acts as an inducer of HO-1 in primary rat hepatocytes. Interestingly, the induction of HO-1 was found in quercetin-treated but not in rutin-treated rat glioma C6 cells[44] and in the hydrogen peroxide-induced apoptosis of RAW264.7 macrophages[45]. However, rutin acted as a strong HO-1 inducer in a rat model of liver ischemia-reperfusion injury[46], suggesting a cell type-dependent activation of this enzyme. Additionally, the nuclear translocation of HO-1 could be involved in the regulation of genes responsible for cytoprotection against oxidative stress[47].

In conclusion, the results of this study demonstrate that rutin and quercetin can ameliorate acute liver damage by at least four mechanisms: acting as scavengers of free radicals, inhibiting NF-κB activation and the inflammatory response, exerting antifibrotic potential and inducing the Nrf2/HO-1 pathway. The rutinoside moiety in position 3 of the C ring could be responsible for more pronounced protective effects against iNOS induction, nitrosative stress and hepatocellular necrosis. The aglycone quercetin exerted higher antioxidant and anti-inflammatory activities and antifibrotic potential than rutin. The antioxidant actions of rutin and quercetin were partially responsible for their beneficial effects in injured liver tissue. However, the antioxidant properties of these flavonoids cannot solely explain the stronger protective activity of rutin against hepatocellular damage. Thus, the modulation of signaling pathways emerges as an important mode of action of these flavonoids, which should be considered as a specific therapeutic strategy. The application of these flavonoids in medical practice should be further confirmed by conveying preliminary placebo-controlled clinical studies.

Acknowledgements

This research was supported by the Ministry of Science, Education and Sport, Republic of Croatia (projects 062-0000000-3554 and 006-0061117-1238).

Author contribution

Robert DOMITROVIĆ designed the research and wrote the paper; Hrvoje JAKOVAC, Vanja VASILJEV MARCHESI, Sanda VLADIMIR-KNEŽEVIĆ, Olga CVIJANOVIĆ, and Žarko TADIĆ performed the research; Željko ROMIĆ contributed new reagents and analytic tools; and Dario RAHELIĆ analyzed the data.

References

1 Gimson AE. Fulminant and late onset hepatic failure. Br J Anaesth 1996; 77: 90–8.

2 Brattin WJ, Glende EA Jr, Recknagel RO. Pathological mechanisms in carbon tetrachloride hepatotoxicity. J Free Radic Biol Med 1985; 1: 27–38.
3 Domitrović R, Jakovac H, Blagojević G. Hepatoprotective activity of berberine is mediated by inhibition of TNF-α, COX-2, and iNOS expression in CCl_4-intoxicated mice. Toxicology 2011; 280: 33–43.
4 Tipoe GL, Leung TM, Liong EC, Lau TY, Fung ML, Nanji AA. Epigallocatechin-3-gallate (EGCG) reduces liver inflammation, oxidative stress and fibrosis in carbon tetrachloride (CCl_4)-induced liver injury in mice. Toxicology 2010; 273: 45–52.
5 Erlund I, Kosonen T, Alfthan G, Maenpaa J, Perttunen K, Kenraali J, *et al*. Pharmacokinetics of quercetin from quercetin aglycone and rutin in healthy volunteers. Eur J Clin Pharmacol 2000; 56: 545–53.
6 Kandaswami C, Middleton E. Free radical scavenging and antioxidant activity of plant flavonoids. Adv Exp Med Biol 1994; 366: 351–76.
7 Rotelli AE, Guardia T, Juárez AO, de la Rocha NE, Pelzer LE. Comparative study of flavonoids in experimental models of inflammation. Pharmacol Res 2003; 48: 601–6.
8 Araújo JR, Gonçalves P, Martel F. Chemopreventive effect of dietary polyphenols in colorectal cancer cell lines. Nutr Res 2011; 31: 77–87.
9 Kwon KH, Murakami A, Tanaka T, Ohigashi H. Dietary rutin, but not its aglycone quercetin, ameliorates dextran sulfate sodium-induced experimental colitis in mice: attenuation of proinflammatory gene expression. Biochem Pharmacol 2005; 69: 395–406.
10 Kwon KH, Murakami A, Ohigashi H. Suppressive effects of natural and synthetic agents on dextran sulfate sodium-induced interleukin-1β release from murine peritoneal macrophages. Biosci Biotechnol Biochem 2004; 68: 436–9.
11 Comalada M, Camuesco D, Sierra S, Ballester I, Xaus J, Gálvez J, *et al*. *In vivo* quercitrin anti-inflammatory effect involves release of quercetin, which inhibits inflammation through down-regulation of the NF-κB pathway. Eur J Immunol 2005; 35: 584–92.
12 Chaudhary A, Willett KL. Inhibition of human cytochrome CYP 1 enzymes by flavonoids of St. John's wort. Toxicology 2006; 217: 194–205.
13 Janbaz KH, Saeed SA, Gilani AH. Studies on the protective effects of caffeic acid and quercetin on chemical-induced hepatotoxicity in rodents. Phytomedicine 2004; 11: 424–30.
14 Janbaz KH, Saeed SA, Gilani AH. Protective effect of rutin on paracetamol- and CCl_4-induced hepatotoxicity in rodents. Fitoterapia 2002; 73: 557–63.
15 Oyaizu M. Studies on products of browning reaction. Antioxidative activities of products of browning reaction prepared from glucosamine. Jpn J Nutr 1986; 44: 307–15.
16 Vladimir-Knežević S, Blažeković B, Štefan MB, Alegro A, Koszegi T, Petrik J. Antioxidant activities and polyphenolic contents of three selected *Micromeria* species from Croatia. Molecules 2011; 16: 1454–70.
17 Blois MS. Antioxidant determinations by the use of a stable free radical. Nature 1958; 181: 1199–200.
18 Domitrović R, Jakovac H, Romić Ž, Rahelić D, Tadić Ž. Antifibrotic activity of *Taraxacum officinale* root in carbon tetrachloride-induced liver damage in mice. J Ethnopharmacol 2010; 130: 569–77.
19 Prieto P, Pineda M, Aguilar M. Spectrophotometric quantitation of antioxidant capacity through the formation of a phosphomolybdenum complex: Specific application to the determination of vitamin E. Anal Biochem 1999; 269: 337–41.
20 Rai S, Wahile A, Mukherjee K, Saha BP, Mukherjee PK. Antioxidant activity of *Nelumbo nucifera* (sacred lotus) seeds. J Ethnopharmacol 2006; 104: 322–7.
21 Anderson ME. Determination of glutathione and glutathione disulfide in biological samples. Methods Enzymol 1985; 113: 548–55.
22 Bradford MM. A rapid and sensitive method for the quantitation of microgram quantities of protein utilizing the principle of protein-dye binding. Anal Biochem 1976; 72: 248–54.
23 Domitrović R, Jakovac H, Marchesi VV, Šain I, Romić Z, Rahelić D. Preventive and therapeutic effects of oleuropein against carbon tetrachloride-induced liver damage in mice. Pharmacol Res 2012; 65: 451–64.
24 Yang YC, Lii CK, Lin AH, Yeh YW, Yao HT, Li CC, *et al*. Induction of glutathione synthesis and heme oxygenase 1 by the flavonoids butein and phloretin is mediated through the ERK/Nrf2 pathway and protects against oxidative stress. Free Radic Biol Med 2011; 51: 2073–81.
25 Rice-Evans CA, Miller NJ, Paganga G. Structure-antioxidant activity relationships of flavonoids and phenolic acids. Free Radic Biol Med 1996; 20: 933–56.
26 Reyes-Gordillo K, Segovia J, Shibayama M, Vergara P, Moreno MG, Muriel P. Curcumin protects against acute liver damage in the rat by inhibiting NF-κB, proinflammatory cytokines production and oxidative stress. Biochim Biophys Acta 2007; 1770: 989–96.
27 Surh YJ, Chun KS, Cha HH, Han SS, Keum YS, Park KK, *et al*. Molecular mechanisms underlying chemopreventive activities of anti-inflammatory phytochemicals: down-regulation of COX-2 and iNOS through suppression of NF-κB activation. Mutat Res 2001; 480-481: 243–68.
28 Vane JR, Botting RM. Anti-inflammatory drugs and their mechanism of action. Inflamm Res 1998; 47 Suppl 2: 78–87.
29 Vodovotz Y, Kim PK, Bagci EZ, Ermentrout GB, Chow CC, Bahar I, *et al*. Inflammatory modulation of hepatocyte apoptosis by nitric oxide: *in vivo*, *in vitro*, and *in silico* studies. Curr Mol Med 2004; 4: 753–62.
30 Wu CH, Wu CF, Huang HW, Jao YC, Yen GC. Naturally occurring flavonoids attenuate high glucose-induced expression of proinflammatory cytokines in human monocytic THP-1 cells. Mol Nutr Food Res 2009; 53: 984–95.
31 Park HH, Lee S, Son HY, Park SB, Kim MS, Choi EJ, *et al*. Flavonoids inhibit histamine release and expression of proinflammatory cytokines in mast cells. Arch Pharm Res 2008; 31: 1303–11.
32 Pryor WA, Squadrito GL. The chemistry of peroxynitrite: A product from the reaction of nitric oxide with superoxide. Am J Physiol 1995; 268: L699–722.
33 Beckman JS. Oxidative damage and tyrosine nitration from peroxynitrite. Chem Res Toxicol 1996; 9: 836–44.
34 Jaeschke H, Gores GJ, Cederbaum AI, Hinson JA, Pessayre D, Lemasters JJ. Mechanisms of hepatotoxicity. Toxicol Sci 2002; 65: 166–76.
35 Jones DJL, Lamb JH, Verschoyle RD, Howells LM, Butterworth M, Lim CK, *et al*. Characterisation of metabolites of the putative cancer chemopreventive agent quercetin and their effect on cyclo-oxygenase activity. Br J Cancer 2004; 91: 1213–9.
36 Raghav SK, Gupta B, Agrawal C, Goswami K, Das HR. Anti-inflammatory effect of *Ruta graveolens* L in murine macrophage cells. J Ethnopharmacol 2006; 104: 234–9.
37 Cutroneo KR. TGF-beta-induced fibrosis and SMAD signaling: oligo decoys as natural therapeutics for inhibition of tissue fibrosis and scarring. Wound Repair Regen 2007; 15: S54–60.
38 Domitrović R, Jakovac H. Antifibrotic activity of anthocyanidin delphinidin in carbon tetrachloride-induced hepatotoxicity in mice. Toxicology 2010; 272:1–10.
39 Reeves HL, Friedman SL. Activation of hepatic stellate cells-a key issue in liver fibrosis. Front Biosci 2002; 7: d808–26.
40 Gressner OA, Lahme B, Siluschek M, Rehbein K, Herrmann J,

Weiskirchen R, *et al*. Activation of TGF-β within cultured hepatocytes and in liver injury leads to intracrine signaling with expression of connective tissue growth factor. J Cell Mol Med 2008; 12: 2717–30.

41 Ferrando-May E, Cordes V, Biller-Ckovrić I, Mirković J, Görlich D, Nicotera P. Caspases mediate nucleoporin cleavage, but not early redistribution of nuclear transport factors and modulation of nuclear permeability in apoptosis. Cell Death Differ 2001; 8: 495–505.

42 Sass G, Barikbin R, Tiegs G. The multiple functions of heme oxygenase-1 in the liver. Z Gastroenterol 2012; 50: 34–40.

43 Liu S, Hou W, Yao P, Li N, Zhang B, Hao L, *et al*. Heme oxygenase-1 mediates the protective role of quercetin against ethanol-induced rat hepatocytes oxidative damage. Toxicol *In Vitro* 2012; 26: 74–80.

44 Chen TJ, Jeng JY, Lin CW, Wu CY, Chen YC. Quercetin inhibition of ROS-dependent and -independent apoptosis in rat glioma C6 cells. Toxicology 2006; 223: 113–26.

45 Chow JM, Shen SC, Huan SK, Lin HY, Chen YC. Quercetin, but not rutin and quercitrin, prevention of H_2O_2-induced apoptosis via anti-oxidant activity and heme oxygenase 1 gene expression in macrophages. Biochem Pharmacol 2005; 69: 1839–51.

46 Acquaviva R, Lanteri R, Li Destri G, Caltabiano R, Vanella L, Lanzafame S, *et al*. Beneficial effects of rutin and *L*-arginine coadministration in a rat model of liver ischemia-reperfusion injury. Am J Physiol Gastrointest Liver Physiol 2009; 296: G664–70.

47 Lin Q, Weis S, Yang G, Weng YH, Helston R, Rish K, *et al*. Heme oxygenase-1 protein localizes to the nucleus and activates transcription factors important in oxidative stress. J Biol Chem 2007; 282: 20621–33.

Acta Pharmacologica Sinica (2012) 33: 1271–1276
 1671-4083/12 $32.00
www.nature.com/aps

Original Article

High prevalence of the B2+C2 subgenotype mixture in patients with chronic hepatitis B in Eastern China

Jun ZHONG, Yue-qiu GAO*, Xue-hua SUN, Xiao-jun ZHU, Man LI

Shanghai University of Traditional Chinese Medicine Affiliated Shanghai Shuguang Hospital, Department of Infectious Diseases, Key Laboratory of Liver and Kidney Diseases, Shanghai University of Traditional Chinese Medicine, Ministry of Education E-institute of Shanghai Municipal Education Commission, Shanghai 200021, China

Aim: To investigate the prevalence of hepatitis B virus (HBV) genotype mixtures among patients with chronic hepatitis B (CHB) in Eastern China.
Methods: A total of 4908 chronic HBV patients from Eastern China were enrolled. HBV genotypes and subgenotypes were determined using a multiplex PCR technique. Serum viral loads and hepatitis B e antigen (HBeAg) levels detected using real-time fluorescent quantitative PCR and ELISA assay, respectively. The presence of precore/basic core promoter (PC/BCP) mutations was examined with PCR and direct sequencing of the amplified products.
Results: HBV genotypes B, C, D, B+C, and B+D were found in 19.21%, 64.75%, 1.49%, 13.63%, and 0.92% of the patients, respectively. In 669 patients with the genotype mixture B+C, the subgenotypes B2+C2 and B2+C1 accounted for 68.13% and 31.87%, respectively, no other subgenotypes were identified. HBV B+C was more frequent in the patients with moderate CHB than in patients with mild CHB. In patients with moderate CHB, the subgenotype mixture B2+C2 was lower than B2+C1 (51.97% *vs* 63.38%), while the opposite situation was found in patients with severe CHB (22.15% *vs* 15.49%). The highest average viral load was found in patients with the genotype B+C mixture. The prevalence of HBV B2+C2 increased in patients from 50 to 59 years of age and was significantly different from the proportion of patients in the same age group with genotype B (23.2% *vs* 15.2%). A double mutation (G1896A) in the PC was significantly more common in subgenotype B2+C2 than in subgenotype B2+C1.
Conclusion: The HBV B2+C2 subgenotype was prevalent in CH patients with a high HBV replication status and correlated with a more severe course of the disease.

Keywords: liver disease; chronic hepatitis; hepatitis B virus; genotype mixture; subgenotype; mutation; Eastern China

Acta Pharmacologica Sinica (2012) 33: 1271–1276; doi: 10.1038/aps.2012.78; published online 3 Sep 2012

Introduction

Hepatitis B virus (HBV) genotypes have distinct geographical distributions and are associated with different clinical outcomes, prognoses, and responses to interferon treatment[1]. Ten HBV genotypes (A–J) and 34 HBV subgenotypes have been identified to date[2]. In China, subgenotypes B2, C2 and C1 are the most common strains[3–5].

Infection with more than one HBV genotype often results in a genotype mixture, *ie*, co-infection or super-infection with multiple HBV genotypes in an infected patient[2]. With the use of multiplex polymerase chain reaction (PCR), genotype mixtures, including A+C, B+C, C+D, A+B+C, C+E, B+C+D, A+D, and A+B, have frequently been identified in HBV-infected subjects[6–8]. The B+C genotype mixture is common in China[8], and A+D is common in Pakistan[9, 10] and Romania[11]. Subgenotype B2 (formerly Ba) is prevalent throughout Asia, including China, whereas the prevalence of subgenotype B1 (Bj) is restricted to Japan. C1 (Cs) was described in Southern Asia, whereas C2 (Ce) was prevalent in the Far East. In China, the prevalence of genotype mixtures varies in different geographic regions. For example, genotype mixtures account for 10.6% of hepatitis cases in Shanghai[2], 22.7% in Jiangsu province[12], 9.6% in Hubei province[13], 1.6% in Yunnan province[14] and 0.78% in Heilongjiang province[15].

The impact of HBV B+C on the natural course of chronic hepatitis B (CHB) infection and the severity of liver damage is still unknown. Yin *et al* reported that genotype mixtures are associated with higher viral load and a more severe course of the disease than HBV genotype C alone[8]. However, the impact of HBV genotype mixture-related factors, such as

* To whom correspondence should be addressed.
E-mail gaoyueqiu@hotmail.com
Received 2012-01-16 Accepted 2012-05-22

serum viral load and HBeAg expression, on the course of infection and the development of liver disease has not yet been fully characterized.

The aims of the present study were to identify the distribution of HBV genotype mixture in Eastern China and to explore the relationship between genotype mixture and gender, age, clinical spectrum of chronic HBV infection, and viral replicative activity.

Materials and methods

Enrollment of subjects

Clinical diagnosis was based on liver function tests, hepatitis virus markers, autoantibodies, tumor markers, ultrasonography, and liver histopathology. The patients met the following criteria: HbsAg-positive for at least 6 months to establish chronic HBV infection and free from other concomitant causes of liver disease (*eg*, hepatitis C or D, HIV infection, alcohol consumption >60 g/d) or relatively rare liver diseases (*eg*, autoimmune hepatitis and metabolic liver disease). None of the patients used drugs or had hepatotoxin exposure. Serum samples were collected from all inpatients and outpatients with chronic hepatitis B and stored at -80 °C until analysis.

Serum samples

A total of 4908 serum samples were obtained from chronic HBV patients who visited the Shanghai Shuguang Hospital from June 2007 to July 2009. All subjects signed an informed consent form and participated in the study voluntarily. All patients were chronic HBV carriers (seropositive for the HBV surface antigen for at least 6 months) and were seronegative for hepatitis C and hepatitis D. All samples were stored at -80 °C until analysis.

Quantitative detection of HBV DNA

The serum HBV DNA loads in patients with chronic HBV infection were measured with real-time fluorescent quantitative PCR using a LightCycler PCR system (FQD-33A, BIOER, Hangzhou, China) with a lower limit of detection of approximately 1000 viral genome copies/mL. The reverse transcription products were denatured at 94 °C for 5 min, followed by 35 cycles of 94 °C for 20 s, 55 °C for 20 s and 72 °C for 40 s. The handling procedures were performed strictly as described by the instructions in the reagent kit (Shenzhen PG Biotech Co, Ltd, China).

Detection of HBeAg

HBeAg was measured at a virological laboratory using an enzyme-linked immunosorbent assay (ELISA) kit as recommended by the manufacturer (Sino-American Biotech Co, Ltd, Shanghai, China). HBV DNA was extracted from 100 μL of serum using the QIAamp DNA Blood Mini kit (QIAGEN GmbH, Hilden, Germany) according to the manufacturer's instructions and suspended in 50 μL distilled water.

HBV genotyping

HBV genotype and subgenotype were determined using a multiplex PCR technique that had been previously developed in our laboratory[16]. The specificity of the multiplex PCR was improved by raising the annealing temperature from 56 °C to 63 °C and adding betaine (Sigma, St Louis, MO, USA) to a final concentration of 1 mol/L.

Mutations within the basal core promoter and precore regions

PCR and direct sequencing of the amplified products were performed as described previously using primers that flanked the basal core promoter and precore regions[17].

Statistical analysis

The data were expressed as the mean±standard deviation (SD) for normally distributed variables. Categorical data were compared by a two-tailed Chi-square test with Yates's correction or Fisher's exact test when the expected number in the cell was below 5. Continuous data were compared by a two-tailed Student's *t*-test or one-way ANOVA, as appropriate. We used R software version 2.5.1 and the SPSS 12.0 statistical package (Statistical Software, Chicago, IL, USA). All reported *P* values were two-tailed, and *P* values <0.05 were considered statistically significant.

Results

Distribution of HBV genotypes in CH patients

A total of 4908 DNA-positive CHB patients were investigated, including 143 hepatocellular carcinoma (HCC) patients, 1697 patients with mild CHB, 1627 patients with moderate CHB and 1441 patients with severe CHB. HBV genotypes B, C, D, B+C, and B+D were found in 19.21%, 64.75%, 1.49%, 13.63%, and 0.92% of these patients, respectively (Table 1). Genotype mixture B+C was more common in the patients with moderate and severe CHB than was genotype B, indicating that HBV coinfection with two HBV genotypes promotes a more severe course of the disease. Genotype C was the most prevalent, followed by B and B+C. Among 669 B+C patients, subgenotype mixture B2+C2 (68.13%, 456) was more common than B2+C1 (31.87%, 213). No other subgenotype mixtures were identified (Table 2).

Clinical and virological differences of the HBeAg-positive and HBeAg-negative patients infected with mixed B+C genotype

The clinical and virological differences of 669 samples infected with mixed B+C were tested, including 341 HBeAg-positive and 328 HBeAg-negative samples. The mean age, DNA load, HBeAg-positive, and frequencies of the G1896A, 1762T/1764A, 1896A/1858T mutations were significantly different ($P<0.05$) between the HBeAg-positive and HBeAg-negative groups.

The mean age of the patients in the HBeAg-negative group was significantly higher than in HBeAg-positive group ($P<0.001$). The male-to-female ratio was lower in the HBeAg-negative group than in the HBeAg-positive group, but this difference was not significant ($P=0.492$). Patients with mixed B+C in the HBeAg-negative group showed a higher tendency than those in the HBeAg-positive group to develop G1896A, 1762T/1764A, 1896A/1858T mutations (Table 3).

Table 1. Distribution of HBV genotypes and genotype mixtures.

	B+C	B	C	D	B+D
n=4908	13.63% (669)	19.21% (943)	64.75% (3178)	1.49% (73)	0.92% (45)
Age	38.06±14.42	42.83±14.20	35.26±11.93	31.86±12.73	37.66±17.12
Male/female	1.98	2.71	2.51	2.01	1.77
Viral load	5.57±1.89	4.80±1.90	4.16±1.49	4.21±1.88	5.01±1.96
HBeAg(+) rate	50.97% (341)	40.7% (384)	18.2% (578)	22.4% (16)	31.7% (14)
CH	665	932	3050	73	45
CHB-mild	23.77% (159)	77.09% (727)	10.56% (336)	84.00% (61)	59.00% (27)
CHB-moderate	55.61% (372)	20.78% (196)	65.26% (2074)	16.00% (12)	38.00% (17)
CHB-severe	20.03% (134)	0.95% (9)	20.15% (641)	0.00% (0)	2.00% (1)
LC/HCC	0.60% (4)	1.17% (11)	4.03% (128)	0.00% (0)	0.00% (0)

Table 2. Clinical relevance of HBV subgenotype mixture B+C.

Subgenotype	B2+C2	B2+C1	X^2	*P*
n=669	68.13% (456)	31.87% (213)		
Age	38.11±13.99	37.90±13.95		
Male/female	1.98 (303/153)	2.44 (151/62)	1.31	0.250
Viral load	5.44±1.98	5.62±1.91		
HBeAg(+) rate	48.23% (220/236)	56.90% (121/92)	4.25	0.039
G1896A	12.58% (57/399)	6.45% (14/199)	5.38	0.02
1762T/1764A	17.74% (81/375)	14.78% (31/182)	1.07	0.30
1896A/1858T	5.45% (25/431)	2.34% (5/208)	3.33	0.068
CHB-mild	25.00% (114)	21.13% (45)	1.20	0.273
CHB-moderate	51.97% (237)	63.38% (135)	7.65	0.006
CHB-severe	22.15% (101)	15.49% (33)	4.02	0.045
LC/HCC	0.88% (4)	0.00% (0)		

Table 3. Clinical and virological differences of the HBeAg-positive and HBeAg-negative patients infected with mixed B/C genotype.

B+C	HBeAg(+)	HBeAg(−)	X^2	*P*
n=669	50.97% (341)	49.03% (328)		
Age	34.03±11.02	46.02±13.37		
Viral load (LEG/mLb)	6.49±1.51	4.54±1.58		
Male/female	2.04 (229/112)	1.83 (212/116)	0.47	0.492
G1896A	7.92% (27/314)	13.41% (44/284)	5.32	0.492
1762T/1764A	13.20% (45/296)	20.43% (67/261)	6.27	0.012
1896A/1858T	3.52% (12/329)	5.49% (18/310)	1.51	0.219

Clinical features of CH patients with subgenotype mixture B2+C2
HBV B+C was less frequent in HCC patients (0.60%, 4), while all HCC patients with mixed genotypes were infected with HBV B2+C2 (Table 2). HBV B2+C2 was more common in patients with moderate CHB than in patients with mild CHB (51.97% *vs* 25.00%, *P*=0.000). After adjustment for age, HBV B2+C2 was more frequent in patients with severe CHB than those with mild CHB in the <30 years old and 50–59 years old groups (*P*=0.048, 0.008, respectively).

Most HBV B2+C2 patients were males, and the male-to-female ratio of HBV B2+C2 decreased with age, although there was no statistically significant difference in the distribution of genotypes between genders (Figure 1).

Patients with genotype C were younger on average than those with genotype B (Table 1). The average age of HBV B2+C2 patients was close to the average age of all patients. The prevalence of HBV B2+C2 increased in patients from 50–59 years of age and was significantly different from the proportion of patients in that age group with genotype B (23.2% *vs* 15.2%, *P*=0.024) (Figure 1). HBV B2+C2 was associated with

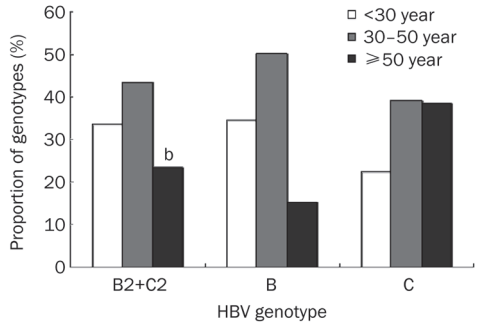

Figure 1. Age-related proportion of genotypes in CH patients infected with HBV B, C, and subgenotype mixture B2+C2. The proportion of patients with HBV B2+C2 went up at 50–59 years stage, significantly different from those with genotype B (23.2% *vs* 15.2%, P=0.024). ^{b}P<0.05.

a more severe course of the disease than for genotype B alone (6.15% *vs* 3.70%, P=0.016) in young CH patients (<30 years) and for genotype C alone (22.15% *vs* 17.29%, P=0.041) in older CH patients (50–59 years).

The average viral load was highest in patients with the genotype mixture B+C (5.57±1.89 log10 copies/mL). The prevalence of B+C varied with the degree of HBV replication, reaching 20.03%, 23.77%, and 55.61% in the severe, mild and moderate replication level groups, respectively. The HBeAg-positive rate was highest in the B+C group and was significantly different from the rates in the genotype B and C groups (P=0.000).

Viral load decreased with age in the group of all HBV patients, while the viral load of HBV B2+C2 patients increased at 50–59 years of age (Figure 2). The prevalence of the G1896A mutation in the HBV B2+C2 group (12.58%) was higher than that of the HBV B2+C1 group (6.45%) (P=0.02). The

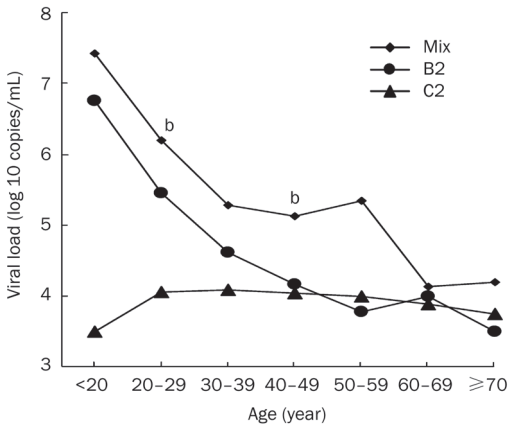

Figure 2. Age-related changes of serum viral load in CH patients infected with HBV B, C, and genotype mixture B2+C2 (mix). Average viral loads in CH patients with HBV B2+C2 were higher than those with B and C in all stages of age. Serum viral load in CH patients decreased with age. However, viral load in patients with HBV B2+C2 went up in 50–59 years group, significantly different from those with B and C (*vs* B: 5.34 *vs* 3.78; P=0.0000; *vs* C: 5.34 *vs* 4.00; P=0.0000, respectively). ^{b}P<0.05.

1762T/1764A mutations in HBV B2+C2 were also frequently found in older patients (50–59 years), but there was no significant difference from the prevalence in the HBV B2+C1 group. The distributions of subgenotype mixture B2+C2 and B2+C1 were significantly different in patients with moderate and severe CHB (P=0.006 and 0.045, respectively) (Table 2).

Discussion

There have been many studies addressing whether HBV genotypes mixtures are associated with specific clinical features, but most previous studies have examined relatively small cohorts[12–14, 18, 19]. This study revealed that the HBV genotypes B, C, D, B+C, and B+D existed in Eastern China. Our study also revealed that subgenotype mixture B2+C2 was prevalent in mixed-genotype patients from Eastern China, where both the HBV C2 and B2 subgenotypes are prevalent[2], consistent with previous reports. These results indicate that similar to single-genotype infections, subgenotype mixtures are associated with the patient's place of birth.

Little is known about the molecular characteristics of HBV genotype mixtures from CHB patients or their association with disease progression. In the present study, HBV B2+C2 was more common than B2+C1 in patients with severe CHB. After adjustment for age, HBV B2+C2 was more frequent in patients with severe CHB than those with mild CHB in the <30 years old and 50–59 years old groups. Genotype B was prevalent in young CH patients and genotype C was prevalent in older CH patients. HBV B2+C2 was associated with a more severe course of the disease than for genotype B alone in young CH patients (<30 years) and for genotype C alone in older CH patients (50–59 years). These results indicated that co-infection or superinfection with multiple genotypes was associated with a poorer prognosis than was single-genotype infection.

The most significant features of HBV B2+C2 were the higher viral load and HBeAg expression in young CH patients (<30 years). Replicative HBV infection stimulates the host immune response that leads to chronic hepatocyte destruction and regeneration with the development of fibrosis and eventually cirrhosis[20]. As an immunoregulatory protein, HBeAg could promote HBV chronicity[21]. HBV genotypes also play a role in viral replication. HBV genotype C exhibits less replication activity in young patients than does genotype B[5]. Our results also confirmed that the average DNA load of patients with genotype B was higher than that in patients with genotype C. These results indicated that HBV B2+C2 in young CH patients (<30 years) was associated with severe liver damage, most likely because of high viral load and the presence of subgenotype B2.

It was notable that the viral load of patients with B2+C2 increased in patients at 50–59 years of age, while viral load and HBeAg expression decreased with age overall. In this study, the prevalence of the G1896A mutation in the HBV B2+C2 group was higher than that of the HBV B2+C1 group. The G1896A mutation was frequently found in subgenotype HBV B2, where it serves as an alternative mechanism for HBeAg seroconversion[22]. Tillmann *et al* have observed

the G1896A mutation among patients with more active liver disease[23], while most investigators did not confirm the correlation between the G1896A mutation and higher viral load[21, 24, 25]. The G1896A mutation most likely develops with time, as it appears to be more common among older subjects. Further experiments will be required to determine whether the G1896A mutation increases the replicative competency of HBV B2+C2.

The 1762T/1764A mutations in HBV B2+C2 were also frequently found in the older patients (50–59 years), but there was no significant difference between patients with mild and severe CHB. The accumulation of 1762T/1764A mutations might be associated with the aging of patients. An *in vitro* study showed that the 1762T/1764A mutations might increase HBV replication activity[25]. Above all, we assumed that mutations in the precore/core promoter region might be partially responsible for the advanced liver disease and elevated viral load in older patients with HBV B2+C2.

In conclusion, HBV B2+C2 was prevalent in CH patients from Eastern China with high HBV replication. Subgenotype HBV B2+C2 was significantly correlated with a more severe course of the disease.

Acknowledgements

This work was supported by grant from Shuguang Project and E-Institute of Shanghai Municipal Education Commission (No E03004).

Author contribution

Jun ZHONG performed the majority of experiments; Yue-qiu GAO, Xue-hua SUN, Xiao-jun ZHU, and Man LI provided vital reagents and analytical tools and were also involved in editing the manuscript; Yue-qiu GAO coordinated the study and collected of all the human material in addition to providing financial support for this work; and Jun ZHONG designed the study and wrote the manuscript.

References

1 Cobleigh MA, Buonocore L, Uprichard SL, Rose JK, Robek MD. A vesicular stomatitis virus-based hepatitis B virus vaccine vector provides protection against challenge in a single dose. J Virol 2010; 84: 7513–22.

2 Cao GW. Clinical relevance and public health significance of hepatitis B virus genomic variations. World J Gastroenterol 2009; 15: 5761–9.

3 Sakamoto T, Tanaka Y, Orito E, Co J, Clavio J, Sugauchi F, *et al.* Novel subtypes (subgenotypes) of hepatitis B virus genotypes B and C among chronic liver disease patients in the Philippines. J Gen Virol 2006; 87: 1873–82.

4 Sugauchi F, Orito E, Ichida T, Kato H, Sakugawa H, Kakumu S, *et al.* Hepatitis B virus of genotype B with or without recombination with genotype C over the precore region plus the core gene. J Virol 2002; 76: 5985–92.

5 Yin J, Zhang H, He Y, Xie J, Liu S, Chang W, *et al.* Distribution and hepatocellular carcinoma-related viral properties of hepatitis B virus genotypes in Mainland China: a community-based study. Cancer Epidemiol Biomarkers Prev 2010; 19: 777–86.

6 Chen J, Yin J, Tan X, Zhang H, Chen B, Chang W, *et al.* Improved multiplex-PCR to identify hepatitis B virus genotypes A-F and subgenotypes B1, B2, C1 and C2. J Clin Virol 2007; 38: 238–43.

7 Kirschberg O, Schuttler C, Repp R, Schaefer S. A multiplex-PCR to identify hepatitis B virus–enotypes A-F. J Clin Virol 2004; 29: 39–43.

8 Yin J, Zhang H, Li C, Gao C, He Y, Zhai Y, *et al.* Role of hepatitis B virus genotype mixture, subgenotypes C2 and B2 on hepatocellular carcinoma: compared with chronic hepatitis B and asymptomatic carrier state in the same area. Carcinogenesis 2008; 29: 1685–91.

9 Alam MM, Zaidi SZ, Shaukat S, Sharif S, Angez M, Naeem A, *et al.* Common genotypes of hepatitis B virus prevalent in injecting drug abusers (addicts) of North West Frontier Province of Pakistan. Virol J 2007; 4: 63.

10 Baig S, Siddiqui A, Chakravarty R, Moatter T. Hepatitis B virus subgenotypes D1 and D3 are prevalent in Pakistan. BMC Res Notes 2009; 2: 1.

11 Constantinescu I, Nedelcu F, Toader MA, Daniela V. Clinical and therapeutical importance of HBV genotyping in Romania. J Med Life 2008; 1: 165–73.

12 Li GZ, Liu XX, Wang XL. HBV genotyping in hepatitis B patients in Jiangsu Province. J Fourth Milit Med Univ 2007; 2: 17–9.

13 Li Y, Wang X, Chen F, Ma R, Wen X, Hu L. Clinical significance of a set of single nucleotide polymorphisms of hepatitis B virus core gene in Chinese Han patients with chronic hepatitis B. J Med Virol 2008; 80: 1885–90.

14 You J, Sriplung H, Chongsuvivatwong V, Geater A, Zhuang L, Huang JH, *et al.* Profile, spectrum and significance of hepatitis B virus genotypes in chronic HBV-infected patients in Yunnan, China. Hepatobiliary Pancreat Dis Int 2008; 7: 271–9.

15 Wang HY, Li D, Liu W, Jin X, Du B, Li YP, *et al.* Hepatitis B virus subgenotype C2 is the most prevalent subgenotype in northeast China. Clin Microbiol Infect 2010; 16: 477–81.

16 Zekri AR, Hafez MM, Mohamed NI, Hassan ZK, El-Sayed MH, Khaled MM, *et al*. Hepatitis B virus (HBV) genotypes in Egyptian pediatric cancer patients with acute and chronic active HBV infection. Virol J 2007; 4: 74.

17 Chan HL, Hussain M, Lok AS. Different hepatitis B virus genotypes are associated with different mutations in the core promoter and precore regions during hepatitis B e antigen seroconversion. Hepatology 1999; 29: 976–84.

18 Firnhaber C, Chen CY, Evans D, Maskew M, Schulz D, Reyneke A, *et al*. Prevalence of hepatitis B virus (HBV) co-infection in HBV serologically-negative South African HIV patients and retrospective evaluation of the clinical course of mono- and co-infection. Int J Infect Dis 2012; 16: e268–72.

19 Zeng G, Wang Z, Wen S, Jiang J, Wang L, Cheng J, *et al*. Geographic distribution, virologic and clinical characteristics of hepatitis B virus genotypes in China. J Viral Hepat 2005; 12: 609–17.

20 Mendy ME, Welzel T, Lesi OA, Hainaut P, Hall AJ, Kuniholm MH, *et al.* Hepatitis B viral load and risk for liver cirrhosis and hepatocellular carcinoma in The Gambia, West Africa. J Viral Hepat 2010; 17: 115–22.

21 Milich D, Liang TJ. Exploring the biological basis of hepatitis B e antigen in hepatitis B virus infection. Hepatology 2003; 38: 1075–86.

22 Liu Y, Zhong Y, Zou Z, Xu Z, Li B, Ren X, *et al.* Features and clinical implications of hepatitis B virus genotypes and mutations in basal core promoter/precore region in 507 Chinese patients with acute and chronic hepatitis B. J Clin Virol 2010; 47: 243–7.

23 Tillmann H, Trautwein C, Walker D, Michitaka K, Kubicka S, Boker K, *et al.* Clinical relevance of mutations in the precore genome of the hepatitis B virus. Gut 1995; 37: 568–73.

24 Cassino L, Laufer N, Salomon H, Campos R, Quarleri J. Hepatitis B precore/core promoter mutations in isolates from HBV-monoinfected and HBV-HIV coinfected patients: a 3-yr prospective study. J Clin Virol 2009; 46: 354–9.

25 Inoue J, Ueno Y, Nagasaki F, Wakui Y, Kondo Y, Fukushima K, *et al*. Enhanced intracellular retention of a hepatitis B virus strain associated with fulminant hepatitis. Virology 2009; 395: 202–9.

Acta Pharmacologica Sinica (2012) 33: 1277–1284
 1671-4083/12 $32.00
www.nature.com/aps

Original Article

Bovine lactoferrin improves bone mass and microstructure in ovariectomized rats via OPG/RANKL/RANK pathway

Jian-ming HOU[#, *], Ying XUE[#], Qing-ming LIN

Provincial Clinical Medical College of Fujian Medical University, Fuzhou 350004, China

Aim: Lactoferrin (LF), an 80-kDa iron-binding glycoprotein, is a pleiotropic factor found in colostrum, milk, saliva and epithelial cells of the exocrine glands. The aim of this study was to evaluate the effects of LF on the bones in ovariectomized (Ovx) rats and to identify the pathways that mediate the anabolic action of LF on the bones.

Methods: Female Sprague-Dawley rats (6-month-old) underwent ovariectomy, and were treated with different doses of LF (10, 100, 1000, and 2000 mg·kg^{-1}·d^{-1}, *po*) or with 7β-estradiol (0.1 mg·kg^{-1}, im, each week) as the positive control. By the end of 6 month-treatments, the bone mass and microstructure in the rats were scanned by micro-computed tomography (micro-CT), and the bone metabolism was evaluated with specific markers, and the mRNA levels of osteoprotegerin (OPG) and the receptor-activator of nuclear factor κB ligand (RANKL) in femur were measured using qRT-PCR.

Results: LF treatment dose-dependently elevated the bone volume (BV/TV), trabecular thickness (TbTh) and trabecular number (TbN), and reduced the trabecular separation (TbSp) in Ovx rats. Furthermore, higher doses of LF (1000 and 2000 mg·kg^{-1}·d^{-1}) significantly increased the bone mineral density (BMD) compared with the untreated Ovx rats. The higher doses of LF also significantly increased the serum levels of OC and BALP, and decreased the serum levels of β-CTx and NTX. LF treatment significantly increased the OPG mRNA levels, and suppressed the RANKL mRNA levels, and the RANKL/OPG mRNA ratio in Ovx rats.

Conclusion: Oral administration of LF preserves the bone mass and improves the bone microarchitecture. LF enhances bone formation, reduces bone resorption, and decreases bone mass loss, possibly through the regulation of OPG/RANKL/RANK pathway.

Keywords: lactoferrin; bone; bone mineral density; OPG/RANKL/RANK pathway; bone turnover

Acta Pharmacologica Sinica (2012) 33: 1277–1284; doi: 10.1038/aps.2012.83; published online 20 Aug 2012

Introduction

Osteoporosis is a common disease that is characterized by reduced bone mass and altered bone microarchitecture, which results in fragility fractures[1]. The bone loss is caused by an imbalance between the activities of osteoclasts and osteoblasts, and it leads to the uncoupling of bone resorption and bone formation[2]. The bone loss found in postmenopausal osteoporosis (PMOP) cases is caused by estrogen deficiency that increases osteoclast activity and bone remodeling — a predominance of bone resorption over bone formation[3]. The increased rate of bone turnover as observed from markers, such as β-CrossLaps (β-CTx) and collagen type I N-telopeptide (NTX), may be an additional risk factor for fractures by exacerbating bone loss. Furthermore, the identification of additional bone formation markers, such as osteocalcin (OC) and bone alkaline phosphatase (BALP), may serve to reduce the risk of osteoporosis and lessen the probability of fractures.

Lactoferrin (LF), an 80-kDa iron-binding glycoprotein that belongs to the transferrin family, is a pleiotropic factor found in colostrum, milk, saliva, and epithelial cells of the exocrine glands[4, 5]. Many studies have demonstrated that lactoferrin has antimicrobial activity and functions as a regulator of immune response[6, 7]. In recent years, several studies have shown that LF acts as a growth factor and has both *in vitro* and *in vivo* anabolic activity in bone[8–12]. Lactoferrin induces the proliferation and differentiation of osteoblast-like cells and inhibits osteoclastogenesis *in vitro*[10, 13]. LF has also been shown to have an inhibitory effect on osteoclast formation[11]. Locally injecting LF above the hemicalvaria in adult mice for 5 successive days resulted in increased bone formation and bone area compared with the controls[8]. In addition, oral LF administered to Ovx rats for 3 months protected against Ovx-induced decreases in bone volume and mineral density

# These authors contributed equally to this work.
* To whom correspondence should be addressed.
E-mail hjm996@yahoo.com.cn
Received 2012-02-17 Accepted 2012-05-30

and led to increased mechanical strength parameters[14]. In a clinical study, 38 healthy, postmenopausal women randomly received either oral RNAse-enriched lactoferrin or a placebo, resulting in an obvious reduction in osteoblast and bone resorption markers in the lactoferrin-treated group[15].

The pathways that are activated by lactoferrin are unknown. Osteoprotegerin (OPG) and the receptor activator of nuclear factor-kB ligand (RANKL) are cytokines that are necessary for regulating bone formation and bone resorption. The RANKL/OPG ratio is the key element regulating the balance between bone formation and bone resorption, and the shortage of estrogen leads to an imbalance in this ratio. OPG is a naturally occurring inhibitor of RANKL; it binds RANKL with high affinity and prevents its interaction with RANK on osteoclasts[16]. Therefore, OPG negatively regulates osteoclast formation and prevents osteoporosis[17]. Studies have shown that excessive osteoclast activity in OPG-knockout mice ($OPG^{-}/^{-}$) results in high bone turnover rate, disorganized matrix and impaired attachment of new bone to old bone in the cement lines[18]. The inability of RANK to bind RANKL leads to the inhibition of osteoclast differentiation and maturation, thereby causing a deficiency of mature osteoclasts at the bone surface[19]. In addition, other cytokines that mediate bone remodeling, such as monocyte-macrophage colony stimulating factor (M-CSF), are also known to promote osteoclastogenesis[20].

In a number of recent studies, osteoblast cultures treated with LF showed positive effects on bone *in vitro*. It is important to study the effects of oral LF in an animal osteoporosis model as observed on bone mass and bone microarchitecture. Moreover, to utilize LF as a therapeutic agent for treating bone loss, a better understanding has to be obtained of the pathways involved in LF's anabolic effects in the bone and its effects on the biochemical markers of bone turnover. Herein, we explored in further details the pathways by which lactoferrin stimulates osteoblast growth.

Materials and methods

Materials

The bovine LF (95% purity with 20% iron saturation) used in this study was produced in Australia. Prior to use, the LF was diluted in distilled water, and the 17β-estradiol (E_2; Shanghai General Pharmaceutical Co, LTD; batch number: 090801) was dissolved in corn oil. All of the rats were treated in accordance with "Fujian experimental animal management measures" and with the approval of the Fujian Provincial Hospital, Fuzhou, China.

Ovx rat model

A total of seventy 6-month-old virgin female Sprague-Dawley rats weighing 300±20 g were purchased from Shanghai SCXK Experimental Animals Co, LTD (qualified number: SCXK (Shanghai) 2007-0005). The rats were housed in individual stainless-steel cages with a controlled temperature of 20±3 °C, a relative humidity of 40%–60% and a 12-h light-dark cycle. All of the rats were given free access to a standard pellet diet and water during the 6-month feeding period. After 1 week of adaptability feeding, 10 rats were randomly assigned to the sham-operated (Sham) group, and the remaining 60 rats were assigned to the ovariectomized (Ovx) group. The Ovx rats were anesthetized with ketamine (100 mg/kg), and both ovaries were removed. The Sham rats had surgery that only resected the fat tissue near the ovaries. After surgery, penicillin was administered intramuscularly at 50 000 U per day, with each dose lasting for three days. One week after the surgery, the Ovx rats were randomly divided into six groups of 10 rats each, as follows: Ovx untreated (Con); Ovx+17β-estradiol 0.1 $mg{\cdot}kg^{-1}{\cdot}week^{-1}$, the positive control ($E_2$); Ovx+LF 10 $mg{\cdot}kg^{-1}{\cdot}d^{-1}$ (LF_1); Ovx+LF 100 $mg{\cdot}kg^{-1}{\cdot}d^{-1}$ (LF_2); Ovx+LF 1.0 $g{\cdot}kg^{-1}{\cdot}d^{-1}$($LF_3$); and Ovx+LF 2.0 $g{\cdot}kg^{-1}{\cdot}d^{-1}$ (LF_4). The doses of LF were chosen according to previous studies in the literature[21].

Treatment

In the Sham and Con groups, the rats were orally intubated with 0.9% physiological saline at a dose of 2 mL/kg. For the Ovx+E_2, the E_2 was dissolved in corn oil and injected into muscle at a dose of 0.1 mg/kg body weight on a weekly basis. The LF was dissolved in distilled water and given orally every day at the appropriate dose. The doses were readjusted every week to accommodate changes in body weight.

Sample collection

After 6 months of treatment, each rat was euthanized, its uterus and subcutaneous fat were removed and weighed, and the femur and the L2-4 vertebrae of each rat were separated from the surrounding muscle. Venous blood was drawn into a Vacutainer (BD Biosciences, NJ, USA) and the serum was separated by centrifugation. The serum specimens were stored at -80 °C until analysis. The right femur was collected in a tube, frozen in liquid nitrogen and stored at -80 °C until analysis. The left femur and L2-4 vertebrae were preserved in 4% paraformaldehyde for the micro-computed tomography scans.

Micro-computed tomography (micro-CT)

Scanning parameters

Each specimen consisted of the proximal femur and L2-4 vertebrae and was evaluated using a microfocus CT system (ZKKS-SHARP Institute of Chinese Science Research). Each sample was scanned at 10-mm intervals at a voltage of 70 kVP, amplitude of 200 mA, scanning resolution of 50 μm, rotating angle of 360 degrees, power of 40 W, frame average of 6 and pixel combination of 1×1.

Three dimensional (3D) reconstruction and bone parameter analysis

The trabecular bone microarchitecture of the proximal femur and L2-4 vertebrae was analyzed with mCT at a 50-μm isotropic image resolution. The trabecular region was isolated from the cortical region in each 2D image by a manual contouring analysis. Model-independent 3D measurement methods were used to reconstruct and define the trabecular bone volume of interest (VOI) for the cancellous bone, and the following

parameters were calculated: trabecular bone volume fraction (BV/TV, %), trabecular thickness (TbTh, mm), trabecular number (TbN, mm^{-1}), trabecular separation (TbSp, mm), and bone mineral density (BMD).

Serum E_2 level and biochemical markers of bone turnover

Total estradiol (E_2), osteocalcin (OC), bone alkaline phosphatase (BALP), β-CrossLaps (β-CTx), and collagen type I N-telopeptide (NTX) levels were determined in serum samples obtained at the time of bone biopsy. E_2, OC, BALP, and β-CTx were measured using an immunoradiometric assay autoanalyzer (R&D, USA). NTX levels were determined by electrochemiluminescence (ECL) assay (Roche Elecsys 2010, Switzerland). The sensitivities of these assays were 1 pg/mL and 50 pg/mL, and their inter-assay variation coefficients were less than 10%.

Quantitative real-time reverse transcription-PCR (qRT-PCR)

The local expression of the RANKL and OPG genes in the trabecular bone of the femur was analyzed by qRT-PCR. A small cube of trabecular bone (proximal femur) was homogenized, and the total RNA was isolated with TRIzol reagent (Invitrogen, Carlsbad, CA, USA)[22]. The extracted RNA was dissolved in RNAse-free distilled water. The quality and quantity of the RNA samples were determined by spectrophotometry, with the ratios of absorbance at 260 nm and 280 nm ranging from 1.8 to 2.0. Next, 5 mg of total RNA was first reverse transcribed into cDNA using a High-Capacity cDNA Kit (DRR037, TaKaRa, Japan) according to the manufacturer's instructions. The quantitative PCR for the local RANKL and OPG gene expression was performed in 96-well plates; the reaction volume was 25 mL/well, which included the SYBR PremixEx Taq II (2×) (DRR081A, TaKaRa, Japan), diluted gene primers, and cDNA. The primer sequences are listed in Table 1. The qRT-PCR was performed using a Thermal Cycler Dice™ Real Time (TP800, TaKaRa). The standard curve method was used to calculate the relative expression levels, with the levels of each gene normalized to β-actin. The data from the qRT-PCR analyses are presented in relative mRNA units. The RANKL/OPG mRNA ratio was calculated from the RANKL/actin and OPG/actin mRNA values.

Statistical analysis

The results are reported as the mean±standard deviation (SD). The data analyses were performed using the Statistical Package for the Social Sciences (SPSS version 16.0) software package. The differences among the 7 groups were analyzed using a one-way ANOVA model followed by *post-hoc* tests. The changes in body weight within a group over time were compared using the paired-samples *t*-test. The variables with unequal variances were analyzed using the Kruskal-Wallis H test. Differences were considered significant at $P<0.05$.

Results

General index changes

The body weights of the rats were not significantly different from each other before the treatment ($P>0.05$, Table 2). By the end of the 6-month experiment, all of the rats had increased

Table 1. The primer sequences for quantitative real-time PCR.

Genes	GenBank numbers	Primer sequence	Product size (bp)
OPG	NM-012870	Forward 5′-ACAATGAACAAGTGGCTGTGCTG-3′ Reverse 5′-CGGTTTCTGGGTCATAATGCAAG-3′	109
RANKL	NM-057149	Forward 5′-GCAGCATCGCTCTGTTCCTGTA-3′ Reverse 5′-GCATGAGTCAGGTAGTGCTTCTGTG-3′	164
β-Actin	NM-031144.2	Forward 5′-GGAGATTACTGCCCTGGCTCCTA-3′ Reverse 5′-GACTCATCGTACTCCTGCTTGCTG-3′	150

Table 2. The body, uterus, and subcutaneous fat weights in the Con, Sham, E_2, and LF groups.

Weights	Numbers		Body (g)		Uterus (g)	Subcutaneous fat (g)
	Initial	Final	Initial	Final	Final	Final
Con	10	7	289.9±19.2	434.1±46[e]	0.15±0.09	20.1±1.3
Sham	10	7	298.0±18.0	358.9±40.5[be]	0.91±0.85	12.3±0.6
E_2	10	8	295.6±13.8	370±42.4[be]	0.85±0.78	13.5±0.7
LF_1	10	7	300.9±14.4	426.1±43.3[e]	0.36±0.55	18.8±1.5
LF_2	10	10	290.1±15.0	393.6±29.4[e]	0.45±0.49	17.5±1.0
LF_3	10	9	294.5±13.8	393.1±35.2[e]	0.60±0.51	15.3±0.8
LF_4	10	8	297.02±18.8	395.3±288[e]	0.86±0.59	13.8±0.7

Con: ovariectomized untreated; Sham: sham-operated; E_2: Ovx+E_2 0.1 mg·kg^{-1}·week^{-1}; LF_1: Ovx+LF 10 mg·kg^{-1}·d^{-1}; LF_2: Ovx+LF 100 mg·kg^{-1}·d^{-1}; LF_3: Ovx+LF 1.0 g·kg^{-1}·d^{-1}; LF_4: Ovx+LF 2.0 g·kg^{-1}·d^{-1}. Mean±SD. [b]$P<0.05$, [c]$P<0.01$ compared with the Con group; [e]$P<0.05$ compared with the initial body weight.

body weight. The Con rats tended to gain more weight than the Sham rats (P<0.05). The final body weights of the LF-treated rats tended to be lower than those of the Con group; however, these differences were not statistically significant (P>0.05, Table 2). In addition, estrogen treatment completely prevented the Ovx-induced weight gain.

The Con rats had uterine tissue atrophy, indicating the success of the surgical procedure (Table 2). The estrogen partly prevented the Ovx-induced uterine atrophy, whereas the LF had no detectable effect on the uterus. The subcutaneous fat weight of the Con rats was significantly greater than that of the Sham rats, but this difference was not statistically significant (P>0.05, Table 2).

Serum E_2 level

At the completion of the experiment, the levels of serum estradiol were comparable between the E_2 and the Sham groups (P>0.05), whereas the Con and the different LF groups had decreased estradiol levels as compared to the Sham group (P<0.01) (Figure 1).

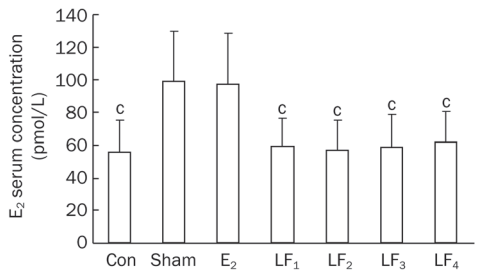

Figure 1. The serum E_2 level in the Con, Sham, E_2, and LF groups at the end of the experiment. Mean±SD. ^cP<0.01 compared with the Sham group.

Micro-computed tomography (micro-CT)

Microstructural parameters of the trabecular bone

As shown in Figures 2 and 3, the ovariectomies significantly reduced BV/TV, TbTh, TbN values and increased the TbSp values in both femur and L2-4 vertebrae of the rats. Treatment with LF or estrogen protected the rats from the Ovx-induced effects on the above biomarker levels.

Bone mineral density (BMD)

At the end of the experiment, the Con rats had markedly reduced BMD in both their femurs and L2-4 vertebrae compared with the Sham and E_2 groups (P<0.01). The BMD values in the rats treated with 1.0 $g{\cdot}kg^{-1}{\cdot}d^{-1}$ and 2.0 $g{\cdot}kg^{-1}{\cdot}d^{-1}$ LF were greater than those in the Ovx control (P<0.05 and P<0.01). However, the lower LF doses (10 $mg{\cdot}kg^{-1}{\cdot}d^{-1}$ and 100 $mg{\cdot}kg^{-1}{\cdot}d^{-1}$) did not significantly alter the BMD (P>0.05, Figure 4). The BMD differences among the groups followed a similar pattern for both L2-4 lumbar vertebrae and femur.

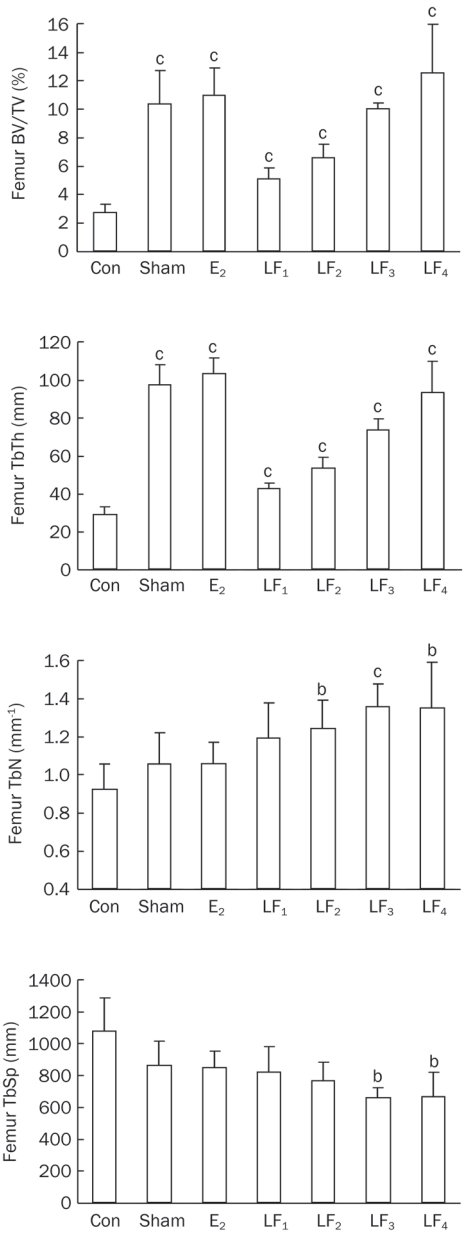

Figure 2. The trabecular bone microstructural parameters of the femurs in the Con, Sham, E_2, and LF groups at the end of the experiment. ^bP<0.05, ^cP<0.01 compared with the Con group. BV=bone volume; TV=tissue volume; TbTh=trabecular thickness; TbN=trabecular number; TbSp=trabecular separation.

Bone turnover markers

The serum levels of OC, BALP, β-CTx, and NTX in the Con group were higher compared with those in the Sham group (P<0.01), with the levels of β-CTx and NTX being noticeably higher than those of OC and BALP. The serum levels of OC, BALP, β-CTx, NTX increased by 17.9%, 14.0%, 47.7%, and 31.7%, respectively, in the Con group compared with the Sham. Although the serum levels of OC and BALP in the different LF groups were higher compared with the Con

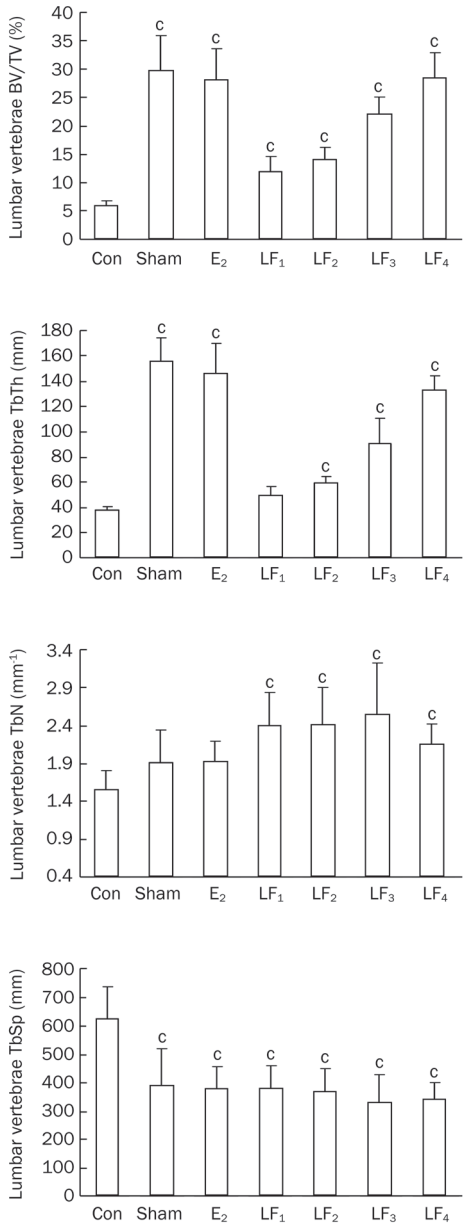

Figure 3. The trabecular bone microstructure parameters of the L2-4 vertebrae in the Con, Sham, E_2, and LF groups at the end of the experiment. $^bP<0.05$, $^cP<0.01$ compared with Con group.

group, these increases were only statistically significant for LF_3 (1 g·kg^{-1}·d^{-1} LF treatment) and LF_4 (2 g·kg^{-1}·d^{-1} LF treatment) groups. Moreover, the serum levels of β-CTx and NTX were lower in the different LF groups compared with the Con group, and these decreases were significant for the LF_3 and LF_4 groups. The serum levels of OC, BALP, β-CTx, and NTX were similar between the E_2 and Sham groups ($P>0.05$, Figures 5 and 6).

The local expression of RANKL and OPG genes in femur

As shown in Figure 7, the local expression of the RANKL gene was higher in the Con group than in the Sham and E_2 groups ($P<0.01$). The groups with 1 g·kg^{-1}·d^{-1} and 2 g·kg^{-1}·d^{-1} LF treatments had significantly lower RANKL mRNA levels in the proximal femur compared with the Con group ($P<0.01$ and $P<0.05$). However, the groups with 10 mg·kg^{-1}·d^{-1} and 100 mg·kg^{-1}·d^{-1} LF treatments did not show significant alterations of the RANKL mRNA levels ($P>0.05$). The local OPG mRNA expression increased in the Sham and E_2 groups compared with the Con group ($P<0.01$). The groups with 1 g·kg^{-1}·d^{-1} and 2 g·kg^{-1}·d^{-1} LF treatment had significantly higher OPG levels compared with the Con group ($P<0.01$ and $P<0.05$); however, the two lower doses of LF did not show significant effects ($P>0.05$). The ratio of RANKL/OPG mRNA in the Con group was significantly higher than that in the Sham and E_2 groups ($P<0.01$). Moreover, there was a significant decrease ($P<0.01$) in the RANKL/OPG mRNA ratio in the proximal femur following treatment with 100 mg·kg^{-1}·d^{-1}, 1 g·kg^{-1}·d^{-1}, and 2 g·kg^{-1}·d^{-1} LF compared with the Con group; however, 10 mg·kg^{-1}·d^{-1} LF treatment did not show any significant change ($P>0.05$) for the same.

Discussion

Previous studies have shown that lactoferrin has an anabolic effect on osteoblasts and osteoclasts *in vitro*[8, 9, 11]. The aim of this study was to evaluate the changes induced by lactoferrin in the Ovx rat model and to identify the pathways that mediate the anabolic action of lactoferrin in bone. We found that LF at concentrations of 1 g·kg^{-1}·d^{-1} and 2 g·kg^{-1}·d^{-1} significantly increased the bone mass and microarchitecture compared with the untreated Ovx rats that suffered from increasing bone loss, severe osteopenia and increased bone resorption. Compared with the untreated Ovx rats, the LF treatment resulted in increased bone formation in the femur and lumbar vertebrae, and these changes were associated with higher bone volume (BV/TV) and trabecular number (TbN). LF also improved the trabecular microarchitecture, which is consistent with the increase in bone mineral density (BMD). Moreover, LF seemed to partially restore trabecular connectivity by increasing trabecular thickness (TbTh) while reducing trabecular separation (TbSp), suggesting that LF could prevent the loss of bone mass after Ovx. These results were confirmed in a series of experiments on a mixed primary culture of murine bone cells. In our study, significant microarchitectural differences were observed between the rats given the LF treatment and the untreated Ovx controls. We need to pay attention to that what in the Guo's study, LF could increase bone mineral density at 8.5- and 85- mg/kg doses[14]. However, similar increases did not occur at the 10 mg·kg^{-1}·d^{-1} and 100 mg·kg^{-1}·d^{-1} LF doses that were used in our study. A possible explanation could be the differences in density and purity of different LF preparations in these studies. As a new anti-osteoporosis agent, LF has been reported to exert beneficial effects on osteoblast proliferation and differentiation as well as inhibit osteoclast activity in bone cell cultures[9, 10].

Bone mass depends on the balance between bone resorption and bone formation within a remodeling unit, and it varies with the number of remodeling units that are activated within

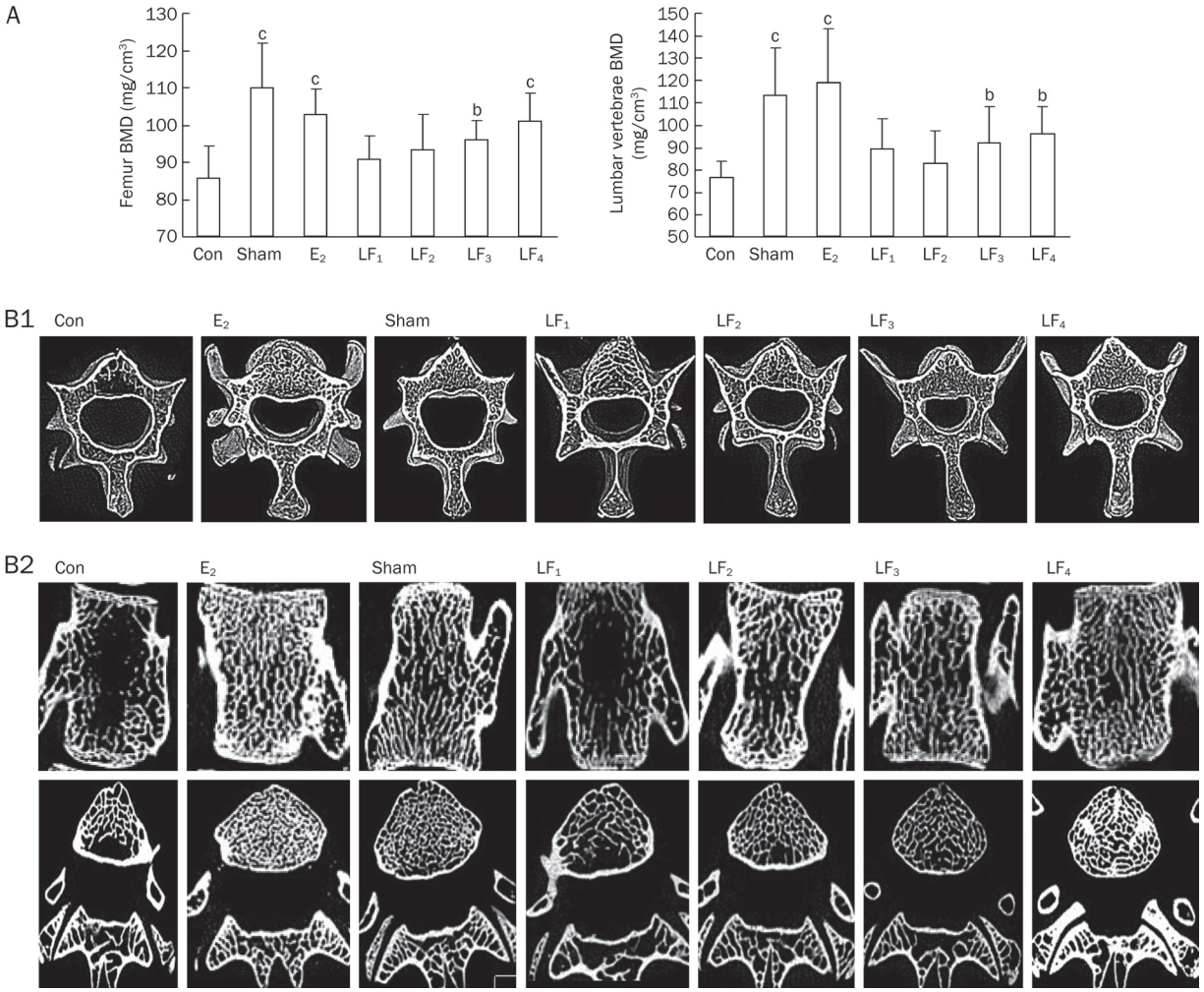

Figure 4. (A) The BMD of the femurs and L2-4 vertebrae in the Con, Sham, E_2, and LF groups at the end of the experiment. $^{b}P<0.05$, $^{c}P<0.01$ compared with Con group. (B1) The trabecular bone microstructure of the L3 vertebrae in the Con, Sham, E_2, and LF groups at the end of the experiment. B1. A representative 3D reconstruction of a cross-section of the bone microstructure in the L3 vertebrae. (B2) Representative 2D images of a coronal section and a cross-section of the bone microstructure in the L3 vertebrae separately from the micro-CT scans. These pictures show that the Con group has severe osteopenia, main bone loss with trabecular thinning, and fewer areas of trabecular bone, which were highly disconnected and partly fractured. However, the LF groups display orderly trabecular arrangements, with more areas of trabecular bone and better connectivity.

a given period of time in a defined area of bone. Osteoblasts and osteoclasts are specialized cells responsible for bone formation and resorption, respectively. Biochemical markers of bone turnover are indicative of events occurring during the bone remodeling cycle. These biochemical markers are divided into two categories: markers of bone formation and markers of bone resorption. These markers reflect the metabolic conversion of bone, predict osteoporosis and indicate the risk of bone fractures. The levels of biochemical markers of bone turnover, both for formation and resorption, continue to increase with age following menopause[23]. In this study, all of the markers displayed this tendency. The serum levels of OC, BALP, β-CTx, and NTX in the Con group were increased after ovariectomy compared with the Sham group. In addition, β-CTx and NTX levels demonstrated stronger changes than OC and BALP levels, suggesting that at 6-months post-ovariectomy, there is enhanced bone resorption resulting in bone loss. However, LF prevented the Ovx-induced bone loss by increasing bone formation over bone resorption.

We also observed that treatment with 1 $g \cdot kg^{-1} \cdot d^{-1}$ and 2 $g \cdot kg^{-1} \cdot d^{-1}$ LF increased the local OPG gene expression in the proximal femur. These elevations in OPG can contribute to a reduced local RANKL/OPG ratio, suggesting that LF may decrease osteoclast differentiation.

Previous studies have shown that osteogenesis is determined by the duration of ovariectomy and diet, factors that regulate the expression of genes involved in bone formation. This regulation specifically allows bone loss to occur following ovariectomy[24, 25] until the end of the osteogenic process. Therefore, the ovariectomy procedure induced negative long-term regulation of bone formation results in the predominance of bone resorption over bone formation. An increase in bone

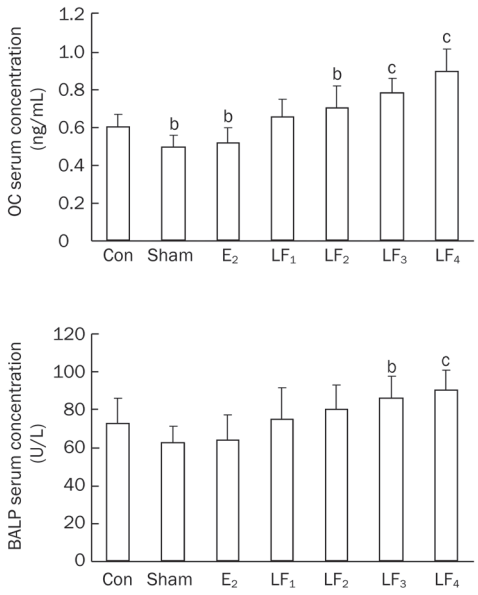

Figure 5. The bone formation makers of serum in the Con, Sham, E_2, and LF groups at the end of the experiment. $^bP<0.05$, $^cP<0.01$ compared with the Con group. OC=Osteocalcin; BALP=bone alkaline phosphatase.

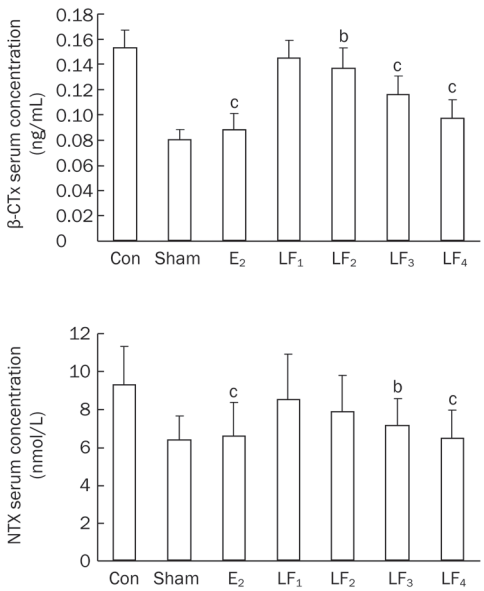

Figure 6. The bone absorption makers of serum in the Con, Sham, E_2, and LF groups at the end of the experiment. $^bP<0.05$, $^cP<0.01$ compared with the Con group. β-CTx=β-CrossLaps; NTX=collagen type I N-telopeptide.

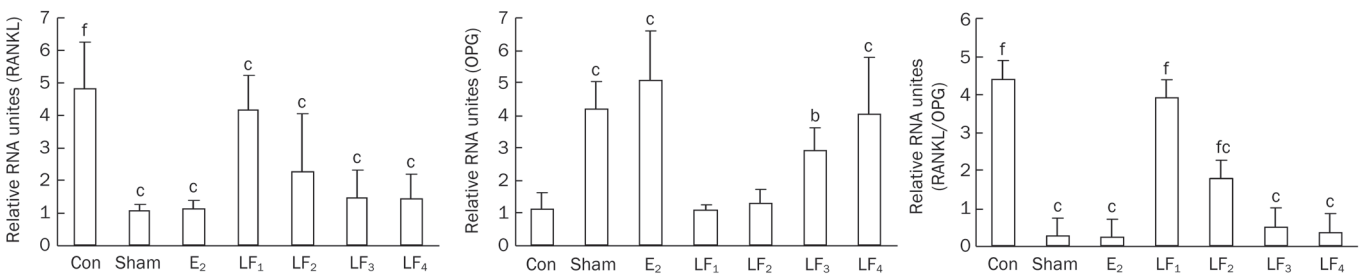

Figure 7. The effects of LF on the local expression of RANKL and OPG mRNA and the RANKL/OPG mRNA ratio in the bone trabecula of the proximal femur. The RANKL and OPG mRNA expression in the proximal femur was determined by qRT-PCR, and the RANKL/OPG mRNA ratio was calculated. Mean±SD. $^bP<0.05$, $^cP<0.01$ compared with the Con group; $^fP<0.01$ compared with the E_2 group..

resorption is a general characteristic of osteoporosis and is primarily regulated by the relative balance between RANKL and OPG levels. The LF treatment induced a bone formation marker expression pattern similar to that observed in the untreated ovariectomized rats. The LF induced a decline in RANKL gene expression in the trabecular bone of the Ovx rats, suggesting that LF prevents bone loss by reducing the expression of RANKL in osteoblasts. The LF treatment did not cause differentiation of the bone marrow stromal cells to an osteoblastic lineage in this ovariectomized rat model. According to previous studies[3], however, the inhibition of bone resorption markers by oral LF suggests that LF may prevent Ovx-induced bone loss via a preferential anti-osteoclastogenic pathway.

RANKL has been shown to have a significant role in the generation, activity, and survival of osteoclasts[26, 27]. OPG is an endogenous antagonist of RANKL and inhibits RANKL action by acting as a soluble decoy receptor, thus balancing bone turnover[28]. In bone, RANKL is expressed most abundantly in MSCs, osteoblasts and T cells[29]. Despite OPG being a known inhibitor of RANKL, its biological effect may depend on the molar ratio between RANKL and OPG[30]. In this study of ovariectomized rats, we demonstrated that although LF treatment seems to have an inhibitory effect on RANKL, it enhances OPG. The RANKL/OPG ratio may be a major mechanism for the increased bone formation and decreased bone resorption observed in the LF treated rats, and this finding suggests that LF decreases osteoclast differentiation.

Nevertheless, this study has several limitations worth discussing. First, the number of rats in this study was small, and there was much variability in the measurements; therefore, additional studies should be conducted to confirm these results. Second, we did not assess the biochemical markers of mineral homeostasis (estrogen, calcium, phosphate and parathyroid hormone); therefore, we cannot evaluate their impact

in this study. Finally, this study did not include information on mechanical bone properties or histological data; thus, we cannot determine whether the routine of daily LF treatment impaired the osteoid mineralization rate or individual osteoblast function.

In conclusion, this study used an ovariectomy-induced osteoporosis rat model to show that orally administered LF preserves bone mass and bone microarchitecture and prevents bone loss in both the femoral and lumbar vertebrae. We also demonstrated that LF has dual effects on both osteoblasts and osteoclasts as well as on the OPG/RANKL/RANK pathway. In summary, LF may be a safe and effective treatment for estrogen-dependent bone loss, and it is possible that OPG/RANKL/RANK signaling may be involved in the LF-induced antiresorptive effect. Further investigations need be performed on the relevance of LF treatment strategy for postmenopausal bone loss in humans with implications on the anabolic effects of LF on bone metabolism.

Acknowledgements

This study was supported by Fujian Science & Technology Major Special Project (No 2010Y0015).

Author contribution

Jian-ming HOU, Ying XUE, and Qing-ming LIN designed the research project; Jian-ming HOU supervised the project; Ying XUE performed the animal assays, serum assays, analyzed the data and wrote the manuscript; and Jian-ming HOU,Ying XUE, and Qing-ming LIN revised the manuscript.

References

1 Garnero P, Delmas PD, Bilezikian JP. Evaluation of risk for osteoporosis fractures. Principles of Bone Biology 2002; 1291–301.
2 Naot D, Grey A, Reid IR, Cornish J. Lactoferrin — a novel bone growth factor. Clin Med Res 2005; 5: 93–101.
3 Omi N, Ezawa I. The effect of ovariectomy on bone metabolism in rats. Bone 1995; 17: 163S–168S.
4 Metz-Boutigue MH, Jollès J, Mazurier J, Schoentgen F, Legrand D, Spik G, *et al*. Human lactotransferrin: amino acid sequence and structural comparisons with other transferrins. Eur J Biochem 1984; 145: 659–76.
5 Lonnerdal B, Iyer S. Lactoferrin: molecular structure and biological function. Annu Rev Nutr 1995; 15: 93–110.
6 Ward PP, Paz E, Conneely OM. Multifunctional roles of lactoferrin: a critical overview. Cell Mol Life Sci 2005; 62: 2540–8.
7 Tomita M, Wakabayashi H, Shin K, Yamauchi K, Yaeshima T, Iwatsuki K. Twenty-five years of research on bovine lactoferrin applications. Biochimie 2009; 91: 52–7.
8 Cornish J, Callon KE, Naot D, Palmano KP, Banovic T, Bava U, *et al*. Lactoferrin is a potent regulator of bone cell activity and increases bone formation *in vivo*. Endocrinology 2004; 145: 4366–74.
9 Grey A, Banovic T, Zhu Q, Watson M, Callon K, Palmano K, *et al*. The low-density lipoprotein receptor-related protein 1 is a mitogenic receptor for lactoferrin in osteoblastic cells. Mol Endocrinol 2004; 18: 2268–78.
10 Grey A, Zhu Q, Watson M, Callon K, Cornish J. Lactoferrin potently inhibits osteoblast apoptosis, via an LRP1-independent pathway. Mol Cell Endocrinol 2006; 251: 96–102.
11 Lorget F, Clough J, Oliveira M, Daury MC, Sabokbar A, Offord E. Lactoferrin reduces *in vitro* osteoclast differentiation and resorbing activity. Biochem Biophys Res Commun 2002; 296: 261–6.
12 Takayama Y, Mizumachi K. Effect of lactoferrin-embedded collagen membrane on osteogenic differentiation of human osteoblast-like cells. J Biosci Bioeng 2009; 107: 191–5.
13 Naot D, Grey A, Reid IR, Cornish J. Lactoferrin: a novel bone growth factor. Clin Med Res 2005; 3: 93–101.
14 Guo HY, Jiang L, Ibrahim SA, Zhang L, Zhang H, Zhang M, *et al*. Orally administered lactoferrin preserves bone mass and microarchitecture in ovariectomized rats. J Nutr 2009; 139: 958–64.
15 Bharadwaj S, Naidu AG, Betageri GV, Prasadarao NV, Naidu AS. Milk ribonuclease-enriched-lactoferrin induces positive effects on bone turnovermarkers in postmenopausal women. Osteoporos Int 2009; 20: 1603–11.
16 Boyle WJ, Simonet WS, Lacey DL. Osteoclast differentiation and activation. Nature 2003; 423: 337–42.
17 Mitchner NA, Harris ST. Current and emerging therapies for osteoporosis. J Fam Pract 2009; 58: S45–9.
18 Amizuka N, Shimomura J, Li M, Seki Y, Oda K, Henderson JE, *et al*. Defective bone remodelling in osteoprotegerin-deficien mice. J Electron Microsc (Tokyo) 2003; 52: 503–13.
19 Dougall WC, Glaccum M, Charrier K, Rohrbach K, Brasel K, De Smedt T, *et al*. RANK is essential for osteoclast and lymph node development. Genes Dev 1999; 13: 2412–24.
20 Manolagos SC, Jilka RL. Bone marrow, cytokines, and bone remodeling. Emerging insights into the pathophysiology of osteoporosis. N Engl J Med 1995; 332: 305–11.
21 Blais A, Malet A, Mikogami T, Martin-Rouas C, Tomé D. Oral bovine lactoferrin improves bone status of ovariectomized mice. Am J Physiol Endocrinol Metab 2009; 296: E1281–8.
22 Chomczynski P, Sacchi N. Single-step method of RNA isolation by acid guanidinium thiocyanate-phenol-chloroform extraction. Anal Biochem 1987; 162: 156–9.
23 Melton LJ 3rd, Khosla S, Atkinson EJ, O'Fallon WM, Riggs BL. Relationship of bone turnover to bone density and fractures. J Bone Miner Res 1997; 12: 1083–91.
24 Schroeder TM, Jensen ED, Westendorf JJ. Runx2: a master organizer of gene transcription in developing and maturing osteoblasts. Birth Defects Res C Embryo Today 2005; 75: 213–25.
25 Marie PJ. Transcription factors controlling osteoblastogenesis. Arch Biochem Biophys 2008; 473: 98–105.
26 Lacey DL, Timms E, Tan HL, Kelley MJ, Dunstan CR, Burgess T, *et al*. Osteoprotegerin ligand is a cytokine that regulates osteoclast differentiation and activation. Cell 1998; 93: 165–76.
27 Kong YY, Yoshida H, Sarosi I, Tan HL, Timms E, Capparelli C, *et al*. OPGL is a key regulator of osteoclastogenesis, lymphocyte development and lymph-node organogenesis. Nature 1999; 397: 315–23.
28 Simonet WS, Lacey DL, Dunstan CR, Kelley M, Chang MS, Lüthy R, *et al*. Osteoprotegerin: a novel secreted protein involved in the regulation of bone density. Cell 1997; 89: 309–19.
29 Rauner M, Sipos W, Pietschmann P. Osteoimmunology. Int Arch Allergy Immunol 2007; 143: 31–48.
30 Sandberg WJ, Yndestad A, Øie E, Smith C, Ueland T, Ovchinnikova O, *et al*. Enhanced t-cell expression of rank ligand in acute coronary syndrome: possible role in plaque destabilization. Arterioscler Thromb Vasc Biol 2006; 26: 857–63.

Acta Pharmacologica Sinica (2012) 33: 1285–1292
 1671-4083/12 $32.00
www.nature.com/aps

Original Article

The natural stilbenoid pinosylvin and activated neutrophils: effects on oxidative burst, protein kinase C, apoptosis and efficiency in adjuvant arthritis

Viera JANČINOVÁ[1, *], Tomáš PEREČKO[1], Rado NOSÁĽ[1], Juraj HARMATHA[2], Jan ŠMIDRKAL[3], Katarína DRÁBIKOVÁ[1]

[1]Institute of Experimental Pharmacology and Toxicology, Slovak Academy of Sciences, Dúbravská cesta 9, 841 04 Bratislava, Slovak Republic; [2]Institute of Organic Chemistry and Biochemistry, Academy of Sciences of Czech Republic, Flemingovo náměstí 2, 166 10 Praha 6, Czech Republic; [3]Institute of Chemical Technology Prague, Faculty of Food and Biochemical Technology, Technická 5, 166 28 Praha 6, Czech Republic

Aim: To investigate the effects of the naturally occurring stilbenoid pinosylvin on neutrophil activity *in vitro* and in experimental arthritis, and to examine whether protein kinase C (PKC) activation served as an assumed target of pinosylvin action.
Methods: Fresh human blood neutrophils were isolated. The oxidative burst of neutrophils was evaluated on the basis of enhanced chemiluminescence. Neutrophil viability was evaluated with flow cytometry, and PKC phosphorylation was assessed by Western blotting analysis. Adjuvant arthritis was induced in Lewis rats with heat-killed *Mycobacterium butyricum*, and the animals were administered with pinosylvin (30 mg/kg, *po*) daily for 21 d after arthritis induction.
Results: In isolated human neutrophils, pinosylvin (10 and 100 μmol/L) significantly decreased the formation of oxidants, both extra- and intracellularly, and effectively inhibited PKC activation stimulated by phorbol myristate acetate (0.05 μmol/L). The inhibition was not due to neutrophil damage or increased apoptosis. In arthritic rats, the number of neutrophils in blood was dramatically increased, and whole blood chemiluminescence (spontaneous and PMA-stimulated) was markedly enhanced. Pinosylvin administration decreased the number of neutrophils (from 69 671±5588/μL to 51 293±3947/μL, P=0.0198) and significantly reduced the amount of reactive oxygen species in blood.
Conclusion: Pinosylvin is an effective inhibitor of neutrophil activity, and is potentially useful as a complementary medicine in states associated with persistent inflammation.

Keywords: pinosylvin; neutrophils; reactive oxygen species; protein kinase C; apoptosis; adjuvant arthritis

Acta Pharmacologica Sinica (2012) 33: 1285–1292; doi: 10.1038/aps.2012.77; published online 30 Jul 2012

Introduction

Neutrophils (neutrophilic polymorphonuclear leukocytes) represent the body's primary line of defense against invading pathogens. Additionally, they have recently been increasingly studied as active participants in the initiation and progression of many pathological conditions, such as ischaemia-reperfusion injury, gout, lupus, acute respiratory distress syndrome and rheumatoid arthritis. All of these conditions are generally accompanied by dysregulated, persistent and excessive activation of neutrophils, resulting in damage of adjacent tissues by neutrophil "destructive hardware", including reactive oxygen or nitrogen species and proteolytic enzymes[1–4]. In rheumatoid arthritis, oxidants can induce cartilage degradation and depolymerize hyaluronan and decrease its lubricative properties; furthermore, they can reduce the protective antioxidant and antiproteinase capacity of synovial fluid and thus participate in joint erosion[1, 5]. Moreover, neutrophils release molecules that can promote inflammation (eicosanoids, chemokines, and cytokines), and the altered recruitment and delayed apoptosis of these cells hinder the resolution of inflammation[2, 4].

From this perspective, novel therapeutic strategies to resolve chronic inflammation are expected to inhibit the formation of neutrophil-derived toxic substances, *eg*, reactive oxygen species, either directly or through enhanced apoptosis. However, inhibition would be directed against extracellularly released oxidants, rather than those formed intracellularly and involved in the initiation of constitutive apoptosis, although the mechanism of radical generation in nonactivated aging neutrophils is not clear[6, 7]. Pharmacological interference with protein kinase C (PKC) activity represents a promising method to modulate

* To whom correspondence should be addressed.
E-mail viera.jancinova@savba.sk
Received 2012-02-28 Accepted 2012-05-22

both neutrophil activity and apoptosis. The isoforms PKCα and βII stimulate the formation of reactive oxygen species at the level of NADPH oxidase activation (by phosphorylation and translocation of $p47^{phox}$ from the cytosol to membranes[8]), while PKCα and δ are involved in antiapoptotic signaling in neutrophils[9, 10].

An inhibitory effect on neutrophil function was discovered for several drugs[11] and natural substances[12–17]. The latter are particularly useful for their low toxicity and ability to control the activity of neutrophils through several mechanisms. For example, *trans*-resveratrol (*trans*-3,4′,5-trihydroxystilbene) repressed the adhesion of neutrophils to endothelial cells, the production of reactive oxygen and nitrogen species, and the liberation of elastase and β-glucuronidase, and it decreased the activities of neutrophil myeloperoxidase and 5- and 15-lipoxygenase (for review see[15]). Regarding the hydrophilic characteristic of resveratrol, its low bioavailability and rapid clearance from the circulation, attention has been focused on its more lipophilic derivatives[18], such as pinosylvin (*trans*-3,5-dihydroxystilbene, Figure 1).

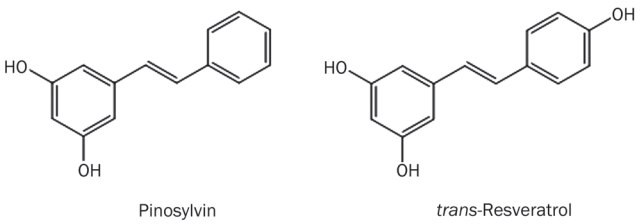

Figure 1. Pinosylvin (*trans*-3,5-dihydroxystilbene) and its related compound *trans*-resveratrol (*trans*-3,4′,5-trihydroxystilbene).

This naturally occurring resveratrol analogue is formed constitutively and after UV irradiation or microbial attack in the wood, needles and leaves of *Pinus* and *Alnus* species[19]. The majority of the data available characterize antifungal, antibacterial and anticancer activities of pinosylvin[20, 21]; however, little is known about its antioxidant and anti-inflammatory effects[22-24]. Previously, we found that pinosylvin improved the effect of methotrexate in experimental arthritis[25, 26], and it intensified the reduction in the number and phagocytic activity of neutrophils, hind paw volume and blood oxidant concentration. In the present paper, the impact of pinosylvin on the viability of human neutrophils and formation of reactive oxygen species was investigated, and protein kinase C activation was examined as an assumed target of pinosylvin action. Moreover, in rats with adjuvant arthritis, the efficacy of pinosylvin was assessed in neutrophils modified by inflammation.

Materials and methods

Chemicals and solutions

Pinosylvin (*trans*-3,5-dihydroxystilbene, 98%) was synthetized and analyzed at the Institute of Organic Chemistry and Biochemistry of the Academy of Sciences of the Czech Republic; details are provided elsewhere[27]. Luminol, isoluminol, PMA (4β-phorbol-12β-myristate-13α-acetate), the Ca^{2+} ionophore A23187, superoxide dismutase, dextran (average MW 464 kDa), zymosan (zymosan A from *Saccharomyces cerevisiae*), firefly luciferase from *Photinus pyralis* and *D*-luciferin sodium salt were purchased from Sigma-Aldrich Chemie (Deisenhofen, Germany); HRP (horseradish peroxidase) and catalase were purchased from Merck (Darmstadt, Germany); and lymphoprep (density 1.077 g/mL) was purchased from Nycomed Pharma AS (Oslo, Norway). Propidium iodide and rh Annexin V-FITC (produced in *E coli* and conjugated with fluorescein isothiocyanate, FITC) was purchased from Bender MedSystems GmbH (Vienna, Austria). *M butyricum* in incomplete Freund's adjuvant, which was used for the induction of adjuvant arthritis, was obtained from Difco Laboratories (Detroit, MI, USA).

Pinosylvin administered to arthritic rats was dissolved in sunflower oil at 30 g/L. For the *in vitro* studies, pinosylvin (1.06 mg) was dissolved in a mixture of 20 μL of 1 mol/L NaOH and 980 μL of Tyrode's solution. The stock solution (5 mmol/L) was further diluted with Tyrode's solution to give pinosylvin sample concentrations of 0.1–100 μmol/L. The corresponding final concentrations of NaOH were 0.4–400 μmol/L; at these concentrations, the solvent agent alone did not reduce the activity or viability of neutrophils. Phosphate-buffered saline (PBS) contained 136.9 mmol/L NaCl, 2.7 mmol/L KCl, 8.1 mmol/L Na_2HPO_4, 1.5 mmol/L KH_2PO_4, 1.8 mmol/L $CaCl_2$, and 0.5 mmol/L $MgCl_2$, pH 7.4. Tyrode's solution consisted of 136.9 mmol/L NaCl, 2.7 mmol/L KCl, 11.9 mmol/L $NaHCO_3$, 0.4 mmol/L $NaH_2PO_4{\cdot}2H_2O$, 1 mmol/L $MgCl_2{\cdot}6H_2O$, and 5.6 mmol/L glucose, pH 7.4. Binding buffer used in flow cytometric analyses contained 10 mmol/L HEPES, 140 mmol/L NaCl, and 2.5 mmol/L $CaCl_2$, pH 7.4.

Whole blood, buffy coat, and neutrophil isolation

Fresh human blood was obtained at the blood bank by venipuncture from healthy male donors (20–50 years) who had not received any medication for at least 7 d. The samples were anticoagulated with 3.8% trisodium citrate (blood to citrate ratio=9:1). Subsequently, the blood was gently mixed with dextran solution (1% final concentration), and erythrocytes were allowed to sediment (1×*g*) at 22 °C for 25 min. A suspension of leukocytes and platelets in plasma (buffy coat) was used for flow cytometric analyses or for neutrophil isolation. For neutrophil isolation, the buffy coat was centrifuged at 500×*g* for 10 min, and the sediment was resuspended in PBS, layered on lymphoprep and centrifuged at 500×*g* for 30 min. Contaminating red blood cells were removed by hypotonic lysis (3 mL of ice-cold deionized water followed by 3 mL of 1.8% NaCl and 4 mL of PBS after 45 s). After centrifugation at 500×*g* for 10 min, neutrophils in PBS were counted, adjusted to a final concentration of 10^4 cells/μL and kept on ice. The final suspension of neutrophils contained more than 96% viable cells, as evaluated by trypan blue exclusion, and was used for a maximum of 2 h – as long as control chemiluminescence remained constant.

Neutrophil count was assessed by a Coulter Counter (Coulter Electronics, High Wycombe, England). In whole blood (diluted 500×), erythrocytes were destroyed with a lysing reagent before counting.

Formation of reactive oxygen species

The oxidative burst of neutrophils was evaluated on the basis of enhanced chemiluminescence[28] in a microtiter plate computer-driven luminometer Immunotech LM-01T (Immunotech, Prague, Czech Republic). The chemiluminescence of whole human blood (diluted 250×) enhanced with luminol (250 μmol/L) was induced with PMA (0.05 μmol/L), opsonized zymosan (0.5 g/L) or the Ca^{2+} ionophore A23187 (1 μmol/L). The chemiluminescence of isolated human neutrophils (5×10^5) was initiated by PMA (0.05 μmol/L) and enhanced with either 5 μmol/L isoluminol (extracellular) or 5 μmol/L luminol in the presence of extracellular scavengers, 100 U/mL superoxide dismutase and 2000 U/mL catalase (intracellular). The formation of oxidants was evaluated on the basis of integrated values of chemiluminescence over 1800 s (isolated neutrophils and A23187-stimulated whole blood) and over 3600 s (whole blood chemiluminescence initiated with PMA or zymosan).

Western blot analysis

The phosphorylation of protein kinase C (PKC) isoenzymes α and βII was detected as previously described[29]. Isolated human neutrophils (5×10^6) were incubated at 37 °C with pinosylvin for 1 min, stimulated with PMA (0.15 μmol/L, 1 min) and rapidly lysed by the addition of solubilization buffer (20 mmol/L Tris-HCl, 5 mmol/L EDTA, 1% Triton, 10% glycerol, 10 mmol/L sodium fluoride, 1 mmol/L sodium orthovanadate, 200 μmol/L PMSF (phenylmethylsulfonylfluoride), 2 μg/mL pepstatin, 2 μg/mL leupeptin, and 2 μg/mL aprotinin, pH 7.4). Then, the samples were sonicated on ice and centrifuged (14 000×*g*, 5 min, 4 °C) to remove unbroken cells. The supernatant was boiled for 5 min with sample buffer (50 mmol/L Tris-HCl, 2% SDS (sodium dodecyl sulphate), 7.5% glycerol, 2.5% mercaptoethanol, and 0.01% bromophenol blue, pH 6.8) and loaded on 9.8% SDS polyacrylamide gels. Proteins (20 μg per lane) were subsequently separated by electrophoresis and immediately transferred electrophoretically to an Immobilon-P Transfer Membrane (Millipore Corp, Badford, MA, USA). Two strips of each membrane were obtained: one for the detection of PKC (area between 60 and 100 kDa) and one for the detection of β-actin (30–60 kDa). β-Actin was used as an internal control to confirm that equal amounts of cellular protein were present in each lane of the gel. Membrane strips were blocked for 60 min with 1% bovine serum albumin in Tris-buffered saline (TBS, 20 mmol/L Tris-HCl, 154 mmol/L NaCl and 0.05% Tween-20, pH 7.5) and subsequently incubated for 60 min in the presence of the following primary antibodies: phospho-PKC alpha/beta II (Thr638/641) antibody (rabbit anti-human, 1:8000, Cell Signaling Technology, Danvers, MA, USA) or β-actin antibody (rabbit anti-human, 1:4000, Cell Signaling Technology, Danvers, MA, USA). The membranes were subsequently washed six times (overall time 40 min) with TBS and incubated for 60 min with the secondary antibody conjugated to horseradish peroxidase (anti-rabbit from donkey, 1:10 000, GE Healthcare Life Sciences, Little Chalfont, UK). After washing, the activity of horseradish peroxidase was visualized using Enhanced Chemiluminescence Western Blotting Detection Reagents (GE Healthcare Life Sciences, Little Chalfont, UK) followed by autoradiography. The bands on the autoradiogram were quantified using the ImageJ program, and the optical density of each PKC band was corrected by the optical density of the corresponding β-actin band.

Measurement of ATP liberation

Pinosylvin cytotoxicity was evaluated on the basis of ATP (adenosine triphosphate) liberation measured by the luciferin-luciferase chemiluminescence method[29]. A suspension of isolated neutrophils (30 000/sample, 30 μL) and 20 μL of Tyrode's solution were incubated with 50 μL of pinosylvin (1–100 μmol/L) for 15 min at 37 °C. Then, 10 μL of a mixture of luciferin (1.6 μg/sample) and luciferase (45 000 U/sample) was added, and chemiluminescence was recorded for 60 s. The chemiluminescence of ATP standards (1–500 nmol/L) was measured in each experiment, and ATP concentrations in samples were calculated from the calibration curve. The total ATP content was assessed immediately after the sonication of neutrophils for 10 s.

Apoptosis assay using flow cytometry

Human plasma buffy coat (see section *Whole blood, buffy coat, and neutrophil isolation*) diluted with binding buffer (460 μL, 200 000 neutrophils) was incubated with 10 μL of pinosylvin (final concentration 1–100 μmol/L) for 10 min at 37 °C. Subsequently, double staining with Annexin V-FITC (5 μL) and propidium iodide (25 μL) was performed, and cells were analyzed on the flow cytometer Cytomics FC 500 (Beckman Coulter, Inc, Brea, CA, USA). From the granulocyte area, 5000 cells were gated, and the percentage of early apoptotic (Annexin positive and propidium iodide negative), late apoptotic (double positive) and viable cells (double negative) was determined according to Perečko *et al*[14].

Effects of pinosylvin in arthritis

Adjuvant arthritis was induced in male Lewis rats (160–180 g, Breeding Farm Dobrá Voda, Slovakia) by a single intradermal injection of heat-killed *M butyricum*[30]. The study was performed in compliance with the Principles of Laboratory Animal Care and was approved by the local Ethics Committee and the State Veterinary and Food Administration of the Slovak Republic. Pinosylvin (30 mg/kg, daily, *po*) was administered over a period of 21 d after arthritis induction; control animals (healthy and arthritic) were treated with the solvent agent (sunflower oil). Each group consisted of 10 rats. The total production of oxidants in neutrophils (spontaneous and stimulated with 0.1 μmol/L PMA) was determined on the basis of luminol-enhanced chemiluminescence and presented as the mean integrated values over 3600 s.

Statistical analysis

All of the values were given as the mean±SEM, and the statistical significance of differences between means was established by Student's *t*-test. *P* values below 0.05 were considered to be statistically significant.

Results

Pinosylvin reduced the oxidative burst of human neutrophils measured in whole blood (Figure 2). It inhibited chemiluminescence initiated by the activation of membrane receptors, increased calcium concentration and the stimulation of protein kinase C at the mean effective concentrations of 10.67±1.07 μmol/L (opsonized zymosan), 12.99±5.64 μmol/L (A23187) and 31.38±8.25 μmol/L (PMA). For comparison, the respective EC_{50} values of the related compound resveratrol were 12.80±0.97 μmol/L, 24.46±7.86 μmol/L and 3.72±0.30 μmol/L (data not shown).

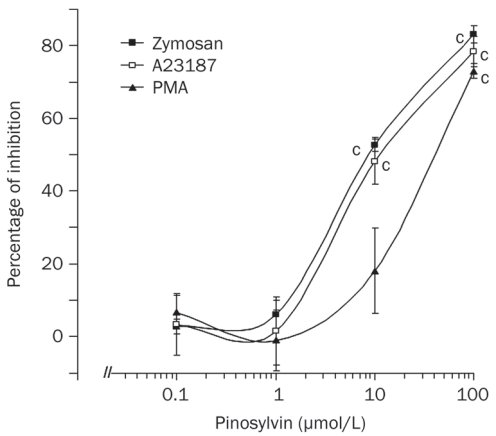

Figure 2. Dose-dependent inhibition of neutrophil chemiluminescence in the presence of pinosylvin. Chemiluminescence, measured in whole blood, was initiated with opsonized zymosan (0.5 g/L), Ca^{2+}-ionophore A23187 (1 μmol/L) or phorbol myristate acetate (PMA, 0.05 μmol/L). Mean±SEM. *n*=6. $^{c}P<0.01$ *vs* control. Mean control values of chemiluminescence, given in relative light units — RLU, were 138375±14776 RLU (zymosan), 26346±3386 RLU (A23187), and 1303872±173251 RLU (PMA).

In isolated neutrophils stimulated with PMA, extra- and intracellular chemiluminescence was recorded separately. As illustrated in Figures 3 and 4, external oxidant formation was much more intensive and reached maximum values sooner than the oxidative burst arising within neutrophils. Pinosylvin decreased both the extracellular and intracellular chemiluminescence of neutrophils at the respective mean effective concentrations of 14.16±1.46 μmol/L and 5.54±1.06 μmol/L; the EC_{50} values assessed for resveratrol were 0.96±0.22 μmol/L and 6.00±0.57 μmol/L, respectively.

The ability of pinosylvin to inhibit chemiluminescence initiated by different mechanisms and its recorded intracellular activity indicated interference of the neutrophil activation

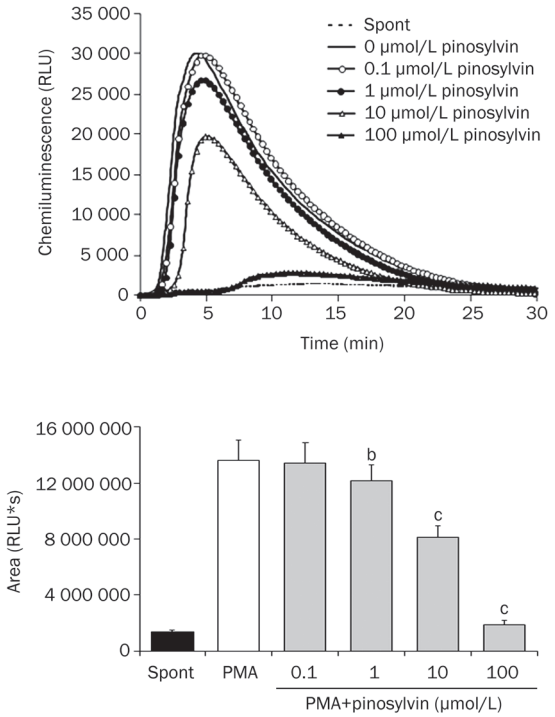

Figure 3. Extracellular chemiluminescence of isolated human neutrophils treated with pinosylvin and stimulated with PMA. Kinetic curves are representative for 6 donors, columns show the mean integral values of chemiluminescence over 1800 s. Mean±SEM. *n*=6. $^{b}P<0.05$, $^{c}P<0.01$ *vs* PMA. Spont, spontaneous chemiluminescence.

cascade by this phytochemical, particularly with a process involved in the effect of all of the stimuli used. Therefore, the influence of pinosylvin on protein kinase C activation was tested in further experiments. The stimulation of neutrophils with PMA was accompanied by increased phosphorylation of the protein kinase C isoenzymes α and βII (Figure 5). Pinosylvin effectively reduced this increase until the values of phosphorylation were comparable with those produced by resting cells.

The observed inhibitory effects were not associated with neutrophil damage because in the presence of pinosylvin no increase in extracellular ATP concentration was recorded (Figure 6). Spontaneous ATP liberation from isolated neutrophils was minimal (approximately 3% of the total ATP content, as determined immediately after complete neutrophil destruction). This amount remained unchanged (or was slightly decreased) after the treatment of neutrophils with pinosylvin (1–100 μmol/L).

As confirmed by flow cytometry (Figure 7 and Table 1), this stilbenoid did not affect spontaneous apoptosis of human neutrophils. Compared with controls, pinosylvin (1-100 μmol/L) did not alter the percentage of viable, apoptotic or dead neutrophils.

To confirm the efficacy of pinosylvin under inflammatory conditions, whole blood chemiluminescence was analyzed in arthritic rats (Figure 8). Adjuvant arthritis was accompanied

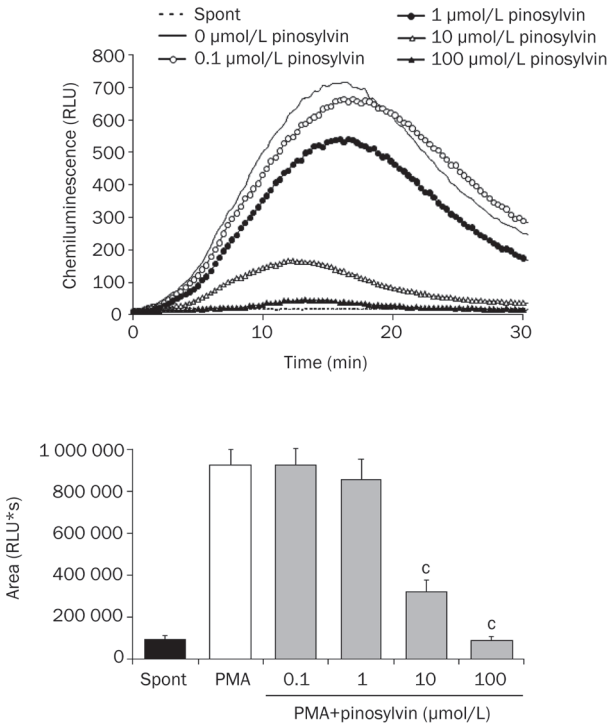

Figure 4. Intracellular chemiluminescence of isolated human neutrophils treated with pinosylvin and stimulated with PMA. Kinetic curves are representative for 6 donors, columns show the mean integral values of chemiluminescence over 1800 s. Mean±SEM. *n*=6, $^{c}P<0.01$ *vs* PMA. Spont, spontaneous chemiluminescence.

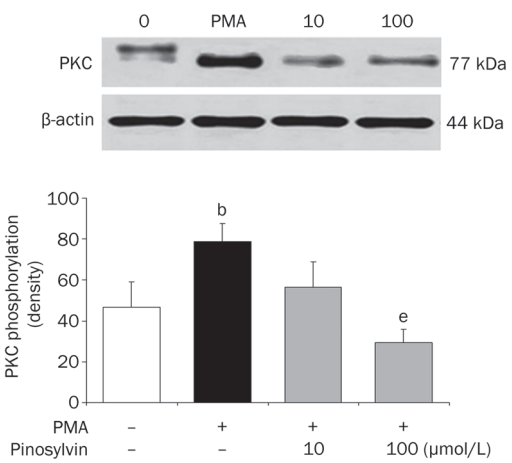

Figure 5. Protein kinase C (PKC) phosphorylation in PMA stimulated human neutrophils treated with 10 and 100 μmol/L pinosylvin (PIN). The degree of phosphorylation is expressed as optical density of PKC bands corrected to β-actin content. Phosphorylated PKC isoenzymes α and βII were isolated by Western blotting and detected by phospho-PKC alpha/beta II (Thr638/641) antibody. Mean±SEM. *n*=8 (neutrophils from 4 donors were examined; in each sample protein separation and PKC detection were performed twice – in two separate experiments), $^{b}P<0.05$ *vs* resting control. $^{e}P<0.05$ *vs* PMA stimulated control. Representative blot manifests elevated phosphorylation of protein kinase C in neutrophils stimulated with PMA, as well as the effect of pinosylvin on this increase.

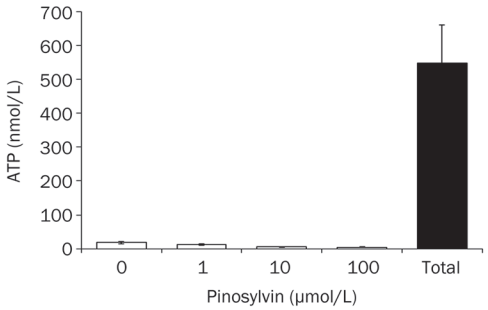

Figure 6. Effect of pinosylvin on the integrity of neutrophil membranes assessed on the basis of ATP liberation. The given values represent the extracellular ATP concentration in samples containing 30 000 neutrophils. Open columns – spontaneous ATP liberation in the absence (0) and in the presence of pinosylvin (1–100 μmol/L); Total, amount of ATP determined immediately after complete neutrophil destruction. Mean±SEM. *n*=8.

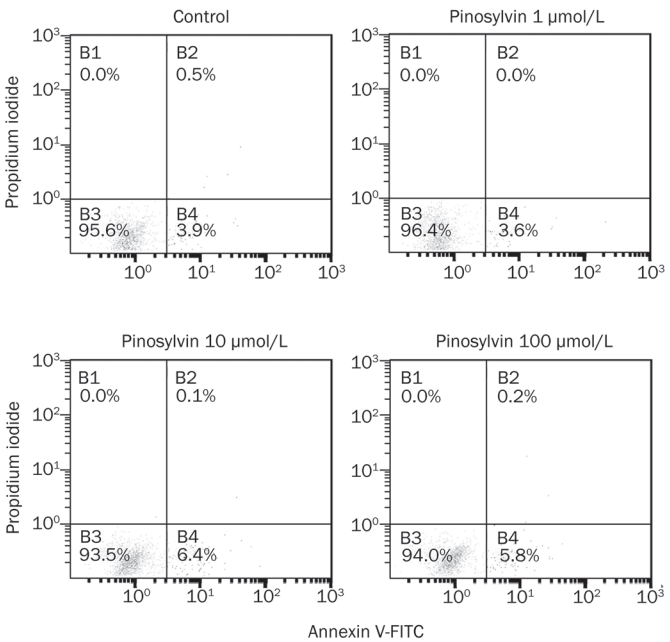

Figure 7. A dot plot of neutrophils stained with propidium iodide and annexin V-FITC indicates cells in three quadrants. Unstained cells are alive and are double negative; they neither express phosphatidylserine on their surface nor do they take up propidium iodide (quadrant B3). Cells stained only with annexin are apoptotic; they have begun to express phosphatidylserine on their surface but have not yet gone through the process that leads to permeabilisation of their cytoplasmic membrane (quadrant B4). Cells stained both with propidium iodide and annexin are necrotic (dead); they take up propidium iodide and also express phosphatidylserine (quadrant B2). Compared to controls, pinosylvin (1–100 μmol/L) did not alter the percentages of viable, apoptotic and dead neutrophils.

by an increased number of neutrophils in the blood and by more pronounced spontaneous and PMA-stimulated chemiluminescence; all of these changes were reduced by oral administration of pinosylvin. The mean neutrophil count, assessed

Table 1. Effect of pinosylvin (PIN) on viability and apoptosis of human neutrophils. Mean±SEM. *n*=8.

	Control	PIN 1 μmol/L	PIN 10 μmol/L	PIN 100 μmol/L
AV^-/PI^- viable cells (%)	90.1±1.6	91.6±1.2	90.1±1.0	85.1±2.9
AV^+/PI^- early apoptotic cells (%)	9.5±1.6	8.0±1.2	9.4±0.9	14.2±2.8
AV^+/PI^+ late apoptotic cells (%)	0.3±0.1	0.3±0.1	0.5±0.2	0.6±0.3

Neutrophil apoptosis was recorded by flow cytometry, using double staining with Annexin-V (A) and propidium iodide (PI).

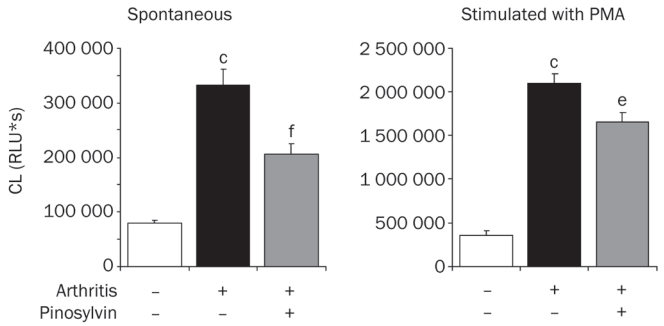

Figure 8. Effect of pinosylvin administration on the formation of reactive oxygen species in adjuvant arthritis. Whole blood chemiluminescence (spontaneous and PMA stimulated) was evaluated on the basis of integral values over 3600 s. Results from three groups of animals are compared — healthy, arthritic without any medication and arthritic animals treated with pinosylvin (30 mg/kg daily, over 21 d). Mean±SEM. *n*=9–10. $^cP<0.01$ *vs* healthy control. $^eP<0.05$, $^fP<0.01$ *vs* arthritic control.

in 1 μL blood, was 16 040±928 (healthy controls), 69 671±5 588 (arthritic animals) and 51 293±3 947 (arthritic rats treated with pinosylvin).

Discussion

The incubation of human neutrophils with pinosylvin resulted in decreased production of reactive oxygen species. Because the effect occurred in the presence of each stimulus used, the interference of a process involved in all mechanisms of chemiluminescence initiation by pinosylvin has been suggested. One of the potential candidates could be the signaling enzyme protein kinase C. Pinosylvin hindered the activation of this enzyme, as indicated by the decreased phosphorylation of protein kinase C isoenzymes α and βII on their catalytic region. Because these isoenzymes participate directly in the activation of neutrophil NADPH oxidase[8], their inhibition may result in reduced oxidant formation and thus explain the decreased chemiluminescence of neutrophils treated with pinosylvin. Similar to resveratrol, a compound related to pinosylvin, protein kinase C inhibition may result from the competition for phorbol ester binding to the C1 domains of the enzyme[31].

Involvement of other mechanisms in the inhibition of chemiluminescence, such as reduced activity of phosphatidylinositol 3-kinase, 5-lipoxygenase, cyclooxygenase, or myeloperoxidase[15, 22], cannot be excluded. However, the repressed expression of NADPH oxidase, which was observed in macrophages treated for 3–6 h with resveratrol[32], seems to be unlikely with respect to the early onset of the pinosylvin effect.

Similarly, the antioxidative activity of pinosylvin may be involved to a lesser extent, because both pinosylvin hydroxyl groups are located in the meta position (with respect to the ethylene bridge of the stilbene molecule), *ie*, in an arrangement that is less favorable for both electron abstraction and the distribution of the unpaired electron[18, 33]. The assessment of lipid peroxyl radical formation[34] and the measurement of human low-density lipoprotein peroxidation[35] confirmed pinosylvin to be a less potent scavenger than resveratrol. Nevertheless, regarding the inhibition of chemiluminescence, we found the activities of these two stilbenoids comparable (*eg*, in neutrophils stimulated with zymosan or the Ca^{2+} ionophore A23187), suggesting that radical scavenging may not be a decisive mechanism of pinosylvin action.

Because activated neutrophils form and liberate reactive oxygen species both extra- and intracellularly[36], it was important to identify which part of the chemiluminescence signal was reduced in the presence of pinosylvin. This stilbenoid was found to be active in both compartments. Radicals formed within neutrophils, which are involved in the redox regulation of signal transduction in neutrophils[3], were reduced more effectively than extracellular oxidants.

The decreased chemiluminescence and inhibited formation of oxidants were not associated with altered neutrophil viability. As shown by the measurement of ATP liberation and the cytometric determination of apoptosis, pinosylvin did not reduce the viability of neutrophils at concentrations up to 100 μmol/L. This result contrasted with its cytotoxic and repressive effect assessed in bacteria, fungi and cancer cells[20, 21] and with the initiation of apoptosis via activation of caspases, which was observed in the presence of other resveratrol derivatives[37].

The efficacy of pinosylvin was further assessed in neutrophils modified by inflammation.

Adjuvant arthritis, a rat model, mimics the immunological and biochemical features of human rheumatoid arthritis. As revealed in the presented experiments, the number of neutrophils increased more than fourfold in adjuvant arthritis, and this increase was accompanied by an elevated concentration of oxidants in the blood. The assessment of chemiluminescence produced by one neutrophil confirmed that neutrophils of arthritic rats responded excessively to PMA stimulation and synthesized more radicals than neutrophils of healthy controls. A similar priming of peripheral neutrophils was observed in

patients with rheumatoid arthritis[38–40]. These alterations were ascribed to the direct effect of proinflammatory cytokines on neutrophil NADPH oxidase activity, which was induced by the increased phosphorylation of $p47^{phox}$, extracellular signal-regulated kinase, and p38 mitogen-activated protein kinase[39, 41].

Orally administered pinosylvin simultaneously decreased the concentration of oxidants and the number of neutrophils, indicating that the beneficial antioxidative effect of this stilbenoid may arise from reduced arthritic neutrophilia (and repressed inflammation) rather than its direct interference with neutrophil activity. The anti-inflammatory activity of pinosylvin, as manifested by reduced hind paw swelling[42], could be ascribed to several mechanisms, such as the reduced synthesis and release of pro-inflammatory mediators, modified eicosanoid synthesis, decreased activity of immune cells and suppressed activation of nuclear factor κB[22–24, 43]. Moreover, resveratrol and α-viniferin, compounds that are structurally related to pinosylvin, were found to induce apoptosis of human rheumatoid arthritis synovial cells[44] and prevent tissue destruction in model arthritis[45]. Finally, the action of pinosylvin might involve decreased expression of inducible NO synthase and reduced formation of nitric oxide, as found in macrophages[26, 46]. This effect may prove beneficial because nitric oxide, if transformed into highly reactive peroxynitrite, can activate proinflammatory signaling[47] and contribute to the pathogenesis of arthritis[48].

Conclusion

Pinosylvin decreased the concentration of oxidants released by activated neutrophils into the extracellular space and the oxidative burst occurring within neutrophils. The inhibition was accompanied by inhibited activation of protein kinase C and the formation of reactive oxygen species in neutrophils. Pinosylvin administered orally reduced the neutrophil count and decreased the concentration of oxidants in the blood of arthritic rats. The observed effects classified pinosylvin as an effective inhibitor of neutrophil activity, which may make it potentially useful as a complementary medicine in pathological states associated with persistent inflammation.

Acknowledgements

We wish to thank Ing Danica MIHALOVA and Mrs Denisa KOMENDOVÁ for their kind assistance and Prof Magda KOUŘILOVÁ-URBANCZIK for English language correcting. The study was supported by grants APVV-0315-07, APVV-0052/10, VEGA-2/0003/10, VEGA-2/0045/11, and GACR-203/07/1227.

Author contribution

Viera JANČINOVÁ, Tomáš PEREČKO, and Katarína DRÁBIKOVÁ contributed to the experimental planning and design, performed the experiments, analyzed and interpreted data, and drafted the manuscript; Rado NOSÁĽ conceived the study and coordinated and supervised the experiments; Juraj HARMATHA and Jan ŠMIDRKAL participated in study conception and synthesized and analyzed pinosylvin.

References

1 Cascao R, Rosário HS, Fonseca JE. Neutrophils: warriors and commanders in immune mediated inflammatory diseases. Acta Reumatol Port 2009; 34: 313–26.
2 Cascao R, Rosário HS, Souto-Carneiro MM, Fonseca JE. Neutrophils in rheumatoid arthritis: More than simple final effectors. Autoimmun Rev 2010; 9: 531–5.
3 Fialkow L, Wang Y, Downey GP. Reactive oxygen and nitrogen species as signaling molecules regulating neutrophil function. Free Rad Biol Med 2007; 42: 153–64.
4 Wright HL, Moots RJ, Bucknall RC, Edwards SW. Neutrophil function in inflammation and inflammatory diseases. Rheumatology 2010; 49: 1618–31.
5 Edwards SW, Hallett MB. Seeing the wood for the trees: the forgotten role of neutrophils in rheumatoid arthritis. Immunol Today 1997; 18: 320–4.
6 El Kebir D, Filep JG. Role of neutrophil apoptosis in the resolution of inflammation. ScientificWorldJournal 2010; 10: 1731–48.
7 Luo HR, Loison F. Constitutive neutrophil apoptosis: Mechanisms and regulation. Am J Hematol 2008; 83: 288–95.
8 Fontayne A, Dang PMC, Gougerot-Pocidalo MA, El Benna J. Phosphorylation of $p47^{phox}$ sites by PKC α, βII, δ, and ζ: Effect on binding to $p22^{phox}$ and on NADPH oxidase activation. Biochmistry 2002; 41: 7743–50.
9 Webb PR, Wang KQ, Scheel-Toellner D, Pongracz J, Salmon M, Lord JM. Regulation of neutrophil apoptosis: A role for protein kinase C and phosphatidylinositol-3-kinase. Apoptosis 2000; 5: 451–8.
10 Kilpatrick LE, Sun S, Mackie DM, Baik F, Li H, Korchak HM. Regulation of TNF mediated antiapoptotic signaling in human neutrophils: role of δ-PKC and ERK1/2. J Leukoc Biol 2006; 80: 1512–21.
11 Burgos RA, Hidalgo MA, Figueroa CD, Conejeros I, Hancke JL. New potential targets to modulate neutrophil function in inflammation. Mini-Rev Med Chem 2009; 9: 153–68.
12 Drábiková K, Perečko T, Nosáľ R, Bauerová K, Poništ S, Mihalová D, *et al*. Glucomannan reduces neutrophil free radical production *in vitro* and in rats with adjuvant arthritis. Pharmacol Res 2009; 59: 399–403.
13 Nosáľ R, Perečko T, Jančinová V, Drábiková K, Harmatha J, Sviteková K. Naturally appearing N-feruloylserotonin isomers suppress oxidative burst of human neutrophils at the protein kinase C level. Pharmacol Rep 2011; 63: 790–8.
14 Perečko T, Drábiková K, Račková L, Číž M, Podborská M, Lojek A, *et al*. Molecular targets of the natural antioxidant pterostilbene: effect on protein kinase C, caspase-3 and apoptosis in human neutrophils *in vitro*. Neuro Endocrinol Lett 2010; 31: 84–90.
15 Alarcón de la Lastra C, Villegas I. Resveratrol as an anti-inflammatory and anti-aging agent: Mechanisms and clinical implications. Mol Nutr Food Res 2005; 49: 405–30.
16 Wu PF, Zhang Z, Wang F, Chen JG. Natural compounds from traditional medicinal herbs in the treatment of cerebral ischemia/reperfusion injury. Acta Pharmacol Sin 2010; 31: 1523–31.
17 Fei R, Fei Y, Zheng S, Gao YG, Sun HX, Zeng XL. Purified polysaccharide from *Ginkgo biloba* leaves inhibits P-selectin-mediated leucocyte adhesion and inflammation. Acta Pharmacol Sin 2008; 29: 499–506.
18 Fan GJ, Liu XD, Qian YP, Shang YJ, Li XZ, Dai F, *et al*. 4,4'-Dihydroxy-*trans*-stilbene, a resveratrol analogue, exhibited enhanced antioxidant activity and cytotoxicity. Bioorg Med Chem 2009; 17: 2360–5.
19 Ludwiczuk A, Saha A, Kuzuhara T, Asakawa Y. Bioactivity guided

isolation of anticancer constituents from leaves of *Alnus sieboldiana* (Betulaceae). Phytomedicine 2011; 18: 491–8.
20 Lee SK, Lee HJ, Min HY, Park EJ, Lee KM, Ahn YH, *et al*. Antibacterial and antifungal activity of pinosylvin, a constituent of pine. Fitoterapia 2005; 76: 258–60.
21 Roupe KA, Remsberg CM, Yáñez JA, Davies NM. Pharmacometrics of stilbenes: Seguing towards the clinic. Curr Clin Pharmacol 2006; 1: 81–101.
22 Adams M, Pacher T, Greger H, Bauer R. Inhibition of leukotriene biosynthesis by stilbenoids from *Stemona* species. J Nat Prod 2005; 68: 83–5.
23 Lee J, Jung E, Lim J, Lee J, Hur S, Kim SS, *et al*. Involvement of nuclear factor-kappaB in the inhibition of pro-inflammatory mediators by pinosylvin. Planta Med 2006; 72: 801–6.
24 Park EJ, Min HY, Ahn YH, Bae CM, Pyee JH, Lee SK. Synthesis and inhibitory effects of pinosylvin derivatives on prostaglandin E_2 production in lipopolysaccharide-induced mouse macrophage cells. Bioorg Med Chem Lett 2004; 14: 5895–58.
25 Bauerová K, Poništ S, Dráfi F, Mihalová D, Paulovičová E, Jančinová V, *et al*. Study of combination of pinosylvin and methotrexate in the model of adjuvant arthritis: Beneficial effect on clinical and non-clinical parameters. Interdisc Toxicol 2010; 3: 32.
26 Jančinová V, Nosáľ R, Lojek A, Číž M, Ambrožová G, Mihalová D, *et al*. Formation of reactive oxygen and nitrogen species in the presence of pinosylvin — an analogue of resveratrol. Neuro Endocrinol Lett 2010; 31: 79–83.
27 Šmidrkal J, Harmatha J, Buděšínský M, Vokáč K, Zídek Z, Kmoníčková E, *et al*. Modified approach for preparing (E)-Stilbenes related to resveratrol, and evaluation of their potential immunobiological effects. Collect Czech Chem Commun 2010; 75: 175–86.
28 Číž M, Pavelková M, Gallová L, Králová J, Kubala L, Lojek A. The influence of wine polyphenols on reactive oxygen and nitrogen species production by murine macrophages RAW 264.7. Physiol Res 2008; 57: 393–402.
29 Jančinová V, Perečko T, Nosáľ R, Košťálová D, Bauerová K, Drábiková K. Decreased activity of neutrophils in the presence of diferuloylmethane (curcumin) involves protein kinase C inhibition. Eur J Pharmacol 2009; 612: 161–6.
30 Bauerová K, Poništ S, Mihalová D, Dráfi F, Kuncírová V. Utilization of adjuvant arthritis model for evaluation of new approaches in rheumatoid arthritis therapy focused on regulation of immune processes and oxidative stress. Interdisc Toxicol 2011; 4: 33–9.
31 Slater SJ, Seiz JL, Cook AC, Stagliano BA, Buzas CJ. Inhibition of protein kinase C by resveratrol. Biochim Biophys Acta 2003; 1637: 59–69.
32 Park DW, Baek K, Kim JR, Lee JJ, Ryu SH, Chin BR, *et al*. Resveratrol inhibits foam cell formation via NADPH oxidase 1-mediated reactive oxygen species and monocyte chemotactic protein-1. Exp Mol Med 2009; 41: 171–9.
33 Queiroz AN, Gomes BAQ, Moraes WM, Borges RS. A theoretical antioxidant pharmacophore for resveratrol. Eur J Med Chem 2009; 44: 1644–9.
34 Stojanovic S, Sprinz H, Brede O. Efficiency and mechanism of the antioxidant action of *trans*-resveratrol and its analogues in the radical liposome oxidation. Arch Biochem Biophys 2001; 391: 79–89.
35 Cheng JC, Fang JG, Chen WF, Zhou B, Yang L, Liu ZL. Structure-activity relationship studies of resveratrol and its analogues by the reaction kinetics of low density lipoprotein peroxidation. Bioorg Chem 2006; 34: 142–57.
36 Karlsson A, Dahlgren C. Assembly and activation of the neutrophil NADPH oxidase in granule membranes. Antioxid Redox Signal 2002; 4: 49–60.
37 Li H, Wu WK, Zheng Z, Che CT, Yu L, Li ZJ, *et al*. 2,3′,4,4′,5′-Pentam ethoxy-*trans*-stilbene, a resveratrol derivative, is a potent inducer of apoptosis in colon cancer cells via targeting microtubules. Biochem Pharmacol 2009; 78: 1224–32.
38 Fairhurst AM, Wallace PK, Jawad AS, Goulding NJ. Rheumatoid peripheral blood phagocytes are primed for activation but have impaired Fc-mediated generation of reactive oxygen species. Arthritis Res Ther 2007; 9: R29.
39 Inaba M, Takahashi T, Kumeda Y, Kato T, Hato F, Yutani Y, *et al*. Increased basal phosphorylation of mitogen-activated protein kinases and reduced responsiveness to inflammatory cytokines in neutrophils from patients with rheumatoid arthritis. Clin Exp Rheumatol 2008; 26: 52–60.
40 Miesel R, Hartung R, Kroeger H. Priming of NADPH oxidase by tumor necrosis factor alpha in patients with inflammatory and autoimmune rheumatic diseases. Inflammation 1996; 20: 427–38.
41 Dang PM, Stensballe A, Boussetta T, Raad H, Dewas C, Kroviarski Y, *et al*. A specific $p47^{phox}$-serine phosphorylated by convergent MAPKs mediated neutrophil NADPH oxidase priming at inflammatory sites. J Clin Invest 2006; 116: 2033–43.
42 Mihalová D, Poništ S, Bauerová K, Nosáľ R, Jančinová V. Comparative study of two stilbene derivatives in the experimental rat model of arthritis based on evaluation of clinical parameters. Interdisc Toxicol 2010; 3: 67.
43 Park EJ, Ahn YH, Pyee JH, Park HJ, Chung HJ, Min HY, *et al*. Suppressive effects of pinosylvin, a natural stilbenoid, on cyclooxygenase-2 and inducible nitric oxide synthase and the growth inhibition of cancer cells. Proc Amer Assoc Cancer Res 2005; 46: 176.
44 Nakayama H, Yaguchi T, Yoshiya S, Nishizaki T. Resveratrol induces apoptosis MH7A human rheumatoid arthritis synovial cells in a sirtuin 1-dependent manner. Rheumatol Int 2012; 32: 151–7.
45 Lee JY, Kim JH, Kang SS, Bae CS, Choi SH. The effects of alpha-viniferin on adjuvant-induced arthritis in rats. Am J Chin Med 2004; 32: 521–30.
46 Harmatha J, Zídek Z, Kmoníčková E, Šmidrkal J. Immunobiological properties of selected natural and chemically modified phenylpropanoids. Interdisc Toxicol 2011; 4: 5–10.
47 Gao Y. The multiple actions of NO. Eur J Physiol 2010; 459: 829–39.
48 Abramson SB. Nitric oxide in inflammation and pain associated with osteoarthritis. Arthritis Res Ther 2008; 10: S2.

Acta Pharmacologica Sinica (2012) 33: 1293–1300
 1671-4083/12 $32.00
www.nature.com/aps

Original Article

Lobolide, a diterpene, blockades the NF-κB pathway and p38 and ERK MAPK activity in macrophages *in vitro*

Xiao-fen LV[1], Si-han CHEN[2], Jie LI[1], Jian-ping FANG[1], Yue-wei GUO[2, *], Kan DING[1, *]

[1]*Glycochemistry and Glycobiology Laboratory, Shanghai Institute of Materia Medica, Chinese Academy of Sciences, Shanghai 201203, China;* [2]*State Key Laboratory of Drug Research, Shanghai Institute of Materia Medica, Chinese Academy of Sciences, Shanghai 201203, China*

Aim: Recent studies have shown that constitutive activation of the nuclear factor κB (NF-κB) plays a key role in chronic inflammation and cancers. The aim of this study was to characterize lobolide, a cembrane diterpene, as a drug candidate targeting the NF-κB signaling pathway.
Methods: A HEK 293/NF-κB-Luc stable cell line was constructed to evaluate the effect of lobolide on NF-κB activation. THP-1 human monocytes and peripheral blood mononuclear cells (PBMCs) from healthy volunteers were tested. Lipopolysaccharide (LPS)-induced TNFα and IL-1β production and activation of the TAK1-IKK-NF-κB pathway were studied using ELISA and Western blot analysis.
Results: In HEK 293/NF-κB-Luc stable cells, lobolide (0.19–50 μmol/L) inhibited NF-κB activation in a concentration-dependent manner with an IC_{50} value of 4.2±0.3 μmol/L. Treatment with lobolide (2.5–10 μmol/L) significantly suppressed LPS-induced production of TNFα and IL-1β in both THP-1 cells and PBMCs. In THP-1 cells, the suppression was partially caused by blockade of the translocation of NF-κB from the cytoplasm to the nucleus via affecting the TAK1-IKK-NF-κB pathway and p38 and ERK MAPK activity.
Conclusion: Lobolide is a potential inhibitor of the NF-κB pathway, which blocks the translocation of NF-κB from the cytoplasm to the nucleus. Lobolide inhibits LPS-stimulated TNFα and IL-1β release, suggesting that the compound might be an anti-inflammatory compound.

Keywords: lobolide; diterpene; monocytes; lipopolysaccharide; NF-κB; TNFα; IL-1β; TAK1; Erk 1/2; p38; inflammation

Acta Pharmacologica Sinica (2012) 33: 1293–1300; doi: 10.1038/aps.2012.100; published online 27 Aug 2012

Introduction

Nonsteroidal anti-inflammatory drugs (NSAIDs) have become one of the most widely used groups of drugs in the history of medicine. It has been estimated that more than 30 million people take NSAIDs daily for relief of symptoms of rheumatoid arthritis, osteoarthritis and other arthritides. The history of NSAIDs can be traced to ancient Egypt, where an extract of willow bark was used to treat inflammation. The active component of the extracts was subsequently identified as the glucoside of salicyl alcohol. Hydrolysis of the carbohydrate moiety produces salicyl alcohol, which can be oxidized to salicylic acid, the actual anti-inflammatory agent[1, 2]. Subsequently, a number of other anti-inflammatory agents have been developed over the past 60 years. These fall into six distinct classes: salicylates, anthranilic acid derivatives, indomethacin and related derivatives, oxicams, phenylalkanoic acid and related derivatives, and pyrazole derivatives[3]. The more traditional NSAIDs, such as aspirin, phenylbutazone, and indomethacin, have excellent anti-inflammatory efficacy and function primarily through a reduction in prostaglandin (PG) synthesis by inhibiting the enzyme prostaglandin endoperoxide synthase. This polypeptide enzyme has both cyclooxygenase and peroxidase activities. It occurs as two isoforms, designated as isoforms 1 and 2, which are referred to as cyclooxygenase (COX-1 and COX-2) in the current literature[4]. COX-1, the constitutive enzyme, is involved primarily in housekeeping functions and is responsible for the production of PGs, while COX-2, the inducible isoform, exclusively modulates inflammatory reactions[5]. NSAIDs inhibit cyclooxygenase activity mainly by

* To whom correspondence should be addressed.
E-mail kding@mail.shcnc.ac.cn (Kan DING);
ywguo@mail.shcnc.ac.cn (Yue-wei GUO)
Received 2012-06-04 Accepted 2012-06-21

inhibiting access of arachidonic acid to the COX active site[6].

NSAIDs also share several unwanted side effects, with the induction of gastrointestinal injury, such as gastric and/or intestinal erosion and/or ulceration with consequent blood loss and anemia, being the most common[7, 8]. These side effects appear to be related to the drugs' inhibition of COX-1 because constitutive expression of COX-2 in normal gastric mucosal tissue is low or absent[9]. However, COX-2 inhibitors may increase the risk of cardiovascular complications, such as heart attack or stroke, especially if they are used for a prolonged time[10]. In this study, we focused on finding NSAIDs that target the nuclear factor-kappa B (NF-κB) signaling pathway, but not COXs.

As an evolutionary conserved family of transcription factors, NF-κB was initially discovered as a regulator of inflammatory responses. In unstimulated immune cells, NF-κB is inactive in the cytoplasm, forming a complex composed of p65 (Rel A), p50 (NF-κB) and an inhibitor of NF-κBα (IκBα)[11]. Through distinct signaling pathways, pro-inflammatory stimuli, such as cytokines and lipopolysaccharide (LPS), converge their signaling on activation of IKKα/β, then phosphorylation and degradation of IκBα. This degradation exposes the nuclear localization signal (NLS) sequences of NF-κB, allowing nuclear translocation of the p50/p65 complex and regulation of the expression of a vast array of genes[12, 13]. Abnormal activation of the transcription factor NF-κB by nuclear translocation of the cytoplasmic complexes plays an important role in some inflammatory diseases via its ability to induce expression of cytokines, chemokines, mediators and immune-related receptor genes. Inhibition of the NF-κB signaling pathway would be an important approach for the treatment of inflammatory diseases.

Lobolide is a cembrane diterpene extracted from the soft coral *Lobophytum* sp of the Lingshui Bay, Hainan Province, China[14]. Soft coral cembrane diterpenes are usually produced as a defense against predators and display cytotoxic, anti-inflammatory, antimicrobial and antiarthritic effects[15]. In the present study, we employed a cell model using luciferase activity regulated by the NF-κB transcription factor to search for new molecules that could suppress NF-κB signaling. Among the candidates, lobolide was identified as an inhibitor of the NF-κB signaling pathway in THP-1 cells. In addition, we further studied the mechanism underlying lobolide's inhibitory activity.

Materials and methods

Preparation of lobolide

Lobolide is a cembrane diterpene, isolated from the *Lobophytum* sp, with a molecular weight of 374 daltons. Its structure (Figure 1) was consistent with previous reports[16]. The purity of this compound was more than 98%, as estimated by high-performance liquid chromatography analysis. Lobolide was dissolved in DMSO (Sigma, St Louis, MO, USA) and stored at -20 °C. For *in vitro* experiments, lobolide was diluted in the culture media specific to the different cells utilized in this study, and the final concentration of DMSO was always 0.1% or lower.

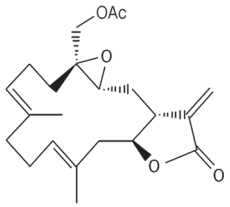

Figure 1. Chemical structure of lobolide.

Generation of a HEK 293/NF-κB-Luc stable cell line

HEK 293 cells with 50%–80% confluence were co-transfected with the pNFκB-TA-Luc vector (Clontech, Palo Alto, CA, USA) and the pcDNA3.1/*myc*-HisB (Invitrogen, Carlsbad, CA, USA) vector at a ratio of 10:1 using Lipofectamine 2000 (Invitrogen, Carlsbad, CA, USA) according to the manufacturer's recommendations. pNFκB-TA-Luc is designed for monitoring NF-κB signaling transduction pathways with four tandem copies of the κB motif linked with the luciferase gene. When the NF-κB transcription factor binds to the κB motif, the luciferase gene is activated and transcribed for expression. Because there is no selectable marker on this plasmid, the pcDNA3.1/*myc*-HisB plasmid was used to supply a selectable marker. After transfection for 12 h, the cells were treated with geneticin (Merck, Darmstadt, Germany). The geneticin-resistant clones were further selected by a luciferase reporter assay, with 1 μg/mL lipopolysaccharide (LPS from *Escherichia coli* O55:B5, Sigma, St Louis, MO, USA) used as a stimulator. The luciferase reporter assay was performed using the Luciferase Assay System (Promega, Madison, WI, USA). Briefly, the cells were lysed with the cell culture lysis reagent, and then, the cell lysates were transferred to 96-well LUMITRAC™ 200 flat bottom plates (Greiner Bio-one, Frickenhausen, Germany). The relative light units (RLUs) were measured immediately after the substrates were added to the cell lysates with a NOVOstar microplate reader (BMG LabTechnologies, Offenburg, Germany). The resultant HEK 293/NF-κB-Luc stable cell lines were maintained in the presence of 0.8 mg/mL geneticin for approximately 2 months.

Short hairpin DNA (shDNA) preparation

shDNA sequences were designed and synthesized by GenePharma (GenePharma Co, Ltd, Shanghai, China) for knockdown of NF-κB/p65 expression. The sequences shown in Table 1 were inserted into the pGPU/GFP/Neo plasmids (GenePharma Co, Ltd, Shanghai, China). The constructed

Table 1. shDNA sequences details of p65 and the negative control.

shDNA	shDNA sequences (sense strand)
Sh p65	5′-GAG TAC CCT GAG GCT ATA ACT-3′
Negative control	5′-GTT CTC CGA ACG TGT CAC GT-3′

pGPU/GFP/Neo-sh p65 plasmids and the negative control (NC) were then transfected into cells.

Reverse transcription-polymerase chain reaction (RT-PCR) and luciferase reporter assay

Transfection of shDNA into the HEK 293/NF-κB-Luc cells (5×10^5/mL in 24-well plates) was performed using Lipofectamine 2000. After transfection for 48 h, the cells were exposed to 1 μg/mL LPS for 6 h. Total RNA was isolated using the TRIzol reagent (Invitrogen, Carlsbad, CA, USA), and 1 μg of RNA was reversely transcribed into cDNA, which was then subjected to 20–30 cycles of PCR (Applied Biosystems, Foster City, CA, USA). The PCR cycles consisted of a 30-s denaturation at 94 °C, a 30-s annealing at 56 °C, and a 30-s extension at 72 °C. The sequences of the PCR primers and the sizes of PCR products are shown in Table 2. RT-PCR was performed in two steps following the instructions included with the RTase M-MLV (RNase H^-) and Taq enzymes (Takara Shuzo, Kyoto, Japan).

Table 2. Primers of p65 and 18S rRNA and their PCR products sizes.

Gene	PCR primers	Products size (bp)
18S rRNA	5′-CGG CTA CCA CAT CCA AGG AA-3′ 5′-GCT GGA ATT ACC GCG GCT-3′	187
p65	5′-CGA CCT GAA TGC TGT GCG GC-3′ 5′-GAT CTC ATC CCC ACC GAG GC-3′	181

For the luciferase reporter assay, the same transfection protocol was used as that for RT-PCR, except that the cells were seeded in 96-well plates. The experiments were repeated thrice.

Cell culture conditions

THP-1 cells (ATCC, TIB-202) were cultured in RPMI-1640 medium (HyClone, Logan, UT, USA) supplemented with 0.05 mmol/L 2-mercaptoethanol and 10% heat-inactivated fetal bovine serum (FBS) (GIBCO-BRL, Grand Island, NY, USA). HEK 293/NF-κB-Luc cells were maintained in Dulbecco's modified essential medium (HyClone, Logan, UT, USA) supplemented with 10% heat-inactivated FBS (GIBCO-BRL, Grand Island, NY, USA). Both cell lines were cultured with 100 U/mL penicillin and 100 g/mL streptomycin and incubated in a humidified atmosphere containing 5% CO_2 at 37 °C.

NF-κB activity inhibition analysis

HEK 293/NF-κB-Luc cells were seeded in 96-well plates at a density of 3×10^5 cells/mL. The cells were first incubated with varying concentrations of lobolide for 15 min, and then, the cells were incubated with LPS (1 μg/mL) for 6 h. Blank and LPS-only controls were also performed; both controls contained 0.1% DMSO (*v/v*), and each treatment was performed in triplicate. The inhibition rate of the compound was calculated using the following formula:

$$\text{Inhibition (\%)}=\frac{RLU_{\text{LPS control}}-RLU_{\text{Compound}}}{RLU_{\text{LPS control}}-RLU_{\text{Blank}}}\times100\%$$

Cytotoxicity assay

THP-1 cells (1×10^4 cells/well) were seeded in 96-well plates and treated with varying concentrations of lobolide for 48 h. A blank control containing 0.1% DMSO (*v/v*) was used, and each experiment was performed triplicate. The cells were exposed to water-soluble WST-8 [2-(2-methoxy-4-nitrophenyl)-3-(4-nitrophenyl)-5-(2,4-disulfophenyl)-2*H*-tetrazolium] (Dojindo Lab, Kumamoto, Japan) for 6 h. The absorbance values were then measured at 450 nm using a microplate reader (BioRad, Hercules, CA, USA). The cytotoxicity of lobolide on the cells was estimated by the following formula:

$$\text{Cytotoxicity (\%)}=\frac{OD_{\text{Blank}}-OD_{\text{Compound}}}{OD_{\text{Blank}}}\times100\%$$

Protein preparation and immunoblotting

THP-1 cells (2×10^6 cells/sample) were washed twice with ice-cold phosphate-buffered saline (PBS). Cell lysates were prepared with radioimmunoprecipitation assay (RIPA) buffer (10 mmol/L Tris, pH 7.4, 150 mmol/L NaCl, 1% Triton X-100, 0.1% deoxycholate, 0.1% sodium dodecyl sulfate, 5 mmol/L ethylenediaminetetraacetic acid), containing 1× complete protease inhibitor cocktail (Sigma, St Louis, MO, USA), 1 mmol/L sodium fluoride (NaF), and 1 mmol/L sodium vanadate (Na_3VO_4). Nuclear proteins were extracted with a CelLytic NuCLEAR Extraction Kit (Sigma, St Louis, MO, USA). The concentrations of whole-cell protein and nuclear protein were determined using the Bio-Rad protein assay kit. The proteins were subjected to SDS-polyacrylamide gel electrophoresis, blotted onto nitrocellulose membranes (Pall Life Sciences, Ann Arbor, MI, USA), and then probed with the following antibodies (Abs): anti-NF-κB p65 (C22B4), anti-IκBα, anti-IKKα, anti-IKKβ, anti-TAK1, anti-phospho-IκBα (Ser32/36) (5A5), anti-phospho-IKKα (Ser180)/IKKβ (Ser181), anti-phospho-TAK1 (Thr184), anti-p38 MAP Kinase, anti-phospho-p38 MAP Kinase (Thr180/Tyr182), anti-Erk1/2 (137F5), anti-phospho-Erk1/2 (Thr202/Tyr204) (197G2), anti-histone H3 (all of the antibodies mentioned above were from Cell Signaling Technology Inc, Beverly, MA, USA) and anti β-actin (Sigma, St Louis, MO, USA). β-Actin was used as a loading control for whole cytoplasmic protein extracts. Histone H3 was used as a loading control for nuclear protein extracts. The blots were developed using Pierce's SuperSignal West Dura Extended Duration Substrate according to the manufacturer's instructions (Thermo Fisher Scientific, Nepean, CA, USA).

PBMC isolation

Peripheral blood mononuclear cells (PBMCs) were isolated from blood samples donated by healthy volunteers by Ficoll-Paque PLUS density centrifugation (Amersham Biosciences,

Uppsala, Sweden). After washing with PBS, PBMCs were ready for the enzyme-linked immunosorbent assay (ELISA).

ELISA

PBMCs were diluted in RPMI-1640, supplemented with 10% heat-inactivated FBS, to 3×10^5 cells/well in 96-well plates and incubated with different concentrations of lobolide for 15 min at 37°C. The cells were then stimulated with LPS (1 μg/mL) for 24 h, and the supernatants were collected and diluted for ELISA quantification. Blank and LPS-only controls, each containing 0.1% DMSO (*v/v*), were also used. The concentrations of the cytokines IL-1β and TNFα were measured using ELISA kits (ExCell, Shanghai, China). The same method was used to determine the relative concentrations of cytokines released by THP-1 cells (1×10^5 cells/well in 96-well plates). Each experiment was repeated thrice.

Indirect immunofluorescence assay and laser scanning confocal microscopy (LSCM) analysis[17]

THP-1 cells, differentiated on coverslips for 24 h by 20 μg/L phorbol 12-myristate 13-acetate (PMA, Sigma, St Louis, MO, USA), were fixed with freshly prepared 4% paraformaldehyde (PFA) for 15 min and permeabilized with 0.3% NP-40 (Sigma, Fluka Chemie AG, Buchs, Switzerland) for 15 min. BSA (3%) was used to block the slides, which were then incubated at 4°C overnight with anti-NF-κB p65 (C22B4) antibody diluted 1:50 in the antibody dilution buffer (ADB) (1×PBS, containing 0.3% Triton X-100 and 1% BSA). Then, the slides were incubated with FITC-conjugated goat anti rabbit IgG (Invitrogen, Carlsbad, CA, USA) (diluted 1:200 in ADB) for 1 h. To identify the nuclei, the FITC-labeled samples were further stained with 25 mg/L propidium iodide (PI) (Sigma, St Louis, MO, USA) for 2 min. Dual-color images were obtained by Olympus Fluoview 1000 laser scanning confocal microscopy (Olympus Fluoview, Mellville, NY, USA).

Statistical analysis

Independent values are expressed as the mean±SD. Significant differences were determined using the two-tailed student's *t* test, with *P* values <0.05 considered significant.

Results

Lobolide blocked NF-κB-driven luciferase expression

HEK 293/NF-κB-Luc stable cell lines were constructed to evaluate the lobolide inhibitory effect on NF-κB activation. The luciferase activity in the stable cell line stimulated by LPS (1 μg/mL) was hundreds of times higher than that in unstimulated cells. To further confirm that the cell model worked well, the HEK 293/NF-κB-Luc stable cell line was transfected with shDNA targeting p65. Small interfering RNA (siRNA) could be synthesized in cells using expression vectors containing a short hairpin structure of DNA. The results demonstrated that luciferase activity was reduced when the expression of p65 was targeted, compared to the negative control (Figure 2). These data indicated that the cell model could be employed to evaluate NF-κB activity after treatment with different compounds. Thus, this cell model was used to screen new anti-inflammatory compounds. Lobolide was shown to have a significant effect on NF-κB activity. To determine the lobolide concentration that results in 50% inhibition (the IC_{50} value), HEK 293/NF-κB-Luc cells were treated with different concentrations of lobolide (0.19, 0.39, 0.78, 1.56, 3.12, 6.25, 12.5, 25, and 50 μmol/L) for 15 min, followed by LPS (1 μg/mL) stimulation for 6 h. Cell extracts in the presence of lobolide were subjected to the luciferase reporter assay. The results showed that NF-κB activity induced by LPS was potently inhibited by lobolide; the IC_{50} value was 4.2±0.3 μmol/L (Figure 3).

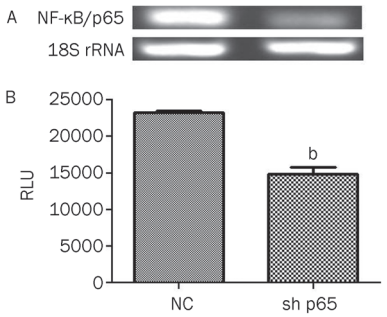

Figure 2. shDNA targeting p65 downregulated p65 expression. (A) HEK 293/NF-κB-Luc cells seeded at a density of 5×10^5 cells/mL in 24-well plates were transiently transfected with shDNA targeting p65 and a random sequence as a negative control (NC) for 48 h and then stimulated with LPS (1 μg/mL) for 6 h. Total RNA was extracted and subjected to RT-PCR analysis to detect cellular levels of p65; 18S rRNA was used as reference. (B) HEK 293/NF-κB-Luc cells (5×10^5 cells/mL) seeded in 96-well plates were transiently transfected with shDNA targeting p65 and the negative control (NC) for 48 h and then induced with LPS (1 μg/mL) for 6 h. The cell lysate was subjected to the luciferase reporter assay. Luciferase expression is represented as relative light units (RLUs). Mean±SD. *n*=3. $^bP<0.05$ *vs* negative control group.

Lobolide attenuated NF-κB/p65 nuclear translocation

To ensure that NF-κB activity inhibition was not due to cytotoxic effects, the cytotoxic effects of varying concentrations of lobolide (0.19, 0.39, 0.78, 1.56, 3.12, 6.25, 12.5, 25, and 50 μmol/L) on THP-1 cells were assessed. Indeed, cell death was induced by lobolide at concentrations above 12.5 μmol/L (Figure 4). THP-1 cells were almost completely killed by 50 μmol/L lobolide. However, cell viability was not significantly affected when the lobolide concentration was equal or less than 12.5 μmol/L (Figure 4). Hence, lobolide concentrations below 10 μmol/L were used in subsequent studies.

The nuclear translocation of NF-κB in THP-1 cells is immediately induced by the bacterial endotoxin LPS. The subcellular localization of NF-κB/p65 was easily detected by indirect immunofluorescence assays and laser scanning confocal microscopy with FITC-labeled NF-κB/p65- (green color in Figure 5A) and PI-stained nuclei (red color in Figure 5A). As shown in Figure 5A, NF-κB/p65 was primarily located in the cytoplasm of the cell in the absence of exogenously provided LPS (as shown in Figure 5A-1a, 1b, 1c). However, the

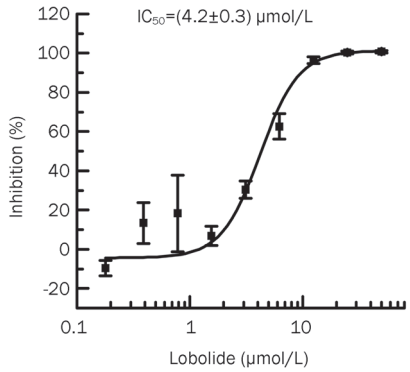

Figure 3. Inhibition of luciferase activity by lobolide. HEK 293/NF-κB-Luc cells (5×10^5 cells/mL) were incubated with varying concentrations of lobolide (0.19, 0.39, 0.78, 1.56, 3.12, 6.25, 12.5, 25, and 50 μmol/L) for 15 min and then exposed to LPS (1 μg/mL) for 6 h. Blank and LPS-only controls, each containing 0.1% DMSO (*v/v*), were used. Cell extracts treated with different concentrations of lobolide were subjected to the luciferase reporter assay. The inhibition rate was calculated using the formula presented in *Materials and methods*. The results were analyzed by the sigmoidal fit function of Origin software (Origin 7.0, Microcal Software, Northampton, MA, USA). Means±SD. *n*=3.

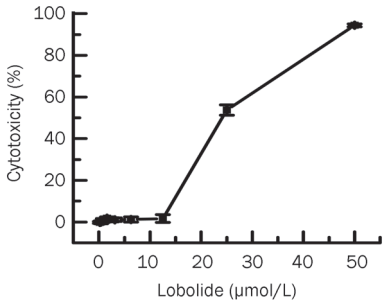

Figure 4. The cytotoxic effects of lobolide on THP-1 cells. THP-1 cells (1×10^5 cells/mL) were incubated with varying concentrations of lobolide (0.19, 0.39, 0.78, 1.56, 3.12, 6.25, 12.5, 25, and 50 μmol/L) for 48 h and then subjected to the WST-8 method, measuring optical density at 450 nm (OD_{450}). A blank containing 0.1% DMSO (*v/v*) was used as the control. The cytotoxicity of lobolide was calculated using the formula found in *Materials and methods*. Mean±SD. *n*=3.

translocation of NF-κB/p65 proteins into the nucleus was significantly induced by LPS (as shown in Figure 5A-2a, 2b, 2c). Interestingly, with the same LPS stimulation, the translocation of NF-κB/p65 from the cytoplasm to nucleus was significantly blocked by pretreatment with 10 μmol/L lobolide (as shown in Figure 5A-3a, 3b, 3c) and 5 μmol/L 2-[(aminocarbonyl) amino]-5-(4-fluorophenyl)-3-thiophenecarboxamide (TPCA-1, Merck, USA) (as shown in Figure 5A-4a, 4b, 4c). TPCA-1 is an inhibitor of IKKα/β and selectively inhibits IKKβ 20-fold more than IKKα[18]. A final concentration of 0.1% (*v/v*) DMSO had no influence on LPS-stimulated NF-κB/p65 translocation to the nucleus, as reported previously (as shown in Figure 5A-5a, 5b, 5c)[19, 20]. Immunoblot analysis showed that the levels of

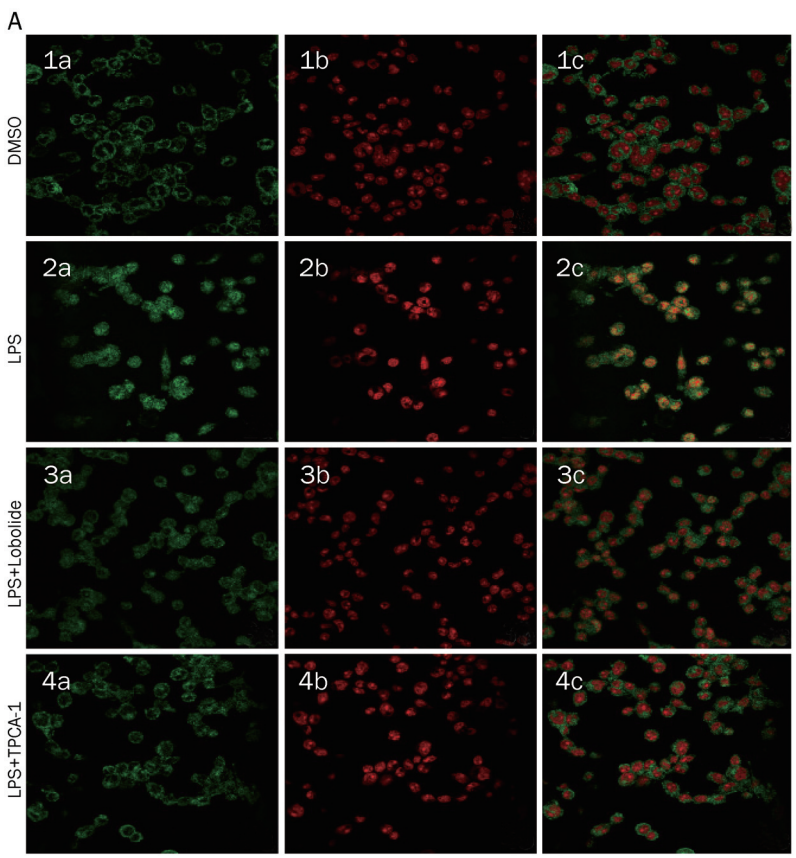

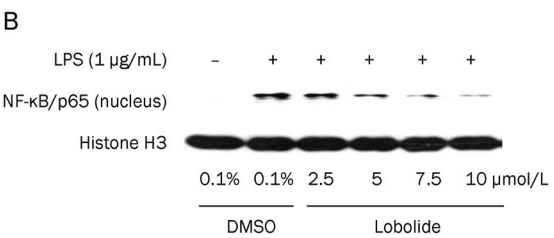

Figure 5. Inhibition of NF-κB/p65 nuclear translocation by lobolide. (A) THP-1 cells were seeded at a density of 2.5×10^5 cells/mL and differentiated by 20 μg/L PMA on coverslips for 24 h. Then, the cells were treated with 10 μmol/L lobolide and 5 μmol/L TPCA-1 for 15 min before being stimulated with 1 μg/mL LPS for 1 h. Blank and LPS-only controls both contained 0.1% DMSO (*v/v*). The subcellular localization of NF-κB/p65 was observed directly by LSCM. a) FITC-labeled NF-κB/p65 in green. b) PI-stained nuclei in red. c) a merged with b. 1) Blank control, without LPS stimulation. 2) LPS-only control. 3) 10 μmol/L lobolide with LPS stimulation. 4) 5 μmol/L TPCA-1 with LPS stimulation. (B) THP-1 cells were seeded at a density of 2×10^6 cells/mL and pretreated with different concentrations of lobolide (2.5, 5, 7.5, and 10 μmol/L) for 15 min prior to treatment with 1 μg/mL LPS for 1 h. Blank and LPS-only controls each contained 0.1% DMSO (*v/v*). Cell lysate was separated by SDS-PAGE and immunoblotted with p65- and histone H3-specific primary antibodies.

NF-κB/p65 proteins in nuclear extracts treated by lobolide were markedly decreased compared to those treated only by LPS (Figure 5B). Furthermore, the NF-κB/p65 nuclear translocation s timulated by LPS was impaired by lobolide in a dose-dependent manner (Figure 5B). These data confirmed that lobolide inhibited LPS-induced NF-κB/p65 nuclear translocation.

Lobolide reduced LPS-induced cytokine production

In most studies, inflammatory cytokine production from mononuclear cells has been investigated by stimulating cells with the gram-negative bacterial component LPS. TNFα and IL-1β are the two main cytokines produced by THP-1 cells and PBMCs in response to LPS stimulation. Their expression is regulated by the NF-κB transcription factor[21]. Because lobolide may inhibit NF-κB translocation from the cytoplasm to the nucleus, we examined TNFα and IL-1β production induced by LPS in the absence or presence of varying concentrations of lobolide. The results showed that lobolide significantly inhibited TNFα and IL-1β production induced by LPS in THP-1 cells and PBMCs in a dose-dependent manner (2.5, 5, 7.5, and 10 μmol/L) (Figure 6). The results also suggested that lobolide effectively blocks the transcription activity of NF-κB. However, the mechanism responsible for this inhibition remains uncertain.

Lobolide attenuated phosphorylation of TAK1 and ERK induced by LPS

The exact mechanism underlying LPS-activated-NF-κB signaling has not yet been fully addressed, but TGFβ-activated kinase (TAK1) and IκB kinases (IKKs) have been suggested to be two important factors[22]. We considered whether lobolide inhibited NF-κB translocation by blocking the TAK1-IKK-NF-κB signaling pathway. To address this question, THP-1 cells were treated with 2.5, 5, and 10 μmol/L lobolide, while cells treated with 2 μmol/L and 5 μmol/L TPCA-1 served as positive controls; Western blot analyses were subsequently performed. Similar to the effects observed in the positive control TPCA-1-treated cells, lobolide inhibited the LPS-activated phosphorylation of TAK1, IKKα/β, and IκBα in a dose-dependent manner and consequently also impaired IκBα degradation (Figure 7A). In addition to the TAK1-IKK-NF-κB signaling pathway activated by LPS in monocytes, two major MAPK signaling pathways, which are the ERK1/2 (the extracellular signal-regulated kinases 1 and 2) and p38 kinase signaling pathways, are also involved in the inflammatory response[23]. Indeed, lobolide also blocked the two MAPK signaling pathways by inhibiting the phosphorylation of ERK1/2 and p38 (Figure 7B).

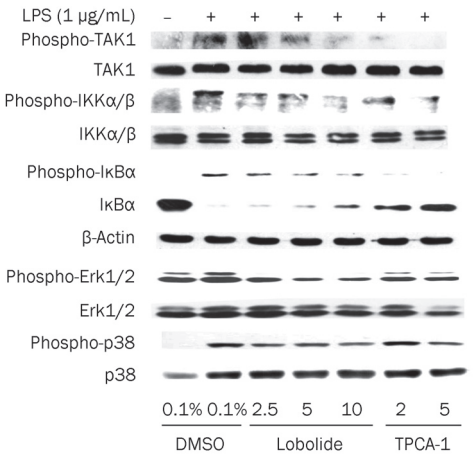

Figure 7. Lobolide inhibited the phosphorylation of TAK1, IKKα/β, IκBα, ERK1/2, and p38 stimulated by LPS and, accordingly, blocked IκBα degradation induced by LPS. THP-1 cells were seeded at a density of 2×10^6 cells/mL and pretreated with different concentration of lobolide (2.5, 5, and 10 μmol/L) and TPCA-1 (2 and 5 μmol/L) for 15 min followed by stimulation with 1 μg/mL LPS for 30 min. Blank and LPS-only controls each contained 0.1% DMSO (*v/v*). TPCA-1 (2 and 5 μmol/L) was used as a positive control. The cell lysate was subjected to SDS-PAGE and probed with antibodies of TAK1, phosphorylated-TAK1, IKKα/β, phosphorylated IKKα/β, IκBα, phosphorylated IκBα, Erk1/2, phosphorylated Erk1/2, p38, and phosphorylated p38 and β-actin (as a loading control).

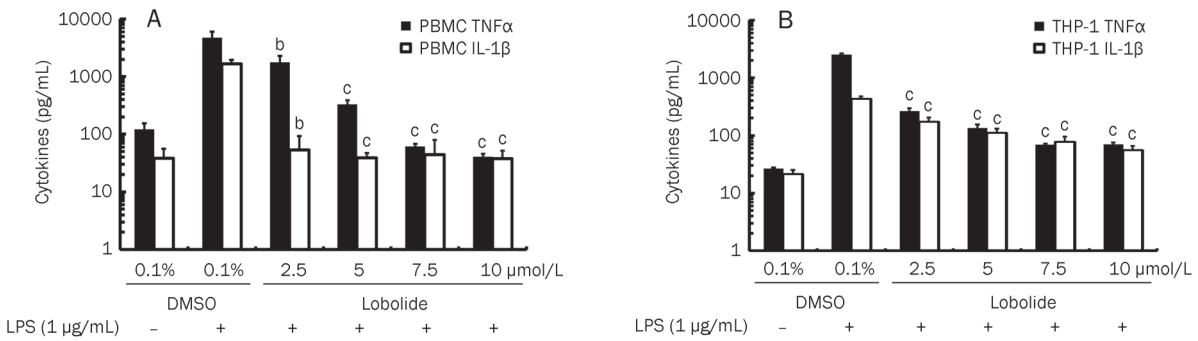

Figure 6. Effects of lobolide on LPS-induced cytokine production in THP-1 cells and PBMCs. THP-1 cells (A) were seeded at a density of 1×10^5 cells/well and pretreated with different concentration of lobolide (2.5, 5, 7.5, and 10 μmol/L) for 15 min, and then stimulated with 1 μg/mL LPS for 24 h. Blank and LPS-only controls each contained 0.1% DMSO (*v/v*). After centrifugation, the supernatants of the cultured media were collected for ELISA. PBMCs (B) were seeded at a density of 3×10^5 cells/well and treated as described in A, followed by ELISA quantitation. $^bP<0.05$, $^cP<0.01$ with respect to treatment with the LPS-only control.

Discussion

NF-κB is an inducible transcription factor that plays an important role in several aspects of human health and disease. The dysregulation of NF-κB and its related pathway is associated with many diseases, ranging from inflammation, cancer, and viral infection to genetic disorders[24]. Because the molecular details are well elucidated, many studies have focused on the pharmacological intervention in the NF-κB signaling pathway for new drug development. The present study focuses on the search for new bioactive molecules with the same purpose. As a member of the diterpenoid group, and extracted from the *Lobophytum* sp, lobolide has previously shown nearly no biological activities except its toxicity to fish. However, we demonstrated that lobolide significantly inhibited the production of the proinflammatory cytokines TNFα and IL-1β at low concentrations (10 μmol/L). These inhibitory effects were mainly caused by a concentration-dependent decrease of NF-κB proteins in the nucleus translocated from the cytoplasm after LPS stimulation. Lobolide also impaired p38 and Erk1/2 MAPKs and TAK1 signaling activated by LPS in monocytes/macrophages. Our data suggest that lobolide might inhibit TNFα and IL-1β products by blocking the NF-κB signaling pathway by attenuating the phosphorylation of TAK, IKK, IKBα, Erk1/2, and p38 as well as IκBα degradation to interfere with p65 translocation from the cytoplasm to nuclei.

TAK1 was first reported as a regulator of MAPK signaling activated by TGF-β[25, 26] and is evolutionally conserved. Drosophila TAK1 is essential for antibacterial innate immunity[27]. When TAK1 is kinase-negatively mutated, the LPS induced NF-κB activation is inhibited[28]. Thus, TAK1 is a critical mediator in the LPS-induced signaling pathway. With LPS stimulated, TAK1 is able to be phosphorylated and form a complex with TRAF6/TAB1/TAB2, which then together translocate from the membrane to the cytosol[22]. The activated TAK1 then phosphorylates downstream targets, such as the IKKs, which leads to the degradation of IκB α and consequent release of NF-κB. TAK1 can also activate p38 by LPS stimulation[29]. Interestingly, p38 also regulates NF-κB-dependent gene transcription by modulating activation of TBP (a TATA-binding protein). TBP is very important for transcriptional regulation of NF-κB by binding to the carboxyl terminus of p65[30]. Thus, we might conclude that the low expression of IL-1β and TNFα in cells treated by lobolide is the combined consequence of inhibition of both TAK1 and p38 phosphorylation and activation. Erk1/2 are other MAP kinases activated by LPS. The activation of Erk1/2 can activate the AP-1 transcription factor and thus lead to iNOS synthesis and NO release, which are well-known inflammatory mediators[31]. Lobolide attenuates p38 and Erk1/2 phosphorylation and activation, the coordination of which is critical for the inflammatory response.

In summary, we showed that the production of the proinflammatory cytokines TNFα and IL-1β was blocked by lobolide. The results revealed that lobolide affected multiple signaling pathways stimulated by LPS in THP-1 cells. Lobolide was implicated in the inhibition of the phosphorylation and activation of TAK1, p38 MAP kinase and Erk1/2 MAP kinase. Thus, lobolide might be a lead compound for anti-inflammatory drug development.

Acknowledgements

The work was supported by the National Natural Science Foundation of China (30870551) and the Key New Drug Creation and Manufacturing Program of China (2009ZX09501-011, 2009ZX09103- 071, and 2009ZX09301-001).

Author contribution

Xiao-fen LV: experimental design, data collection and analysis, manuscript writing; Si-han CHEN: data collection and assembly; Jie LI: data collection and assembly; Jian-ping FANG: conception and design; Yue-wei GUO: preparation of the compounds, conception and design; Kan DING: conception and design, manuscript revision.

References

1 Vane JR, Flower RJ, Botting RM. History of aspirin and its mechanism of action. Stroke 1990; 21: IV12–23.
2 Wright V. Historical overview of NSAIDs. Eur J Rheumatol Inflamm 1993; 13: 4–6.
3 Frolich JC. A classification of NSAIDs according to the relative inhibition of cyclooxygenase isoenzymes. Trends Pharmacol Sci 1997; 18: 30–4.
4 Simon LS. Role and regulation of cyclooxygenase-2 during inflammation. Am J Med 1999; 106: 37S–42S.
5 Suleyman H, Demircan B, Karagoz Y. Anti-inflammatory and side effects of cyclooxygenase inhibitors. Pharmacol Rep 2007; 59: 247–58.
6 Kiefer JR, Pawlitz JL, Moreland KT, Stegeman RA, Hood WF, Gierse JK, *et al*. Structural insights into the stereochemistry of the cyclooxygenase reaction. Nature 2000; 405: 97–101.
7 Lazzaroni M, Bianchi Porro G. Gastrointestinal side-effects of traditional non-steroidal anti-inflammatory drugs and new formulations. Aliment Pharmacol Ther 2004; 20: 48–58.
8 Burdan F, Szumilo J, Klepacz R, Dudka J, Korobowicz A, Tokarska E, *et al*. Gastrointestinal and hepatic toxicity of selective and non-selective cyclooxygenase-2 inhibitors in pregnant and non-pregnant rats. Pharmacol Res 2004; 50: 533–43.
9 Warner TD, Giuliano F, Vojnovic I, Bukasa A, Mitchell JA, Vane JR. Nonsteroid drug selectivities for cyclo-oxygenase-1 rather than cyclo-oxygenase-2 are associated with human gastrointestinal toxicity: a full *in vitro* analysis. Proc Natl Acad Sci U S A 1999; 96: 7563–8.
10 Ray WA, Stein CM, Daugherty JR, Hall K, Arbogast PG, Griffin MR. COX-2 selective non-steroidal anti-inflammatory drugs and risk of serious coronary heart disease. Lancet 2002; 360: 1071–3.
11 Baldwin AS Jr. The NF-kappa B and I kappa B proteins: new discoveries and insights. Annu Rev Immunol 1996; 14: 649–83.
12 Cordle SR, Donald R, Read MA, Hawiger J. Lipopolysaccharide induces phosphorylation of MAD3 and activation of c-Rel and related NF-kappa B proteins in human monocytic THP-1 cells. J Biol Chem 1993; 268: 11803–10.
13 Donald R, Ballard DW, Hawiger J. Proteolytic processing of NF-kappa B/I kappa B in human monocytes. ATP-dependent induction by proinflammatory mediators. J Biol Chem 1995; 270: 9–12.
14 Chen SH, Huang H, Guo YW. Four new cembrane diterpenes from the Hainan soft coral *Lobophytum* sp. Chin J Chem 2008; 26: 5.
15 Li G, Zhang Y, Deng Z, van Ofwegen L, Proksch P, Lin W. Cytotoxic

cembranoid diterpenes from a soft coral *Sinularia gibberosa*. J Nat Prod 2005; 68: 649–52.
16 Kashman Y, Carmely S, Groweiss A. Further cembranoid derivatives from the red sea soft corals alcyonium flaccidum and lobophytum crassum. J Org Chem 1981; 46: 3592–6.
17 Yoo CG, Lee S, Lee CT, Kim YW, Han SK, Shim YS. Effect of acetylsalicylic acid on endogenous I kappa B kinase activity in lung epithelial cells. Am J Physiol Lung Cell Mol Physiol 2001; 280: L3–9.
18 Podolin PL, Callahan JF, Bolognese BJ, Li YH, Carlson K, Davis TG, *et al*. Attenuation of murine collagen-induced arthritis by a novel, potent, selective small molecule inhibitor of IkappaB Kinase 2, TPCA-1 (2-[(aminocarbonyl)amino]-5-(4-fluorophenyl)-3-thiophenecarboxamide), occurs via reduction of proinflammatory cytokines and antigen-induced T cell proliferation. J Pharmacol Exp Ther 2005; 312: 373–81.
19 Olsen LS, Hjarnaa PJ, Latini S, Holm PK, Larsson R, Bramm E, *et al*. Anticancer agent CHS 828 suppresses nuclear factor-kappa B activity in cancer cells through downregulation of IKK activity. Int J Cancer 2004; 111: 198–205.
20 Zhang WJ, Wei H, Hagen T, Frei B. Alpha-lipoic acid attenuates LPS-induced inflammatory responses by activating the phosphoinositide 3-kinase/Akt signaling pathway. Proc Natl Acad Sci U S A 2007; 104: 4077–82.
21 Sharif O, Bolshakov VN, Raines S, Newham P, Perkins ND. Transcriptional profiling of the LPS induced NF-kappaB response in macrophages. BMC Immunol 2007; 8: 1.
22 Shim JH, Xiao C, Paschal AE, Bailey ST, Rao P, Hayden MS, *et al*. TAK1, but not TAB1 or TAB2, plays an essential role in multiple signaling pathways *in vivo*. Genes Dev 2005; 19: 2668-81.
23 Blackwell TS, Christman JW. Sepsis and cytokines: current status. Br J Anaesth 1996; 77: 110–7.
24 Wong ET, Tergaonkar V. Roles of NF-kappaB in health and disease: mechanisms and therapeutic potential. Clin Sci (Lond) 2009; 116: 451–65.
25 Ulevitch RJ, Tobias PS. Receptor-dependent mechanisms of cell stimulation by bacterial endotoxin. Annu Rev Immunol 1995; 13: 437–57.
26 Kobayashi K, Hernandez LD, Galan JE, Janeway CA Jr, Medzhitov R, Flavell RA. IRAK-M is a negative regulator of Toll-like receptor signaling. Cell 2002; 110: 191–202.
27 Vidal S, Khush RS, Leulier F, Tzou P, Nakamura M, Lemaitre B. Mutations in the Drosophila dTAK1 gene reveal a conserved function for MAPKKKs in the control of rel/NF-kappaB-dependent innate immune responses. Genes Dev 2001; 15: 1900–12.
28 Irie T, Muta T, Takeshige K. TAK1 mediates an activation signal from toll-like receptor(s) to nuclear factor-kappaB in lipopolysaccharide-stimulated macrophages. FEBS Lett 2000; 467: 160–4.
29 Lee J, Mira-Arbibe L, Ulevitch RJ. TAK1 regulates multiple protein kinase cascades activated by bacterial lipopolysaccharide. J Leukoc Biol 2000; 68: 909–15.
30 Carter AB, Knudtson KL, Monick MM, Hunninghake GW. The p38 mitogen-activated protein kinase is required for NF-kappaB-dependent gene expression. The role of TATA-binding protein (TBP). J Biol Chem 1999; 274: 30858–63.
31 Kristof AS, Marks-Konczalik J, Moss J. Mitogen-activated protein kinases mediate activator protein-1-dependent human inducible nitric-oxide synthase promoter activation. J Biol Chem 2001; 276: 8445-52.

Acta Pharmacologica Sinica (2012) 33: 1301–1310
 1671-4083/12 $32.00
www.nature.com/aps

Original Article

Migfilin sensitizes cisplatin-induced apoptosis in human glioma cells *in vitro*

Jing FAN[1, #], Yun-wei OU[1, 2, #], Chuan-yue WU[3], Chun-jiang YU[2], Yong-mei SONG[1, *], Qi-min ZHAN[1]

[1]*State Key Laboratory of Molecular Oncology, Cancer Institute and Cancer Hospital, Chinese Academy of Medical Sciences and Peking Union Medical College, Beijing 100021, China;* [2]*Department of Neurosurgery, Beijing Sanbo Brain Hospital, Capital Medical University, Beijing, China;* [3]*Department of Pathology, University of Pittsburgh, PA 15261, USA*

Aim: Filamin binding LIM protein 1, also known as migfilin, is a skeleton organization protein that binds to mitogen-inducible gene 2 at cell-extracellular matrix adhesions. The aim of this study was to investigate the role of migfilin in cisplatin-induced apoptosis in human glioma cells, to determine the functional domains of migfilin, and to elucidate the molecular mechanisms underlying the regulation of cisplatin-related chemosensitivity.

Methods: The human glioma cell lines Hs683, H4, and U-87 MG were transfected with pEGFP-C2-migfilin to elevate the expression level of migfilin. RNA interference was used to reduce the expression of migfilin. To determine the functional domains of migfilin, U-87 MG cells were transfected with plasmids of migfilin deletion mutants. After treatment with cisplatin (40 μmol/L) for 24 h, the cell viability was assessed using the MTS assay, and the cell apoptotic was examined using the DAPI staining assay and TUNEL analysis. Expression levels of apoptosis-related proteins were detected by Western blot analysis.

Results: Overexpression of migfilin significantly enhanced cisplatin-induced apoptosis in Hs683, H4, and U-87 MG cells, whereas down-regulation of migfilin expression inhibited the chemosensitivity of these cell lines. The N-terminal region of migfilin alone was able to enhance the cisplatin-induced apoptosis. However, despite the existence of the N-terminal region, mutants of migfilin with any one of three LIM domains deleted led to a function loss. Furthermore, apoptotic proteins (PARP and caspase-3) and the anti-apoptotic protein Bcl-xL were modulated by the expression level of migfilin in combination with cisplatin.

Conclusion: The LIM1-3 domains of migfilin play a key role in sensitizing glioma cells to cisplatin-induced apoptosis through regulation of apoptosis-related proteins.

Keywords: filamin binding LIM protein 1 (migfilin); glioma; cisplatin; apoptosis; PARP; caspase-3; Bcl-xL

Acta Pharmacologica Sinica (2012) 33: 1301–1310; doi: 10.1038/aps.2012.123; published online 17 Sep 2012

Introduction

Glioma, the most common type of brain tumor, originates from glial cells of the central nervous system[1]. Glioblastoma multiforme (GBM) is the grade IV glioma that represents the most invasive form of malignant brain tumors. The growth of glioblastoma cells exhibits infiltration into contiguous tissue throughout the brain, which challenges the complete resection of gliomas and might be partially responsible for the high rates of disease recurrence. Thus, in spite of extensively applied multimodal therapies, glioblastoma patients commonly receive a poor prognosis with median survival duration of less than 14 months[1–3]. However, in recent years, targeted therapy has provided novel therapeutic insights into improving the sensitivity of malignant cells to systemic radiotherapy or chemotherapy[2].

The connection between the extracellular matrix (ECM) and adjacent cells plays a significant role in cell fate determination, including differentiation, proliferation, migration and apoptosis[4]. Filamin binding LIM protein 1 (FBLIM1), also known as migfilin, is characterized as a skeleton organization protein that binds to mitogen-inducible gene 2 (Mig-2) at cell-ECM adhesions[5–7]. It has been elucidated that migfilin colocalizes with Mig-2 and binds to Mig-2 through its C-terminal domain, which is functionally required for the morphological maintenance of cells[5]. Moreover, the N-terminus of migfilin mediates integrin activation through competitively binding to the site of filamin immunoglobulin-like domain IgLFN21, disaggregating the filamin/integrin complex and promoting talin/integrin interaction[8, 9]. Notably, migfilin consists of

# These authors contributed equally to this work.
* To whom correspondence should be addressed.
E-mail ymsong.2008@gmail.com
Received 2012-05-24 Accepted 2012-07-20

three structural parts, which possess disparate functions and act as indispensable biding domains, including an N-terminal region, a central proline-rich region and a C-terminal region. The C-terminal region has three sequential LIM domains[8]. In addition, two types of migfilin isoforms have been differentiated as migfilin(s) and FBLP-1[4, 8]. Migfilin(s) is a splicing variant with a proline-rich region deleted, resulting in the loss of the VASP binding site[4, 5]. FBLP-1 is missing the third LIM domain, which most likely interferes with the interaction of Mig-2[4]. Thus, it appears that the functional domains of migfilin, partially presented in migfilin variants, are responsible for distinct downstream signaling through binding to corresponding proteins.

Currently, the DNA-alkylating agent temozolomide is widely used to treat glioblastoma patients, showing a quite modest survival benefit[10, 11]. Unfortunately, no effective second-line chemotherapy drug can be utilized for glioblastoma patients when chemoresistance to temozolomide occurs[12]. Meanwhile, the mechanism of chemoresistance to regular chemotherapeutic agents is poorly understood[10, 12]. Cisplatin is an anti-cancer drug that specifically causes DNA damage, including DNA interstrand and intrastrand cross-links, and is widely applied for the treatment of malignant solid tumors[13, 14]. Overcoming the ineffectiveness of cisplatin in gliomas and possibly providing an alternative therapeutic strategy for glioma patients would be beneficial. In this study, we report that migfilin plays an important role in sensitizing glioblastoma cells to cisplatin-induced apoptosis, which might be a novel therapeutic target for gliomas.

Materials and methods

Cell lines and culture conditions

As previously described, the human glioma cell lines Hs683, H4, and U-87 MG (purchased from Cell Resource Centre, IBMS, CAMS/PUMC), were cultured in DMEM (GIBCO) culture medium containing 10% fetal bovine serum (GIBCO)[15]. Cells were incubated at 37 °C in a humidified atmosphere with 5% CO_2.

Reagents

Mouse monoclonal anti-migfilin antibody was produced as previously described[5]. Antibodies specific to Bcl-xL, Bcl-2, Caspase-3, and PARP were purchased from Cell Signaling Technology Inc. Anti-p53 antibody was purchased from Santa Cruz Biotechnology Inc. Anti-beta-actin antibody was obtained from Sigma. Goat anti-mouse IgG and goat anti-rabbit IgG were purchased from Promega Inc. The anti-cancer drug cisplatin was diluted to the concentration of 1 mg/mL (obtained from Cancer Hospital, Chinese Academy of Medical Sciences).

Plasmids, siRNAs and transient transfections

The plasmids containing different types of cDNAs of migfilin deletion mutants, which were inserted into pEGFP-C2 vectors encoding green fluorescent protein (GFP), were generated by Clontech[16]. The siRNAs utilized were as follows: migfilin siRNA (5′-AGGGGCAUCCACAGACAUCTT-3′) and control siRNA (5′-UUCUCCGAACGUGUCACGU-3′). U-87 MG cells were seeded and cultured without antibiotics at 37 °C overnight. Cells were then transfected with plasmids or siRNAs using Lipofectamine 2000 (Invitrogen) in serum-free DMEM. After a 4-h incubation, the serum-free culture medium was changed to DMEM with 10% FBS. Cells were then incubated for 24–48 h in preparation for subsequent assays.

MTS assay

Cells were seeded into 96-well culture plates at 5×10^3 cells per well, incubated overnight, and transfected with plasmids or siRNAs. At 24 h post-transfection, cisplatin was supplemented in the DMEM medium at a final concentration of 40 umol/L, and cells were maintained for 24 h. Twenty microliters of MTS (CellTiter 96 aqueous one solution reagent, Promega) diluted in 100 μL of culture medium was added to each well of the 96-well culture plates. Cells were incubated for 2 h, and then the absorbance of each well at 490 nm was recorded using a 96-well plate reader (Bio-Rad Inc). All of the experiments were performed in triplicate and repeated three times.

DAPI staining

Cells were cultured on glass coverslips in 6-well plates for 24 h, transfected with plasmids or siRNAs and then treated with or without cisplatin (following the drug treatment described above). Cells subsequently were fixed with ice-cold 100% methanol overnight at 4 °C. After triple washes in phosphate-buffered saline (PBS) for 5 min each, cells were incubated with 100 nmol/L DAPI (Sigma) for 5 min at room temperature in the dark. Following triple rinses in PBS for 5 min each, coverslips were placed on slides and the edges sealed. Slides were viewed using upright fluorescence microscopy (BX51, Olympus) and pictures were captured by the Image-Pro Discovery software. Values were calculated in at least 9 different views and presented as percentage of positive apoptotic cells stained.

TUNEL apoptosis assay

TdT-mediated dUTP-biotin nick-end labeling (TUNEL) is a method used for apoptosis detection by determining the exposure end of the fragmentation of nuclear chromatin, which is one of the criteria of late stage apoptosis. The *in situ* cell death detection kit POD (Roche) was used to determine early stage apoptotic cells.

Western blotting

Eighty micrograms of protein extracts was loaded and separated by 10% SDS-PAGE gel (100 V, 1 h) and then transferred to PVDF membrane (12 V, 2 h). After blocking with 2% bovine serum albumin (BSA) at room temperature for 30 min, the membrane was incubated overnight with specific primary apoptosis-related antibodies, such as anti-migfilin (1:1000), anti-Bcl-xL (1:500), anti-Bcl-2 (1:500), anti-PARP (1:500), anti-Caspase-3 (1:500), and anti-p53 (1:1000). Mouse anti-beta-actin (1:5000) monoclonal antibody was used as control with a 1 h

incubation. Next, goat-anti-mouse IgG (1:2000) and goat-anti-rabbit IgG (1:3000) conjugated with horseradish peroxidase (HRP) were used to probe the membrane at room temperature for 1 h. The membrane was rinsed in triplicate in PBS/Tween 0.1% for 5 min each. The chemiluminescent substrate was then added to the membrane. Photographs were taken by Image Reader LAS-4000 (LAS-4000, Fujifilm Inc.) and analyzed by Multi Gauge V3.2 software.

Statistic analysis

Data were presented as the mean±SD. For the comparison of two groups, we used the Student's *t*-test to determine statistically significant differences. *P* values less than 0.05 were considered to be statistically significant.

Results

Migfilin sensitizes cisplatin-induced apoptosis in glioma cells

We first investigated whether migfilin played an important role in the cisplatin-induced apoptosis in gliomas. The human glioma cell lines Hs683, H4, and U-87MG were transiently transfected with the pEGFP-C2-migfilin plasmid, causing migfilin overexpression, and also with migfilin siRNA, leading to the knockdown of migfilin (Figures 1A, 1B, and 1C). Using dose-response experiments, we determined that the final treatment concentrations of cisplatin at 35, 50, and 40 μmol/L caused 50% cell death in Hs683, H4, and U-87MG cells, respectively.

With the treatment of cisplatin, cell viability rates of the cell lines Hs683, H4, and U-87 MG were significantly reduced when migfilin expression levels were upregulated ($P<0.05$, $P<0.05$, and $P<0.01$, respectively) (Figures 1D, 1E, and 1F). The viability rates of Hs683, H4, and U-87 MG cells were markedly increased with reduced expression levels of migfilin after cisplatin treatment ($P<0.05$, $P<0.05$, and $P<0.05$, respectively) (Figure 1D, 1E, and 1F).

Morphological evaluation using DAPI staining was performed to analyze the rates of apoptotic cells showing nuclear condensation and fragmentation. Significant increases in cisplatin-induced apoptotic cells in the cell lines Hs683, H4, and U-87 MG were detected when expression levels of migfilin were elevated ($P<0.01$, $P<0.05$, and $P<0.05$, respectively) (Figures 1G, 1H, and 1I). However, apoptotic cell levels decreased significantly in migfilin-knockdown groups in Hs683, H4, and U-87 MG cells, in contrast to respective cell line control groups ($P<0.05$, $P<0.05$, and $P<0.05$, respectively) (Figures 1G, 1H, and 1I).

In addition, we observed similar results using the TUNEL staining assay. After exposure to cisplatin, the level of early-stage-apoptotic Hs683, H4, and U-87 MG cells was positively correlated with migfilin expression levels (Figures 2A, 2B, and 2C). However, the modulation of migfilin did not directly influence the apoptotic rates of the glioma cells without cisplatin supplement. Therefore, migfilin can sensitize cisplatin-induced apoptosis, whereas downregulation of migfilin can inhibit cisplatin-induced apoptosis in glioma cells.

The LIM domain of migfilin plays a key role in cisplatin-induced apoptosis

To assess the functional domains of migfilin that affect the chemosensitivity of glioma cells, we transfected cells with various deletion-mutants of migfilin. Specifically, plasmids encoding different types of GFP-tagged migfilin mutants[16] were transfected to express mutant forms of migfilin in the U-87 MG cell line. As shown in Figure 3, migfilin(s), a splicing variant of migfilin, lacks a proline-rich region. PR-LIM1-3 lacks the N-terminal region, whereas the vector N-ter only expresses the N-terminal residues of migfilin. LIM1-3 lacks of the N-terminus and the proline-rich regions, whereas ΔLIM1N possesses a mutant LIM1 domain in addition to the mutations of the LIM1-3 vector. The C243 and C306 vectors possess the LIM2 domain mutant and the LIM3 domain mutant, respectively.

Western blotting was conducted to detect GFP protein expression levels in migfilin-mutant transfectants to assess the efficacy of the transient transfections (Figure 4A). As with wild-type migfilin, U-87 MG cells transfected with migfilin(s), N-ter, PR-LIM1-3, and LIM1-3 demonstrated decreased survival rates when treated with cisplatin ($P<0.05$) (Figure 4B). Moreover, migfilin(s), N-ter, PR-LIM1-3, and LIM1-3 vector transfectants showed increased apoptotic cell rates when treated with cisplatin, compared to treated control vector transfectants (approximately 1.71-fold, 2.41-fold, 1.59-fold, and 2.24-fold changes, respectively; $P<0.05$). In contrast, ΔLIM1N, C243 and C306 vector transfectants did not significantly differ from the control group ($P>0.05$) (Figure 4C). TUNEL-stained apoptotic areas were significantly increased in cisplatin-treated cells transfected with migfilin(s), N-ter, PR-LIM1-3, and LIM1-3 vectors ($P<0.05$), and apoptotic areas were relatively static in cells transfected with the ΔLIM1N, C243, and C306 vectors ($P>0.05$) (Figure 4D). Therefore, we observed that the N-terminus alone affects cisplatin-induced apoptosis in U-87 MG cells. In addition, cells transfected with PR-LIM1-3 and LIM1-3 vectors containing a deleted N-terminal region were also sensitive to cisplatin-induced apoptosis. Furthermore, we found that cell transfection with the C243 and C306 vectors, which possess the entire length of the N-terminus but contain mutated LIM domains, led to a loss of protein function, thus demonstrating that the C-terminal LIM domains may play a key role in wild-type migfilin and migfilin(s) protein activities. Furthermore, mutants of migfilin with any one of LIM domain deletions also resulted in function loss, indicating the importance of the integrity of all three LIM domains.

Migfilin enhances cisplatin-induced apoptosis through the regulation of Bcl-xL and Caspase-3 expression

To investigate the underlying molecular mechanisms involved in the cisplatin-related sensitivity of U-87 MG cells, we detected expression levels of apoptosis-associated proteins in the cellular extracts of migfilin transfectants. With strict efficacy control of transient transfection with vectors and siRNA (Figure 5A and 5C), we found that without cisplatin treat-

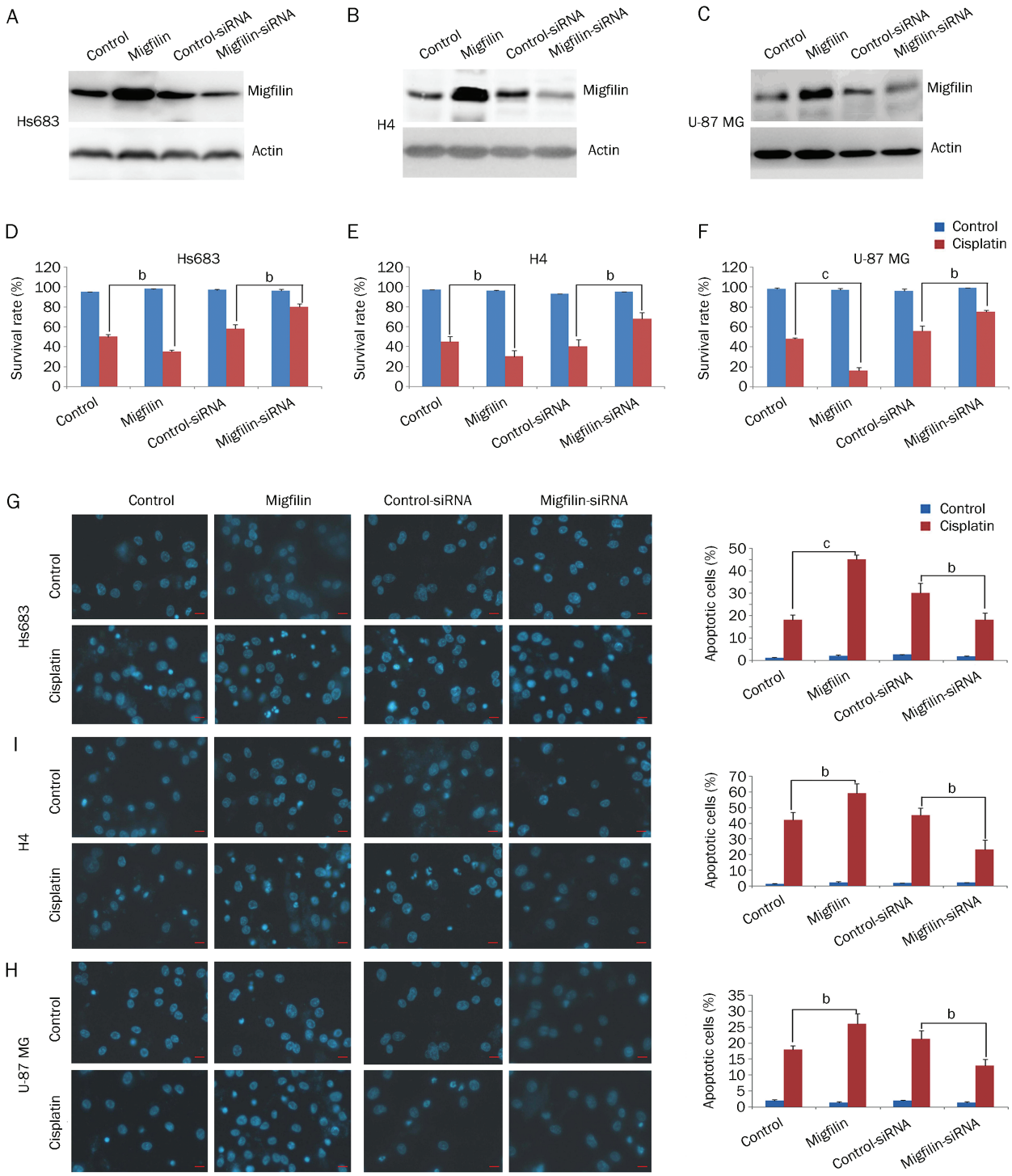

Figure 1. Regulation of migfilin sensitizes cisplatin-induced apoptosis. (A) Hs683 cells, (B) H4 cells, and (C) U-87 MG cells were examined for expression levels of migfilin by Western blotting after transfection of control vector, pEGFP-C2-migfilin vector, control siRNA, and migfilin siRNA, respectively. (D) Hs683 cells, (E) H4 cells, and (F) U-87 MG cells were examined for the effects of migfilin expression on cell viability and were analyzed by the MTS viability assay. Cells were treated with cisplatin for 24 h. (G) Hs683 cells, (H) H4 cells, and (I) U-87 MG cells were analyzed by DAPI staining for cisplatin-sensitivity. Apoptotic cells were stained with light blue (400×objective). The scale bars stand for 10 μm. Mean±SD. n=3. $^{b}P<0.05$, $^{c}P<0.01$ *vs* control.

ment, there were no alterations in the expression of apoptotic proteins such as PARP and Caspase-3 in migfilin transfectants (Figure 5B). However, with cisplatin treatment, regulation of migfilin was positively related to the expression of cleaved

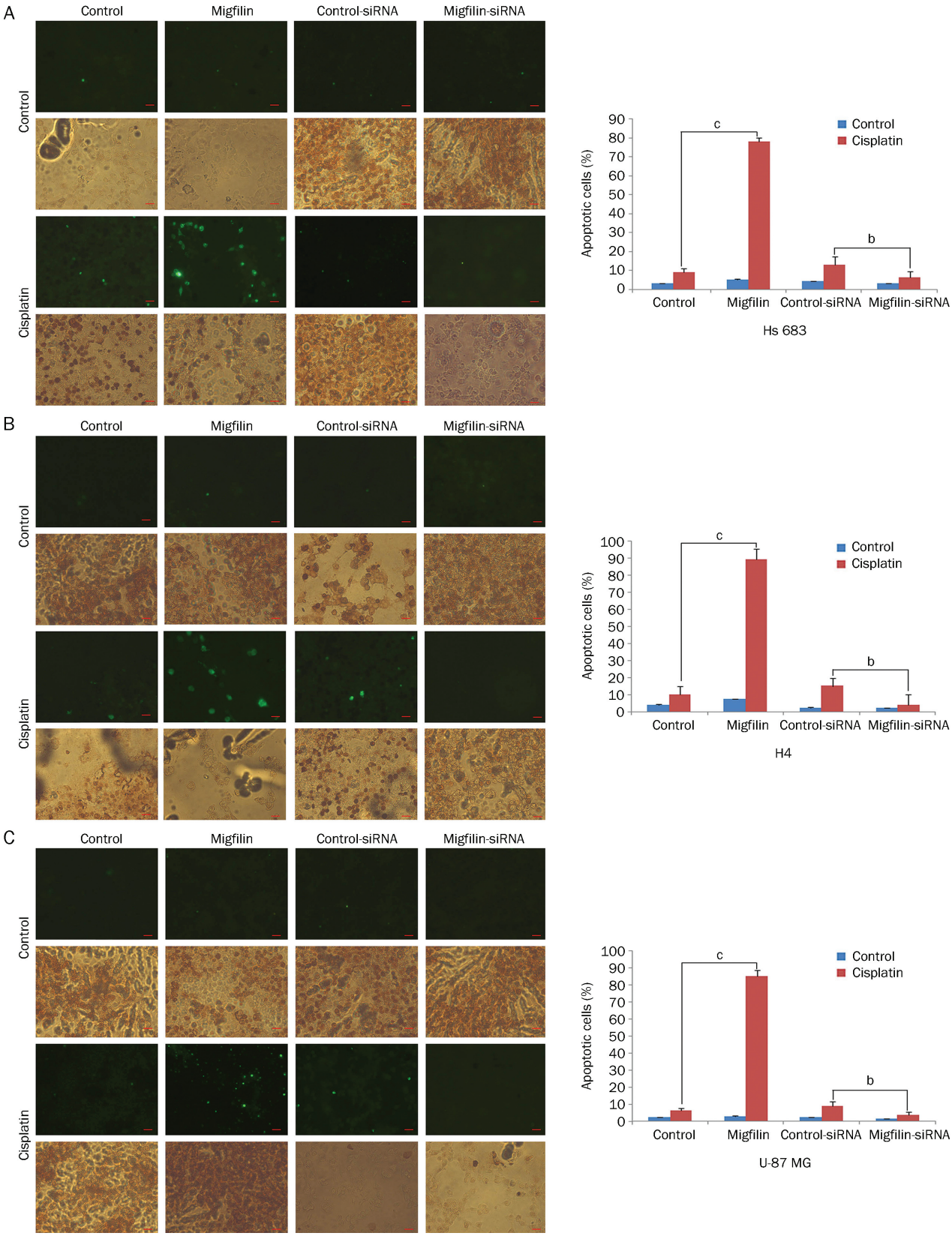

Figure 2. Regulation of migfilin sensitizes cisplatin-induced apoptosis. (A) Hs683 cells, (B) H4 cells, and (C) U-87 MG cells were analyzed by the TdT-mediated dUTP-biotin nick-end labeling (TUNEL) assay for the detection of early-stage-apoptotic cells. Apoptotic cells were determined by both DAB-stained positive areas (brown areas) and fluorescein-stained areas (green areas) (400×objective). The scale bars stand for 20 um. Apoptotic cell rates were calculated under 9 different views. Mean±SD. n=3. $^{b}P<0.05$, $^{c}P<0.01$ *vs* control.

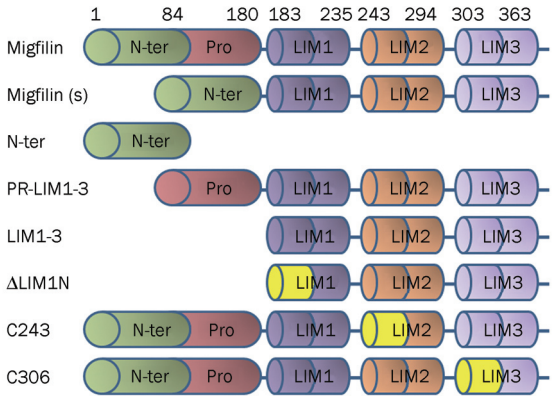

Figure 3. Schematic structure of the wild-type migfilin and different deletion mutants of migfilin.

PARP and cleaved Caspase-3 (Figure 5B).

Moreover, we observed that after exposure to cisplatin, the migfilin-mutant transfectants, including migfilin(s), N-ter, PR-LIM1-3, and LIM1-3, showed increased expression of cleaved PARP and cleaved Caspase-3, compared to the control group, whereas ΔLIM1N, C243, and C306 transfectants had no significant impact on the expression of apoptotic proteins (Figure 5D).

We further investigated upstream apoptosis-related proteins. Expression levels of Bcl-2 and p53 showed no differences in migfilin-overexpression and migfilin-knockdown transfectants with or without cisplatin treatment (Figure 6A). With cisplatin treatment, expression of the anti-apoptotic protein Bcl-xL was negatively associated with the expression level of migfilin (Figure 6A). Transfectants of functional migfilin-mutant vectors, including migfilin(s), N-ter, PR-LIM1-3, and LIM1-3, consistently resulted in the downregulation of Bcl-xL (Figure 6B). Thus, it has been suggested that migfilin plays an important role in the chemosensitivity of glioma cells through modulating Bcl-xL and Caspase-3 expression.

Discussion

Programmed cell death (PCD) has been regarded as a key point in development, and PCD disorders play a role in a wide range of diseases, such as neuro-degeneration, autoimmune diseases, cardiovascular diseases, and cancer[17]. Apoptosis-resistance, growth signal autonomy and insensitivity to anti-growth signals are major factors in the malignant transformation of cells, ultimately leading to unlimited cell proliferation[18]. In this study, we have demonstrated that migfilin plays a key role in regulating cisplatin-induced cellular apoptosis in glioblastoma cells. In addition, we found that U-87 MG cells transfected with N-terminus, PR-LIM1-3 and LIM1-3 vectors containing mutant migfilin were sensitized to cisplatin-induced apoptosis. However, C243 and C306 vector transfectants that contained a full length N-terminus and mutated LIM domains led to a function loss. Therefore, the LIM domain likely plays a key role in wild-type migfilin and migfilin(s) protein activities. It is also probable that the N-terminus fragment is involved in a different mechanism of regulating chemosensitization than the LIM region. We speculate that the LIM1-3 domain might function to influence the conformational space or protein-binding sites of the N-terminus to ultimately perform the regulation of cisplatin-induced apoptosis in wild-type migfilin. Moreover, in addition to interacting with Mig-2[5], the C-terminal LIM domains have been implicated in the localization of migfilin to cell-cell adhesions through regulation of the cadherin–β-catenin complex[4, 16]. Previous studies have reported that the regulation of cell-cell junctions by E-cadherin could influence cisplatin-based chemoresistance[19–21]. In human glioma cells, expression levels of E-cadherin, β-catenin and PARP are regulated in ZEB2-mediated cellular apoptosis[22]. Therefore, it seems likely that the LIM domain of migfilin participates in cisplatin-induced apoptosis via remodeling of cell-cell or cell-matrix adhesions.

In addition to acting as a focal adhesion protein involved in cell-cell and cell-ECM adhesion, migfilin is a candidate oncogene that has distinct potential in becoming a biological marker of human leiomyosarcomas (LMS)[23]. In human mammary epithelial cells, downregulation of migfilin directly leads to anoikis by interacting with Src[24]. Therefore, migfilin appears to be an anti-apoptotic candidate oncogene in addition to being a gene with the apoptotic functions described in this paper. While paradoxical, this is not the first incidence of an oncogene promoting apoptosis. Activation of the oncogene Ras sensitizes chemotherapeutic agent-induced apoptosis both in HCT116 cells[25] and in embryonic stem cells[26]. The oncogene c-myc has also been reported to enhance cisplatin-induced apoptosis by inhibiting NF-κB signaling, which represses the expression of Bcl-2 families in mouse pancreatic cancer cells[27]. In addition, E1A has been proposed to be an immortalization oncoprotein that exhibits the anti-tumor properties of cell-cycle arrest and apoptosis induction[25, 28, 29]. The paradox caused by the dual function of oncogenes might derive from the functions of targeted genes downstream of the oncogenes, which could counteract the intrinsic anti-apoptotic function of oncogenes[25, 30–32]. It has also been proposed that cell growth and apoptosis are closely linked and that apoptosis might trigger the early progression of tumorigenesis[33, 34].

Cisplatin is a strong, widely used anti-cancer therapeutic drug that causes DNA damage and programmed cell death and is activated in a p53-independent pathway[35, 36]. Here, we have demonstrated that with the treatment of cisplatin, expression levels of cleaved Caspase-3 and PARP were elevated and accompanied by increased migfilin expression. Bcl-xL expression levels were negatively modulated by the expression level of migfilin and did not affect the expression level of p53 in glioblastoma cells. The anti-apoptotic factors Bcl-2 and Bcl-xL appear to be the most significant regulators involved in irradiation- and chemotherapy-induced apoptosis, particularly in a p53-dispensable pathway[27, 34, 37, 38]. The suppression of Bcl-xL induced by intrinsic or extrinsic upstream signals can result in the activation of apoptosis[37]. In the nervous system, expres-

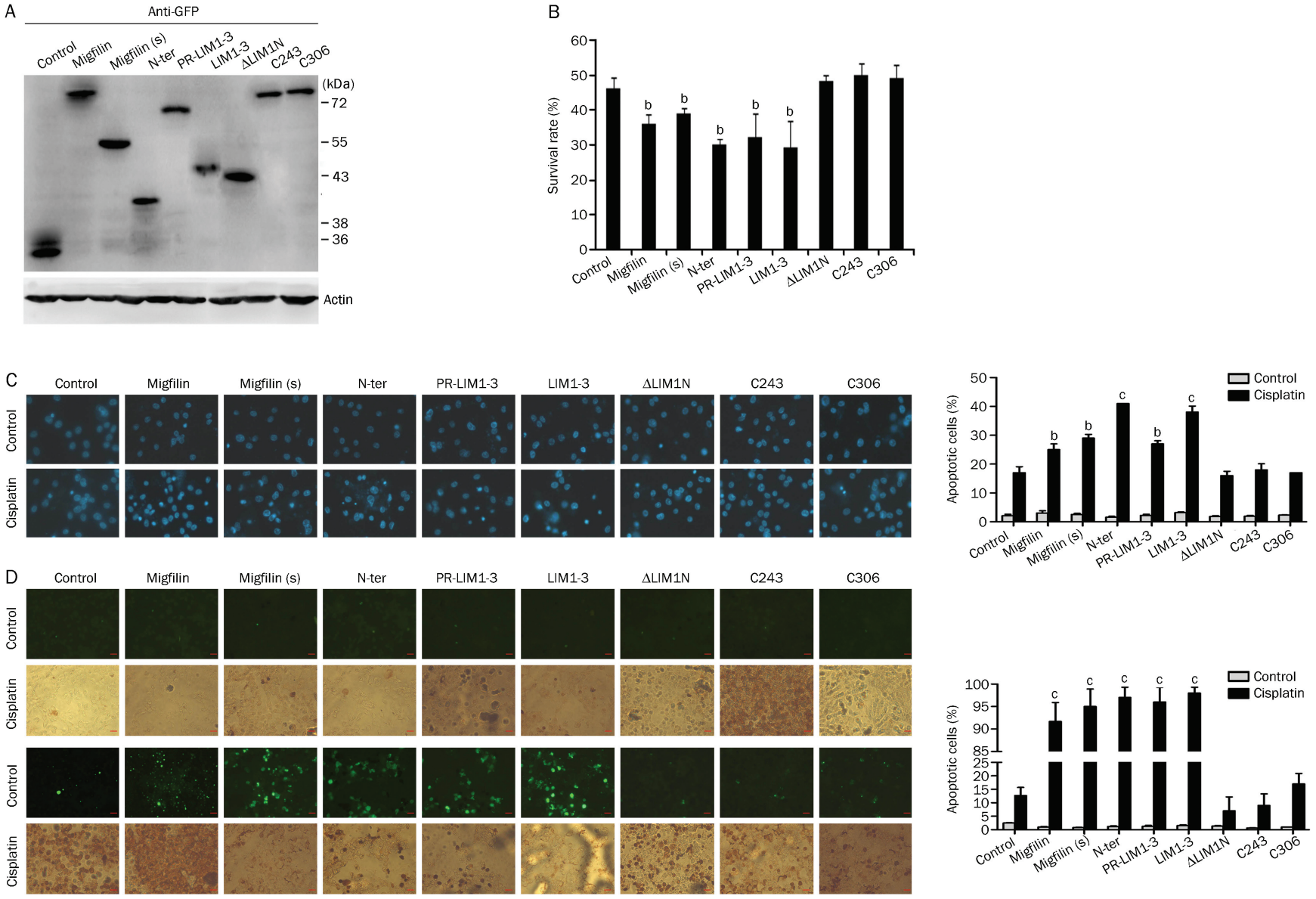

Figure 4. Functional domains of migfilin were determined in U-87 MG cells. (A) Cellular extracts of transfectants of migfilin mutant vectors with the GFP flag were detected for expression levels of GFP by Western blotting. (B) The MTS viability assay was performed to demonstrate the cell viability of transfectants of migfilin, migfilin(s), N-ter, PR-LIM1-3, LIM1-3, ΔLIM1N, C243, and C306 with cisplatin treatment (n=3. Mean±SD). (C) Apoptotic cell rates of migfilin-mutant transfectants with or without cisplatin treatment were examined by DAPI staining. Apoptotic cells were stained with light blue (400×objective; n=3. Mean±SD). (D) Using the TUNEL staining assay, apoptotic cells of migfilin-mutant transfectants with or without cisplatin treatment were determined by both DAB-stained positive areas (brown areas) and fluorescein-stained areas (green areas) (400×objective). Apoptotic cell rates were calculated under at least 9 different views. Mean±SD. n=3. $^{b}P<0.05$, $^{c}P<0.01$ *vs* control.

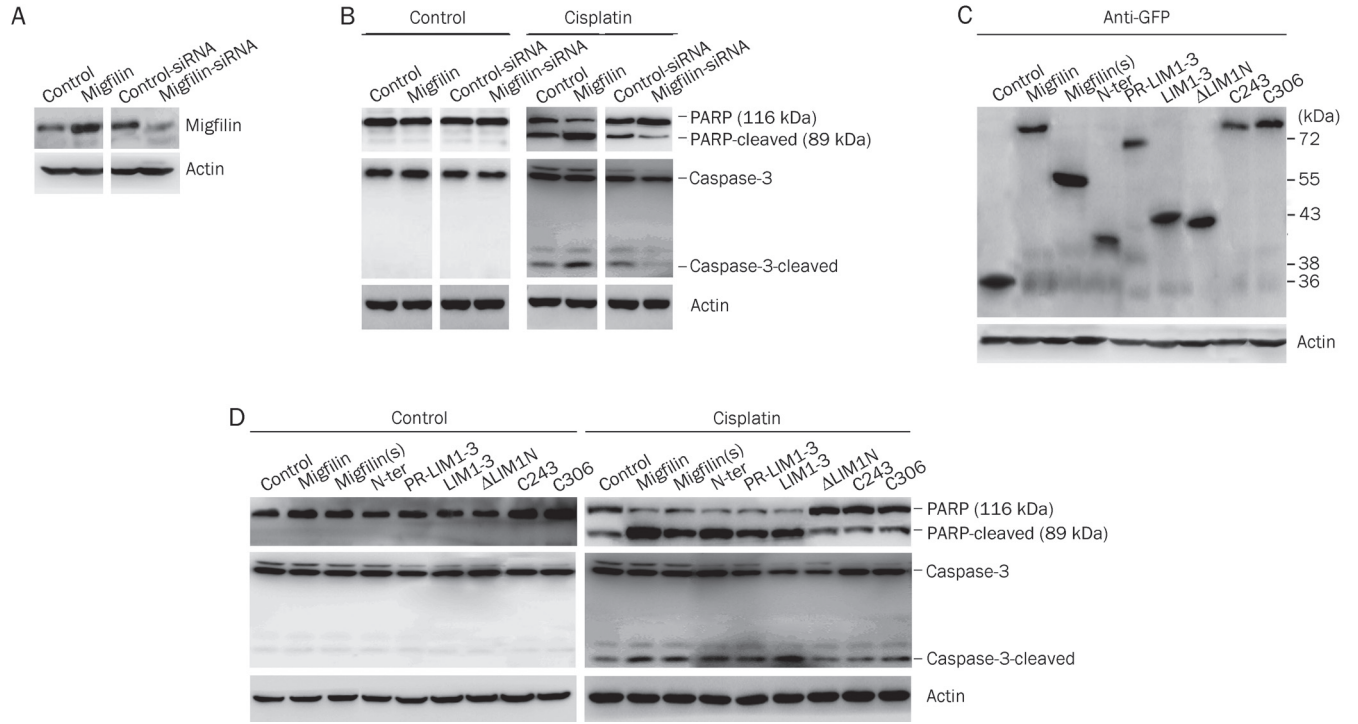

Figure 5. Expression of proapoptotic proteins in U-87 MG transfectants. (A) Migfilin expression levels were examined by Western blotting to determine the efficacy of transient transfections of migfilin vectors and siRNAs. (B) Expression levels of the proapoptotic proteins PARP and Caspase-3 were determined by Western blotting in migfilin-overexpression and migfilin-knockdown transfectants with or without cisplatin treatment. (C) Cellular extracts of transfectants of U-87 MG-migfilin mutants were examined for the expression levels of GFP protein by Western blotting. (D) Expression levels of PARP and Caspase-3 were detected by Western blotting in migfilin-mutant transfectants with or without cisplatin treatment.

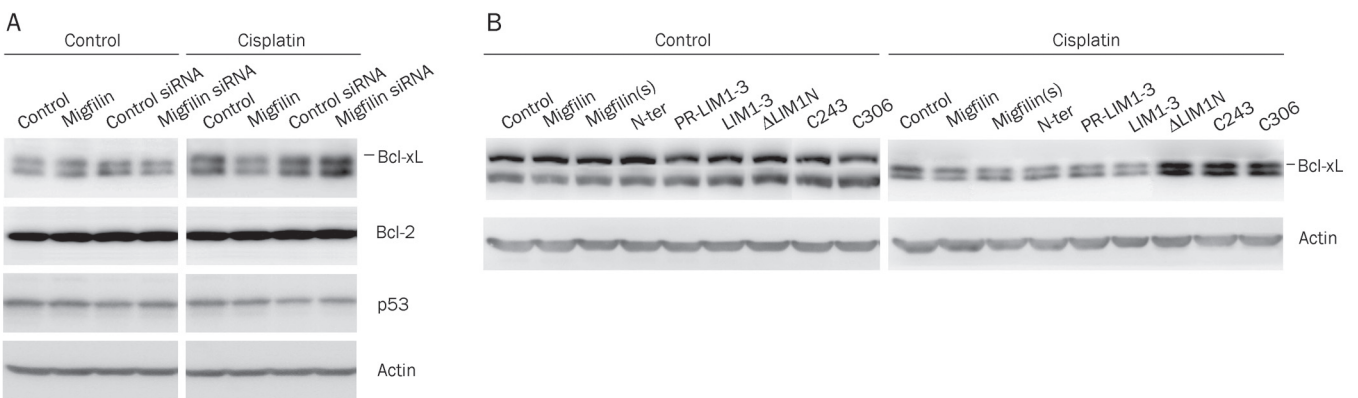

Figure 6. Expression of apoptosis-related proteins in U-87 MG transfectants. (A) Expression levels of the apoptosis-related proteins Bcl-xL, Bcl-2, and p53 were determined by Western blotting in migfilin-overexpression and migfilin-knockdown transfectants with or without cisplatin treatment. (B) Expression levels of Bcl-xL were detected by Western blotting in migfilin-mutant transfectants with or without cisplatin treatment.

sion of endogenous Bcl-xL plays a vital role in the protection of neurons from DNA damage-induced apoptosis, while Bcl-xL deficiency causes activation of caspase-3 and neuronal cell death with or without p53-deficiency[39]. Essentially, the level of Bcl-xL has been associated with the chemosensitivity and regulation of apoptosis[40]. Suppression of Bcl-xL deamidation causes chemoresistance to cisplatin-induced apoptosis, which is maintained through suppressing the proapoptotic ability of BH3 domain-only proteins in fibroblasts[41]. In this study, upregulation of migfilin was found to sensitize glioblastoma cells to cisplatin-induced apoptosis through a mitochondria-dependent pathway. Migfilin regulates functional Bcl-xL expression to respond to the DNA damage caused by cisplatin. Given that a variety of tumors lack p53 activity, chemotherapeutic agent-induced apoptosis relies on p53-independent signaling[41, 42].

Our results establish a link between the functional domain of migfilin and cisplatin-mediated chemosensitivity in human gliomas. Moreover, migfilin might be considered a promising novel therapeutic target, through its interference with chemotherapy-induced cytotoxicity in glioblastomas, and could serve as an important molecular target for drug discovery.

Acknowledgements

This work is supported by funding from the 973 National Key Fundamental Research Program of China (2009CB521801) and the National Natural Science Foundation of China (81071633 and 81021061).

Author contribution

Yong-mei SONG and Chun-jiang YU designed this research; Yong-mei SONG and Qi-min ZHAN supervised the research; Yun-wei OU and Jing FAN performed the research; Yun-wei OU analyzed the data; Jing FAN wrote the paper; Chuan-yue WU contributed plasmids and anti-migfilin antibody.

References

1 Westphal M, Lamszus K. The neurobiology of gliomas: from cell biology to the development of therapeutic approaches. Nat Rev Neurosci 2011; 12: 495–508.
2 Wick W, Weller M, Weiler M, Batchelor T, Yung AW, Platten M. Pathway inhibition: emerging molecular targets for treating glioblastoma. Neuro Oncol 2011; 13: 566–79.
3 Riddick G, Fine HA. Integration and analysis of genome-scale data from gliomas. Nat Rev Neurol 2011; 7: 439–50.
4 Wu C. Migfilin and its binding partners: from cell biology to human diseases. J Cell Sci 2005; 118: 659–64.
5 Tu Y, Wu S, Shi X, Chen K, Wu C. Migfilin and Mig-2 link focal adhesions to filamin and the actin cytoskeleton and function in cell shape modulation. Cell 2003; 113: 37–47.
6 Takafuta T, Saeki M, Fujimoto TT, Fujimura K, Shapiro SS. A new member of the LIM protein family binds to filamin B and localizes at stress fibers. J Biol Chem 2003; 278: 12175–81.
7 Shi X, Ma YQ, Tu Y, Chen K, Wu S, Fukuda K, *et al*. The MIG-2/integrin interaction strengthens cell-matrix adhesion and modulates cell motility. J Biol Chem 2007; 282: 20455–66.
8 Ithychanda SS, Das M, Ma YQ, Ding K, Wang X, Gupta S, *et al*. Migfilin, a molecular switch in regulation of integrin activation. J Biol Chem 2009; 284: 4713–22.
9 Kiema T, Lad Y, Jiang P, Oxley CL, Baldassarre M, Wegener KL, *et al*. The molecular basis of filamin binding to integrins and competition with talin. Mol Cell 2006; 2: 337–47.
10 Gong X, An Z, Wang Y, Guan L, Fang W, Strömblad S, *et al*. Kindlin-2 controls sensitivity of prostate cancer cells to cisplatin-induced cell death. Cancer Letters 2010; 299: 54-62.
11 Baldwin RM, Garratt-Lalonde M, Parolin DA, Krzyzanowski PM, Andrade MA, Lorimer IA. Protection of glioblastoma cells from cisplatin cytotoxicity via protein kinase Ci-mediated attenuation of p38 MAP kinase signaling. Oncogene 2006; 25: 2909–19.
12 Zhang S, Wan Y, Pan T, Gu X, Qian C, Sun G, *et al*. MicroRNA-21 inhibitor sensitizes human glioblastoma U251 stem cells to chemotherapeutic drug temozolomide. J Mol Neurosci 2012; 47: 346–56.
13 Eastman A. Activation of programmed cell death by anticancer agents: cisplatin as a model system. Cancer Cells 1990; 2: 275–80.
14 Siddik ZH. Cisplatin: mode of cytotoxic action and molecular basis of resistance. Oncogene 2003; 22: 7265–79.
15 Micallef J, Taccone M, Mukherjee J, Croul S, Busby J, Moran MF, *et al*. Epidermal growth factor receptor variant III-induced glioma invasion is mediated through myristoylated alanine-rich protein kinase C substrate overexpression. Cancer Res 2009; 69: 7548–56.
16 Gkretsi V, Zhang Y, Tu Y, Chen K, Stolz DB, Yang Y, *et al*. Physical and functional association of migfilin with cell-cell adhesions. J Cell Sci 2005; 118: 697–710.
17 Fuchs Y, Steller H. Programmed cell death in animal development and disease. Cell 2011; 147: 742–58.
18 Hanahan D, Weinberg RA. The hallmarks of cancer. Cell 2000; 100: 57–70.
19 Livshits G, Kobielak A, Fuchs E. Governing epidermal homeostasis by coupling cell–cell adhesion to integrin and growth factor signaling, proliferation, and apoptosis. Proc Natl Acad Sci U S A 2012; 109: 4886–91.
20 Fuchs M, Hermannstädter C, Hutzler P, Häcker G, Haller F, Höfler H, *et al*. Deletion of exon 8 increases cisplatin-induced E-cadherin cleavage. Exp Cell Res 2008; 314: 153–63.
21 Nakamura T, Kato Y, Fuji H, Horiuchi T, Chiba Y, Tanaka K. E-cadherin-dependent intercellular adhesion enhances chemoresistance. Int J Mol Med 2003; 12: 693–700.
22 Qi S, Song Y, Peng Y, Wang H, Long H, Yu X, *et al*. ZEB2 mediates multiple pathways regulating cell proliferation, migration, invasion, and apoptosis in Glioma. PLoS One 2012; 7: e38842.
23 Papachristou DJ, Gkretsi V, Tu Y, Shi X, Chen K, Larjava H, *et al*. Increased cytoplasmic level of migfilin is associated with higher grades of human leiomyosarcoma. Histopathology 2007; 51: 499–508.
24 Zhao J, Zhang Y, Ithychanda SS, Tu Y, Chen K, Qin J, *et al*. Migfilin interacts with Src and contributes to cell-matrix adhesion-mediated survival signaling. J Biol Chem 2009; 284: 34308–20.
25 Klampfer L, Huang J, Sasazuki T, Shirasawa S, Augenlicht L. Oncogenic Ras promotes butyrate-induced apoptosis through inhibition of gelsolin expression. J Biol Chem 2004; 279: 36680–8.
26 Brooks DG, James RM, Patek CE, Williamson J, Arends MJ. Mutant K-ras enhances apoptosis in embryonic stem cells in combination with DNA damage and is associated with increased levels of p19(ARF). Oncogene 2001; 20: 2144–52.
27 El-Kady A, Sun Y, Li YX, Liao DJ. Cyclin D1 inhibits whereas c-Myc enhances the cytotoxicity of cisplatin in mouse pancreatic cancer cells via regulation of several members of the NF-kappaB and Bcl-2 families. J Carcinog 2011; 10: 24.
28 Frisch SM, Mymryk JS. Adenovirus-5 E1A: paradox and paradigm. Nat Rev Mol Cell Biol 2002; 3: 441–52.
29 Yamaguchi H, Chen CT, Chou CK, Pal A, Bornmann W, Hortobagyi GN, *et al*. Adenovirus 5 E1A enhances histone deacetylase inhibitors-induced apoptosis through Egr-1-mediated Bim upregulation. Oncogene 2010; 29: 5619–29.
30 Harrington EA, Fanidi A, Evan GI. Oncogenes and cell death. Curr Opin Genet Dev 1994; 4: 120–9.
31 Fanidi A, Harrington EA, Evan GI. Cooperative interaction between c-myc and Bcl-2 proto-oncogenes. Nature 1992; 359: 554–6.
32 Evan G, Harrington E, Fanidi A, Land H, Amati B, Bennett M. Integrated control of cell proliferation and cell death by the c-myc oncogene. Philos Trans R Soc Lond B Biol Sci 1994; 345: 269–75.
33 Tang D, Lotze MT, Kang R, Zeh HJ. Apoptosis promotes early tumorigenesis. Oncogene 2011; 30: 1851–4.
34 Pelengaris S, Khan M, Evan GI. Suppression of Myc-induced apoptosis in beta cells exposes multiple oncogenic properties of Myc and triggers carcinogenic progression. Cell 2002; 109: 321–34.

35 Tomasini R, Seux M, Nowak J, Bontemps C, Carrier A, Dagorn JC, *et al*. TP53INP1 is a novel p73 target gene that induces cell cycle arrest and cell death by modulating p73 transcriptional activity. Oncogene 2005; 24: 8093–104.

36 Gong JG, Costanzo A, Yang HQ, Melino G, Kaelin WG Jr, Levrero M, *et al*. The tyrosine kinase c-Abl regulates p73 in apoptotic response to cisplatin-induced DNA damage. Nature 1999; 399: 806–9.

37 Maclean KH, Keller UB, Rodriguez-Galindo C, Nilsson JA, Cleveland JL. c-Myc augments gamma irradiation-induced apoptosis by suppressing Bcl-XL. Mol Cell Biol 2003; 23: 7256–70.

38 Zhang X, Zhao J, Kang S, Yi M, You S, Shin DS, *et al*. A novel cromakalim analogue induces cell cycle arrest and apoptosis in human cervical carcinoma HeLa cells through the caspase- and mitochondria-dependent pathway. Int J Oncol 2011; 39: 1609–17.

39 Klocke BJ, Latham CB, D'Sa C, Roth KA. p53 deficiency fails to prevent increased programmed cell death in the Bcl-X(L)-deficient nervous system. Cell Death Differ 2002; 9: 1063–8.

40 Amundson SA, Myers TG, Scudiero D, Kitada S, Reed JC, Fornace AJ Jr. An informatics approach identifying markers of chemosensitivity in human cancer cell lines. Cancer Res 2000; 60: 6101–10.

41 Deverman BE, Cook BL, Manson SR, Niederhoff RA, Langer EM, Rosová I, *et al*. Bcl-xL deamidation is a critical switch in the regulation of the response to DNA damage. Cell 2002; 111: 51–62.

42 Evan GI, Vousden KH. Proliferation, cell cycle and apoptosis in cancer. Nature 2001; 411: 342–8.

Acta Pharmacologica Sinica (2012) 33: 1311–1318
 1671-4083/12 $32.00
www.nature.com/aps

Original Article

The important roles of RET, VEGFR2 and the RAF/MEK/ERK pathway in cancer treatment with sorafenib

Wei-feng MAO[1, #], Min-hua SHAO[2, #], Pin-ting GAO[3], Ji MA[1], Hui-juan LI[1], Gai-ling LI[2], Bao-hui HAN[2, *], Chong-gang YUAN[1, *]

[1]Biology Department, East China Normal University, Shanghai 200062, China; [2]Department of Respiratory Disease, Shanghai Chest Hospital, Shanghai Jiao Tong University, Shanghai 200030, China; [3]Shanghai Medical College (MD Program), Fudan University, Shanghai 200032, China

Aim: To elucidate the roles of receptor tyrosine kinases RET and VEGFR2 and the RAF/MEK/ERK signaling cascade in cancer treatment with sorafenib.
Methods: The cell lines A549, HeLa, and HepG2 were tested. The enzyme activity was examined under cell-free conditions using 384-well microplate assays. Cell proliferation was evaluated using the Invitrogen Alarmar Blue assay. Gene expression was analyzed using the Invitrogen SYBR Green expression assays with a sequence detection system. Protein expression analysis was performed using Western blotting.
Results: Sorafenib potently suppressed the activities of cRAF, VEGFR2, and RET with IC_{50} values of 20.9, 4, and 0.4 nmol/L, respectively. Sorafenib inhibited cRAF, VEGFR2, and RET via non-ATP-competitive, ATP-competitive and mixed-type modes, respectively. In contrast, sorafenib exerted only moderate cytotoxic effects on the proliferation of the 3 cell lines. The IC_{50} values for inhibition of A549, HeLa, and HepG2 cells were 8572, 4163, and 8338 nmol/L, respectively. In the 3 cell lines, sorafenib suppressed the cell proliferation mainly by blocking the MEK/ERK downstream pathway at the posttranscriptional level, which in turn regulated related gene expression via a feed-back mechanism.
Conclusion: This study provides novel evidence that protein kinases RET and VEGFR2 play crucial roles in cancer treatment with sorafenib.

Keywords: sorafenib (BAY 43-9006); cancer; protein kinase; VEGFR2; RET; RAF/MEK/ERK pathway

Acta Pharmacologica Sinica (2012) 33: 1311–1318; doi: 10.1038/aps.2012.76; published online 3 Sep 2012

Introduction

Cancer, known medically as a malignant neoplasm, is responsible for a large number of deaths worldwide. The development of tumor chemotherapy led to the recent discovery of sorafenib (BAY 43-9006). Sorafenib, a multiple kinase inhibitor and novel oral bis-aryl urea compound that exhibits a strong anticancer effect, has been approved by the US Food and Drug Administration for the treatment of advanced renal cell carcinoma and hepatocellular carcinoma[1–5]. Many studies suggest that sorafenib could inhibit tumor growth by targeting protein kinases[6–9]. In the past few years, accumulating evidence has indicated that protein kinases play critical roles in cancer development, as they are critical components of the cellular signal transduction cascades; accordingly, kinases have become the most important targets for drug development. The receptor tyrosine kinases VEGFR-2 and RET and the RAF serine/threonine kinases are the important targets of sorafenib in cancer treatment.

VEGFR-2 (Flk-1 in mice and KDR, kinase insert domain-containing receptor, in humans) is an important receptor tyrosine kinase that plays a critical role in tumor angiogenesis, which is an important process for the growth, progression, and metastasis of solid tumors[10]. VEGFR-2 can be activated by extracellular signals and then induce downstream signal transduction pathways to regulate cellular activities. In tumors, however, VEGFR-2 is usually found to be aberrantly expressed or constitutively phosphorylated. Thus, VEGFR-2 has become a central focus of molecularly targeted cancer therapy.

Another important protein kinase is the receptor tyrosine kinase RET. This kinase was often found to be abnormally activated in the thyroid, generally through sporadic and

* To whom correspondence should be addressed.
E-mail cgyuan@bio.ecnu.edu.cn (Chong-gang YUAN);
xkyyhan@gmail.com (Bao-hui HAN)
Received 2012-01-16 Accepted 2012-05-08

inherited gene mutations. Hence, it has been hypothesized that the oncogene RET and the RET receptor tyrosine kinase might contribute to the development of cancer[11, 12]. Indeed, the oncogenic activation of the RET gene is recognized as an early pathogenic event in cancers, and it subsequently induces downstream signaling events involving the MEK/ERK-, PI3K/AKT-, and phospholipase Cγ (PLCγ)-dependent pathways[13, 14].

The MEK/ERK pathway is also called the RAF/MEK/ERK serine/threonine kinase cascade, as its upstream molecules belong to the RAF kinase family of serine/threonine kinases[15]. As a critical messenger, RAF can direct the upstream signal to activate MEK1/2, which, in turn, activates ERK1/2[16, 17]. Activated ERK1 or ERK2 then either phosphorylates its target proteins in the cytoplasm or translocates to the nucleus, where the main targets are transcription factors that regulate proliferation-, differentiation- or survival-related genes. Therefore, the RAF/MEK/ERK serine/threonine kinase cascade is a key pathway that is involved in the development of cancers and is considered a potential important target for sorafenib treatment[18].

However, the mechanism by which sorafenib inhibits tumor cells and how kinases respond to sorafenib treatment are largely unclear. Therefore, this study aims to elucidate the events at the biomolecular level in three cell lines (A549, HeLa, and HepG2) after sorafenib treatment. Because different cancers might be regulated by different mechanisms, we selected three cell lines that have different metastatic potential, and enzyme kinetic, cytology, RT-PCR and Western blotting assays were conducted. Specifically, one serine/threonine kinase, cRAF, and two tyrosine kinases, VEGFR2 and RET, and their potential downstream MEK/ERK pathway targets were examined. An understanding of the molecular events in cancer cells treated with sorafenib not only is necessary to obtain a better insight into genotype-phenotype correlations but also is crucial for the discovery of new therapeutic approaches.

Materials and methods

Compounds

Sorafenib was produced by the Chemistry Department, Chinese Pharmaceutical University (Nanjing, China); staurosporine, PI-103, and mitomycin C were purchased from Sigma Aldrich, Germany.

Kinases

cRAF (Y340D and Y341D) and VEGFR2 (KDR) were purchased from Invitrogen. RET was expressed in Sf9 cells using an Invitrogen baculovirus system and then purified by His/GST affinity and Supdex35/75/200 chromatography. The recombinant proteins were then analyzed by SDS-PAGE, and the molecular weights were determined using LS-MS/MS, model API3000.

Activity assays

Using 384-well microplate assays, an enzyme titration, the ATP K_m, a time course, and a positive-control IC_{50} were employed to validate the kinases. The CRAFs were analyzed using the Invitrogen LanthaScreen Tb-activity assay with 0.01 nmol/L kinase, 200 nmol/L Fluorescein-MAP2K1, 50 mmol/L HEPES (pH 7.5), 10 mmol/L $MgCl_2$ and 0.01% Brij35 for 1 h at 23 °C; the reaction was terminated with 30 mmol/L EDTA and 2 nmol/L phospho-MAP2K1 antibody. Cisbio HTRF technology was employed to analyze the activity of optimized concentrations of RET and VEGFR2, with 50 mmol/L HEPES (pH 7.5), 10 mmol/L $MgCl_2$, ATP K_m, 0.01% Brij35, and 500 nmol/L STK1 peptide for 1 h at 23 °C. For the IC_{50} test, the sorafenib concentration was 10 μmol/L for 11 doses in duplicate, with 3-fold dilutions of ATP K_m. For the MOA study, 6 ATP concentrations (1/3-, 1-, 3-, 9-, 27-, and 81-fold ATP K_m) were used at the same serial dilution as in the IC_{50} test. The readouts were analyzed using the PerkinElmer Envision2104 reader in Htrf/FRET module. The Inh% was analyzed using Excel. The IC_{50} Shift and the Lineweaver-Burk and double-reciprocal plots were drawn using Graphpad Prism 5.

Cell culture

The A549, HeLa and HepG2 cells were obtained from ATCC. A549 was cultured in F12, 10% FBS, and 2 mmol/L glutamine at 37 °C under 5% CO_2; the HeLa and HepG2 cells were cultured in DMEM-HG, 10% FBS, and 2 mmol/L glutamine.

Cell proliferation

The cells were detached using accutase (Millipore) and counted using trypan blue staining and a ViaCell (Beckman Coulter). The A549 (5×10^3 cells), HeLa (3×10^3 cells), and HepG2 (1×10^4 cells) cells were then plated in triplicate in 96-well microplate in the presence of sorafenib, mitomycin C, or vehicle (DMSO, 0.2%) for 0, 24, 48, and 72 h. The cell proliferation assay was evaluated using Invitrogen Alarmar Blue by adding 10 μL of the reagents after 96 h.

RT-PCR

The A549 (5×10^3), HeLa (3×10^3) and HepG2 (1×10^4) cells were plated in 30-mm dishes for 24, 48, and 72 h, and each cell line (5×10^5) was also plated for 2, 4, and 8 h. Sorafenib at 5 μmol/L or 1 μmol/L or vehicle (DMSO, 0.2%) were applied for 2, 4, and 8 h as described above.

The RNA extraction, cDNA synthesis, and quantitative real-time PCR amplification were performed using the RNeasy kit (Qiagen) according to the manufacturer's instructions. For the cDNA synthesis, 200 ng of mRNA was used with the Omniscript RT kit (Qiagen), following the manufacturer's instructions, with oligo (dT)20 primers (Qiagen). A 1-μg sample of cDNA was used for each qPCR, which was performed in triplicate.

Primers for ERK (forward 5′–3′, GCGCTACACCAACCTCTCGT; reverse 5′–3′, CACGGTGCAGAACGTTAGCTG), VEGFR2 (forward 5′–3′, CACCACTCAAACGCTGACATGTA; reverse 5′–3′, GCTCGTTGGCGCACTCTT), RAF1 (forward 5′–3′, GAACGACAGGACGTTGGG; reverse 5′–3′, GCTGATCGTCTTCCAAGCTC), and RET (forward 5′–3′,

CTAGCCGCAGTCCCTCC; reverse 5′–3′, AAGCATCCCTCGAGAAGTAGA), were designed for the RT-PCR. GAPDH, ACTB, and B2M were used as the endogenous controls in all of the experimental analyses. Invitrogen Sybgreen expression assays and an ABI Prism 7900HT sequence detection system (Applied Biosystems, Foster City, CA, USA) were employed for the gene expression analyses with the ΔΔCt method, which determines the fold change in gene expression relative to a comparator sample (control). The PCR primers were purchased from Shanghai Generay Biotech Company.

Effects of sorafenib on three cell lines at the transcriptional level

To demonstrate the effect of sorafenib on cells at the transcription level, the mRNA concentrations of four genes, RET, VEGFR2, cRAF and ERK, were detected using RT-PCR assays. Each cell line was treated with sorafenib at two concentrations, 1 and 5 μmol/L, and the cells were collected after 2, 4, and 8 h; cells without sorafenib treatment were used as the controls (0 h). The total mRNA was extracted and quantified for use in RT-PCR assays. The ratio of the target mRNA content in the treatment group to the controls was calculated.

Western blotting

After their respective treatments, the cells were lysed in lysis solution (Cell Signaling Technology, Danvers, MA, USA) supplemented with sodium fluoride (10 mol/L; Fisher) and phenylmethylsulfonyl fluoride (100 g/mL; Sigma-Aldrich). The lysates were centrifuged at 14 000×*g* for 30 min, and the supernatants were aspirated to determine the protein concentration using BCA reagents (Pierce, ThermoFisher, Rockford, IL, USA). Each 80 μg sample was fractionated in either 8% or 12% SDS-polyacrylamide gels, and the separated proteins were transferred to nitrocellulose. The blots were probed for the proteins of interest using primary antibodies followed by a secondary antibody-horseradish peroxidase conjugate. The Super Signal chemiluminescence substrate (Pierce) and the GE Image Quant analyzer were used for the detection.

The anti-ERK (total) and anti-RET (pY1062) antibodies were obtained from Santa Cruz Biotechnology (Santa Cruz, CA, USA). Anti-Erk (pT202/pY204), anti-VEGFR2 (pY1214), anti-RET (pY1016), anti-MEK1 (pT292), and anti-MEK1 (p298) were obtained from Invitrogen. Anti-VEGFR2 (total), anti-VEGFR2 (pY1175), anti-RET (total), anti-RET (pY905), and anti-MEK (total) were purchased from Cell Signaling.

Effects of sorafenib on the three cell lines at the post-transcriptional level

To investigate the effect of sorafenib on the post-transcriptional events in cells, the expression and phosphorylation level of the following four proteins were detected by Western blot assays: VEGFR2, RET, MEK, and ERK. Each cell line was treated with two concentrations of sorafenib, 1 and 5 μmol/L, and the cells were then collected after 2, 4, and 8 h. Cells without sorafenib treatment were used as the controls (0 h). The total proteins were extracted and quantified in Western blot assays.

Statistical analysis

All statistical analysis was taken under student *t*-test with SPSS 18.0. $P<0.05$ was considered statistically significant for two-side *P*-value test.

Results

Sorafenib inhibits the activity of kinases by different inhibition mechanisms under cell-free conditions

The effect of sorafenib on enzyme activity was measured by assays one hour after the drug was applied. Sorafenib inhibited the activity of cRAF, with an IC_{50} of 20.9 nmol/L and 0.4 nmol/L and 4 nmol/L for RET and VEGFR2, respectively. The data for cRAF agreed with the previous report of an IC_{50} of 19 nmol/L. In contrast, the results for VEGFR2 and RET were quite different from the reported data of 90 nmol/L and 4 nmol/L, respectively (Figure 1). The double-reciprocal plot shows that the linear regression alignments converge on the Y axis (Figure 2A, 2C), indicating that sorafenib is an ATP-competitive compound for RET and KDR, a result that is consistent with Wilhelm's[8]. However, this effect was not observed for cRAF (Figure 2E), and, when ATP was added, the IC_{50} for cRAF was consistent with the different concentrations (1/3-, 1-, 3-, 9-, 27-, and 81-fold ATP K_m) (Figure 2F), which indicated that sorafenib inhibited cRAF activity through a non-ATP-competitive mode. For KDR/VEGFR2, the IC_{50} rose consistently with the increase in the ATP concentration (Figure 2D), suggesting that sorafenib inhibited the KDR/VEGFR2 activity through an ATP-competitive mechanism. For RET, the IC_{50} improved with the increase in the ATP concentration in a non-homogeneous manner (Figure 2B), which demonstrated that sorafenib inhibited the RET activity through a mixed-type inhibition. In summary, sorafenib targets the ATP-binding site of the kinases and inhibits their activities by different inhibition mechanisms under cell-free conditions.

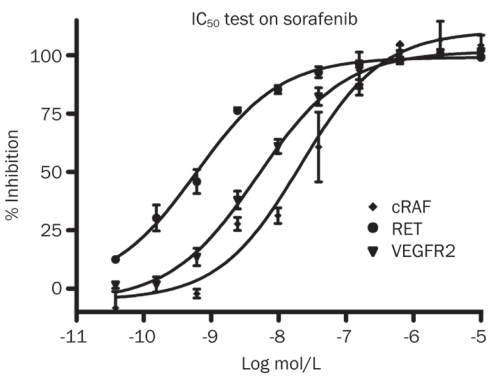

Target name	Reported IC_{50} (nmol/L)	Test IC_{50} (nmol/L)
cRAF	19±5.7	20.9
KDR/VEGFR2	90±27	4
RET	4±0.8	0.4

Figure 1. Sorafenib inhibits kinase activity of cRAF, RET, and VEGFR2 with different IC_{50} under cell-free condition.

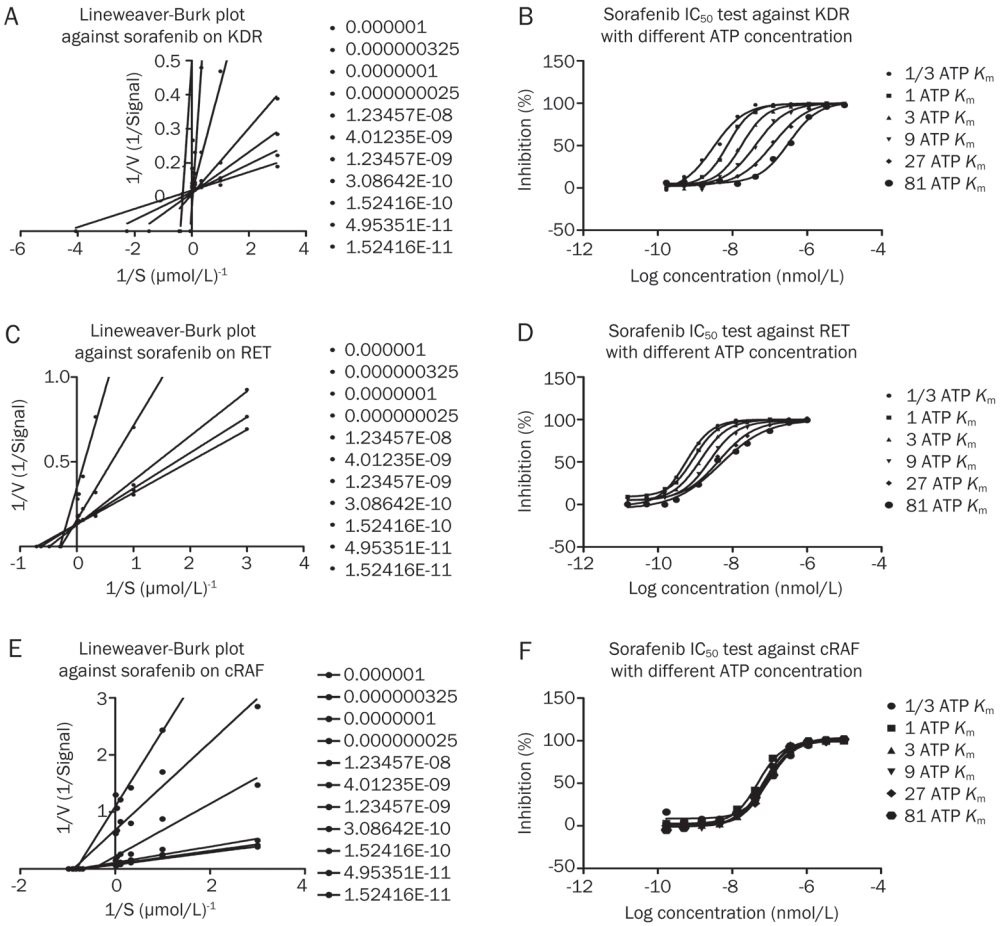

Figure 2. Double-reciprocal plot of kinetic data from assays of KDR, RET, and cRAF protein kinase activity at different concentrations of sorafenib. ATP concentrations in the reaction mixture varied from 1/3 ATP K_m to 81 fold ATP K_m. Sorafenib concentrations are from 100 μmol/L to 1.6 nmol/L with 3-fold dilution and the concentration of peptides were kept constant at 2 μmol/L. *V* is picomoles of phosphate/60 min. Double-reciprocal plot shows the linear regression alignments are converge on Y axis, which means sorafenib is an ATP competitive compound on KDR, RET, which is consistent with reported. The IC_{50} of RET, KDR are 0.4 nmol/L, 4 nmol/L in sequence.

Sorafenib inhibits proliferation in A549, HeLa and HepG2 cells

The effect of sorafenib on cell proliferation was examined at 72 h in the A549, HeLa, and HepG2 cell lines. Sorafenib displayed a moderate dose-dependent inhibition of cell proliferation. The IC_{50} values for the A549, HeLa, and HepG2 cells were 8572 nmol/L, 4163 nmol/L, and 8338 nmol/L, respectively, and the maximum inhibition was 88%, 78%, and 94% for each of the three cell lines, respectively. Figure 3 shows the inhibition of cell proliferation by 20 μmol/L sorafenib in the three cell lines compared with the cells treated with DMSO (controls).

Sorafenib activates RET expression and inhibits VEGFR2 expression independent of the RAF/MEK/ERK pathway at the transcriptional level in A549 cells

In the A549 cells, the expression of RET increased significantly at 2 h after treatment with 1 μmol/L sorafenib and then decreased, whereas the VEGFR2 expression notably decreased in every treatment group (Figure 4A). In contrast, the cRAF and ERK expression levels were not significantly affected, even though the cRAF expression showed a slight decrease at 5 μmol/L sorafenib. These results suggested that sorafenib could activate RET expression and inhibit VEGFR2 expression independent of the RAF/MEK/ERK pathway at the transcriptional level in A549 cells.

Sorafenib inhibits VEGFR2 expression but has no effect on the RAF/MEK/ERK pathway at the transcriptional level in HeLa cells

The same assay as described above for the A549 cells was performed using HeLa cells. The results showed that sorafenib up-regulated the expression of RET; conversely, sorafenib significantly down-regulated the expression of VEGFR2 at the transcription level (Figure 4B). A similar result was found for the HeLa cells in that sorafenib showed no effect on cRAF and ERK expression. These results suggested that sorafenib could inhibit VEGFR2 expression but had no effect on the RAF/MEK/ERK pathway at the transcriptional level in HeLa cells.

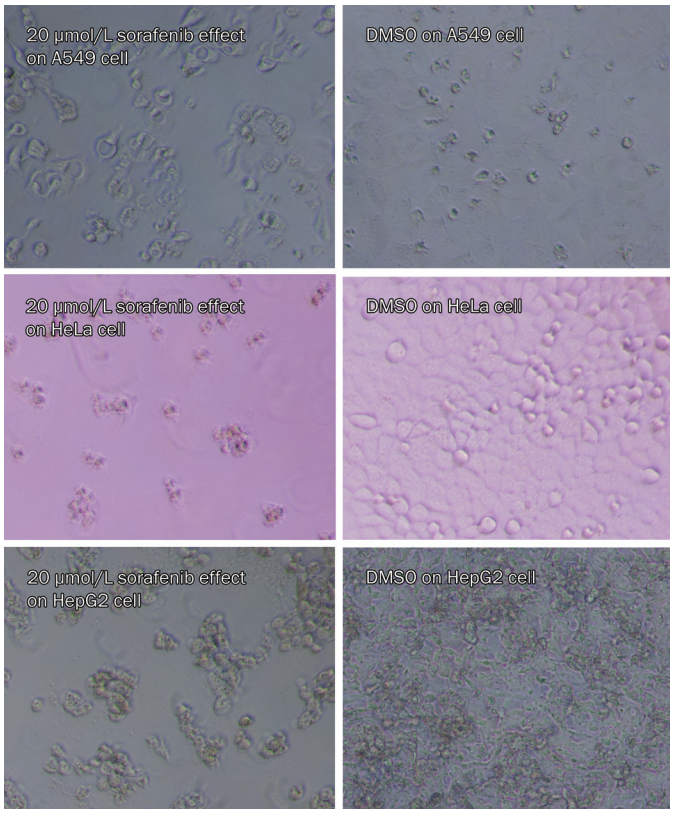

Figure 3. Sorafenib moderately inhibited proliferation of A549, HeLa and HepG2 cells. Sorafenib was added to A549, HeLa, and HepG2 cells, and cultured for 72 h in culture medium, meanwhile, DMSO was added to controls. Sorafenib displayed moderate cytotoxicity to cell proliferation dose-dependently.

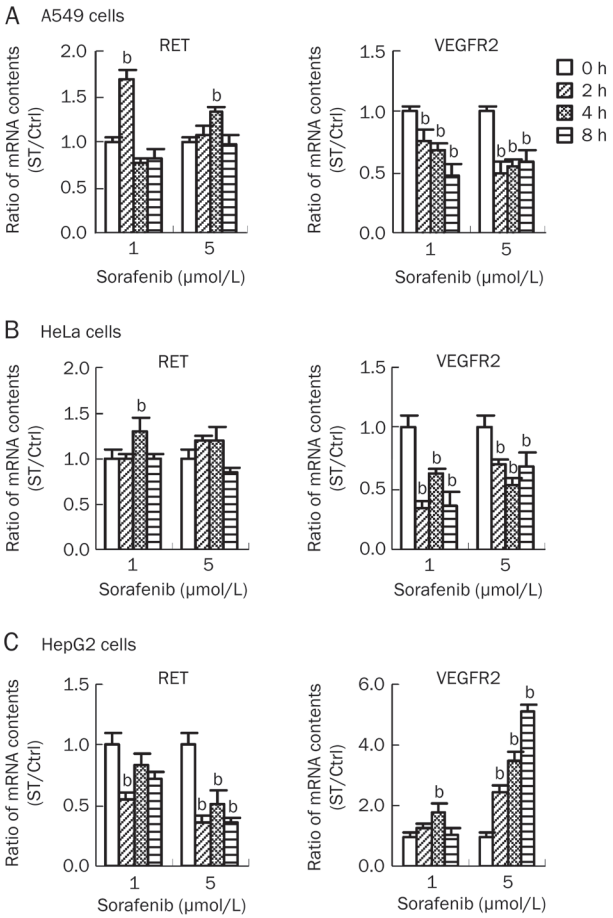

Figure 4. Sorafenib affected RET and VEGFR2 gene expression in A549, HeLa, and HepG2 cells. Three cell lines were treated by sorafenib with two concentration gradients, 1 and 5 μmol/L, and then collected after 2, 4, and 8 h. Cells without sorafenib treatment were as the controls (0 h). Total mRNA was extracted and quantified to be used in RT-PCR assays. Ratio for mRNA content in treatment group compared with controls was calculated. (A) Sorafenib up-regulated RET gene expression and down-regulated VEGFR2 gene expression in A549 cells. (B) Sorafenib up-regulated RET gene expression and down-regulated VEGFR2 gene expression in HeLa cells which was similar to that in A549 cells. (C) Sorafenib down-regulated RET gene expression and up-regulated VEGFR2 gene expression in HepG2 cells which opposite to that in the above two cell lines.

Sorafenib inhibits RET expression dose-dependently and activates VEGFR2 expression dose- and time-dependently but has no effect on the RAF/MEK/ERK pathway at the transcriptional level in HepG2 cells

The results for the HepG2 cell line showed that RET expression was dose-dependently down-regulated by sorafenib at the transcriptional level. The expression of VEGFR2 was initially up-regulated and then down-regulated with 1 μmol/L sorafenib, but it was persistently activated in a time-dependent manner at 5 μmol/L (Figure 4C). As in the other two cell lines, sorafenib showed no effect on cRAF and ERK expression. These results suggested that sorafenib dose-dependently inhibited RET expression and dose- and time-dependently activated VEGFR2 expression but had no effect on the RAF/MEK/ERK pathway at the transcriptional level in HepG2 cells.

Sorafenib directly inhibits RET and VEGFR2 phosphorylation and blocks the downstream signaling of the MEK/ERK pathway at the post-transcriptional level in A549 cells

The results for the A549 cells indicated a significant dose-dependent decrease of RET and VEGFR2 phosphorylation (Figure 5A) but showed a notable dose-dependent increase of RET and VEGFR2 expression. These findings suggest that sorafenib directly inhibited RET and VEGFR2 phosphorylation, altering the ratio of phosphorylated to unmodified proteins, which then led to an increase in RET and VEGFR2 expression. We found that sorafenib dose-dependently up-regulated the expression and activated the phosphorylation of MEK and ERK (Figure 5A), which indicated that sorafenib might inhibit the downstream targets of the MEK/ERK pathway. The increase in the expression and phosphorylation of MEK and ERK can be explained by a feedback regulation mechanism. Therefore, we concluded that sorafenib acts by directly inhibiting the phosphorylation of RET and VEGFR2 and blocking the MEK/ERK downstream pathway at the post-

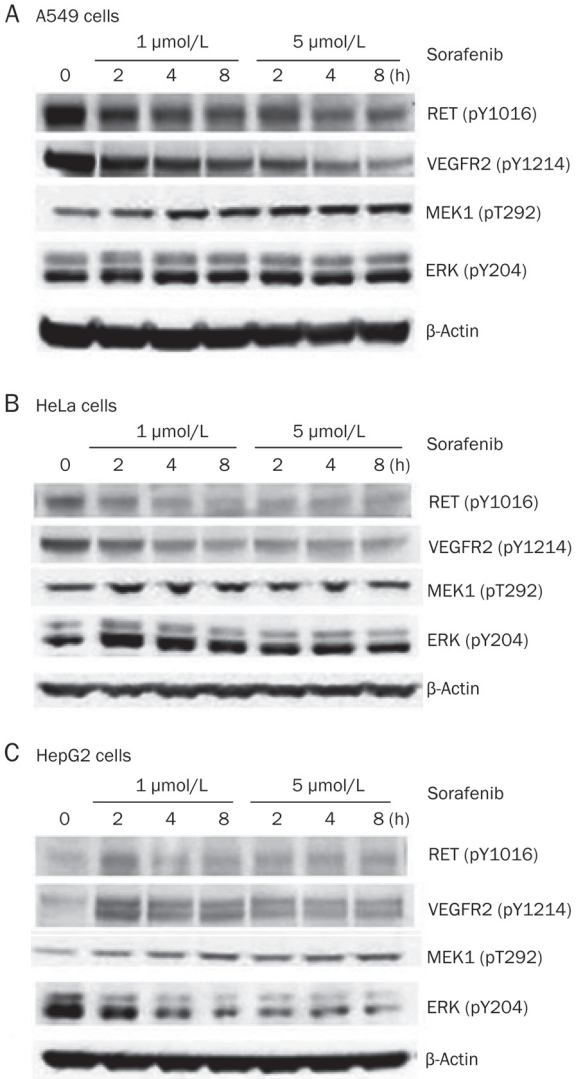

Figure 5. Sorafenib affected the phosphorylation of receptor tyrosine kinase RET and VEGFR2, as well as MEK/ERK kinases signaling cascades in three cell lines. Three cell lines were treated by sorafenib with two concentration gradients, 1 and 5 μmol/L/L, and then collected after 2, 4, and 8 h, cells without sorafenib treatment were as the controls (0 h). Total proteins were extracted and quantified to be used in Western blot assays. (A) Sorafenib inhibited RET and VEGFR2 phosphorylation dose-dependently while activated MEK and ERK phosphorylation in A549 cells. (B) Sorafenib also inhibited RET and VEGFR2 phosphorylation, and slightly activated MEK and ERK phosphorylation in HeLa cells. (C) Sorafenib activated the phosphorylation of RET, VEGFR2, and MEK, but inhibited ERK phosphorylation in HepG2 cells.

transcriptional level in A549 cells.

Sorafenib directly inhibits RET and VEGFR2 phosphorylation and blocks the downstream MEK/ERK pathway at the post-transcriptional level in HeLa cells

In HeLa cells, RET and VEGFR2 phosphorylation also decreased notably, as in the A549 cells (Figure 5B), which suggested that sorafenib also directly inhibited the phosphorylation of RET and VEGFR2 in HeLa cells. The MEK and ERK phosphorylation level first increased and then decreased (Figure 5B), indicating that sorafenib targeted the downstream signaling molecules of the MEK/ERK pathway. The observed mechanism was similar to that in the A549 cells. Consequently, sorafenib directly inhibited RET and VEGFR2 phosphorylation and blocked the MEK/ERK downstream pathway at the post-transcriptional level in HeLa cells.

Sorafenib targets the RET and VEGFR downstream molecules and blocks the MEK/ERK pathway by inhibiting ERK phosphorylation at the post-transcriptional level in HepG2 cells

In the HepG2 cells treated with sorafenib, the expression of RET was little altered, but its phosphorylation level rose at 2 h after treatment and then decreased to a low level (Figure 5C). This result suggested that sorafenib might target the downstream molecule of RET, disrupting the balance of the related pathways. VEGFR2 phosphorylation significantly increased after sorafenib treatment, which also suggested that sorafenib might target the downstream molecule of VEGFR2 (Figure 5C). Regarding the MEK/ERK pathway, ERK phosphorylation was significantly inhibited by sorafenib, which led to a notable increase in the upstream MEK phosphorylation (Figure 5C), demonstrating that sorafenib blocked the MEK/ERK pathway by directly inhibiting ERK phosphorylation. Therefore, in the HepG2 cell line, sorafenib targeted the downstream molecules of RET and VEGFR2, while blocking the MEK/ERK pathway by inhibiting ERK phosphorylation at the post-transcriptional level.

Discussion

Receptor tyrosine kinases play major roles in the development of cancer and represent effective targets for specific therapeutic approaches. Indeed, receptor kinase-based therapies have attained wide-spread clinical use, for example, in breast cancer (the inhibition of HER2 by Herceptin)[19], in gastrointestinal stromal tumors (the inhibition of c-Kit by Gleevec)[20, 21], and in non-small cell lung cancer (the inhibition of EGF receptor by Gefitinib)[22]. Recently, the orally administered multikinase inhibitor sorafenib was found to exert a prominent activity against tumors. Thus, to verify the anticancer mechanism of sorafenib, we performed a series of trials *in vitro*.

In the present study, we found that sorafenib has a higher IC_{50} than that described by Wilhelm *et al*[8], with IC_{50} values of 20 nmol/L against cRAF *in vitro* under cell-free conditions. However, the drug shows a more potent inhibition of VEGFR-2, at IC_{50}=4 nmol/L, than that reported by Wilhelm *et al*, at IC_{50}=90 nmol/L[8]. In addition, RET was significantly inhibited by sorafenib, with an IC_{50}=0.4 nmol/L, much lower than the value reported by Wilhelm *et al*, at IC_{50}=4 nmol/L. Iván Plaza-Menacho also found that sorafenib inhibited the activity of the purified recombinant kinase domain of wide-type RET and the mutant RET^{V804M}, with IC_{50} values of 5.9 and 7.9 nmol/L, respectively, which also suggested that sorafenib is an inhibitor of RET[23].

Several therapeutic avenues are available to block the activ-

ity of protein kinases. Drugs that bind reversibly to the ATP-binding site within the kinase domain or to a small pocket that is immediately adjacent to the ATP-binding site are used to block the enzymatic activity of the kinase. Because of similarities within the three-dimensional structure of the kinase domain, ATP-competitive inhibitors can have cross-reactivity with other structurally related kinases. The data obtained in the present study indicate that sorafenib is an ATP-competitive inhibitor of VEGFR2 and RET but not cRAF: sorafenib inhibited the activities of cRAF, VEGFR2 and RET through non-ATP-competitive, ATP-competitive and mixed-type inhibition modes, respectively. In summary, sorafenib could target the ATP-binding site of kinases and inhibit the activity of kinases by different inhibition mechanisms under cell-free conditions. This is a novel discovery, and further studies will be conducted to verify the conclusions.

As different cancers might be regulated by different mechanisms, we selected three cell lines having different metastatic potentials (A549, HeLa, and HepG2). At the transcriptional level, we found that sorafenib could briefly activate RET expression and inhibit VEGFR2 expression independent of the RAF/MEK/ERK pathway in A549 cells; at the post-transcriptional level, sorafenib directly inhibited the phosphorylation of RET and VEGFR2 and blocked the downstream factors of the MEK/ERK pathway. Therefore, we hypothesized that sorafenib inhibited the proliferation of A549 cells through anti-proliferation and anti-angiogenesis processes. Moreover, whereas the anti-proliferation process is a post-transcriptional event, anti-angiogenesis refers to many molecular processes from transcription to post-translational modification. The two kinases RET and VEGFR2 could be the targets of sorafenib treatment, but they may not be the upstream messengers of the MEK/ERK kinases pathway. The downstream signaling molecules of the MEK/ERK kinase pathway are also potential candidates for the sorafenib treatment of lung cancer.

According to the results for HeLa cells, we found that sorafenib could inhibit VEGFR2 expression but had no effect on the RAF/MEK/ERK pathway at the transcriptional level. At the post-transcriptional level, sorafenib directly inhibited RET and VEGFR2 phosphorylation and blocked the downstream factors of the MEK/ERK pathway. Therefore, the mechanism of the sorafenib-mediated inhibition of proliferation in HeLa cells is similar to that of A549 cells. RET, VEGFR2 and the downstream signaling molecules of the MEK/ERK kinase pathway are also important potential targets for sorafenib in the treatment of cervical cancer.

In contrast to the results in the above cell lines, sorafenib inhibited RET expression and activated VEGFR2 expression in the HepG2 cells, with little effect on the RAF/MEK/ERK pathway at the transcriptional level. Moreover, sorafenib targeted the downstream molecules of RET and VEGFR2 and blocked the MEK/ERK pathway by inhibiting ERK phosphorylation at the post-transcriptional level. It is clear that anti-proliferation and anti-angiogenesis pathways are also involved in the response to sorafenib treatment in hepatic cancer. The mechanism, however, differs from lung and liver cancer, which might be attributable to the similar origin of lung and liver tissues.

Our results indicated that sorafenib is an inhibitor of the phosphorylation of protein kinase RET and VEGFR2 under cell-free conditions as well as in A549 and HeLa cells. In HepG2 cells, sorafenib markedly inhibited kinase ERK phosphorylation, though the drug did not exhibit a significant inhibition on the phosphorylation of RET and VEGFR2. In addition, based on the present results, the MEK/ERK kinase signaling cascade is clearly an important effective target pathway for cancer treatment. Therefore, it is confirmed that kinases indeed play crucial roles in the effective mechanism of sorafenib and are important effective targets for specific therapeutic approaches. Moreover, sorafenib inhibited cell proliferation mainly by blocking post-translational modifications, which then regulated the related gene expression via a feed-back mechanism. Interestingly, we found that the two kinases, RET and VEGFR2, displayed similar bimolecular alterations, even though they acted in the reaction to sorafenib treatment through different mechanisms in the three cell lines, a finding that could be explained by the results of mechanism of action (MOA) that sorafenib is an ATP-competitive inhibitor of VEGFR2 and RET. In addition, we hypothesized that RET and VEGFR2 were involved in a similar signaling pathway due to their similar biomolecular alteration in the different cell lines treated with sorafenib.

In summary, we found that sorafenib was effective in inhibiting the proliferation of cancer cells by inhibiting kinases through different competitive mechanisms. The receptor tyrosine kinases RET and VEGFR2 and the MEK/ERK kinase signaling cascade are important targets for cancer treatment with sorafenib, even though these factors participate in different pharmacological mechanisms in different cell lines. Furthermore, according to their similar biomolecular alteration in the different cell lines treated with sorafenib, kinases RET and VEGFR2 may be involved in a similar signaling pathway. Therefore, the present study was consistent with previous results and provided more evidence for kinases as the targets in cancer therapy and partially revealed the pharmacological mechanism, including molecules downstream of the MEK/ERK kinase pathway and the pathways initiated by RET or VEGFR2, of sorafenib in cancer treatment. However, there are still many aspects of the mechanisms that remain to be elucidated. In future studies, we will perform kinase spectrum screening to identify additional protein kinases involved in the mechanisms of cancer treatment, such as the downstream molecules of the MEK/ERK kinase pathway and the pathways in which RET and VEGFR2 are involved.

Acknowledgements

This work was supported by grants from the Science and Technology Commission of Shanghai Municipality in China (No O5JC14068 and 075407059).

Abbreviations

RET, the rearranged during transfection receptor; Raf, v-raf

1 murine leukemia viral oncogene homolog 1; VEGFR2, vascular endothelial growth factor receptor 2; KDR, kinase insert domain receptor; MEK, mitogen-activated protein kinase; ERK, extracellular signal-regulated kinase; PI3K, phosphatidylinositol 3-kinase; AKT, protein kinase B; PLCγ, phospholipase Cγ; HER2, human epidermal growth factor receptor 2; Kit, stem cell factor receptor; EGF, epidermal growth factor.

References

1 Lyons JF, Wilhelm S, Hibner B, Bollag G. Discovery of a novel Raf kinase inhibitor. Endocr Relat Cancer 2001; 8: 219–25.
2 Awada A, Hendlisz A, Gil T, Bartholomeus S, Mano M, de Valeriola D, *et al*. Phase I safety and pharmacokinetics of BAY 43-9006 administered for 21 days on/7 days off in patients with advanced, refractory solid tumours. Br J Cancer 2005; 92: 1855–61.
3 Sridhar SS, Hedley D, Siu LL. Raf kinase as a target for anticancer therapeutics. Mol Cancer Ther 2005; 4: 677–85.
4 Strumberg D, Richly H, Hilger RA, Schleucher N, Korfee S, Tewes M, *et al*. Phase I clinical and pharmacokinetic study of the novel Raf kinase and vascular endothelial growth factor receptor inhibitor BAY 43-9006 in patients with advanced refractory solid tumors. J Clin Oncol 2005; 23: 965–72.
5 Liu L, Cao Y, Chen C, Zhang X, McNabola A, Wilkie D, *et al*. Sorafenib blocks the RAF/MEK/ERK pathway, inhibits tumor angiogenesis, and induces tumor cell apoptosis in hepatocellular carcinoma model PLC/PRF/5. Cancer Res 2006; 66: 11851–8.
6 Jane EP, Premkumar DR, Pollack IF. Coadministration of sorafenib with rottlerin potently inhibits cell proliferation and migration in human malignant glioma cells. J Pharmacol Exp Ther 2006; 319: 1070–80.
7 Zhu AX. Beyond sorafenib: novel targeted therapies for advanced hepatocellular carcinoma. Expert Opin Investig Drugs 2010; 19: 663–72.
8 Wilhelm SM, Carter C, Tang L, Wilkie D, McNabola A, Rong H, *et al*. BAY 43-9006 exhibits broad spectrum oral antitumor activity and targets the RAF/MEK/ERK pathway and receptor tyrosine kinases involved in tumor progression and angiogenesis. Cancer Res 2004; 64: 7099–109.
9 Carlomagno F, Anaganti S, Guida T, Salvatore G, Troncone G, Wilhelm SM, *et al*. BAY 43-9006 inhibition of oncogenic RET mutants. J Natl Cancer Inst 2006; 98: 326–34.
10 Aragon-Ching JB, Dahut WL. VEGF inhibitors and prostate cancer therapy. Curr Mol Pharmacol 2009; 2: 161–8.
11 Cuccuru G, Lanzi C, Cassinelli G, Pratesi G, Tortoreto M, Petrangolini G, *et al*. Cellular effects and antitumor activity of RET inhibitor RPI-1 on MEN2A-associated medullary thyroid carcinoma. J Natl Cancer Inst 2004; 96: 1006–14.
12 Antonelli A, Fallahi P, Ferrari SM, Mancusi C, Colaci M, Santarpia L, *et al*. RET TKI: potential role inthyroid cancers. Curr Oncol Rep 2012; 14: 97–104.
13 Jhiang SM. The RET proto-oncogene in human cancers. Oncogene 2000; 19: 5590–7.
14 Takahashi M. The GDNF/RET signaling pathway and human diseases. Cytokine Growth Factor Rev 2001; 12: 361–73.
15 Wellbrock C, Hurlstone A. BRAF as therapeutic target in melanoma. Biochem Pharmacol 2010; 80: 561–7.
16 Wellbrock C, Karasarides M, Marais R. The RAF proteins take centre stage. Nat Rev Mol Cell Biol 2004; 5: 875–85.
17 Kolch W. Coordinating ERK/MAPK signalling through scaffolds and inhibitors. Nat Rev Mol Cell Biol 2005; 6: 827–37.
18 Ranieri G, Gadaleta-Caldarola G, Goffredo V, Patruno R, Mangia A, Rizzo A, *et al*. Sorafenib (BAY 43-9006) in hepatocellular carcinoma patients: from discovery to clinical development. Curr Med Chem 2012; 19: 938–44.
19 Molina MA, Codony-Servat J, Albanell J, Rojo F, Arribas J, Baselga J. Trastuzumab (herceptin), a humanized anti-Her2 receptor monoclonal antibody, inhibits basal and activated Her2 ectodomain cleavage in breast cancer cells. Cancer Res 2001; 61: 4744–9.
20 Heinrich MC, Corless CL, Demetri GD, Blanke CD, von Mehren M, Joensuu H, *et al*. Kinase mutations and imatinib response in patients with metastatic gastrointestinal stromal tumor. J Clin Oncol 2003; 21: 4342–9.
21 Heinrich MC, Maki RG, Corless CL, Antonescu CR, Harlow A, Griffith D, *et al*. Primary and secondary kinase genotypes correlate with the biological and clinical activity of sunitinib in imatinib-resistant gastrointestinal stromal tumor. J Clin Oncol 2008; 26: 5352–9.
22 Feld R, Sridhar SS, Shepherd FA, Mackay JA, Evans WK. Use of the epidermal growth factor receptor inhibitors gefitinib and erlotinib in the treatment of non-small cell lung cancer: a systematic review. J Thorac Oncol 2006; 1: 367–76.
23 Plaza-Menacho I, Mologni L, Sala E, Gambacorti-Passerini C, Magee AI, Links TP, *et al*. Sorafenib functions to potently suppress RET tyrosine kinase activity by direct enzymatic inhibition and promoting RET lysosomal degradation independent of proteasomal targeting. J Biol Chem 2007; 282: 29230–40.

Acta Pharmacologica Sinica (2012) 33: 1319–1324

www.nature.com/aps

Original Article

Enhanced antitumor effects of BPD-MA-mediated photodynamic therapy combined with adriamycin on breast cancer in mice

Zhong-sheng TONG*, Pei-tian MIAO, Ting-ting LIU, Yong-sheng JIA, Xiao-dong LIU

Medical Department of Breast Oncology, Tianjin Medical University Cancer Institute and Hospital, Tianjin 300060, China

Aim: Photodynamic therapy (PDT) is an emerging treatment used to eradicate premalignant and early-stage cancers and to reduce tumor size in end-stage cancers. In this study, we investigated the effects of a combination of benzoporphyrin derivative monoacid ring A (BPD-MA)-mediated PDT with adriamycin (ADM) on 4T1 breast carcinoma cells *in vivo* and the mechanisms underlying this effect.
Methods: Normal BALA/c female mice bearing 4T1 breast carcinoma xenografts were tested. The animals were treated with PDT (BPD-MA 1 mg/kg, iv, plus single-dose laser irradiation) or ADM (5 mg/kg, iv) alone, or a combination of PDT with ADM. The tumor growth rate was determined by measuring the tumor weight. Cell apoptosis was measured with flow cytometry, and the expression of apoptosis-related molecules was assessed using Western blot. Microvessel density (MVD) was determined with immunohistochemical staining.
Results: Compared to PDT or ADM alone, PDT plus ADM produced a combined inhibition on the tumor growth, prolonged life span, and enhanced apoptosis in the mice bearing 4T1 subcutaneously xenografted tumors. The combination of PDT and ADM exerted additive effects on the upregulation of Bax and the downregulation of Bcl-2, and on the reduction of MVD in 4T1 xenografted tumors.
Conclusion: Our results demonstrate that PDT plus ADM exerts enhanced *in vivo* antitumor effect on breast cancer, which is closely associated with the cooperative regulation of extrinsic apoptotic pathways and the inhibition of tumor angiogenesis. Thus, PDT plus ADM is a promising combined treatment strategy for breast carcinoma.

Keywords: breast cancer; photodynamic therapy; benzoporphyrin derivative monoacid ring A (BPD-MA); adriamycin; xenograft; apoptosis; Bax; Bcl-2; angiogenesis

Acta Pharmacologica Sinica (2012) 33: 1319–1324; doi: 10.1038/aps.2012.45; published online 30 Jul 2012

Introduction

Breast cancer is the most common malignant disease among women in China. For management purposes, breast cancer is categorized into operable or advanced breast cancer. Advanced breast cancer is either a locally advanced or metastatic disease. Locally advanced breast cancer (LABC) is characterized by varying clinical presentations, such as the presence of a large primary tumor (>5 cm), associated with or without skin or chest-wall involvement or with fixed (matted) axillary lymph nodes or with disease spread to the ipsilateral internal mammary or supraclavicular nodes in the absence of any evidence of distant metastases[1, 2]. This wide presentation spectrum makes the management of LABC a challenge for oncologists.

Photodynamic therapy (PDT) is increasingly being recognized as an attractive alternative treatment modality for superficial cancer[3, 4], and this therapy has already been used on patients suffering from cancers of the skin or mouth. Additionally, it is presumed that this form of therapy may replace the use of radiotherapy in a number of breast cancer patients. Wyss *et al* showed that PDT offers a minimally invasive outpatient treatment modality for recurrent breast cancer on the chest wall with few side effects, high patient satisfaction and possible repetitive application[5].

PDT utilizes a photosensitizer and light to generate reactive oxygen species and creates an opportunity for targeted lesion destruction. Careful selection of the photosensitizer and light source is required to achieve the desired efficacy during the PDT treatment of cancer. Benzoporphyrin derivative monoacid ring A (BPD-MA) is a second-generation photosensitizer for PDT that has yielded good results in phase I clinical trials[6]. However, BPD-MA-mediated PDT in breast carcinoma is still obscure.

* To whom correspondence should be addressed.
E-mail tonghang@medmail.com.cn
Received 2012-01-06 Accepted 2012-04-05

Chemotherapy is one of the most conventional therapeutic strategies for the treatment of human cancers. Conventional chemotherapy drugs include adriamycin (ADM), cisplatin and 5-fluorouracil. ADM is commonly used in the treatment of a wide range of cancers, including hematological malignancies, many types of carcinomas, and soft tissue sarcomas. Although the mechanism is not yet fully understood, ADM is generally believed to kill cancer cells by DNA intercalation, which eventually leads to cell death. Despite these merits, most serious adverse effect of ADM is life-threatening heart damage. It is therefore crucial to explore novel approaches to reduce drug dosage, minimize side effects and enhance therapeutic efficacy to promote the application of ADM in breast cancer chemotherapy. In this study, our aim was to investigate the combined effect of BPD-MA-mediated PDT plus ADM on 4T1 breast carcinoma cells *in vivo* and the underlying mechanism.

Materials and methods

Cell lines

The 4T1 breast carcinoma cell line was cultured in RPMI-1640 (Invitrogen, Carlsbad, CA, USA) supplemented with 10% heat-inactivated fetal bovine serum (Gibco BRL, Grand Island, NY, USA), 100 units/mL penicillin (Sigma, St Louis, MO, USA), and 100 μg/mL streptomycin (Sigma, St Louis, MO, USA) and maintained in 5% CO_2 at 37 °C.

Animal experiments

Five- to six-week-old female normal BALB/c mice were purchased from the Institute of Laboratory Animal Science in the Chinese Academy of Medical Sciences. 4T1 cells were collected and prepared as a 0.2-mL cell suspension containing 8×10^6 cells; the cells were inoculated subcutaneously (sc) into the right flank of normal BALB/c mice using a sterile 22-gauge needle after alcohol preparation of the skin and manual restraint. Tumor sizes were measured using a caliper, and tumor volume was calculated using the formula (length×width^2)/2.

Treatment was started when the tumor mass reached approximately 100–150 mm^3 in volume (d 4). On d 4, the mice were treated with ADM (5 mg/kg) via tail vein injection. On d 5, the mice were treated with BPD-MA (1 mg/kg) via tail vein injection and were irradiated with a single dose of laser light (690 nm, energy density of 120 J/cm^2) 24 h later. On the indicated day, all tumors were collected to measure the tumor weights. All animal experiments were performed according to a protocol approved by the National Guidelines for Use and Care of Animals.

Western blot

To determine the levels of protein expression, tumor tissues were lysed in RIPA lysis buffer [50 mmol/L Tris-HCl (pH 8.0), 150 mmol/L NaCl, 0.1% SDS, 1% NP-40, 0.25% sodium deoxycholate, and 1 mmol/L EDTA] containing a cocktail of freshly added protease inhibitors (Roche, USA) for 30 min on ice and subsequently centrifuged at 13 000 r/min for 10 min. Total protein concentration of the whole-cell extracts was measured using Bradford reagent (Bio-Rad, Hercules, CA, USA). The proteins were resolved by SDS-PAGE (Bio-Rad, Hercules, CA, USA). After electrophoresis, the proteins were electrotransferred onto polyvinylidene fluoride membranes (Millipore, Bedford, MA, USA), blocked with 5% skim milk, and probed with the Bcl-2, Bax or β-actin primary antibody (Upstate Biotechnology, Lake Placid, NY, USA) that had been diluted in PBS/BSA followed by horseradish peroxidase (HRP)-conjugated secondary antibody (Sigma, St Louis, MO, USA). Binding was detected by enhanced chemiluminescence (Millipore, Bedford, MA, USA).

Apoptosis assay

Single-cell suspensions were made from tumor tissues, washed twice in PBS and incubated with 10 μL (20 μg/mL) of Annexin V-FITC according to the manufacturer's instructions. The cells were incubated with 5 μL (50 μg/mL) of propidium iodide for 2 min on ice and were analyzed with a FACScan flow cytometer (Beckman Counter Epics XL, USA). This assay discriminates between intact cells (FITC$^-$/PI$^-$), early apoptotic cells (FITC$^+$/PI$^-$), late apoptotic cells (FITC$^+$/PI$^+$) and necrotic cells (FITC$^-$/PI$^+$).

Immunohistochemistry

Tumors were excised, fixed in 4% paraformaldehyde, and processed for paraffin embedding. Tumor tissue sections were immunostained using CD34[7] (Santa Cruz Biotechnology, USA) in addition to biotinylated secondary antibodies and horseradish peroxidase-conjugated anti-biotin from the ABC-Peroxidase Kit (Vector Laboratories, Burlingame, CA, USA) according to the manufacturer's instructions. Tumors were viewed under a light microscope (Olympus-IX70, Tokyo, Japan).

Statistical analysis

Results are expressed as the mean±SD, and two-tailed *t*-tests were used to evaluate the inter-group differences with Prism 5.0 software (GraphPad, USA). The statistical significance was set at $P<0.05$, and $P<0.01$ indicates a highly significant difference.

Results

PDT plus ADM suppresses *in vivo* 4T1 breast carcinoma growth

To determine whether PDT plus ADM inhibits 4T1 breast carcinoma growth *in vivo*, we carried out tumor growth experiments using 4T1 xenografted tumors in a normal BALB/c mouse model. As shown in Figure 1, tumor growth was more significantly retarded in the PDT plus ADM group compared with the PDT or ADM single treated group ($P<0.01$), indicating that PDT plus ADM combination treatment remarkably suppressed tumor growth *in vivo*. To assess PDT plus ADM-mediated prolongation of survival time of mice bearing 4T1 breast carcinoma cells, the mouse survival rate was investigated. As shown in Figure 2, the survival rate was significantly increased in the PDT plus ADM group compared with the PDT- or ADM-single treated group ($P<0.01$). These results

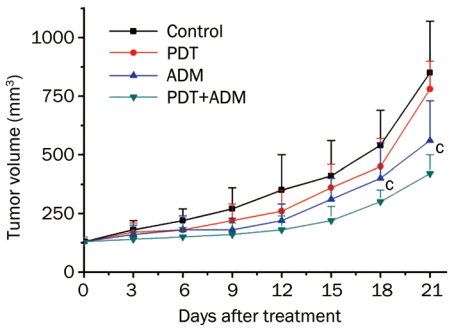

Figure 1. PDT plus ADM inhibits the 4T1 tumor growth in normal BALB/c mice. 4T1 cells were collected and inoculated into female normal BALB/c mice subcutaneously (sc) on one side of flank, 8×10^6 cells/0.2 mL. The tumor sizes were measured using a caliper, tumor volume was calculated using the formula: (length×width^2)/2. On Day 21, all tumors were collected to measure the tumor weights. Mean±SD. n=6. ^cP<0.01.

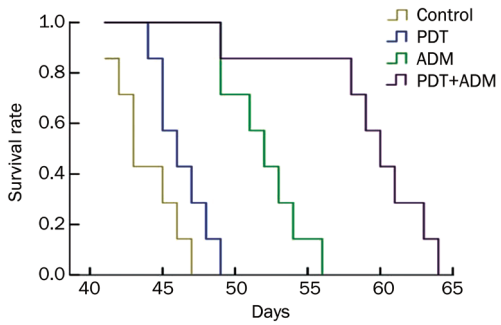

Figure 2. Effect of PDT plus ADM on the life span of 4T1 transplantable murine breast carcinoma in normal BALB/c mice. Survival time of mice treated with PDT plus ADM was significantly longer than that of non-treated, single PDT and ADM-treated mice. Mean±SD. n=6. ^cP<0.01.

indicated that the combination of PDT and ADM prolongs the survival time of 4T1 breast carcinoma-bearing mice.

PDT plus ADM enhances apoptosis in 4T1 breast carcinoma cells

We determined that PDT plus ADM enhanced apoptosis in 4T1 breast carcinoma cells (Figure 3). To examine whether PDT plus ADM combination treatment elicited enhanced apoptosis in breast carcinoma tissues, single-cell suspensions produced from different treatments of 4T1 breast carcinoma tissues were stained with Annexin V (early apoptotic marker) and PI (late apoptotic marker). Apoptosis of 4T1 breast carcinoma cells was subsequently analyzed by flow cytometry. As shown in Figure 4A, the combination of Ad-PDT with ADM more efficiently induced 4T1 breast carcinoma apoptosis than PDT or ADM single. To further address the underlying molecular mechanism by which PDT plus ADM combination treatment results in an enhanced antitumor effect, the expression of apoptosis-related proteins, such as Bax and Bcl-2, was determined by Western blot analysis in differentially treated 4T1 xenografted tumor tissues. As shown in Figure 4B, expression of Bax in the PDT, ADM, and PDT plus ADM groups signifi-

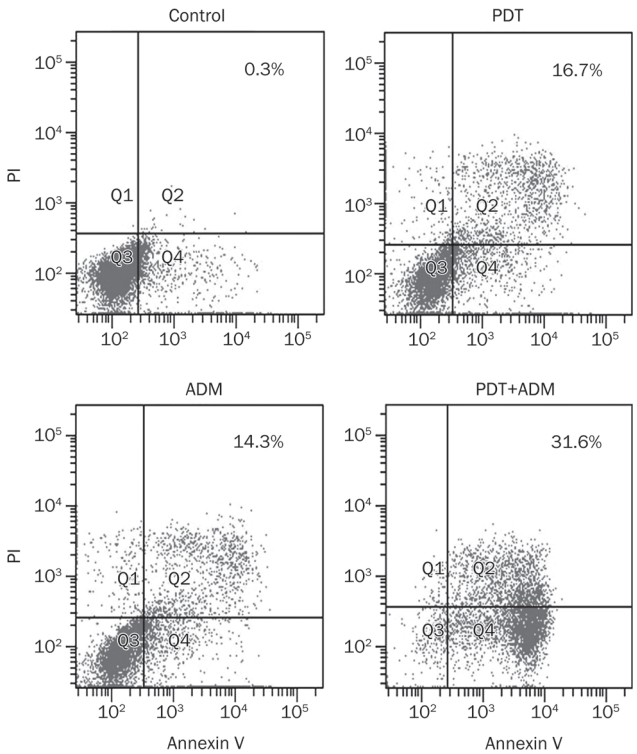

Figure 3. PDT plus ADM enhances apoptosis in 4T1 breast carcinoma cells. 4T1 breast carcinoma cells were treated with PDT (0.5 μg/mL, 2J/cm^2), ADM (1 μg/mL), PDT plus ADM, then the apoptotic cells were assessed by flow cytometry after 24 h, respectively.

cantly increased, whereas the expression of Bcl-2 decreased in comparison with the control group. These results indicate that PDT plus ADM remarkably suppressed 4T1 breast carcinoma growth and induced apoptosis, which was closely associated with cooperative regulation of the intrinsic apoptotic pathway.

PDT plus ADM reduces tumor vessel CD34 expression and MVD

The positive expression of CD34 was mainly represented as brownish yellow or brownish granules in vascular endothelial cells. In all collected 4T1 xenografted tumors, CD34 expression in tumor vascular endothelial cells in the PDT plus ADM combination treatment group was weaker than in the PDT- or ADM-single treated groups (Figure 5A), which indicated that PDT plus ADM additively or synergistically downregulates CD34 expression in 4T1 xenografted tumor vessels. Furthermore, the MVD (Figure 5B) in the PDT plus ADM group was significantly less than that in the PDT- or ADM-single groups. This result indicated that PDT plus ADM has a combined effect on the reduction of MVD in 4T1 xenografted tumors, which may be another important mechanism responsible for the PDT plus ADM-mediated *in vivo* combined growth inhibition of 4T1 xenografted tumors in a normal BALB/c mouse model.

Discussion

At present, PDT is being tested in the oncology clinic to treat

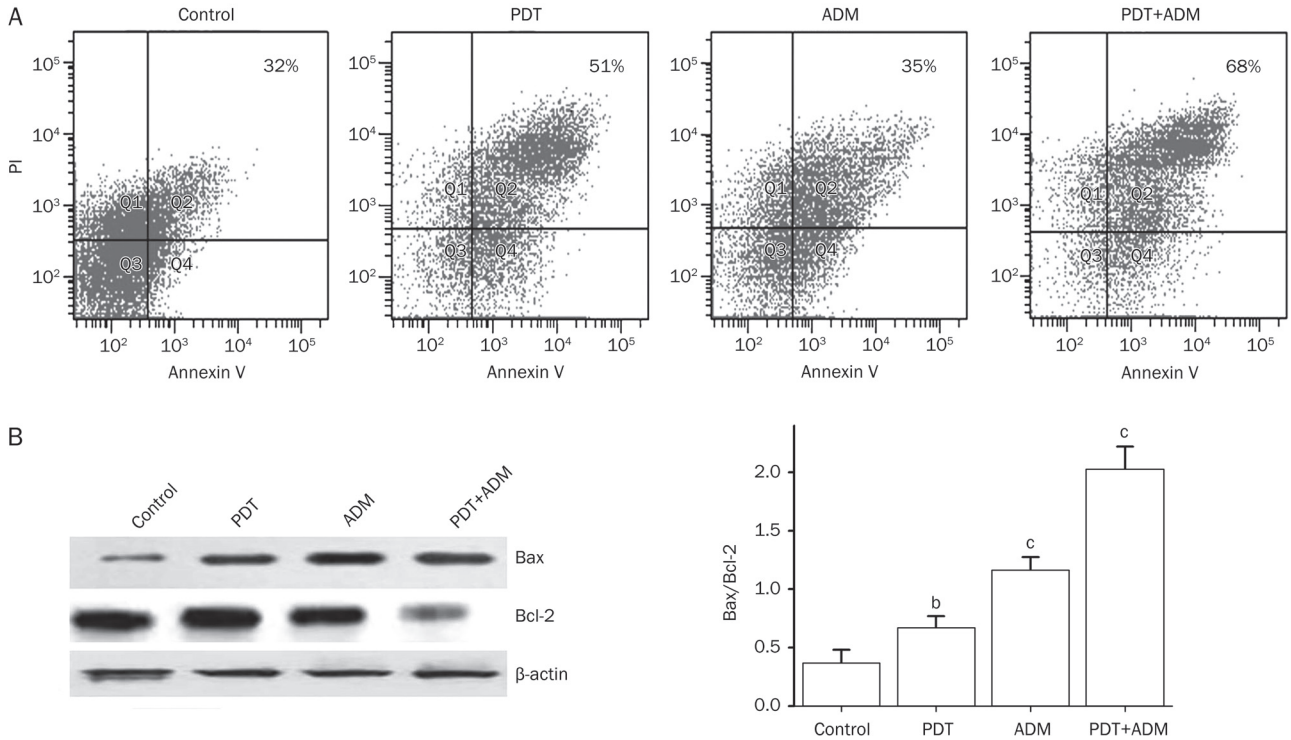

Figure 4. PDT plus ADM enhances apoptosis by cooperatively regulating extrinsic apoptotic pathways. Normal BALB/c mice bearing 4T1 breast carcinoma were treated with PDT, ADM, PDT plus ADM, then the apoptotic cells and expression of apoptosis-related proteins in 4T1 tumor tissues were assessed by flow cytometry and Western blot analysis after 21 d, respectively. (A) PDT plus ADM enhances apoptosis in 4T1 breast carcinoma cells. The apoptotic cells were analyzed using Annexin V/PI double staining by flow cytometry. The Annexin V single-positive cells (early apoptotic cells) in the total cell population represented apoptotic cells. PDT plus ADM enhanced apoptosis in 4T1 tumor cells ($^bP<0.05$, compared with PDT and ADM group, one-way repeated measures ANOVA and multiple comparisons, $n=6$ replicates per condition). (B) PDT plus ADM cooperatively regulates extrinsic apoptotic pathways. Total tumor tissue lysates of treated and untreated 4T1 tumors were analyzed by immunoblotting with a panel of antibodies specific for Bcl-2 and Bax. The quantities of protein expression were normalized to the internal control β-actin measured in the same samples. PDT plus ADM combination treatment elicited an additive effect on the altered expression of apoptosis-related proteins such as Bcl-2 and Bax. Mean±SD. $n=3$. $^bP<0.05$, $^cP<0.01$.

cancers of the head and neck, brain, lung, pancreas, intraperitoneal cavity, breast, prostate and skin[8]. The combination of various therapeutic modalities with non-overlapping toxicities is a commonly used strategy to improve the therapeutic index of treatments in modern oncology. However, the combined effect of PDT and ADM, an attractive chemotherapy drug, on breast cancer is still unknown. Therefore, we designed this study to address the therapeutic effect and potential mechanism of PDT plus chemotherapy by combining PDT with ADM and treating breast carcinoma cells in a normal BALB/c mouse model. We first assessed the inhibition of 4T1 breast carcinoma growth by PDT plus ADM. We found that PDT plus ADM significantly inhibited 4T1 breast carcinoma growth in a normal BALB/c mouse model. Additionally, the combination of PDT plus ADM prolonged the survival time of 4T1 breast carcinoma-bearing mice. To further address the underlying mechanism involved in the enhanced PDT plus ADM-induced antitumor activity, the expression of apoptosis-related proteins Bcl-2 and Bax in different 4T1 breast carcinoma treatment groups was assessed by Western blot analysis. Tumor development requires a combination of defects that allows nascent neoplastic cells to become self-sufficient for cell proliferation and insensitive to signals that normally restrain cell growth. The evasion of apoptosis has proven to be critical for the development and sustained growth of cancer. The Bcl-2 protein family is known to be a key regulator of apoptosis and an important determinant of cell fate[9]. Mitochondria participate in apoptosis through a range of mechanisms that vary between vertebrates and invertebrates. In vertebrates, they release intermembrane space proteins, such as cytochrome *c*, to promote caspase activation in the cytosol. This process is the result of the loss of integrity of the outer mitochondrial membrane caused by proapoptotic members of the Bcl-2 family[9]. Moreover, Pluta *et al*[10] showed that decreased Bax protein expression in breast cancer cells may suggest a potential means of apoptosis avoidance in tumor cells. Correlations among Bax protein, p53 and caspase-3 expression are probably associated with an active apoptotic mechanism in breast cancer cells expressing the Bax protein. Wu *et al*[11] also reported that Bax activation is not essential for mitochondrial outer membrane permeabilization but essential for Drp1-mediated mitochondrial fission during the apoptosis caused by Photofrin-

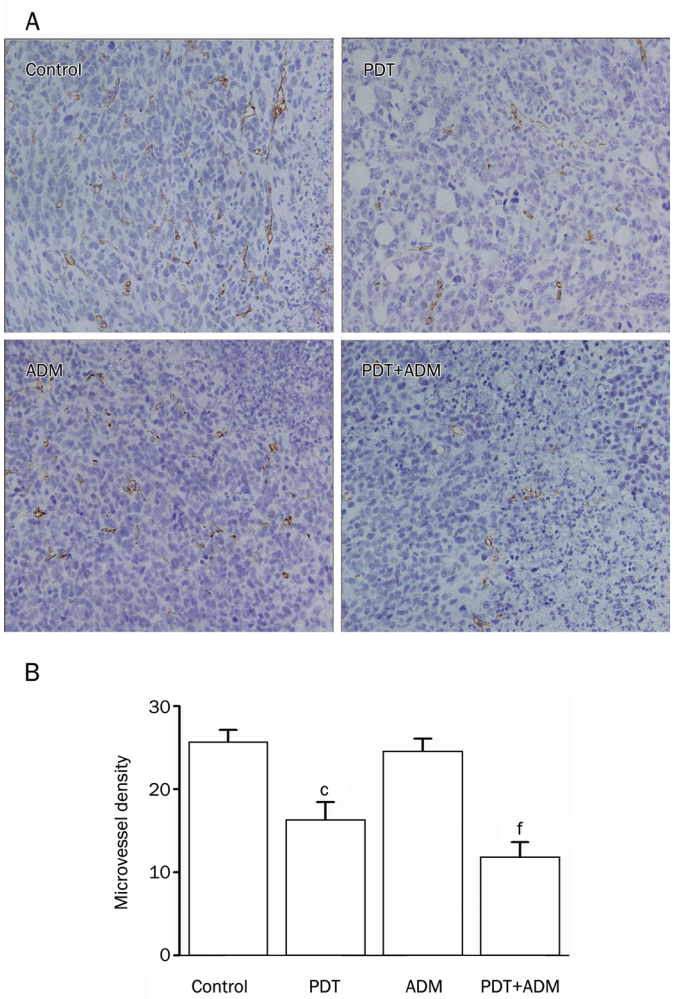

Figure 5. Combined inhibition of tumor angiogenesis *in vivo*. (A) Immunohistochemical detection for CD34 expression in 4T1 breast carcinoma sc xenografted tumors. Representative pictures for different treatment groups are shown. The positive expression of CD34 was mainly represented as brownish yellow or brownish granules in tumor vascular endothelial cells. (B) The tumor MVD in different treatment groups. PDT plus ADM combination treatment synergistically inhibited *in vivo* angiogenesis of 4T1 breast carcinoma sc xenografted tumors ($^{c}P<0.01$ *vs* control group, one-way repeated measures ANOVA and multiple comparisons, $n=6$ mice per condition, $n=5$ observations per representative section). $^{f}P<0.01$ *vs* PDT or ADM single treatment group.

PDT. The ratio of anti- to pro-apoptotic molecules constitutes a rheostat that sets the threshold of susceptibility to apoptosis for the intrinsic apoptotic pathway, which promotes pore formation in the mitochondrial outer membrane, leading to the loss of mitochondrial integrity and the release of cytochrome *c* into the cytosol[12–14]. Western blot results showed that PDT plus ADM combination treatment elicited an additive effect on the altered expression of apoptosis-related proteins, leading to the cooperative activation of the intrinsic apoptotic pathway, which may closely account for the PDT plus ADM-mediated growth inhibition and apoptosis in 4T1 breast carcinoma cells.

Angiogenesis has been a common prognostic indicator for breast carcinoma in the last decade. Indeed, previous studies have shown that higher intratumoral microvessel density is statistically correlated with a greater incidence of metastasis and that intratumoral microvessel density is an independent prognostic indicator for overall and relapse-free survival in early-stage invasive breast carcinomas[15, 16]. In addition to directly killing cancer cells, PDT appears to shrink or destroy tumors in other ways. The photosensitizer can damage blood vessels in the tumor, thereby preventing the cancer from receiving necessary nutrients[17–19]. Gomer *et al*[20] showed that bovine endothelial cells were significantly more sensitive to PDT with porfimer sodium than smooth muscle cells or fibroblasts from the same species. To explore the combined effect of PDT plus ADM on tumor angiogenesis *in vivo*, the MVD in 4T1 xenograft tumour tissues was determined by CD34 immunohistochemistry analysis. We found that PDT plus ADM downregulated CD34 expression and suppressed angiogenesis in 4T1 breast carcinoma, which may be another important mechanism involved in the PDT plus ADM-mediated *in vivo* combined growth inhibition of 4T1 xenografted tumors in normal BALB/c mice.

Taken together, the PDT plus ADM combined treatment resulted in *in vivo* combined growth inhibition and enhanced apoptosis, as well as imparting an additive effect on Bax upregulation and Bcl-2 downregulation in 4T1 breast carcinomas. This treatment also reduced CD34 expression and MVD in 4T1 xenografted tumors. Most importantly, the enhanced *in vivo* antitumor effect elicited by PDT plus ADM was closely associated with an increase in Bax expression and a decrease in the ratio of anti- to pro-apoptotic molecules of Bcl-2 by cooperatively regulating intrinsic apoptotic pathways and the *in vivo* combined inhibition of tumor angiogenesis. Therefore, our results indicate that BPD-MA-mediated PDT plus ADM is a potential combined treatment strategy against breast carcinoma.

Acknowledgements

This work was supported by the Natural Science Foundation of Tianjin [No 10JCYBJC11500].

Author contribution

Zhong-sheng TONG designed research; Pei-tian MIAO performed research; Xiao-dong LIU contributed new reagents or analytic tools; Ting-ting LIU analyzed data; Yong-sheng JIA wrote the paper.

References

1 Buchholz TA. Introduction: locally advanced breast cancer. Semin Radiat Oncol 2009; 19: 193–4.
2 Gould J, Fitzgerald B, Fergus K, Clemons M, Baig F. Why women delay seeking assistance for locally advanced breast cancer. Can Oncol Nurs J 2010; 20: 23–9.
3 Triesscheijn M, Baas P, Schellens JH, Stewart FA. Photodynamic therapy in oncology. Oncologist 2006; 11: 1034–44.
4 Agostinis P, Berg K, Cengel KA, Foster TH, Girotti AW, Gollnick SO, *et al*. Photodynamic therapy of cancer: an update. CA Cancer J Clin 2011; 61: 250–81.

5 Wyss P, Schwarz V, Dobler-Girdziunaite D, Hornung R, Walt H, Degen A, *et al*. Photodynamic therapy of locoregional breast cancer recurrences using a chlorin-type photosensitizer. Int J Cancer 2001; 93: 720–4.
6 Aveline B, Hasan T, Redmond RW. Photophysical and photosensitizing properties of benzoporphyrin derivative monoacid ring A (BPD-MA). Photochem Photobiol 1994; 59: 328–35.
7 Weidner N. Measuring intratumoral microvessel density. Methods Enzymol 2008; 444: 305–23.
8 Dolmans DE, Fukumura D, Jain RK. Photodynamic therapy for cancer. Nat Rev Cancer 2003; 3: 380–7.
9 Kelly PN, Strasser A. The role of Bcl-2 and its pro-survival relatives in tumourigenesis and cancer therapy. Cell Death Differ 2011; 18: 1414–24.
10 Pluta P, Smolewski P, Pluta A, Cebula-Obrzut B, Wierzbowska A, Nejc D, *et al*. Significance of bax expression in breast cancer patients. Pol Przegl Chir 2011; 83: 549–53.
11 Wu S, Zhou F, Zhang Z, Xing D. Bax is essential for Drp1-mediated mitochondrial fission but not for mitochondrial outer membrane permeabilization caused by photodynamic therapy. J Cell Physiol 2011; 226: 530-41.
12 Martinou JC, Youle RJ. Mitochondria in apoptosis: Bcl-2 family members and mitochondrial dynamics. Dev Cell 2011; 21: 92–101.
13 Fletcher JI, Meusburger S, Hawkins CJ, Riglar DT, Lee EF, Fairlie WD, *et al*. Apoptosis is triggered when prosurvival Bcl-2 proteins cannot restrain Bax. Proc Natl Acad Sci U S A 2008; 105: 18081–7.
14 Eissing T, Waldherr S, Allgower F, Scheurich P, Bullinger E. Response to bistability in apoptosis: roles of bax, bcl-2, and mitochondrial permeability transition pores. Biophys J 2007; 92: 3332–4.
15 Vartanian RK, Weidner N. Correlation of intratumoral endothelial cell proliferation with microvessel density (tumor angiogenesis) and tumor cell proliferation in breast carcinoma. Am J Pathol 1994; 144: 1188–94.
16 Weidner N. Current pathologic methods for measuring intratumoral microvessel density within breast carcinoma and other solid tumors. Breast Cancer Res Treat 1995; 36: 169–80.
17 Chen B, Pogue BW, Luna JM, Hardman RL, Hoopes PJ, Hasan T. Tumor vascular permeabilization by vascular-targeting photosensitization: effects, mechanism, and therapeutic implications. Clin Cancer Res 2006; 12: 917–23.
18 Bhuvaneswari R, Gan YY, Soo KC, Olivo M. The effect of photodynamic therapy on tumor angiogenesis. Cell Mol Life Sci 2009; 66: 2275–83.
19 Lisnjak IO, Kutsenok VV, Polyschuk LZ, Gorobets OB, Gamaleia NF. Effect of photodynamic therapy on tumor angiogenesis and metastasis in mice bearing Lewis lung carcinoma. Exp Oncol 2005; 27: 333–5.
20 Gomer CJ, Rucker N, Murphree AL. Differential cell photosensitivity following porphyrin photodynamic therapy. Cancer Res 1988; 48: 4539–42.

Acta Pharmacologica Sinica (2012) 33: 1325–1331
 1671-4083/12 $32.00
www.nature.com/aps

Original Article

Luteolin reduces the invasive potential of malignant melanoma cells by targeting β3 integrin and the epithelial-mesenchymal transition

Jun-shan RUAN[1, 3, #], Yu-ping LIU[1, #], Lei ZHANG[1], Ling-geng YAN[1], Fang-tian FAN[1], Cun-si SHEN[1], Ai-yun WANG[1], Shi-zhong ZHENG[1], Shao-ming WANG[3], Yin LU[1, 2, *]

[1]Department of Clinical Pharmacy, College of Pharmacy, Nanjing University of Chinese Medicine, Nanjing 210029, China; [2]Jiangsu Key Laboratory for Pharmacology and Safety Evaluation of Chinese Materia Medica, Nanjing 210029, China; [3]Fujian Provincial Hospital, Clinical College of Fujian Medical University, Fuzhou 350001, China

Aim: To investigate whether luteolin, a highly prevalent flavonoid, reverses the effects of epithelial-mesenchymal transition (EMT) *in vitro* and *in vivo* and to determine the mechanisms underlying this reversal.
Methods: Murine malignant melanoma B16F10 cells were exposed to 1% O_2 for 24 h. Cellular mobility and adhesion were assessed using Boyden chamber transwell assay and cell adhesion assay, respectively. EMT-related proteins, such as E-cadherin and N-cadherin, were examined using Western blotting. Female C57BL/6 mice (6 to 8 weeks old) were injected with B16F10 cells (1×10^6 cells in 0.2 mL per mouse) via the lateral tail vein. The mice were treated with luteolin (10 or 20 mg/kg, ip) daily for 23 d. On the 23rd day after tumor injection, the mice were sacrificed, and the lungs were collected, and metastatic foci in the lung surfaces were photographed. Tissue sections were analyzed with immunohistochemistry and HE staining.
Results: Hypoxia changed the morphology of B16F10 cells *in vitro* from the cobblestone-like to mesenchymal-like strips, which was accompanied by increased cellular adhesion and invasion. Luteolin (5−50 μmol/L) suppressed the hypoxia-induced changes in the cells in a dose-dependent manner. Hypoxia significantly decreased the expression of E-cadherin while increased the expression of N-cadherin in the cells (indicating the occurrence of EMT-like transformation), which was reversed by luteolin (5 μmol/L). In B16F10 cells, luteolin up-regulated E-cadherin at least partly via inhibiting the β3 integrin/FAK signal pathway. In experimental metastasis model mice, treatment with luteolin (10 or 20 mg/kg) reduced metastatic colonization in the lungs by 50%. Furthermore, the treatment increased the expression of E-cadherin while reduced the expression of vimentin and β3 integrin in the tumor tissues.
Conclusion: Luteolin inhibits the hypoxia-induced EMT in malignant melanoma cells both *in vitro* and *in vivo* via the regulation of β3 integrin, suggesting that luteolin may be applied as a potential anticancer chemopreventative and chemotherapeutic agent.

Keywords: luteolin; epithelial mesenchymal transition; melanoma; hypoxia; E-cadherin; N-cadherin; β3 integrin FAK

Acta Pharmacologica Sinica (2012) 33: 1325–1331; doi: 10.1038/aps.2012.93; published online 17 Sep 2012

Introduction

Skin cancers, including basal cell carcinoma, squamous-cell carcinoma and melanoma, are common human cancers. The gradual increase of skin cancers has recently attracted worldwide attention[1]. Despite the relatively low incidence of melanoma, its mortality rates are the highest among all skin cancers[2, 3]. The incidence of melanoma has increased steadily in Western countries and have doubled worldwide during the last two decades. Metastatic melanoma patients exhibit only an average 6- to 9-month survival period after diagnosis[2, 4].

Epithelial-mesenchymal transition (EMT) refers to the transition from an epithelial to a mesenchymal cell state under physiological and pathological conditions, which is characterized by altered cell morphology and gene expression[5]. Recent studies have demonstrated that the EMT processes in primary and secondary colon, liver, and breast cancer are strongly associated with infiltration transfer in tumor cells[5, 6].

EMT in melanoma not only induces the morphological changes of cancer cells, but also play an essential role in cancer progression[7]. The increased invasive ability of melanoma cells is associated with increased expression levels of EMT-related genes such as snai1, MMP9, twist and vimentin. Additionally, the expression of cell-cell adhesion protein E-cadherin

# These authors contributed equally to this work.
* To whom correspondence should be addressed.
E-mail profyinlu@163.com
Received 2012-03-02 Accepted 2012-06-08

and metastasis suppressor gene Kiss1 were downregulated in these cells[5, 7–9].

Moreover, clinical studies have shown that melanoma metastasis occurs during EMT and that the biomarkers of EMT can be utilized for the clinical diagnosis and prognosis of progressive melanoma metastasis[8, 9]. Furthermore, these studies also suggested that EMT-related genes promoted a metastatic phenotype in primary cutaneous malignant melanoma (CMM) by conferring specific adhesive, invasive, and migratory properties, which further clarified the biological activity of aggressive tumors, providing new diagnostic and prognostic markers, as well as potential therapeutic targets for patients. Therefore, effectively blocking or abrogating EMT will facilitate the treatment of melanoma[10].

Recently, EMT has been verified as a new therapeutic target for the treatment of skin ulcers, fibrosing alopecia, and malignant cutaneous cancers including squamous cell carcinoma and melanoma[11], and the regulatory mechanisms of EMT have also been extensively elucidated.

Furthermore, as a highly prevalent flavonoid in plants, luteolin exhibits favorable biological activity and potential anti-tumor capacity[12] and has also been reported to induce the apoptosis of tumor cells and to inhibit EMT in PC3 cells[13]. In this study, the reversal of EMT was investigated in B16F10 malignant melanoma cells in both *in vitro* and *in vivo* animal experiments.

Materials and methods

Cell culture

Murine malignant melanoma B16F10 cells were obtained from the American Type Culture Collection and cultivated in DMEM medium (Invitrogen) supplemented with 10% FBS (Life Technologies, Grand Island, NY,USA) and 100 units/mL each of penicillin and streptomycin at 37 °C in a 5% CO_2 incubator. The hypoxia-induced model was established by exposing the cells to 1% O_2 for 24 h according to a previously described method[14]. All the culture media and other substances for cell culture were purchased from Life Technologies.

Reagents and antibodies

Luteolin, which was purchased from Helin Biological Engineering Co, Ltd (Xi'an, China), was dissolved at indicated concentrations in dimethylsulfoxide (DMSO). The concentration of DMSO was maintained below 0.1% by adding the medium. The antibodies against N-cadherin, E-cadherin, β3 integrin, and GAPDH were purchased from BioWorld Technology (St Louis Park, MN, USA); vimentin, snail, slug, and ZEB1 antibodies were purchased from Cell Signaling Technology (USA); and the antibodies against FAK and p-FAK were purchased from Signalway Antibody (Pearland, TX, USA).

Cell migration assay

In vitro cell migration assays were performed using 24-well transwell plates (Corning Incorporated Costar, Lindfield, NSW, Australia)[15]. B16F10 cells were grown to a confluence of 80% and incubated with different concentrations of luteolin and 1% O_2 for 24 h. After trypsinization, and resuspension in serum-free DMEM, the cell concentration was adjusted to 1×10^6 before seeding into 24-well transwell plates. Two hundred microliters containing cells (5×10^5) in serum-free medium were added to the upper and the lower wells, which contained DMEM medium with 10% FBS. Two hundred microliters of the cell suspension was added to the transwell upper and lower chambers containing DMEM medium with 10% FBS. After incubation for 8 h, the remaining cells in the upper chamber were removed with a cotton swab, the cell membrane surface was wiped, and the lower side of the filter harboring migrated B16F10 cells was fixed with 4% paraformaldehyde for 30 min. The migrating cells were then stained with 0.5% Coomassie brilliant blue for 10 min and counted by microscopy. Six fields per filter were randomly selected for calculation and analysis

Cell adhesion assay

B16F10 cells were seeded into 6-well plates in normal medium for 24 h and then incubated in 1% O_2 for 24 h, and the control cells were treated with vehicle (0.1% DMSO) or luteolin (5, 10, 25, and 50 μmol/L) and incubated at 37 °C for 24 h. The attached cells were trypsinized, counted and seeded into gelatin-coated 96-well plates at approximately 2.5×10^4 cells per well in normal medium for 1 h. Then, the medium was discarded, and the cells were washed twice with phosphate-buffered saline (PBS) to remove the non-adherent cells. The cells that had been subjected to Rose Bengal staining were then photographed to assess the adhesion activities. Finally, the cells were fixed, stained, and solubilized for absorbance measurements at 570 nm using a VersaMax microplate reader (Molecular Devices) and Softmax Pro Software.

Western blot analysis

After stimulation, all the cells were washed with cold PBS and lysed in RIPA buffer. Cell extracts were transferred to microcentrifuge tubes, mixed, and incubated on ice for 10 min. After one freeze/thaw cycle, the samples were centrifuged at 12000×*g* at 4 °C for 5 min. Supernatant samples were subjected to SDS-PAGE and then electrotransferred to PVDF. The blots were incubated with primary antibodies overnight. After serial washes with Tris-buffered saline-Tween-20, the membranes were incubated with the secondary antibody. Immunoreactive bands were visualized using a peroxidase-conjugated secondary horseradish antibody and subsequent ECL detection (Amersham Pharmacia Biotech, Bucks, UK).

Experimental lung metastasis models

C57BL/6 mice (female, approximately 6 to 8 weeks old, 20 g) were purchased from Slac Animal Inc (Shanghai, China). The mice were housed under specific pathogen-free conditions and handled in a laminar flow air cabinet. The experiments were approved by the Animal Ethics Committees of Nanjing University of Chinese Medicine and performed strictly according to the NIH guide for the Care and Use of Laboratory Animals.

The experimental metastasis model was established by the methods described previously[15, 16]. B16F10 cells (1×10^6 cells in 0.2 mL per mouse) were injected into C57BL/6J mice via the lateral tail vein, following which the mice were randomly divided into different groups. Then, the mice were intraperitoneally injected with luteolin at the doses of 10 or 20 mg/kg mouse body weight, and the control animals were injected with saline daily. The animals were weighed every 3 days. All the mice were sacrificed on the 23rd day after tumor injection. Their lungs were then removed and fixed, and the metastatic foci at the lung surfaces were photographed.

Immunohistochemical analysis

Immunohistochemistry was performed as described previously[16]. The slides were incubated with an appropriate antibody at 4 °C overnight, and the tissue sections were incubated in the blocking buffer containing the corresponding secondary antibody at room temperature for 15 min the following day. After washing with PBS, the immunohistoreactivity was visualized using diaminobenzidine (DAB) under a light microscope at the indicated magnification.

Hematoxylin/eosin (HE) staining analysis

Hematoxylin/eosin staining analysis was performed as previously described[17]. Specimens were examined and photographed under a microscope after staining. Ten immunoreactive areas were randomly selected, and the lung tissue sections for each animal were measured using the Optimas image analyzer (Optimas Corporation USA). Three animals per group were examined.

Statistical analysis

Each experiment was conducted in triplicate, and the data were expressed as the mean±SD. Data were analyzed using a one-way analysis of variance and a protected Fisher's least significant difference test for multiple comparisons (SPSS 10.0, SPSS Inc, USA). $P<0.05$ was considered to be statistically significant.

Results

Inhibition of hypoxia-induced cell adhesion and motility by luteolin in B16F10 cells

Hypoxia is an important feature of the tumor microenvironment[18]. The established hypoxia tumor cell model shows that hypoxia induced morphological changes of tumor cells from the original cobblestone-like to mesenchymal-like strips (Figure 1B). This process was accompanied by increased cellular adhesion and invasion, which were inhibited dramatically by

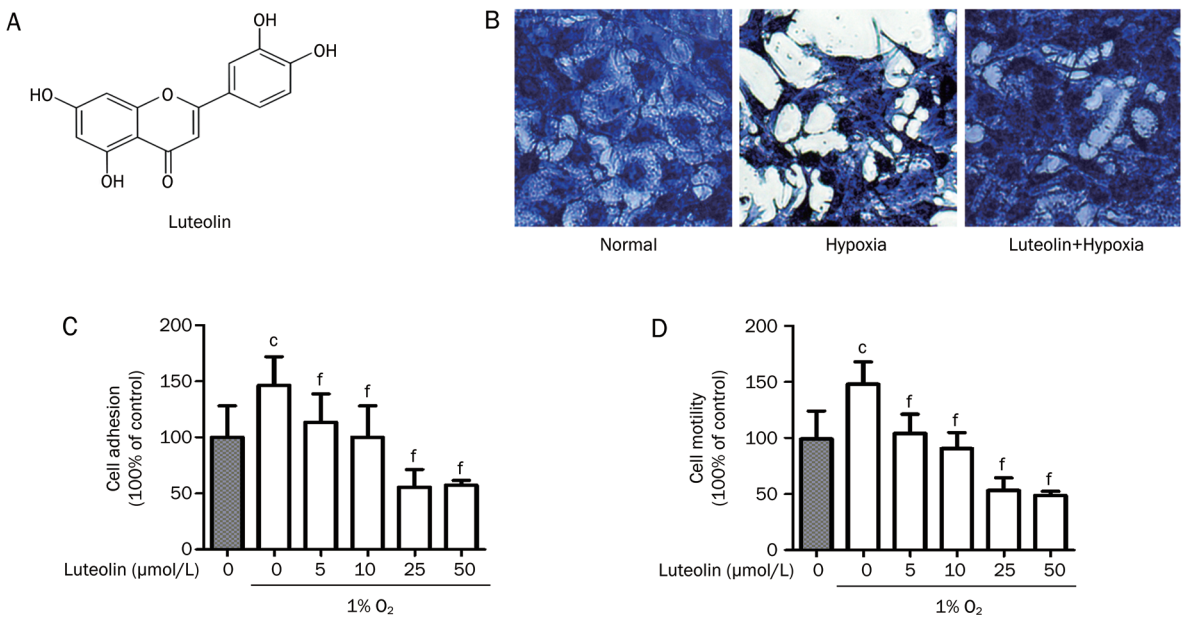

Figure 1. Inhibition of hypoxia-induced cell adhesion and motility by luteolin in B16F10 cells. (A) Molecular structure of luteolin, 3′,4′,5,7-tetrahydroxyflavone, CAS 491-70-3. (B) B16F10 cells were incubated at atmospheric or 1% O_2 in a 37 °C incubator for 24 h and then treated with 25 μmol/L luteolin or 0.1% DMSO and stained with 0.5% Coomassie Brilliant Blue for 10 min. Phenotypic changes of the cells were then monitored. The B16F10 cells, which typically exhibit an epithelial phenotype with well-developed cell junctions, acquired a spindle shape and lost cell contacts under hypoxic conditions. Luteolin blocked the transformation of cell morphology induced by hypoxia. (C) The cells were cultured in atmospheric or 1% O_2 for 24 h and then treated with vehicle (0.1% DMSO) or luteolin (5–50 μmol/L) for 24 h. The cells were trypsinized and seeded into a gelatin-coated 96-well plate in normal growth medium. After incubation for 1 h, the cells were subjected to a cell adhesion assay. Quantitative results are shown as the mean±SD. $n=3$. $^cP<0.01$ *vs* control. $^fP<0.01$ *vs* the hypoxia control group. (D) The cells were cultured in atmospheric or 1% O_2 for 24 h and then treated with vehicle (0.1% DMSO) or luteolin (5–50 μmol/L) for 24 h. Next, cells were subjected to Boyden chamber transwell assays. The migrated cells were visualized and counted from six randomly selected fields (200×magnification) using an inverted microscope. Quantitative results are shown as the mean values±SD. $n=3$. $^cP<0.01$ *vs* control. $^fP<0.01$ *vs* the hypoxia control group.

luteolin in a dose-dependent manner (Figure 1C, 1D).

Hypoxia-induced EMT blocked by luteolin

E-cadherin (epithelial marker) and N-cadherin (mesenchymal marker) are the most important EMT markers[19]. In this study, E-cadherin and N-cadherin were discovered to be expressed in hypoxic microenvironments, and hypoxia could significantly inhibit the expression of E-cadherin while inducing that of N-cadherin in tumor cells, indicating the occurrence of EMT-like transformation. Western blot analysis revealed that 5 μmol/L luteolin could inhibit the expression of N-cadherin and boost the expression of E-cadherin (Figure 2A).

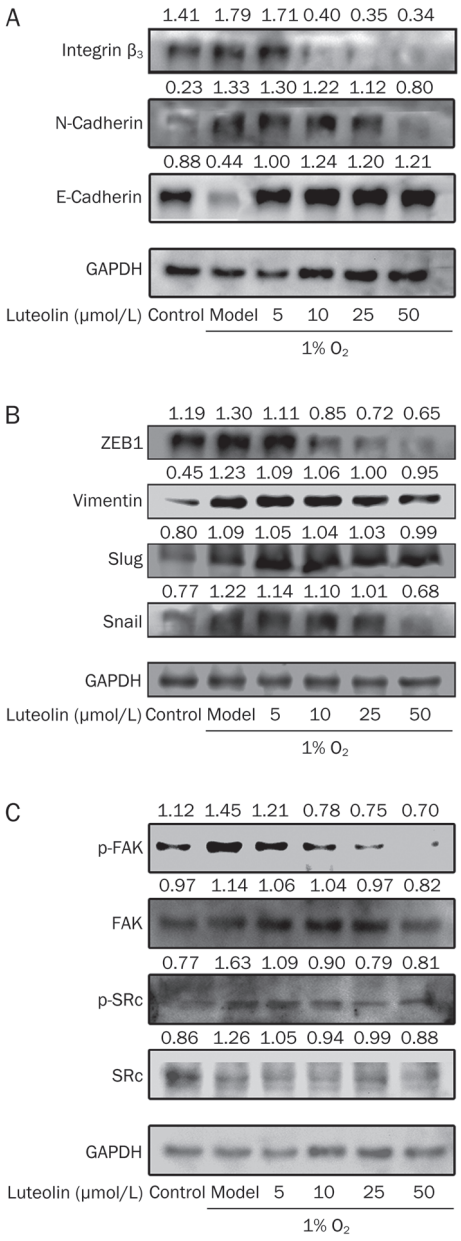

Figure 2. Luteolin blocks hypoxia-induced EMT. B16F10 cells were cultured in atmospheric or 1% O_2 for 24 h and then treated with vehicle (0.1% DMSO) or luteolin (5–50 μmol/L) for 24 h. Next, the cells were subjected to Western blotting with the indicated antibodies. GAPDH was used as a loading control.

Moreover, the possible mechanisms of luteolin-regulated EMT were also determined by first examining the expression levels of E-cadherin-regulating transcription factors such as snail, slug, ZEB1, and vimentin after the treatment of luteolin. The results verified that the expression of ZEB1 could be inhibited by 10 μmol/L luteolin. Snail and vimentin could be regulated by doses of luteolin above 25 μmol/L, whereas slug was not significantly affected by luteolin (Figure 2B). In contrast, 5 μmol/L luteolin was sufficient to regulate the expression of E-cadherin, suggesting that luteolin might control EMT by other pathways.

Inhibitory effects of luteolin on EMT by regulation of β3 integrin

The integrin/FAK signal pathway was recently reported to regulate EMT[8, 20]. In the present study, luteolin inhibited the expression of integrins in B16F10 cells, and the down-regulation of integrin was accompanied by the up-regulation of E-cadherin. Figure 2A and 2C suggest that luteolin inhibited the expression of integrin beta3 and the phosphorylation of FAK, but it did not affect the regulation of the phosphorylation of SRC.

In vivo reversal of melanoma EMT by luteolin

The above *in vitro* experiments confirmed that luteolin could reverse EMT in tumor cells. As EMT is closely related to tumor metastasis[21], we hypothesized that luteolin would inhibit the lung metastasis of melanoma and validated this notion by the experimental metastasis model (Figure 3A).

As shown in Figure 3B, melanoma metastatic nodules are widely distributed in the lungs of the control mice, whereas fewer nodes were detected in the other two groups. Consistently, further statistical analysis revealed a significant 50% reduction of the metastatic colonization of the lungs of the mice that were treated with 10 or 20 mg/kg luteolin for 23 days (Figure 3C).

Furthermore, consistent with the *in vitro* data, immunohistochemical staining results revealed that luteolin could increase the expression of E-cadherin while reducing the expression of vimentin and integrin (Figure 4).

Discussion

EMT drives the invasion and metastasis of epithelial-derived cancers[21, 22]. Luteolin (3′,4′,5,7-tetrahydroxyflavone), which is a common active flavonoid that is abundant in *Lonicera japonica* and *Hedyotis diffusa*, as well as in a vast and diverse array of other plants, has been widely used in the treatment of melanoma[12, 23]. The antitumor effects of luteolin have been well documented in several different human cancers[24–26]; furthermore, luteolin has been reported to elicit anti-EMT effects in cancer cell lines such as PC3 and A431[27, 28]. However, studies investigating the impact of luteolin on the invasion and migration of melanoma cells undergoing EMT and the signaling pathways associated with luteolin remain limited.

Generally, EMT requires a variety of complex signaling

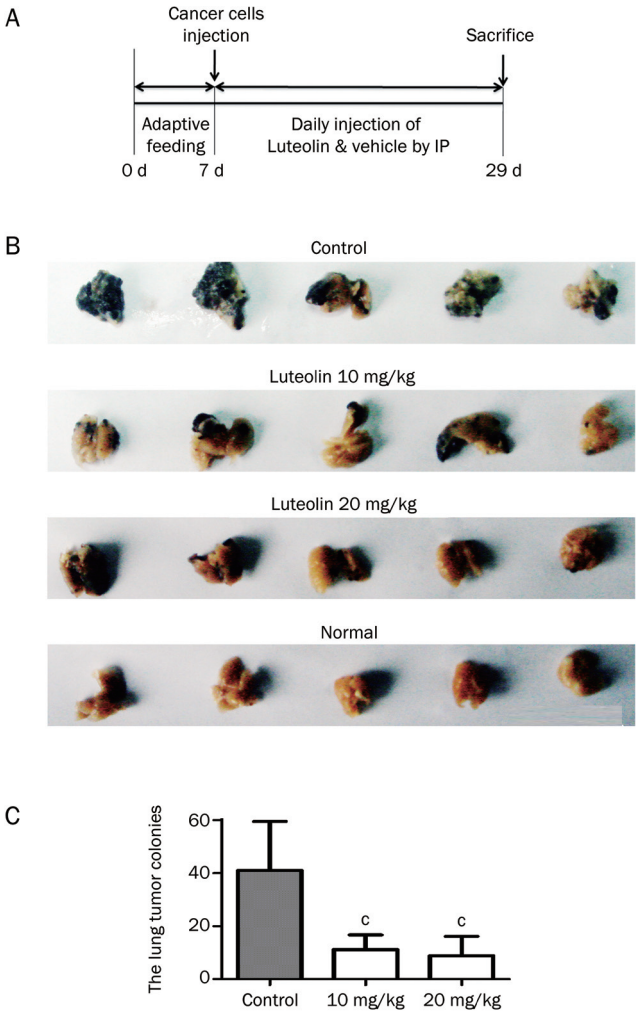

Figure 3. Luteolin inhibits the lung metastasis in B16F10 melanoma tumor. In the experimental metastasis model, all the mice were sacrificed on the 23rd day after tumor injection (A). Their lungs were then removed and fixed, metastatic foci at lung surfaces were photographed (B) and the number of lung metastases foci in each group were detected (C). Mean±SEM. n=5. ^{c}P<0.01 vs control.

systems, which have been indicated to be closely related to the hypoxic tumor microenvironment[18]. In this study, we demonstrated that hypoxia induced EMT in melanoma cancer cells, a phenomenon that has been previously demonstrated in breast cells, ovarian carcinoma cells and renal cell carcinoma[29–31]. Cadherin switching, which is also a key factor in the EMT process, plays a crucial role in cellular phenotype and biological behaviors[32]. The down-regulation of E-cadherin and the up-regulation of N-cadherin cause the cancer cells to be more invasive. The co-treatment of B16F10 cells with 1% O_2 and luteolin reduced the hypoxia-induced switching of E-cadherin to N-cadherin, supporting the hypothesis that luteolin is able to reverse EMT.

Moreover, we elucidated the possible mechanism underlying the control of EMT by luteolin. A variety of cell growth factors, such as HGF, FGF, EGF, IGF, VEGF, TGF, regulate the expression of E-cadherin and N-cadherin to enable EMT via nuclear transcription factors such as snail, slug, and ZEB1[18, 19, 33, 34]. First, the expression levels of E-cadherin regulation transcription factors such as snail, slug, ZEB1 and vimentin after the treatment of luteolin were determined. Whereas the expression of ZEB1 was inhibited by 10 μmol/L luteolin, snail and vimentin expression was regulated only by doses of luteolin that were higher than 25 μmol/L, luteolin did not significantly affect slug expression (Figure 2B). The expression of E-cadherin could be regulated by 5 μmol/L luteolin. Thus, luteolin likely controls EMT via other pathways.

Numerous studies have shown that the expression and function of integrins are involved in cancer metastasis[35]. Integrins affects cellular behaviors by both providing a docking space for ECM proteins on the cell surface and relaying molecular cues in the cellular environment, which affect morphology, growth, survival and the migration of the cells[36, 37]. This study verified that integrins could directly regulate the effect of EMT on the expression of FAK without requiring transcription factors. The down-regulation of β3 integrin that was induced by luteolin was accompanied by an up-regulation of E-cadherin (Figure 2A). The results suggest that luteolin inhibits hypoxia-induced EMT, at least in part by inhibiting the expression of β3 integrin. Consistently, the animal experiments also verified that luteolin was able to regulate the expression of β3 integrin and E-cadherin.

EMT was previously demonstrated to be closely associated with tumor metastasis. We confirmed the anti-metastatic effects of luteolin in melanoma cells by using an experimental metastasis model. Immunohistochemical assessment of lung tissues further validates the above *in vitro* results.

In conclusion, we have demonstrated that the biological function and activities of luteolin are sufficient to block the tumor progression in B16F10 cell line. In general, luteolin reversed cadherin switching, down-regulated EMT markers, moderated the expunging of cell-cell interactions, suppressed the invasiveness of B16F10 cells and inhibited the EMT process. Thus, luteolin might represent a potential chemopreventative and anticancer chemotherapeutic agent that can block the progression of tumors, specifically by reversing EMT in cancer cells.

Acknowledgements

This project was supported in part by the National Natural Science Foundation of China (No 81173174), the National Key Technologies R & D Program of China during the 11th Five-Year Plan Period (No 2008BAI51B02), the PhD Programs Foundation of Ministry of Education of China (No 20113237110008), the Natural Science Foundation of Jiangsu Province (Nos BK2010085 and 2010562), Jiangsu Provincial Projects of International Cooperation and Exchanges of Jiangsu Province I (SBZ200900175) Educational Commission of Jiangsu Province (No 09KJA360002), Six Talents Peak Topics in Jiangsu Province (08-A-012), Open Project of Jiangsu Key Laboratory for Pharmacology and Safety Evaluation of Chinese Materia Medica (P09013), Jiangsu College Graduate Research and Innovation

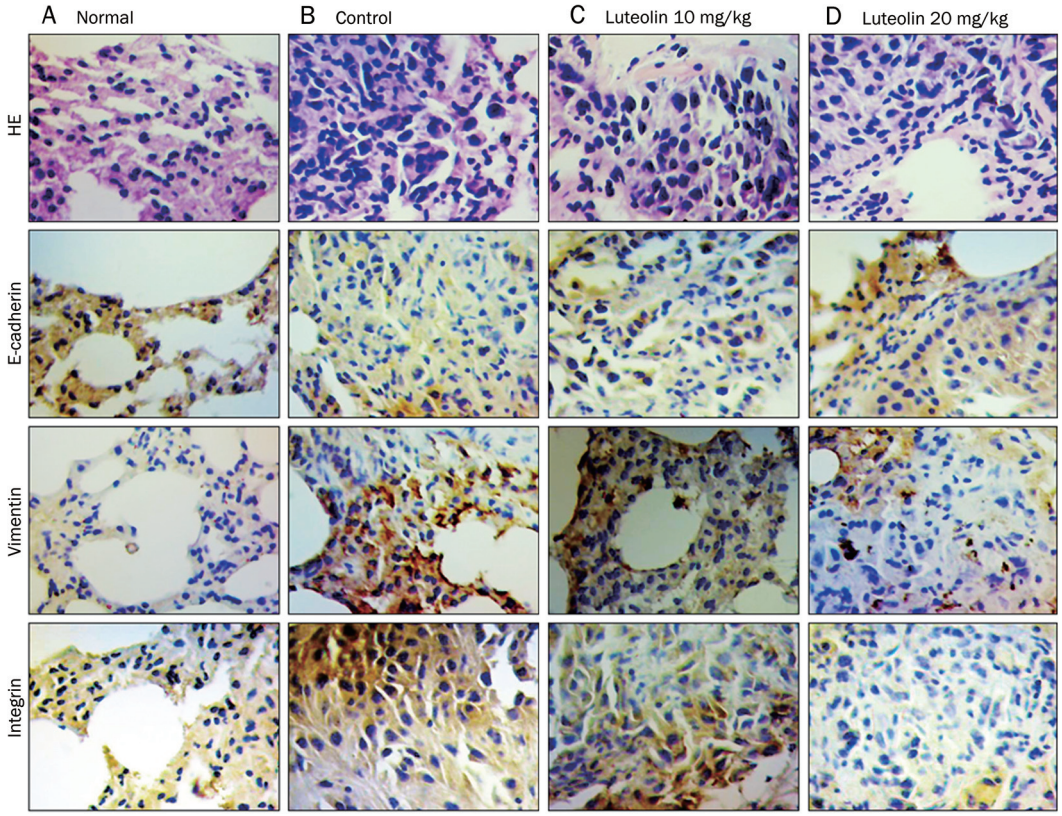

Figure 4. Luteolin reverses melanoma EMT *in vivo*. Immunohistochemical analysis of E-cadherin, vimentin, and β3 integrin protein expression in tumor tissue samples.

Projects (2012-622 and CXLX11_0771), and a project of the Priority Academic Program Development of Jiangsu Higher Education Institutions.

Author contribution

Jun-shan RUAN, Yu-ping LIU, Ai-yun WANG, Shi-zhong ZHENG, Shao-ming WANG, and Yin LU designed the study. Jun-shan RUAN, Yu-ping LIU, Lei ZHANG, Ling-geng YAN, Fang-tian FAN, and Cun-si SHEN performed the experiments. Jun-shan RUAN and Yu-ping LIU wrote the manuscript.

References

1 Hutchinson L. Skin cancer: Novel resistance mechanism revealed. Nat Rev Clin Oncol 2012; 9: 5.
2 Berk DR, LaBuz E, Dadras SS, Johnson DL, Swetter SM. Melanoma and melanocytic tumors of uncertain malignant potential in children, adolescents and young adults — the Stanford experience 1995–2008. Pediatr Dermatol 2010; 27: 244–54.
3 Virgili G, Gatta G, Ciccolallo L, Capocaccia R, Biggeri A, Crocetti E, *et al*. Incidence of uveal melanoma in Europe. Ophthalmology 2007; 114: 2309–15.
4 Weir HK, Marrett LD, Cokkinides V, Barnholtz-Sloan J, Patel P, Tai E, *et al*. Melanoma in adolescents and young adults (ages 15–39 years): United States, 1999–2006. J Am Acad Dermatol 2011; 65: S38–49.
5 Mani SA, Guo W, Liao MJ, Eaton EN, Ayyanan A, Zhou AY, *et al*. The epithelial-mesenchymal transition generates cells with properties of stem cells. Cell 2008; 133: 704–15.
6 Dave B, Mittal V, Tan NM, Chang JC. Epithelial-mesenchymal transition, cancer stem cells and treatment resistance. Breast Cancer Res 2012; 14: 202.
7 Kushiro K, Chu RA, Verma A, Nunez NP. Adipocytes promote B16BL6 melanoma cell invasion and the epithelial-to-mesenchymal transition. Cancer Microenviron 2012; 5: 73–82.
8 Sun H, Hu K, Wu M, Xiong J, Yuan L, Tang Y, *et al*. Contact by melanoma cells causes malignant transformation of human epithelial-like stem cells via alpha V integrin activation of transforming growth factor beta1 signaling. Exp Biol Med (Maywood) 2011; 236: 352–65.
9 Toh B, Wang X, Keeble J, Sim WJ, Khoo K, Wong WC, *et al*. Mesenchymal transition and dissemination of cancer cells is driven by myeloid-derived suppressor cells infiltrating the primary tumor. PLoS Biol 2011; 9: e1001162.
10 Lin K, Baritaki S, Militello L, Malaponte G, Bevelacqua Y, Bonavida B. The role of B-RAF mutations in melanoma and the induction of EMT via dysregulation of the NF-kappaB/Snail/RKIP/PTEN circuit. Genes Cancer 2010; 1: 409–20.
11 Alonso SR, Tracey L, Ortiz P, Perez-Gomez B, Palacios J, Pollan M, *et al*. A high-throughput study in melanoma identifies epithelial-mesenchymal transition as a major determinant of metastasis. Cancer Res 2007; 67: 3450–60.
12 Lin Y, Shi R, Wang X, Shen HM. Luteolin, a flavonoid with potential for cancer prevention and therapy. Curr Cancer Drug Targets 2008; 8: 634–46.
13 Zhou Q, Yan B, Hu X, Li XB, Zhang J, Fang J. Luteolin inhibits invasion of prostate cancer PC3 cells through E-cadherin. Mol Cancer Ther 2009; 8: 1684–91.
14 Jo M, Lester RD, Montel V, Eastman B, Takimoto S, Gonias SL.

Reversibility of epithelial-mesenchymal transition (EMT) induced in breast cancer cells by activation of urokinase receptor-dependent cell signaling. J Biol Chem 2009; 284: 22825–33.
15 Chen L, Lu Y, Wu JM, Xu B, Zhang LJ, Gao M, *et al*. Ligustrazine inhibits B16F10 melanoma metastasis and suppresses angiogenesis induced by vascular endothelial growth factor. Biochem Biophys Res Commun 2009; 386: 374–9.
16 Chen W, Lu Y, Wu J, Gao M, Wang A, Xu B. Beta-elemene inhibits melanoma growth and metastasis via suppressing vascular endothelial growth factor-mediated angiogenesis. Cancer Chemother Pharmacol 2011; 67: 799–808.
17 Zhang LJ, Chen L, Lu Y, Wu JM, Xu B, Sun ZG, *et al*. Danshensu has anti-tumor activity in B16F10 melanoma by inhibiting angiogenesis and tumor cell invasion. Eur J Pharmacol 2010; 643: 195–201.
18 Jiang J, Tang YL, Liang XH. EMT: a new vision of hypoxia promoting cancer progression. Cancer Biol Ther 2011; 11: 714–23.
19 Jing Y, Han Z, Zhang S, Liu Y, Wei L. Epithelial-mesenchymal transition in tumor microenvironment. Cell Biosci 2011; 1: 29.
20 Hakomori SI. Glycosynaptic microdomains controlling tumor cell phenotype through alteration of cell growth, adhesion, and motility. FEBS Lett 2010; 584: 1901–6.
21 Rhim AD, Mirek ET, Aiello NM, Maitra A, Bailey JM, McAllister F, *et al*. EMT and dissemination precede pancreatic tumor formation. Cell 2012; 148: 349–61.
22 Mani SA, Guo W, Liao MJ, Eaton EN, Ayyanan A, Zhou AY, *et al*. The epithelial-mesenchymal transition generates cells with properties of stem cells. Cell 2008; 133: 704–15.
23 Nakashima S, Matsuda H, Oda Y, Nakamura S, Xu F, Yoshikawa M. Melanogenesis inhibitors from the desert plant Anastatica hierochuntica in B16 melanoma cells. Bioorg Med Chem 2010; 18: 2337–45.
24 Selvendiran K, Koga H, Ueno T, Yoshida T, Maeyama M, Torimura T, *et al*. Luteolin promotes degradation in signal transducer and activator of transcription 3 in human hepatoma cells: an implication for the antitumor potential of flavonoids. Cancer Res 2006; 66: 4826–34.
25 Byun S, Lee KW, Jung SK, Lee EJ, Hwang MK, Lim SH, *et al*. Luteolin inhibits protein kinase C(epsilon) and c-Src activities and UVB-induced skin cancer. Cancer Res 2010; 70: 2415–23.
26 Tang X, Wang H, Fan L, Wu X, Xin A, Ren H, *et al*. Luteolin inhibits Nrf2 leading to negative regulation of the Nrf2/ARE pathway and sensitization of human lung carcinoma A549 cells to therapeutic drugs. Free Radic Biol Med 2011; 50: 1599–609.
27 Zhou Q, Yan B, Hu X, Li XB, Zhang J, Fang J. Luteolin inhibits invasion of prostate cancer PC3 cells through E-cadherin. Mol Cancer Ther 2009; 8: 1684–91.
28 Lin YS, Tsai PH, Kandaswami CC, Cheng CH, Ke FC, Lee PP, *et al*. Effects of dietary flavonoids, luteolin, and quercetin on the reversal of epithelial-mesenchymal transition in A431 epidermal cancer cells. Cancer Sci 2011; 102: 1829–39.
29 Zeng R, Yao Y, Han M, Zhao X, Liu XC, Wei J, *et al*. Biliverdin reductase mediates hypoxia-induced EMT via PI3-kinase and Akt. J Am Soc Nephrol 2008; 19: 380–7.
30 Sumual S, Saad S, Tang O, Yong R, McGinn S, Chen XM, *et al*. Differential regulation of Snail by hypoxia and hyperglycemia in human proximal tubule cells. Int J Biochem Cell Biol 2010; 42: 1689–97.
31 van MH, Verslype C, Windmolders P, van ER, Nevens F, van PJ. Characterization of a cell culture model for clinically aggressive hepatocellular carcinoma induced by chronic hypoxia. Cancer Lett 2012; 315: 178–88.
32 Theys J, Jutten B, Habets R, Paesmans K, Groot AJ, Lambin P, *et al*. E-cadherin loss associated with EMT promotes radioresistance in human tumor cells. Radiother Oncol 2011; 99: 392–7.
33 Thiery JP, Acloque H, Huang RY, Nieto MA. Epithelial-mesenchymal transitions in development and disease. Cell 2009; 139: 871–90.
34 Rhim AD, Mirek ET, Aiello NM, Maitra A, Bailey JM, McAllister F, *et al*. EMT and dissemination precede pancreatic tumor formation. Cell 2012; 148: 349–61.
35 Goetz JG, Minguet S, Navarro-Lerida I, Lazcano JJ, Samaniego R, Calvo E, *et al*. Biomechanical remodeling of the microenvironment by stromal caveolin-1 favors tumor invasion and metastasis. Cell 2011; 146: 148–63.
36 Qian F, Vaux DL, Weissman IL. Expression of the integrin alpha 4 beta 1 on melanoma cells can inhibit the invasive stage of metastasis formation. Cell 1994; 77: 335–47.
37 Selivanova G, Ivaska J. Integrins and mutant p53 on the road to metastasis. Cell 2009; 139: 1220–2.

Acta Pharmacologica Sinica (2012) 33: 1332–1336
 1671-4083/12 $32.00
www.nature.com/aps

Original Article

Pharmacokinetics and tolerance of dehydroandrographolide succinate injection after intravenous administration in healthy Chinese volunteers

Qian CHEN, Yun LIU, Yan-mei LIU, Gang-yi LIU, Meng-qi ZHANG, Jing-ying JIA, Chuan LU, Chen YU*

Central Laboratory, Shanghai Xuhui Central Hospital, Shanghai 200031, China

Aim: Dehydroandrographolide succinate (DAS) is extracted from herbal medicine *Andrographis paniculata* (Burm f) Nees. DAS injection is used in China for the treatment of viral pneumonia and upper respiratory tract infections. The aim of this study is to investigate the pharmacokinetics and tolerance of DAS injection in healthy Chinese volunteers.

Methods: This was a single-center, randomized, single-dose, three-way crossover design study. Nine eligible subjects were randomly divided into 3 groups, and each group sequentially received 80, 160, or 320 mg of DAS infusion according to a three-way Latin square design. Plasma and urine samples were collected and determined using an LC-MS/MS method. Safety and tolerability were determined via clinical evaluation and adverse event monitoring.

Results: For the 80, 160, and 320 mg dose groups, the mean C_{max} were 4.82, 12.85, and 26.90 mg/L, respectively, and the mean AUC_{0-12} were 6.18, 16.95, and 40.65 mg·L^{-1}·h, respectively. DAS was rapidly cleared, with a mean T_{max} of 0.94–1.0 h and a $t_{1/2}$ of approximately 1.51–1.89 h. Approximately 10.1%–15.5% of the intravenous DAS dose was excreted unchanged in urine within 24 h in the 3 groups, and more than 90% of unchanged DAS was excreted between 0 and 4 h. The pharmacokinetic profile was similar between male and female subjects. No serious or unexpected adverse events were found during the study, but one mild adverse event (stomachache) was reported.

Conclusion: This study shows that DAS has nonlinear pharmacokinetic characteristics. To guarantee the effective concentration, mul¬tiple small doses are recommended in clinical regimens.

Keywords: dehydroandrographolide succinate; herbal medicine; pharmacokinetics; tolerance; LC-MS/MS analysis

Acta Pharmacologica Sinica (2012) 33: 1332–1336; doi: 10.1038/aps.2012.79; published online 20 Aug 2012

Introduction

Dehydroandrographolide succinate (DAS, 14-deoxy-11, 12-didehydroandrographolide-3,19-disuccinate, Yanhuning) is obtained by extraction from the well-known herbal medicine *Andrographis paniculata* (Burm f) Nees, which belongs to the *Acanthaceae* family and the *Andrographis* genus (Figure 1). DAS is usually administered through injection after salification with potassium or a combination of potassium and sodium salt[1, 2].

In China, DAS injection is widely used for the treatment of viral pneumonia and viral upper respiratory tract infections because of its immunostimulatory, anti-infective and anti-inflammatory effect[3–5]. It has also been reported that DAS can show anti-atherosclerosis and anti-diabetic nephropathy effects by the regulation of intracellular signaling transduction and clearance of reactive oxygen species[6, 7].

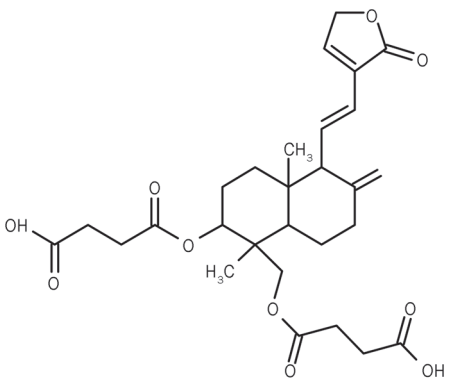

Figure 1. Chemical structure of DAS with the molecular formula $C_{28}H_{36}O_{10}$ and molecular weight 532.59 Da.

* To whom correspondence should be addressed.
E-mail clab001@126.com
Received 2011-12-22 Accepted 2012-05-22

Numerous traditional Chinese herbs and extracted drugs have been used in clinical treatment without safety and pharmacokinetic studies in humans, and their appropriate use has been determined based on thousands of years of experience. Injectable DAS is one of these types of drugs, and it is widely used in China. Only a few studies have been conducted on the pharmacokinetics of DAS tablets or injection in rabbit or rat plasma[8–10]. Currently, there is no information on human pharmacokinetics. The objectives of this study were to assess the pharmacokinetics, safety, and tolerance of DAS injection in healthy adult subjects and to evaluate the potential pharmacokinetic differences between male and female subjects.

Materials and methods

This study was approved by the Independent Ethics Committee (IEC) of Shanghai Xuhui Central Hospital. The study was conducted in accordance with the guidelines on good clinical practice recommended by the SFDA of China[11] and with the ethical standards for human experimentation established by the Declaration of Helsinki[12]. All of the subjects were informed of the study's aim, procedures, and risks by a clinical investigator. Each subject gave written informed consent to participate in the study.

Subjects

Healthy, nonsmoking Chinese males and females aged 18 to 40 years with a body mass index (BMI) between 19 and 25 kg/m^2 were recruited. Each subject met the following criteria: (1) no contraindication or sensitization response to DAS or any related drugs; (2) no history of significant cardiac, hepatic, renal, pulmonary, neurologic, gastrointestinal, or hematologic diseases; (3) no drug abuse, alcoholism or smoking in the recent year; (4) normal vital signs, physical examination, ECG and laboratory findings and negative for HIV and hepatitis B/C; and (5) no pregnancy or lactation for female subjects. Volunteers who took any prescription drugs two weeks before or during the study period or any over-the-counter remedies (including nutritional supplements) one week before or during the study period were excluded. Additionally, volunteers who suffered from serious disease, took part in drug trials, or donated blood in the prior three months were excluded.

Drug

DAS injection was formulated and supplied by Chongqing Yaoyou Pharma Co, Ltd (Chongqing, China). It is a yellowish powder, and each vial contained 80 mg of DAS (lot number 09081530).

Study design

This was a single-center, randomized, three-way crossover design study. Using a computer-generated table of random numbers provided by a statistician, nine eligible subjects were randomly divided into three groups and intravenously administered 80, 160, and 320 mg of DAS, respectively, in three treatment periods. Each subject received three intravenous doses of DAS according to the order of the three-way Latin square design (Table 1). The interval between two treatment periods was more than 7 half-lives.

Table 1. Dose of intravenous infusion of DAS injection received in 9 subjects during 3 treatment period

Group	*n*	Period 1	Period 2	Period 3
1	3	80 mg	160 mg	320 mg
2	3	160 mg	320 mg	80 mg
3	3	320 mg	80 mg	160 mg

For intravenous infusion, DAS was diluted in 250 mL of a 5% glucose injection and infused using a pump at a constant rate of 250 mL per 60 min.

Sample collection

Plasma and urine samples were collected and analyzed for DAS concentrations. Blood samples (3 mL) and plasma were collected predose and at 0.167, 0.33, 0.5, 1, 1.167, 1.333, 1.5, 2.0, 2.5, 3.0, 4.0, 6.0, 8.0, 10.0, and 12.0 h after dosing in each treatment period. The collected blood samples were centrifuged at 1500×*g* for 5 min at room temperature (25±5 °C) within 30 min of the collection time. The separated plasma was stored below -30 °C. Urine for the DAS assay was collected predose and 0–4, 4–8, 8–12, and 12–24 h after dosing in each treatment period. After the total volume of urine for each time range was measured, 6 mL was stored below -30 °C until analysis were conducted.

Drug analysis

A liquid chromatography tandem mass spectrometry (LC-MS/MS) method for determining DAS in human plasma and urine was established and validated[13]. The analytical method for the plasma consisted of the following steps: 50 μL of human plasma, 5 μL of internal standard (IS) working solution, and 100 μL of precipitant (acetonitrile/methanol, 90:10, *v/v*) were mixed by shaking in a 1.5-mL polypropylene tube for 10 s and centrifuged at 15000×*g* for 3 min. In total, 50 μL of the supernatant was diluted with 450 μL water/acetonitrile (60:40, *v/v*) in sample vials, and 2 μL of the dilution was injected to LC-MS/MS. The analytical method for the determination of DAS in human urine involved sample dilution and direct injection into the high-pressure liquid chromatography tandem mass spectrometry system (Applied Biosystems API 5500, CA, USA).

The lower limit of quantitation for the plasma and urine assay was 10 ng/mL, and the linear calibration range was 10–5000 ng/mL. Chromatographic separation was achieved on a Shiseido Capcell C18 MG III column (100 mm×2.0 mm id, 5 μm), which was preceded by a Phenomenex C18 guard column (4 mm×3 mm id, 5 μm particle size). The mobile phase consisted of 50/50 (*v/v*%) acetonitrile and water (containing 0.02% formic acid), and the flow rate was 0.3 mL/min. The

mass transitions were 531.2–99.0 (*m/z*) for DAS and 267.0–252.1 (*m/z*) for the IS.

Precision and accuracy were evaluated with six replicates of quality control (QC) samples at four different concentrations (10, 30, 500, and 4000 ng/mL) with three consecutive runs. The interday and intraday accuracy of the plasma and urine quality control samples were 95.3%–112.6% of nominal, and the interday and intraday precision were less than 7%[14].

Pharmacokinetic calculations

The pharmacokinetic parameters of DAS were estimated using a standard non-compartmental method[14] with Drug and Statistics software, version 2.1 (University of Science and Technology, Hefei, China). Individual serum concentration-time curves were constructed, and C_{max} and T_{max} were obtained by inspection of the plasma concentration data. AUC_{0-12} was calculated using the linear trapezoidal method for ascending concentrations and the log trapezoidal method for descending concentrations. $AUC_{0-\infty}$ was calculated as $AUC_{0-\infty}=AUC_{0-12}+C_{12}/k_e$, where C_{12} represented the last measurable concentration and k_e was the slope of the linear regression of the natural logarithm-transformed (ln) plasma concentration-time curve in the terminal phase. The plasma elimination half-life ($t_{1/2}$) was calculated using the equation $t_{1/2}=\ln 2/k_e$[14].

DAS urine concentrations, urine volumes from individual collection intervals, and nominal times of collection intervals were used to calculate urinary pharmacokinetic parameters. The amount of DAS excreted unchanged in the urine in each collection interval was determined by the product of the urine concentration and the urine volume. Ae_{0-24} is the sum of DAS collected over all collection intervals (0 to 24 h). The percentage of DAS dose recovered in the urine (urine recovery, $Ae\%_{0-24}$) in 24 h was calculated as Ae_{0-24} divided by the administered dose and multiplied by 100.

Safety and tolerance

Safety and tolerance were determined by clinical evaluation, including physical examinations, vital signs (body temperature, blood pressure, heart rate, and breathing rate), 12-lead electrocardiograms and laboratory measurements (hematology, serum chemistry, and urinalysis). Adverse events (AEs) were monitored throughout the study. All of the AEs were recorded and evaluated in terms of intensity (mild, moderate, or severe), duration, severity, outcome, and relationship to study drug. Serious adverse events (SAEs) were defined as death or life-threatening, led to disability, required hospitalization, or required medical intervention to prevent permanent impairment or damage.

Statistical analysis

DAS pharmacokinetic parameters (AUC, C_{max}, T_{max}, and CLz) were analyzed using an analysis of variance (ANOVA) model appropriate for the variances among dose groups. DAS pharmacokinetic parameter values between female and male subjects were analyzed using a *t*-test. Descriptive statistics were used to summarize demographic data and assess safety variables, including AEs, laboratory assays, vital signs and electrocardiograms. Adverse events are presented as reported frequencies and percentages.

Results

Study population

A total of 9 healthy male (n=6) and female (n=3) volunteers were enrolled in the study. All of the subjects were non-smokers, with a mean age of 24.3 years (range: 21.3-29 years), a mean weight of 57.4 kg (range: 49.0–69.8 kg) and a mean BMI of 21.1 (range: 19.1–24.0 kg/m^2). All of the participants completed the study as planned.

Pharmacokinetics

The mean plasma DAS concentration *versus* time profile is presented in Figure 2. The principal pharmacokinetic parameters of DAS are summarized in Table 2. Mean values of the time to peak plasma concentration (T_{max}) of the three dose groups ranged from 0.94 to 1.0 h. Plasma DAS concentrations declined rapidly, with short mean elimination half-lives of approximately 1.51–1.89 h. For the 80, 160, and 320

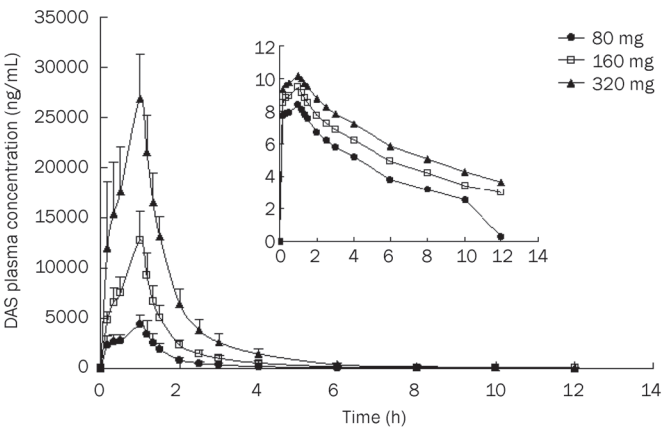

Figure 2. Mean plasma concentrations versus time profiles following single-dose intravenous administration of 80–320 mg DAS injection in Chinese healthy subjects.

Table 2. Pharmacokinetics parameters of DAS (mean±SD) following intravenous administration of DAS injection in healthy Chinese subjects (n=9). ^cP<0.01 *vs* 80 mg.

Parameters	80 mg	160 mg	320 mg
AUC_{0-12} (mg·L^{-1}·h)	6.18±1.09	16.95±2.48^c	40.65±7.53^c
$AUC_{0-\infty}$ (mg·L^{-1}·h)	6.21±1.10	16.99±2.49^c	40.74±7.53^c
$t_{1/2}$ (h)	1.51±0.37	1.80±0.26	1.89±0.34
T_{max} (h)	0.94±0.30	0.94±0.17	1.00±0.00
C_{max} (mg/L)	4.82±0.96	12.85±2.76^c	26.90±4.37^c
MRT_{0-12} (h)	1.41±0.13	1.48±0.14	1.54±0.13
CLz (L/h)	13.27±2.42	9.60±1.40^c	8.07±1.35^c
$Ae\%_{0-24}$ (%)	12.33±3.42	15.56±2.41	10.17±2.74

mg dose groups, mean C_{max} values were 4.82, 12.85, and 26.90 mg/L, respectively; mean AUC_{0-12} values were 6.18, 16.95, and 40.65 mg·L^{-1}·h^{-1}, respectively; and mean $AUC_{0-\infty}$ values were 6.21, 16.99, and 40.74 mg·L^{-1}·h^{-1}, respectively. The AUC and C_{max} of plasma DAS increased disproportionately to dose, while the clearance rate (13.27, 9.60, and 8.07 mL/min, respectively) decreased as the dose increased in the 80, 160, and 320 mg dose groups. The standardized C_{max} and AUC values of the 80 mg group were statistically significantly different (P<0.01) compared with the other dose groups (Table 3). Approximately 10.1%–15.5% of the intravenous DAS dose was excreted unchanged in urine within 24 h, and more than 90% of unchanged DAS was excreted from 0 to 4 h. Statistical comparisons indicated that none of the pharmacokinetic parameters were significantly different between female and male subjects (Table 4).

Table 3. The standardized pharmacokinetics parameters of DAS (mean±SD) based on 80 mg following intravenous administration of DAS injection in healthy Chinese subjects (n=9). ^{c}P<0.01 *vs* 80 mg.

Parameters	80 mg	160 mg	320 mg
AUC_{0-12} (μg·L^{-1}·h)	6.18±1.09	8.48±1.24^{c}	10.16±1.88^{c}
$AUC_{0-\infty}$ (μg·L^{-1}·h)	6.21±1.10	8.49±1.25^{c}	10.19±1.88^{c}
C_{max} (μg/L)	4.82±0.96	6.42±1.38^{c}	6.72±1.09^{c}
CLz (L/h)	13.27±2.42	4.80±0.70^{c}	2.02±0.34^{c}

Safety and tolerance

One mild adverse event was reported during the study. Subject 06 had a stomach ache 24 h post-dose (320 mg) in period 3, which resolved spontaneously in 2 h. No serious adverse events were reported. No clinically significant changes in laboratory values, vital signs, or electrocardiogram safety parameters were observed.

Discussion

In this study, pharmacokinetic parameters were not proportional to dose. AUC and C_{max} values increased slightly more compared with the dose among the 80 mg, 160 mg and 320 mg dose groups. In contrast, the plasma clearance rate was significantly less than dose proportional over the dose range. A similar phenomenon occurred in the rat pharmacokinetic study of DAS and may be attributed to the saturation of metabolic enzymes by the increase in dosage. This hypothesis can also explain the decrease in the clearance rate in the high-dose group. This result can guide clinical prescription to avoid an overdose of DAS and reduce the risk of possible accumulation after drug administration.

Plasma concentrations rapidly decreased from C_{max}, with a $t_{1/2}$ of approximately 1.51–1.89 h. Because DAS has a high C_{max}, a short $t_{1/2}$ and is less than dose proportional, multiple small doses are recommended. Infusion should be maintained at an appropriate speed to extend the effective period and avoid high dose accumulation. Urine pharmacokinetic data showed that the concentration of DAS in the urine decreased rapidly within 24 h after drug administration, and more than 90% of unchanged DAS was excreted within the first 4 h. However, for the 80-, 160-, and 320-mg dose groups, the urinary excretion of the prototype drug in urine were 12.33±3.42, 15.56±2.41 and 10.17±2.74, respectively. These results indicate that DAS injection is rapidly cleared from the plasma, and most DAS may be excreted after being transformed to metabolites.

The pharmacokinetic parameters of DAS were similar in both female and male subjects. However, the limitations of our study are that only a small number of female subjects were enrolled, and more observations are required in a further study to determined gender differences.

In conclusion, DAS injection is safe and well tolerated over the dose range (single doses of DAS injection up to 320 mg) of intravenous infusion in young, healthy male and female subjects. No serious or unexpected adverse events occurred during the study, and all of the subjects remained in good compliance. AUC and C_{max} increased slightly more with increasing dosage; however, plasma clearance showed a decreasing trend as the dose increased. DAS is rapidly cleared from the blood, and most of the drug was excreted after transformation to metabolites. This pharmacokinetic study showed that DAS has nonlinear pharmacokinetic characteristics. To guarantee the effective concentration, multiple small doses are recommended in the clinical regimen of DAS.

Table 4. Pharmacokinetics parameters of DAS (mean±SD) following intravenous administration of DAS injection in male and female Chinese subjects.

Parameters	80 mg		160 mg		320 mg	
	M (n=6)	F (n=3)	M	F	M	F
AUC_{0-12} (mg·L^{-1}·h)	6.02±1.02	6.51±1.39	16.37±2.06	18.11±3.33	37.79±4.82	46.36±9.78
$AUC_{0-\infty}$ (mg·L^{-1}·h)	6.04±1.03	6.53±1.38	16.40±2.07	18.16±3.33	37.89±4.81	46.45±9.78
$t_{1/2}$ (h)	1.57±0.45	1.40±0.08	1.74±0.23	1.93±0.23	2.04±0.23	1.59±0.22
T_{max} (h)	1.03±0.07	0.78±0.54	1.00±0.00	0.83±0.29	1.00±0.00	1.00±0.00
C_{max} (mg/L)	4.67±0.80	5.15±1.35	12.27±2.26	14.00±3.85	26.84±3.33	27.01±6.96
CLz (L/h)	13.61±2.59	12.58±2.37	9.89±1.28	9.02±1.72	8.56±1.06	7.11±1.55

M, male; F, female.

Acknowledgements

We acknowledge Yaoyou Pharma Co, Ltd (Chongqing, China) for providing dehydroandrographolide injection for the study and Wei WANG (Shanghai Xuhui Central Hospital, Shanghai, China) for her help in ECG reporting and clinical observation analysis.

Author contribution

Yan-mei LIU, Yun LIU and Chen YU designed the research; Yun LIU, Yan-mei LIU and Jing-ying JIA conducted the research; Gang-yi LIU, Meng-qi ZHANG and Chuan LU measured the concentration of DAS; Qian CHEN and Yun LIU analyzed data; Qian CHEN wrote the paper; and Chen YU critically revised the manuscript.

References

1 Pfisterer PH, Rollinger JM, Schyschka L, Rudy A, Vollmar AM, Stuppner H. Neoandrographolide from *Andrographis paniculata* as a potential natural chemosensitizer. Planta Med 2010; 76: 1698–700.

2 Liu XW, Fang Y, Wang Q, Li R, Tan JJ, Chao RB. Identification of main related substances in potassium sodium dehydroandrographolide succinate. Yao Xue Xue Bao 2010; 45: 641–6.

3 Akbar S. *Andrographis paniculata*: a review of pharmacological activities and clinical effects. Altern Med Rev 2011; 16: 66–77.

4 Deng WL, Liu JY, Nie RJ. Pharmacological studies on 14-deoxy-11, 12-didehydroandrographolide-3, 19-disuccinate. I. Anti-inflammatory activity (author's transl)]. Yao Xue Xue Bao 1980; 15: 590–7.

5 Chao WW, Lin BF. Isolation and identification of bioactive compounds in *Andrographis paniculata* (Chuanxinlian). Chin Med 2010; 13: 17.

6 Lee MJ, Rao YK, Chen K, Lee YC, Chung YS, Tzeng YM. Andrographolide and 14-deoxy-11,12-didehydroandrographolide from Andrographis paniculata attenuate. J Ethnopharmacol 2010; 132: 497–505.

7 Parichatikanond W, Suthisisang C, Dhepakson P, Herunsalee A. Study of anti-inflammatory activities of the pure compounds from *Andrographis paniculata* (burm.f.) Nees and their effects on gene expression. Int Immunopharmacol 2010; 10: 1361–73.

8 Xu XQ, Hu GL, Shen JC, Li Q, Wang XR. Determination of andrographolide and dehydroandrographolide in *Andrographis paniculata* nees materials and related patent medicines by reversed-phase high performance liquid chromatography. Se Pu 2002; 20: 446–8.

9 Han FM, Cai WT, Xia QS, Chen Y. Pharmacokinetics of dehydroandrographolide of Chuanxinlian Tablet in rat. China Journal of Traditional Chinese Medicine and Pharmacy 2005; 20: 206–9.

10 Zhang ZY, Liao GT, Wang BN. Pharmacoinetics study on monopotassium salt of 14-deoxy-11,12-didehdroandographolide-3,19-disuccinate (DAS-K). West China Journal of Pharmaceutical Sciences 1991; 6: 129–31.

11 State Food and Drug Administration of China. Guideline for Good Clinical Principles. Available at http://www.sda.gov.cn/WS01/CL0053/24473.html. Accessed August 6, 2003.

12 World Medical Association Declaration of Helsinki (WMA). Ethical Principles for Medical Research Involving Human Subjects. Adopted by the 18th WMA General Assembly, Helsinki, Finland, June 1964, and amended by the 52nd WMA General Assembly, Edinburgh, Scotland, October 7, 2000. Available at http://www.wma.net/e/policy/b3.htm. Accessed September 20, 2007.

13 Li SJ, Yang D, Zhang M, Zhou J, Li R, Lu C, *et al*. Determination of dehydroandrographolide succinate in human plasma by liquid chromatography tandem mass spectrometry (LC-MS/MS): Method development, validation and clinical pharmacokinetic study. J Chromatogr B Analyt Technol Biomed Life Sci 2010; 878: 2274–9.

14 Center for Drug Evaluation, State Food and Drug Administration of China. Guidance for clinical pharmacokinetics studies of chemical drug. Available at http://www.cde.org.cn/zdyz.do?method=largePage&id=2070. Accessed March, 2005.